Fitzgerald, Scott K. (2024) *Investigating stimulated luminescence within complex silicates to explore charge mobility and trap distribution.* MSc(R) thesis.

Investigating stimulated luminescence within complex silicates to explore charge mobility and trap distribution.

Scott K. Fitzgerald

A thesis presented for the degree of Master of Science (Research)

Abstract

The mechanisms behind charge storage and transport within feldspars are of key research interest to explain and model the observed behaviours of irradiated feldspars following stimulation. There is no general consensus on whether infra-red stimulated luminescence (IRSL) in feldspars is due to a single fundamental trap or multiple traps, or whether relaxation mechanisms are tunnelling derived or charge movement through band-tail states and conduction band.

Four separate investigations, using 22 feldspar samples which were previously used in several studies of feldspar luminescence, from four feldspar families (K-Feldspar, Albite, Plagioclase and Microcline samples as well as the F1 IAEA standard material), have been conducted to examine how post-IRSL phenomena can be used to model charge storage and transportation within the material lattice of feldspars. The investigations included the measurement of both post-IR post-stimulation phosphorescence (PSP) and post-IR photo-transferred thermoluminescence (PTTL) at different temperatures and following different stimulation wavelengths to characterise variability in relaxation times on the order of microseconds to minutes.

This work highlights the intrinsic complexities of the lattices of feldspars, noting that most changes made appeared to have a measurable effect on either the decay lifetimes or the PTTL peak activation energies or lifetimes. This implies that a distribution of trapping systems must exist within the lattice to allow the observed variability in behaviour. The decay lifetimes of the post-IR PSP decay corresponded to the lifetimes of the PTTL peaks, suggesting a relationship between the two phenomena. This was then exploited by first modelling the potential activation energies of PTTL peak lifetimes that were approximately equal to the computed PSP decay component lifetimes at room temperature. A cryogenic investigation then confirmed that these predicted PTTL peaks were observed, for the first time, in feldspars.

These results demonstrate that, within feldspars, post-IR PTTL and PSP are representative of charge storage in multiple trap systems and transport of charge can be described by band-tail state movement post-stimulation, with no evidence of significant tunnelling.

Declaration

The material presented in this thesis summarises the results of independent research carried out at the Scottish Universities Environmental Research Centre (SUERC), East Kilbride. The research was supervised by Professor David Sanderson (SUERC), Dr. Alan Cresswell (SUERC), and Dr. Loic Martin (SUERC).

This thesis is the result of my own research, and any published or unpublished work of other researchers has been given full acknowledgement in the text.

Signed:

March, 2023

Contents

List of Figures

1. Introduction

Luminescence is the emission of photons from an insulator or semiconductor and has been described as "the memory of accumulated exposure to nuclear radiation" (Aitken, 1998). This exposure memory relates the trapping of electrons in defect positions within their host lattice because of interactions with ionising radiation at some point in the host material's history, before being emitted as a detectable photon. Most importantly, the wavelength (λ) of this emitted photon is not related to the energy of the incident radiation but is dependent on the nature of the host material lattice (McKeever, 1985).

Geochronology is a key area of study into our planet's history and requires measurement techniques which are sensitive enough to probe up to millions of years into the past. In this regard, luminescence dating is one of the few techniques that can be used to determine the age of silicate-bearing sediments and artefacts. This is particularly the case when considering deposition of sedimentary material across an area as luminescence dating will be able to determine the last period of sunlight exposure rather than the initial exposure upon weathering of the sediment grains from the parent rock or sediment. Obtaining an accurate chronology of depositional events is especially important in relation to studies of climate change and environmental reconstruction (Aitken, 1998).

Geochronological research only includes a small sample of luminescence applications and more will be discussed later in this chapter, but luminescence studies have an increasing relevance to science and the world at large today.

1.1 Theoretical Overview

1.1.1 Stimulated Luminescence

The electronic structure of silicate minerals consists of electron filled valance bands and empty conduction bands with a band gap between them. The properties of these bands can vary across materials and are affected by physical conditions within the crystal lattice structure of silicate minerals, such as by impurities and defects. This can create different intermediate levels within the energy band gap.

Enclosed in sediments, minerals will be exposed to ionizing radiation, which will create free electrons and holes within the atomic structure (Cameron, 1991). In the case of complex silicate materials, most of these free electrons and holes will relax over time, but some of these free charge carriers can become trapped at intermediate energy levels. This trapped charge can be released, with energy released as single photons of light, via stimulation by either heating the material (known as thermoluminescence, TL) or exposure to light (photo-stimulated luminescence, PSL). PSL is differentiated by the range of wavelengths used during stimulation and includes infra-red stimulated luminescence (IRSL), optical wavelengths (OSL), and violet light (VSL). Stimulated materials with trapped electron states or holes produce a detectable photon count. This detectable count is a measure of the accumulated radiation dose and is exploited for radiation dosimetry and for dating in both geology and archaeology via luminescence spectroscopy. Luminescence based research is a key tool used by modern scientists to probe ancient systems such as previous climate cycles and geological processes (Mejdahl, 1985; Aitken 1985; Preusser et al 2008; Duller 2008), as well as archaeological research (Anthony et al. 2001) and general dosimetry research such as the detection of irradiated foods (Sanderson et al 1988; Sanderson 1991; Sanderson et al 1996, 2003a, 2003b).

This phenomenon will be further explored and discussed in Section 2. The investigation detailed in this thesis will involve the use of PSL/IRSL and TL.

1.1.2 Stimulated Luminescence in Feldspars

Luminescence spectroscopy is a powerful tool which is used by scientists to study defects in feldspars. These defects interact with electromagnetic radiation by absorption and emission of photons through photo-electric interactions that can result in the spontaneous and measurable emission of photons (luminescence). When used in spectroscopy this luminescence can vary based on the method used to study it, varying from optically stimulated luminescence/photostimulated luminescence, radioluminescence and thermoluminescence; these investigative methods involve the use of stimulation by photons, ionizing radiation, or applied heat, respectively.

IRSL in feldspars was first reported by Hütt et al. (1988) who reported the existence of an electron trap at 2eV which could be stimulated indirectly using a xenon lamp with optical filters that allowed near-IR stimulation with photon energies ~1.4eV. This generated considerable research interest in the phenomenon and resulted in other laboratories using infra-red LED arrays for photostimulated luminescence (PSL) research into the optical detrapping process (Bailiff et al. 1989). Following these initial works, which measured IRSL response in feldspar minerals at a range of temperatures, several models were developed to describe the observed excitation spectrum of potassium feldspar. Hütt proposed that the transport of charge carriers from the ground state to an excited state from where, on account of an additional thermal activation energy the carriers enter the conduction band and subsequently recombine with emission centres.

Later investigations into the luminescence properties of feldspars (Sanderson et al. 1988; Clark & Sanderson, 1994) used an excitation spectrometer with a xenon lamp and a monochromator to demonstrate a variation in response to stimulation from two different IR (840nm and 900nm) and green (590nm) wavelengths reflecting variations in the mineralogy of the samples. Since the xenon lamp has strong IR emission lines (with clusters of lines in the 820-840 nm region and from 880-900 nm) raw excitation spectra contained multiple power-modulated IR stimulation peaks. However, when spectra are power normalised, or alternative light sources used, the main IR resonance bands can be seen as broad excitation continua (Bailiff and Poolton, 1991; Bailiff and Barnett, 1994; Clark and Sanderson 1994, Poolton et al. 2002a, b). This result highlights differences in sample trap structure and distribution across feldspar families. The Clark and Sanderson study reported that the PSL sensitivity varied by three orders of magnitude across the sample set, whereas the peak ratio of the selected wavelengths varies by less than an order of magnitude. This indicated that the traps responsible for the luminescence signals vary between different feldspars, and that the differences in response to different stimulation wavelengths reflected differences in trap properties. Further work by Clark (1992) and Clark and Sanderson (1994) looked at the PSL spectra of feldspars using a scanning spectrometer with a 300 W Cermax xenon lamp and a tungsten-halogen lamp. This further work recreated the peaks discovered by Hütt et al. (1988), while also noting the existence of multiple components in the PSL spectra which varied in their thermal stability, suggesting that multiple traps of different activation energies were contributing to the PSL spectra. The results from these investigations indicated that the mobility of free charge through the band-tail states in feldspars via shallower/deeper traps was responsible for stimulation response mechanisms and accounted for delayed emission phenomena such as phosphorescence and phototransferred thermoluminescence (PTTL).

The specifics of the mechanism of IRSL production in feldspars remains an ongoing question of the roles of single (Kars et al 2013; Andersen et al 2012; Jain et al 2015) or multiple trapping states (Bailiff and Barnett 1994; Clark and Sanderson 1994). Baril and Huntley (2003) reported a difference in the luminescence spectra and the phosphorescence spectra of 13 cut rock feldspars and 20 feldspar separates and noted a luminescence dependence on the mode of excitation. Baril and Huntley (2003) also suggested that only certain traps were interacting with the luminescence centres and stated that models “involving recombination via a ‘conduction band’ in the traditional sense cannot account for these observations” and raised the possibility for modelling the recombination as “direct tunnelling of the electron from the excited level of the trap to the luminescence centre.”

Short (2003) reported that the sample emission intensity increased with sample temperature for all samples, with intensity of some samples plateauing above 80°C, and one feldspar sample’s intensity decay being unaffected by temperature. Short attributed this thermally independent decay rate to “quantum tunnelling from a principal trap responsible for IRSL emission”. Huntley et al. (2007) investigated eight plagioclase samples and suggested that this principal trap in plagioclase feldspars had a tunnelling rate which was related to the Ca content of the feldspar sample.

Murray et al. (2009) explored the relationship between TL and IRSL further, reporting that charge released during IRSL and TL occupied the same network of shallow traps, indicating a charge transport mechanism during excitation and relaxation. Murray et al. also noted that there was a clear relationship between IR stimulation and the loss of TL signal at 140°C but stated that this lost TL signal did not contribute to IRSL.

Jain and Ankjærgaard (2011) put forward a revised model for IRSL in feldspars based on the concept of feldspars having a single fundamental trap. Jain and Ankjærgaard proposed that the observed behaviour of stimulated feldspar samples, such as through processes like photoluminescence, could be explained using quantum tunnelling. This model was supported by Andersen et al. (2012) who stated that based on Red-IR excitation (700–1050 nm) of three samples "luminescence spectroscopy as a function of preheat temperature and stimulation temperature in K-feldspars arise from a single electron trapping centre". Andersen et al. suggested that "the dosimetric signals, IRSL, and the post IR-IRSL in K-feldspars arise from a single electron trapping centre". Also noted are the interactions between excited electrons with either the band tail states or the conduction band in transition processes akin to hydrogen atom transitions (Huntley et al. 2007; Thomsen et al. 2011; Andersen et al. 2012; Kumar et al. 2018). The extent of these interactions is noted as being temperature dependent (Jain et al. 2011). Li and Li (2011a) reported that when K-Feldspar grains were subjected to an IRSL signal at 50°C, then at 100-200°C, there was a stability dependence based on the stimulation time and the sample temperature. Li and Li concluded that the IRSL signal obtained at 50°C was from the shallow traps, while the post-IR IRSL obtained from the 100-200°C temperature range was composed of charge released from the deeper traps.

In practice, this predicts that charge carriers released during either thermal decay or IRSL/OSL/TL stimulation do not necessarily travel to the nearest recombination centre and can recombine at centres further from the trap through quantum tunnelling – however the probability of this distant recombination will decrease the further from the trap this centre is. This result was supported by a recent study (Lamothe et al. 2020) which reported that after stimulation, a sizeable proportion of recombined charge remained available for further tunnelling near the "principal trap", suggesting that while the vast majority of charge does not travel far from the principal trap, it can travel to farther centres. The study by Lamothe reasoned that during the heating process, the charge carriers have increased access to band-tail states, allowing them to “random walk” from the trap and then recombine at centres located at further distances from the principal trap (Morthekai et al. 2012). It should be noted that, despite decades of research the exact defect which forms the principal trap has not yet been directly identified (Bonfiglioli et al. 1959; Short, 2003; Riedesel et al. 2019) but a study detailed by Riedesel et al. (2019) looked at determining the width of band-tail states of a small range of feldspar via optical probing and reported that an approximate trap or cluster of traps existed at a depth of about 2.04 eV and that an excited state energy at 1.44eV. While the study noted that the depth of the probed trap(s) and the associated main excited state seemed to be independent of feldspar composition, the difference between the width of the band-tail states accessible from the ground state of the trap(s) and the full sub-conduction band-tail width seemed to be related to sample K-content.

The key problems in the literature surrounding the single fundamental trap interpretation of IRSL in feldspars are centred around a few key points. As described previously, some studies such as Andersen et al. (2012) and Short (2003) observe behaviour which they attribute to charge packets tunnelling from a fundamental trap to a recombination centre from a small selection of samples. Baril and Huntley (2003) makes passing reference to tunnelling as a possible explanation of why only certain traps were interacting with the luminescence centres. However, this passing reference to tunnelling as an explanation for this phenomena is equal to not mentioning tunnelling at all. Furthermore, the description of feldspars as having a fundamental trap for the purpose of stimulated luminescence is at odds with the results of earlier TL exploration of feldspars, such as those reported in Sanderson et al. (1988) and Spencer (1996), these TL investigations revealed a complex network of TL peaks.

1.1.2 Current Uses

Luminescence Dating

Luminescence dating is a technique which sees use across several disciplines. It is used to determine the age of a material by recording the intensity of the signal released when the material is stimulated, either optically or thermally, to determine the equivalent dose the material has been exposed to (Daniels et al. 1953; Anthony et al. 2001; Li and Li, 2011; Guralnik et al. 2013; Schmidt and Kreutzer, 2013). When this equivalent dose has been obtained it is then compared with the dose rate, which is the rate at which the material has been dosed by ionizing radiation, and an age can then be calculated using the following:

$$\text{Age} = \text{Equivalent dose}/\text{Dose rate}$$

This age is the time which has passed since the last zeroing event which had previously cleared the material of stored charge. From this zeroing event, trapped charge is assumed to accumulate due to ionizing radiation from both the material itself and its surroundings at a rate assumed to be constant for the dating period. This technique is used to date events on a 10^2-10^6 year timescale (Klasen et al. 2016).

Stimulated luminescence in personal dosimeters

Typically consisting of calcium fluoride or lithium fluoride, thermoluminescence dosimeters contain several impurities within their crystal lattices to function as trapping site for energetic electrons when they are exposed to ionizing radiation (Muniz et al. 1999; Horowitz and Yossian, 1995; Izewska and Rajan, 2012). These introduced impurity trapping sites are chemically stable, holding the energetic electrons in a higher energy level until they are heated, whereby these trapped electrons drop to lower energy levels and release a detectable photon.

The intensity of these emitted photons is a measure of the dose absorbed by the dosimeter. However, TLDs may only be read once because the read-out process destroys the stored information and effectively zeros the dosimeter again.

OSL dosimeters work in a similar way to TL dosimeters, with the key difference being the materials used in the dosimeter design and the readout method. OSL dosimeters usually consist of aluminium oxide which is placed behind different filters – usually an open window, aluminium, copper, and plastic. These different materials are used to filter out X-Ray, gamma, and beta radiation for simultaneous measurements.

Within this type of dosimeter, the carbon doped aluminium oxide acts to trap charges freed up by ionizing radiation passing through the crystal lattice. As such the number of trapped charges within the dosimeter is proportional to the dose received. Measurement of the dosimeter occurs by subjecting the aluminium oxide to a flash of light and recording the intensity of the induced luminescence. OSL dosimeters can be read out more than once due to the measurement not completely emptying the traps where the charges are stored.

1.2 Project Aims

As outlined in 1.1.2 there exists a problem in the literature regarding the modelling of charge trapping and mobility within feldspars following stimulation. These are important mechanisms to understand how these processes work will allow more accurate measurements and description of these phenomena – allowing more precise dating or detection.

This thesis aims to use stimulated luminescence to determine the model which best describes charge storage and transport within an array of complex silicates. The work presented here investigates a variety of up to 22 feldspar samples from four distinct feldspar families (including K-Feldspar, Albite, Plagioclase and Microcline samples as well as the F1 IAEA standard material) which were used by previous studies (Clark and Sanderson, 1994; Fitzgerald, 2020; Fitzgerald et al. 2022) and characterised by SEM analysis to model the storage and movement of charge within these samples.

The samples were first investigated using a modified SUERC portable OSL reader with 890nm and 940nm LEDs as stimulation sources. This experiment built on previous work (Clark, 1992; Fitzgerald, 2020; Fitzgerald 2022) and measured the IRSL response and the post IRSL decay from each of these samples to determine the effect that different stimulation wavelengths have on the post stimulation phosphorescence (PSP) decay. This phenomenon, as will be discussed in later sections, is a key indicator of charge mobility within the sample lattice. As such, being able to measure this decay to observe the variance, if it exists, across the sample set will be needed to understand the effect that the complex lattice structures of feldspars have on this mechanism.

The samples were also investigated at microsecond-order timescales with the use of a modified SUERC excitation spectrometer with a fast MCS card (Multi-Channel Scaler). This used the same samples and stimulation wavelengths as discussed above but investigated how the post stimulation phosphorescence decay varies at microsecond order timescales as the stimulation temperature is adjusted. The temperature range was constrained between -100°C and 100°C. Similar investigations have been previously conducted in literature (Chithambo, 2007; Ankjærgaard and Jain, 2010ab; Jain and Ankjærgaard, 2011; Morthekai et al. 2012). This experiment aimed to evaluate the frequency factor for the states responsible for this decay, and compare them with those which had been estimated for the decays measured at room temperature on the SUERC portable reader.

The samples were then investigated using a combination of the modified SUERC portable OSL reader, a SUERC TL reader, and two different Risø readers. This investigated PTTL in these samples following IR stimulation in order to characterise the activation energies and lifetimes of the states responsible for the post-stimulation decays which were explored in the investigations described above. Similar investigations have been conducted in the literature (Bailiff et al. 1977; Kim et al. 2018; Chithambo et al. 2018; Fitzgerald et al. 2022). This experiment aimed to calculate the activation energies of these states across the sample set.

A final investigation was conducted on a sub-set of samples following the results obtained from the three investigations described above which predicted the existence of thermally unstable TL peaks which would be measurable at cryogenic temperatures. This investigation was a novel cryogenic experiment using the SUERC stimulation spectrometer as a TL reader and aimed to probe thermally unstable charge storage sites by stimulating the samples at cryogenic temperatures and measuring the post-IR PTTL. This investigation aimed to verify that these predicted thermally unstable sites existed.

2 Research Background

2.1 Feldspar Structure

Feldspars comprise a family of minerals accounting for almost half of the mass of the Earth's crust (Rudnick et al. 2003). The structure of feldspar crystals is based on aluminosilicate tetrahedra, with silicon or aluminium ions surrounded by four oxygen ions, with each oxygen ion forming part of a neighbouring tetrahedron.

Charge balance is provided by cations (sodium, calcium, potassium, or barium). Compositionally they can be grouped as alkali feldspars (containing potassium or barium with varying sodium content) and plagioclase feldspars (containing sodium and calcium in varying proportions). Major alkali feldspar groups include orthoclase ($KAlSi_3O_8$ with a monoclinic structure), microcline ($KAlSi_3O_8$ with a triclinic structure), sanidine ($(K,Na)\ AlSi_3O_8$) and anorthoclase ($(Na,K)\ AlSi_3O_8$). Plagioclase groups range from albite ($NaAlSi_3O_8$) to anorthite ($CaAl_2Si_2O_8$). The structural state of feldspars is controlled by thermal history, with regards to the cooling rate of the parent rock following crystallisation (Alexander, 2007).

Broadly the complex compositional forms of feldspars can be represented on a ternary diagram (Figure 2.1) (Deer et al. 1996).

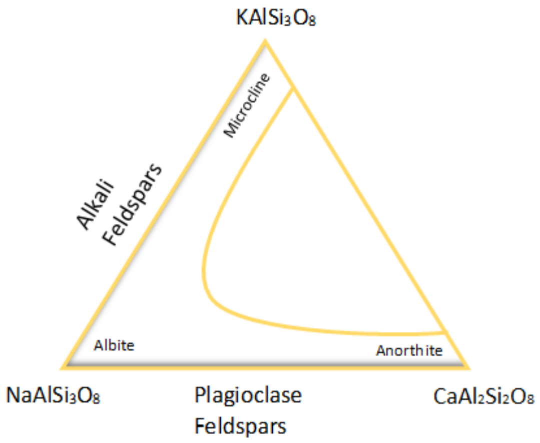

Figure 2.1 – Example of a ternary diagram which highlights the different families of feldspars.

2.2 Band Theory of Solids

The energy band model originated in 1928, developed by Felix Bloch, and is fundamental to understanding the properties of solids in modern physics. Bloch's model supposes that for a large number N of identical atoms in a region, these atoms are placed so far apart that their interactions with each other are negligible. As such, all these atoms have the same energy level diagram, allowing an energy level diagram to be determined for the entire system of atoms. This allows the exclusion principle (that every electron must occupy one quantum-mechanical state) to be applied, permitting each state to be occupied by N electrons instead of just one.

The theory then states that as the atoms in this system are uniformly pushed together factors such as electrical interactions and the exclusion principle will cause the wave functions of the valence and inner electrons to distort. However, the inner electrons will be less affected than the valence electrons, causing a sharp energy level gap. The corresponding energies also shift as a result, with the valence electron wave function becoming less localised and extending over more atoms. This gives the system a state of the form such that what could once accommodate N electrons now has energy states of N closely spaced levels (Figure 2.2). Between these levels are forbidden gaps where there are no allowed energy levels (Young and Freedman, 2014).

The nature of the energy bands determines the material's electrical conductivity properties. The occupation and spacing of these bands are important in this regard and is referred to as the energy gap.

A material is classed as an insulator if, at a given temperature, the valence band is filled and the next highest band, the conduction band, is completely empty.

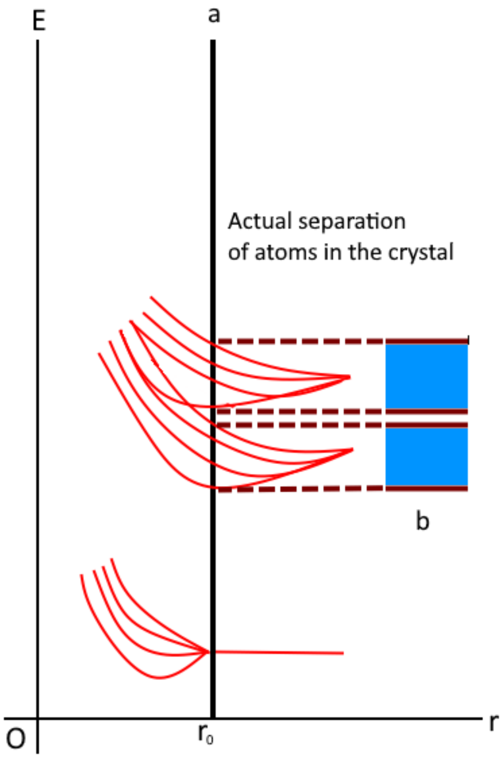

Figure 2.2 – A diagram recreated from Young and Freedman (2014) showing the origin of energy bands in a solid. (a) has the distance between atoms; (r) decreases, the energy levels spread into bands. The vertical line at r0 shows the actual atomic spacing in the crystal. (b) represents the symbolic representation of energy bands.

Feldspars are insulating crystals, with their luminescence properties being determined by a small proportion of impurity atoms that reside within lattice defects. As such, the electron energy states within the crystal lattice can be considered as derivatives of the energy states which exist in the individual atoms or ions which compose the lattice. Depending on the lattice defects within a specific feldspar, an energy level within the feldspar may take the form of several discrete band levels or a continuous distribution of band levels because of electronic transitions between ions in free space across these levels. As such, the shape of absorption and emission spectra can be strongly affected by the characteristics of the feldspar lattice crystal.

The narrow energy levels which exist in the ions in free space that were discussed above are expanded into valence bands in the lattice (B and C in Figure 2.3). As feldspars are insulators, these bands are filled by electrons and as such electrical conduction cannot take place within these bands even if electrical fields are applied. Above the valence bands there is an empty band (A in Figure 2.3) corresponding to the states of freed electrons called the conduction band. Any transition into the conduction band from the valance band results in a positively charged hole in the lattice which can create a current.

Furthermore, lattice defects can result in localised (electron) states forming between the band levels within the feldspar crystal (D and G in Figure 2.3). An electron may be raised into the conduction band from the valance band, or from the localised electron states by processes such as photoconduction (where an incident photon can knock a trapped electron into the conduction band by imparting enough energy into it). However, if the electron is not given sufficient energy through this interaction it will remain within an electron trap (G) or remain in a bound excited state (D) which would result in no photoconduction within the lattice until more energy is applied to it. Once excited, charges can return to the ground state through luminescence centres where electrons and holes recombine.

This process occurs in two stages, with the freed charge ionizing before dropping from the conduction band to an excited state and then from this excited state to a trapping site (from D to G in Figure 2.3). During the second part of this transition, light can be emitted by the transient freed charge losing energy when it recombines, the wavelength of this emitted photon corresponds to the energy lost during this process. The traps located within the localised electron states are normally empty and are filled by capturing charges which are excited by various processes over time – the study of the charge held by these traps is applied to numerous disciplines, as summarised in the previous section.

As electrons are fermions, each lattice energy state can only have one electron. The distribution of these energy states is temperature dependent, as at absolute zero each available energy state will be filled by one electron from the ground state to the fermi energy (the maximum energy of a state). For increasing temperatures above 0K, each state can only be occupied by one electron but the probability that some of the electrons can have energies greater than the fermi energy increases. This is described by the Fermi-Dirac distribution.

Depending on the feldspar lattice structure, the defect-induced electron traps can be energetically close enough to the conduction band such that electrons from these electron traps can be excited to the conduction band by either photoconductive or thermal processes, both of which are used in luminescence spectroscopy (Levy, 1985; Alexander, 2007; Visocekas et al. 2014; Reidesel, 2020; Kumar, 2019).

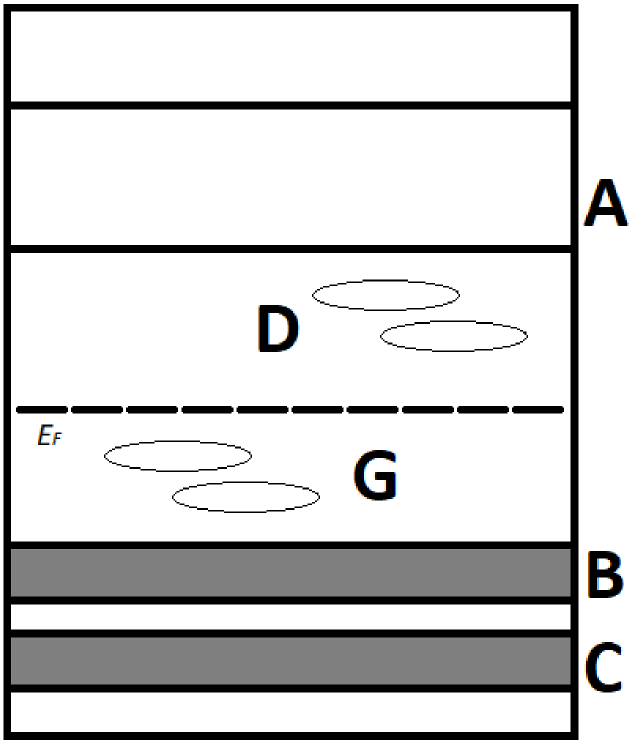

Figure 2.3 – Feldspar band levels. A represents the empty band, B and C are the valence bands, D represents the excited electron states excited states and G represents electron traps. E_f is the Fermi energy, which denotes the highest energy level that freed charge can attain at absolute zero.

2.3 Luminescence Modelling

2.3.1 Charge Storage and Mobility

A further process to consider when discussing luminescence in feldspars is the idea of retrapping. This is where trapped electrons that are freed by stimulation become recaptured within localised electron states without a detectable photon being emitted. As such, an expanded view is needed when considering the behaviour of charge movement and storage within the crystalline structures of feldspars. While work on modelling this phenomenon had started in the pre-war scientific community, with Jablonksy (1935) being the first to investigate the effect that temperature had on the production of phosphorescence over time, it was Randall and Wilkins (1945a, b) who are credited with laying the foundations of phosphorescence and thermoluminescence modelling. Randall and Wilkins reported that the frequency of the retrapping is strongly related to the number of electron traps or luminescence centres within these localised electron states, and that this is closely related to the lattice structure of the host crystal. Also worth considering is the energy carried by the freed electron, and the proclivity of these trapping sites/luminescence centres to capturing excited electrons – and whether this proclivity is altered by the imparted energies of the electrons.

To model the charge storage and mobility within feldspars – or indeed any material capable of phosphorescence, one must create a situation where all the luminescence centres are filled by continually irradiating the sample. If this irradiated material has yet to have any traps filled, and more luminescence centres than traps, then further irradiation while the luminescence centres are filled will ensure that all the excited electrons will end up captured by the empty traps. Following this continued irradiation there are no empty luminescence centres, and all the excited electrons will be captured by the formerly empty traps. As the traps are filled, the luminescence centres are emptied by emission processes and subsequently capture the electrons that are released from the traps, causing detectable luminescence. The intensity of this luminescence increases with time and reaches an equilibrium value when all the traps are filled. Randall and Wilkins (1945b) derived a relationship which described the growth of luminescence in the above scenario over time.

$$\frac{dN}{dt} = I_e - A_2(n - n_1 + N)N - A_1 n_1 N \qquad [2.1]$$

Where N is the number of electrons in the conduction band per unit volume, t is unit time, n is the number of traps per unit volume, n_x the number of empty luminescence centres per unit volume, A_x the constants expressing the relative probability of capture of an electron by an empty trap and empty luminescence centre, and I_e the intensity of the exciting light. $\frac{dN}{dt}$

represents the rate of recombination for free electrons with either electron traps or recombination centres.

[2.1] represents the starting state of the scenario described in the above paragraph. At this stage, with $\frac{dN}{dt} = 0$ and $N = \frac{I_e}{A_1n_1+A_2(n-n_1)^2}$, Randall and Wilkins substituted this expression for N back into Equation 2.1 for a relationship which described the rate traps are filled:

$$\frac{d(n-n_1+N)}{dt} = NA_2(n - n_1 + N) \qquad [2.2]$$

Randall and Wilkins further simplified this equation to:

$$\frac{dn_1}{dt} = -NA_2(n - n_1) \qquad [2.3]$$

This simplified expression is also roughly equivalent to the rate at which the traps in the system are filled. Randall and Wilkins substituted the above expression for N into [2.3] for a result of:

$$\frac{dn_1}{dt} = \frac{I_eA_2(n-n_1)}{A_1n_1} + A_2(n - n_1) \qquad [2.4]$$

Which was then integrated for:

$$\left(1 - \frac{A_1}{A_2}\right) n_1 - \frac{A_1}{A_2} nlog \left(n - \frac{n_1}{n}\right) = I_et \qquad [2.5]$$

[2.5] allows the representation of changes in n_1 with respect to time, as such the fluorescence given off by the emptying electron traps, I, is A_1Nn_1 or, using the same relationship for N given above:

$$I = I_e(1 - \frac{A_2}{A_1\left(1-\frac{n}{n_1}\right)})^{-1} \qquad [2.6]$$

For a better idea of how this fluorescence changes over time as charge moves within the crystal and is emitted, [2.5] and [2.6] should be evaluated separately.

In the case of n_1 being small, Eq. 2.5 gives the result of $n_1 = I_et$.

So, using this result and [2.6] the following result is obtained:

$$I = A_1 N n_1 = \frac{A_1}{A_2 \frac{I_e^2 t}{n}} \qquad [2.7]$$

This is a straight line and shows that initially, for small values of n_1, the growth of fluorescence is described by a line with slope $\frac{A_1}{A_2 \frac{I_e^2}{n}}$.

For $n_1 \rightarrow n$, the same method can be used to return the result of:

$$(n - n_1) \propto \exp\left(\frac{-I_e t A_2}{A_1 n}\right) \qquad [2.8]$$

Which shows that as the flow of electrons from localised electron states to luminescence centres reaches an equilibrium point, the growth of fluorescence can be modelled using an exponential curve. [2.7] and [2.8] can each be used to return values of $\frac{A_1}{A_2}$.

Randall and Wilkins noted in this derivation that this model is limited to illumination of a crystal by a uniform source, and that the escape rate of electrons from traps towards the luminescence centres is finite due to thermal motion within the lattice – as well as the continued absorption of the exciting light. Additional assumptions are implicit in the derivation, particularly with regards to multi-trap systems and the dose variant response of the crystal (Levy, 1985).

2.3.1 Emission Processes

Thermoluminescence

Thermoluminescence (TL) is a luminescence phenomenon of an insulator or semiconductor which can be observed when the solid is thermally stimulated. TL is fundamentally different from incandescence, the light spontaneously emitted from a substance when it is heated above 200°C due to black body radiation (Young and Freedman, 2014).

There are three essential ingredients necessary to produce TL:

- The material must be an insulator or a semiconductor (this is because conductors do not produce luminescence of any kind as their conduction band is not empty).
- The material must have at some time absorbed energy during exposure to ionising radiation.

- The luminescence emission is triggered by heating the material (Bos, 2007).

The main application of TL is in radiation dosimetry since for some materials, the emitted light can be proportional to the absorbed dose to which the material has been exposed (Bos, 2017). It is also used in geological or archaeological dating using thermochronometry which compares the TL profile of a sample as measured with comparable samples of a known dose to estimate the age of a material using the dose rate of the location (Brown et al. 2017).

When the intensity of TL emission is measured alongside the sample temperature as it is heated, a TL glow curve can be observed. Figure 2.4 shows an example of a TL glow curve. From this glow curve it is possible to determine a TL peak by determining the temperature at which the peak emitted intensity was measured.

Analysis	**Advantages**	**Limitations**
Curve Fitting	Suitable for well defined, small number of TL peaks	Ambiguous solutions in the presence of many TL peaks
		Fitting with non-first-order peaks returns invalid superpositions
Various heating rate method (VHRM) (Hoogenstraaten, 1958)	Provides energy and frequency factor for well-defined TL peaks	Only dominant peaks
	Little interference from side peaks	Systematic errors due to thermal lag at high heating rates
Initial rise method (IRM) + step-annealing (Garlick and Gibson, 1948)	Provides E estimation independent from frequency factor	Difficult to resolve strongly overlapped peaks
	Independent of kinetic order	Frequency factor is not determined
Fractional Glow (Gobrecht and Hoffmann, 1966)	Trap depths can be determined without any knowledge of the specific kinetics of the charge carriers	Requires relatively high level of accumulated TL so it is difficult to apply to younger samples
1D deconvolution (Agersnap Larsen, 1999; Agersnap Larsen et al. 1999)	Provides a description of the TL curve for first order processes	It is assumed that all peaks have the same frequency factor
2D deconvolution (Whitley et al. 2002)	Removes the limitation of 1D deconvolution	Strongly affected by noise
		Requires curves with various heating rates of various step annealing

Table 2.1 - TL analysis methods of relevance for temperature sensing (Yukihara et al. 2018).

Several methods have been proposed over the years to determine the frequency factor and activation energy of TL peaks, these variables are important for dosimetry as they can be used to model the lifetimes of the trapping states for charges. The most often used methods are listed in Table 2.1, which has been taken from Yukihara et al (2018), along with main references and comments on their advantages and limitations.

Curve fitting is a method of attaining the activation energy and frequency factor of a TL peak by replotting it as the log intensity against 1/kT where k is Boltzmann's constant and T is the temperature in Kelvin.

VHRM is similar to curve fitting, but the TL glow curve is weighted to account for the heating rate.

1D and 2D deconvolution involve plotting the TL glow curve against simulated TL glow curves with set parameters to attain a best-fit description for the measured TL glow curve via the simulated component TL peaks.

These methods rely on information computed from detectable luminescence signals generated from electrons which have been thermally evicted from a localised electron state and given thermal assistance into the conduction band before entering a recombination centre. As such, the TL intensity (I) at a particular temperature and time is equal to the product of a recombination probability constant R and the rate of change of the trap population $\frac{dn}{dt}$. Spencer (1996) shows a derivation describing this relationship as follows:

$$I(T,t) = -R\frac{dn}{dt} \qquad [2.9]$$

The rate of release of charge carriers is the product of the trap population n and the probability function expressed in [2.10].

$$Probability\ Function = \frac{dn}{dt} = se^{-\frac{E}{kT}} \qquad [2.10]$$

Where s is the frequency factor of the system, E is the energy depth of the localised electron state, k is Boltzmann's constant (8.617x10^{-5} eVK^{-1}), and T is the temperature of the system. The frequency factor describes the specific parameters for the localised electron states within the crystal.

Therefore, combining [2.9] and [2.10] gives the first order kinetic equation:

$$I(T,t) = Rsne^{-\frac{E}{kT}} \qquad [2.11]$$

For a linear TL ramp, a uniform heating rate, κ (Ks^{-1}), is employed, where:

$$\kappa = \frac{dT}{dt} \qquad [2.12]$$

Rearranging [2.17] for an expression with respect to dt and combining it with [2.16] gives:

$$\frac{dn}{dT} = -\frac{s}{\kappa}ne^{-\frac{E}{kT}} \qquad [2.13]$$

Equation [2.18] gives the integral [2.19] by separation of variables:

$$\int \frac{1}{n}dn = -\frac{s}{\kappa}\int e^{-\frac{E}{kT}}\,dT \qquad [2.14]$$

This relationship can be solved for temperature boundary conditions T and charge population n for time t=t, and initial conditions of T, n_o and t=0 to give a solution for n(T), thus:

$$n(T) = n_o exp\left[-\frac{E}{kT} + \frac{s}{\kappa}\int_{T_0}^{T} e^{-\frac{E}{kT}}\,dT\right] \qquad [2.15]$$

[2.15] can be substituted back into [2.11] to give the peak shape expression for first order kinetics:

$$I(T) = Rsn_0 exp\left[-\frac{E}{kT} + \frac{s}{\kappa}\int_{T_0}^{T} e^{-\frac{E}{kT}}\,dT\right] \qquad [2.16]$$

This relationship can be used to generate a simulated first order TL peak shape as was done by Spencer (1996).

TL peaks are asymmetrical and are weighted towards the lower temperature side of the peak maximum (Prakash, 2013). TL peaks then have a long tail that drops off rapidly as temperature rises past the peak maximum. The TL peak position depends on the variation of activation energy E and frequency factor(s) s of the thermal trap(s) in the material, and the heating rate

$\kappa$of the measurement. The height of the peak is also dependent on the charge population n, which is closely related to the radiation dose that the material has been exposed to. In real samples, TL measurement produces a glow curve which comprises of several TL peaks that vary in temperature proximity to each other and may be clustered together forming composite broad features or continua. In other material there may also be distinct TL peaks (Figure 2.4).

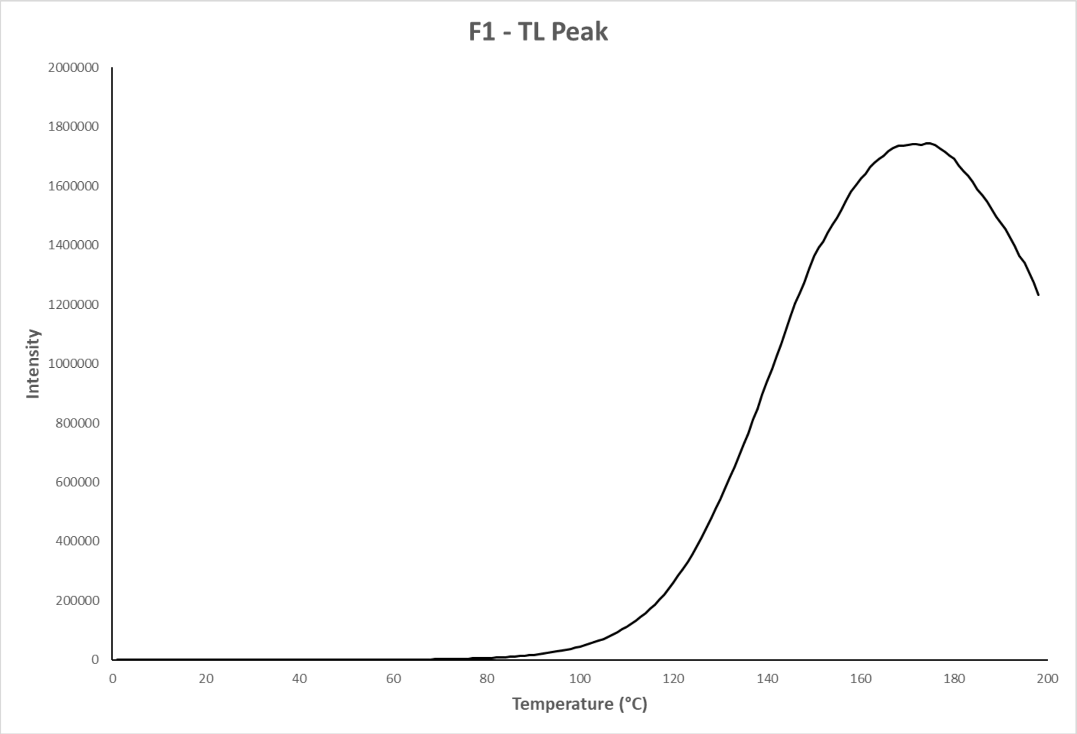

Figure 2.4 – An example TL plot of one of the K-Feldspars used in this thesis. The F1 reference feldspar has a prominent peak at ~170°C following irradiation.

Importantly for research purposes, TL suffers from thermal quenching at higher temperatures above the peak maximum, resulting in considerable decrease of luminescence intensity as temperature increases (Van den Eeckhout et al. 2013).

Photo Stimulated Luminescence

Photo stimulated luminescence (PSL) is the emission of detectable luminescence when an irradiated material is exposed to photons. When stimulated, the emitted photons have an energy corresponding to the energy lost during recombination. As such their wavelength is specific to the energy gap between the conduction band and the recombination centres. A PSL emission spectrum provides information on the energy levels of the recombination centres/sites whereas the PSL excitation spectrum of a material provides information on the energy levels of the electron trapping sites.

The storage of photon energy is comparable to that of thermoluminescence (TL) with the key difference being that the stimulation of PSL needs light to free the trapped electrons whereas TL requires heating of the material. As such, a similar approach to TL kinetics can be considered for PSL, whereby the luminescence emitted is related to the eviction rate by optical processes. One such treatment proposed by Clark (1992) is summarised below:

$$P(\lambda) = \phi(\lambda)\sigma(T, \lambda) \qquad [2.17]$$

Where P(λ) is the probability of a charge carrier being evicted when stimulated by light of a wavelength $\lambda \pm \delta\lambda$ per unit time (s^{-1}), $\phi(\lambda)$ is the total incident photon flux at wavelength $\lambda \pm \delta\lambda$ per unit area per unit time (m^2s^{-1}), and σ(T, λ) is the photon eviction cross section at wavelength $\lambda \pm \delta\lambda$ and at temperature T (m^2). Equation [2.17] determines that the probability of a charge carrier being photo-evicted from a single trapping site is proportional to both the total photon flux incident upon it and to the photo-ejection cross section, with temperature and stimulation wavelengths being key variables to consider.

$$EvictionRate = nP(\lambda) \qquad [2.18]$$

There are two eviction mechanisms for trapped charge carriers which are relevant to this thesis, thermal and photo-eviction. If photoexcitation is taking place at temperatures lower than the trap depth, eviction by optical processes will dominate; with thermal processes dominating when the temperature is greater than the trap activation energy.

Equations describing combined optical and thermal eviction only hold true for a single trap and centre model and for no interaction between thermal and optical eviction. Such interactions are difficult to model accurately:

$$I(\lambda) = \frac{Q(\lambda)A\phi(\lambda)}{\mu(\lambda)}\left[1 - e^{-\mu(\lambda)x}\right]p_r n\sigma(T, \lambda) \qquad [2.19]$$

where Q(λ) is the quantum efficiency of the detector for wavelength λ, A is the sample area (m^2), $\mu(\lambda)$ is the photon absorption coefficient at wavelength λ with an uncertainty $\delta\lambda$, x is the trapped charge carrier depth beneath the illuminated surface (m), and p_r is the assumed fixed radiative recombination probability. This relation supposes that if the optical absorption coefficients, quantum efficiencies and photon flux across the spectral excitation range are known, then the excitation spectra could be transformed to give an indication of the specific properties of the sample, such as the densities of the populated trap and the trap photo eviction cross sections (Clark, 1992). This is a critical relationship for determining charge storage and mobility within feldspars (Şahiner et al. 2017)..

Phosphorescence

Scientific work on the nature of phosphorescence began in the 20th century, particularly after the development of photomultipliers capable of single photon counting. Work conducted at the turn of the century were among the first to report that charges within crystals because of irradiation resulted in detectable photon emission (Jablonski, 1935; Herman and Hofstadter, 1940; Randall and Wilkins, 1945), and that the resulting photoconduction current and emission took place over a period – decaying away slowly when in the dark and in the absence of any stimulating fields. The mechanism driving this release was reported to be the retrapping of excited electrons which are then released over time.

Following on from the investigations detailed in the previous section, the work presented by Randall and Wilkins can be used in conjunction with later publications such as Shockley and Read (1952), and Braunlich (1979) to derive a relationship between the probability of an electron being ejected from a localised electron state, and the activation energy of that state. It is known that the lifetime of trapped charge carriers is both dependent on the depth of the trapping site/localised electron state and the temperature. The depth of this trapping site is a measure of the difference between the energy of a trapping state and the energy of the relevant band. The population of these released charge carriers across energy states and at different temperatures has an energy distribution which is governed by the Boltzmann distribution. As the temperature of the system increases, the average energy of the trapped charge carriers increases and the probability of trapped charge carriers with enough energy to be evicted from the trap also increases.

This eviction probability for these trapped charge carriers from a trap can be derived from the principle of detailed balance with Shockley-Read statistics. These statistics describe electron transitions between energy bands using electron traps and other localised states.

Braunlich (1979) derived a relationship to describe kinetic interactions within crystalline structures which result in empirical data that fit an Arrhenius equation. Braunlich described that such a system out of equilibrium, after the result of stimulation, could be described by an equation of the form:

$$\frac{d[n_D]}{dt} = \alpha[n_A]^m[n_B]^n[n_c]^l \qquad [2.20]$$

Where n_D is the concentration of the product resulting from the reaction between the reactants n_A, n_B and n_C, and α is the rate coefficient for the relaxation of the system. The reaction described by [2.20] is of m-th order in n_A, n-th order in n_B, and l-th order in n_C. In the case of phosphorescence in a crystalline structure, the empirical data which is recorded represents the detected luminescence and is related to the probability that an electron will become evicted from the localised electron states for every unit of time.

The rate coefficient in this relaxing system is equivalent to the electron eviction probability described above, and has the form of [2.10]:

$$v = s\sigma N \qquad [2.21]$$

Where s is the average thermal velocity of an electron in the conduction band (ms^{-1}), $\sigma$is the capture cross section of the localised electron state (m^2), and N is the density of free states in the conduction band (m^{-3}). This relationship is important for understanding the fundamentals of electron movement through a material as its temperature changes and can be used to determine peak emission temperatures for localised electron states of known activation energies.

Post-Stimulation Phosphorescence in Feldspars

Following stimulation, a delayed luminescence signal can be observed in feldspars (McKeever et al. 1997; Sanderson and Clark, 1994; Poolton et al. 2009; Andersen et al. 2012). This late luminescence (which from now on will be referred to as post-stimulation phosphorescence or PSP) decays slowly rather than stopping immediately after stimulation has taken place. PSP is attributed to the temporary storage of electrons in localised electron states below the conduction band which are gradually released as the crystal relaxes (Kars et al. 2013).

Kars et al. (2013) investigated the PSP from feldspars after optical stimulation and recorded that this luminescence decay occurred for at least 100s – with the decay noted as lasting longer than the measurement time. They noted that the PSP intensity was dependent on three key factors: the number of electrons evicted during stimulation, the recombination route taken and the recombination probability. Furthermore, Kars et al. (2013) noted that the PSP decay rate was dominated by the recombination pathway, retrapping and recombination probability – a key difference which implied that the decay rate would be the same regardless of stimulation intensity.

It is reasonable to state that such a lengthy decay is unlikely to solely originate from the recombination of electrons already present in the conduction band and electrons already located in recombination centres at the conclusion of the preceding stimulation. This is because luminescence decays from these kinds of excited electrons typically last much less than a microsecond (Tsukamoto et al. 2010). One explanation for this "slower" PSP decay ($>10^{-6}$s timescale) is that charge stored in localised electron states close to the conduction band can tunnel to nearby recombination centres following stimulation (Ankjærgaard and Jain, 2010). Ankjærgaard and Jain (2010) related this slower PSP decay component to tunnelling from unstable localised electron states to states with energies not greater than the Fermi energy for the system; proposing that the crystal relaxing at non-null temperatures (>0K) following stimulation would cause a transfer of charge from these deeper traps into shallow traps in the vicinity of the recombination centres. Ankjærgaard and Jain (2010) pointed to the difference in decay shape between the PSP following different stimulation wavelengths. This result indicated that different shallow states were occupied following stimulation with different wavelengths.

Photo-Transferred Thermoluminescence (PTTL)

PTTL in various materials has been reported and investigated by several papers (Herman and Hofstadter, 1940; Sunta, 1979; Qin et al. 2015; Alzahrani et al. 2016; Chithambo et al. 2018). This phenomenon occurs following the stimulation of a TL sample with photons of certain wavelengths to excite populated traps and other localised energy states to release charge carriers. These released charge carriers can be retrapped by other non-filled TL traps or enter recombination centres in the crystal and recombine. As such, repeating a TL measurement after photo stimulating a sample will return a different TL peak at a lower temperature, allowing investigation into these newly filled TL traps.

This is an important phenomenon for researchers as it shows that the electrons pass through the conduction band during the phosphorescence process and can be re-trapped.

The study of PTTL is one of the sources of information in understanding the role of charge carriers during luminescence processes in phosphorescent materials (Alzahrani et al. 2016). However, the precise nature of the charge transfer processes which take place in irradiated materials following stimulation by either optical or thermal methods remains debated in the literature, and the raw experimental data may be interpreted in several ways.

2.3.2 Discussion of modelling results

The studies of Randall and Wilkins (1945a, b), McKeever and Morris (1994), McKeever (1994), Alzahrani et al (2016), Yukihara et al (2018) and many others have investigated the mechanisms behind OSL, PTTL and TL processes in phosphorescent materials and have explained the decay of luminescence signals in terms of the reduction of radiative recombination centres over time.

These models use a determined ratio of these centres such that there are a small number of the luminescence centres available when compared with the other localised electron states. McKeever and Morris (1994) simulated decay curves with these parameters and found that a qualitative similarity in the ratio of luminescence centres to recombination centres for a sample of quartz was clearly demonstrated by the decay curve of the numerical model used in that study. Furthermore, their model assumed that electrons are optically stimulated from a deep, thermally disconnected trap – thus being a thermally isolated process at certain temperature ranges, with some electrons recombining at luminescence centres. This subsequently resulted in the reduction of the number of these centres available for recombination as the stimulation continued, resulting in the decay of the luminescence intensity over time. This was found to be directly related to the reduction in available lower activation energy traps and shallower electron states. This model, crucially, does not allow for electrons to not recombine after optical stimulation and allows them to instead transfer to states of lower activation energies from which they can be thermally ejected to give PTTL. According to this model PTTL will decay with time under optical stimulation because of the reduction in the number of available luminescence centres.

As described above, retrapping and emission via processes such as PTTL are phenomena which are difficult to explain from the perspective of first order kinetics of a single system. Such complex mechanisms require the interpretation of numerous interdependent first-order systems which correspond to conditions where there are more vacancies than filled states, in addition to there being sufficient available luminescence centres. If the eviction probability for a localised electron state in the band tail of the crystal is high, the lifetime of the charge carrier will be short enough to appear as if the freed charge carriers are transported directly to the recombination centre and not being retrapped at all. However, for a measured sample with lower eviction probabilities there will be a noticeable delay from the point of view of a laboratory detector for the same charge carrier journey. This is a clear example of non-first order kinetics and is of particular use when investigating clustered defects in a crystal which may be responsible for producing these kinds of time-delayed localised electron states (Townsend et al. 2021).

With respect to thermal stimulation, first order kinetics can be assumed as the temperature passes the peak maximum due to the lifetime of the trapped charge becoming shorter (Bos, 2017). The same effect is also noted in materials subjected to photo stimulated luminescence if the intensity of the stimulation source (such as a laser or LED) is increased. Such high-power lasers, when used to measure the PSL of phosphorescent materials, give rise to high eviction probabilities and thus low trapped lifetimes (Clark,1992). For the case of this thesis, which does not adjust the intensity per unit surface of the stimulating LEDs, the effect of retrapping could be significant and must be considered when modelling the PSL decays.

Determining the reasons why a particular curve has specific dynamics from the curve itself can be exceedingly difficult, requiring determination of multiple key variables involved in the emission probability of charge carriers. Consequently, it may be that an alternative stimulation technique would be required such as pulsing (Sanderson and Clark, 1994). Pulsed photo stimulated luminescence (PPSL), involving short pulses ($t \sim 10^{-6}$s) from a stimulating source such as an LED, could be arranged so that the delay between any two pulses is long enough to allow time for the evicted charge carriers to relax from the conduction band to lower energy states. Crucially, PPSL allows the system to return to some form of equilibrium before the next perturbation from another pulse as charge carriers trapped in thermally unstable traps have time to become retrapped in thermally stable traps.

2.4 Theoretical Summary

The theoretical framework laid out in this chapter has introduced the principles of luminescence research and luminescence phenomenon. An introduction to feldspar structure and the band theory of solids was followed by the presentation of the rate equations describing charge carrier transport in the band tail states of phosphorescent materials, as well as relationships describing the mechanisms of phosphorescence, photo stimulated luminescence and thermoluminescence. These expressions have been derived from first principles where possible and consist of phosphorescence rate equations which describe photo and thermal stimulations for a one trap and one centre model. Further considerations have been given to extensions required for multi trap/centre systems. Also derived was an expression describing a first order TL peak, as well as a theoretical discussion on what mechanisms are responsible for the shape of this peak and its perceived accuracy as describing the physical processes inside the crystal. The phenomena of PSP and phototransferred thermoluminescence have also been examined, with a look into their implications for charge carrier movement within relaxing crystalline structures, as well as the nature of charge storage sites themselves.

The expressions derived in this section allow the modelling of charge mobility and storage based on luminescent measurements from feldspars. The implications of these variables on charge stored in feldspar crystalline structures will be discussed further in Chapter 5.

3 Instrumentation

This section will expand on the experimental apparatus used over the course of this thesis, with comments on their use and, if necessary, modification over the course of the project.

3.1 SEM

A Hitachi S-3400N Scanning Electron Microscope with an Oxford Instruments INCA X-ray analyser was used to analyse the sub-optical characteristics of the samples used in this investigation (Fitzgerald, 2020). Under ideal conditions, the SEM is capable of producing a high-quality back-scattered electron image (with a resolution of 10nm at 3kV and 3nm at 30kV) due to its vacuum pressure capabilities, low aberration objective lens and quad bias gun circuit. The resolution is greatest when the lens aperture is set to 30 micrometers, with the sample chamber held at vacuum and the gun circuit using a low voltage acceleration/probe current.

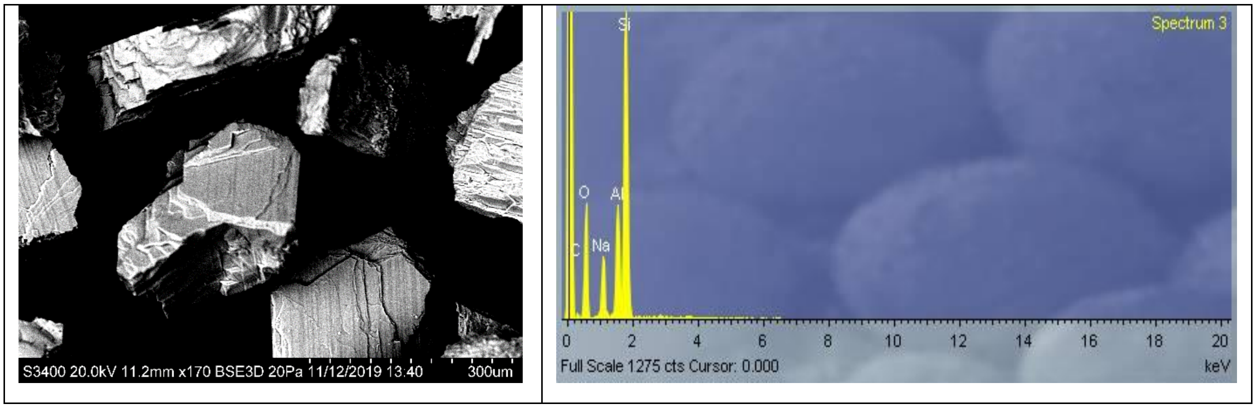

Figure 3.1 – Example of a backscattered image of the sample RC14 from the SEM (left) and a spectrum of one grain's surface (right).

The image quality obtained from the SEM was less than those possible under ideal conditions, but still sufficient to identify sub-optical laminations on the surface of individual grains. The INCA analyser and software was used to measure X-ray spectra for areas of individual grains with the energy of X-ray peaks used to identify major elements within each area. Thus, allowing the confirmation of each sample classification as reported in Table 4.1. An example of a backscattered electron image and INCA spectra is shown in Figure 3.1.

3.2 Elsec 9022 Irradiator Unit

An Elsec 9022 Irradiator Unit was used in this investigation to irradiate each sample aliquot used for IRSL and TL measurements with an appropriate dose. The irradiator unit is a computer-controlled irradiation system which has two strontium-90 beta-sources. A block diagram of the irradiator unit is shown in Figure 3.2. The source used in this investigation had a dose rate of ~0.37Gys^{-1}.

Each source is mounted in a heavy-duty lead and steel containment box which has a graphite inner lining to reduce bremsstrahlung radiation. Each box is mounted on top of its own sample handling unit which is capable of fitting a sample tray with a capacity of 64 samples per tray in machined positions for 10mm aliquots.

Sample irradiation is carried out using an X-Y stepper motor which takes the sample tray and positions it underneath the source box after being commanded by the control computer. The source box has a spring-loaded rotating solenoid which allows the source to be moved over a hole in the shielding to allow irradiation when the solenoid is energised. When the solenoid is not energised, the source will be secure in a safe position within the shielding.

During irradiation the X-Y stopping motor can be programmed to jitter the sample plate around in a circle to even out the sample irradiation. This sequence can be customised using the command computer.

Following the completion of irradiation, the stopping motor returns the sample tray to the withdrawal position at the entry gate of the sample handling unit.

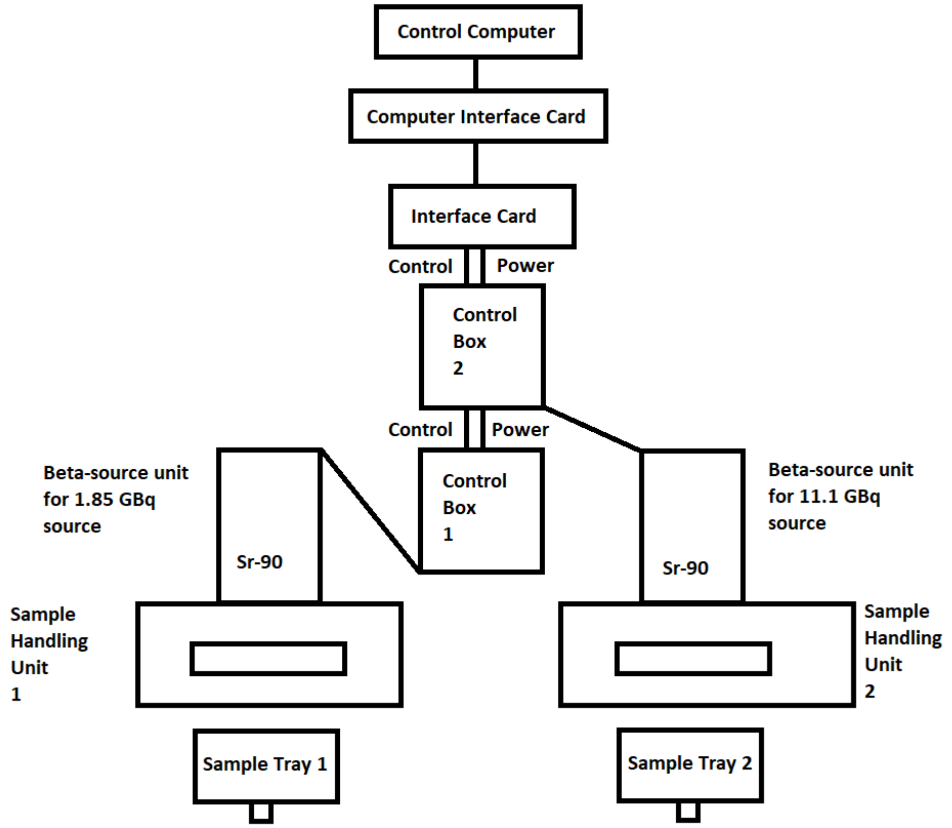

Figure 3.2 – The set-up for the Elsec 9022 Irradiator Unit.

3.3 Portable OSL Reader

A variation of the SUERC Portable OSL instrument (Sanderson & Murphy, 2010) was used in this thesis (Figure 3.3). The SUERC POSL reader was developed to perform precise luminescence measurements during fieldwork, it consists of a control unit that includes the power supply and diode control circuits, connected to a computer with installed control software, and of the sample chamber. The sample chamber consists of LED mounts for IRSL (880 nm) and OSL (470 nm) stimulations, a filter holder, a photomultiplier tube, and the aluminium sample chamber itself.

The portable OSL instrument used in this investigation has been modified as described in Francoz (2019) to utilise two sets of IR diodes at 890nm and 940nm to stimulate luminescence from samples. The TSHF6410 890nm diode has a radiant intensity of 70 mW/sr and TSL6400

940nm diode has a radiant intensity of 40 mW/sr, with three of each diodes being used in each array. It should be noted that this imbalance will have no effect on the net counts measured over sufficiently long periods as all charge which is sensitive to IRSL that is trapped in the sample lattice will be emptied. The sample chamber of the portable reader includes a 50mm diameter stage mount which is inserted into the portable reader with a central recess to position 1 cm discs at a constant height for stimulation work (Fitzgerald, 2022).

The portable OSL instrument is also equipped with RG830 long pass filters and a 3mm BG39 filter (Figures 3.4 and 3.5 show each respective filter's transmittance spectra) which are mounted on the detector head, these filters prevent the photomultiplier tube from being saturated by the LEDs during stimulation and allow the observation of particular emission wavelengths. As such the detected photons were in the blue/UV region. This OSL reader produces signals which are 2-3 orders of magnitude higher than those obtained using 1 cm discs in a Risø DA20 reader equipped with standard U340 detection filters (Francoz, 2019).

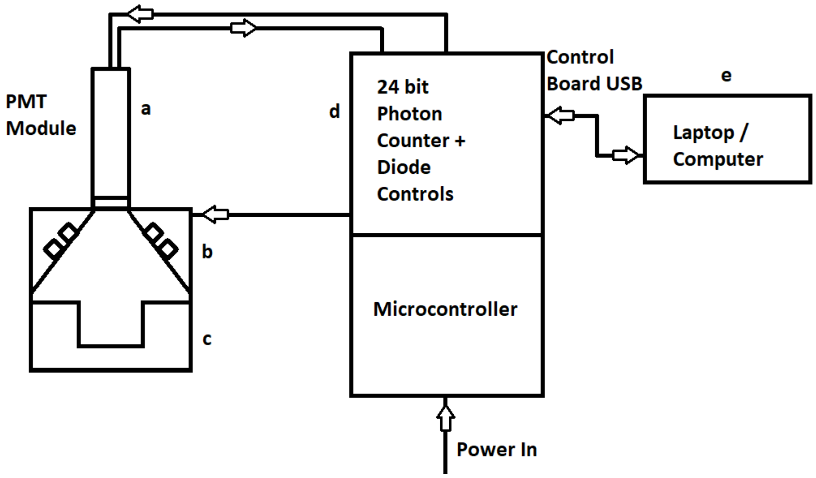

Figure 3.3 – A schematic of the SUERC Portable OSL reader. (a) is the Senstech photomultiplier module (Bialkali cathode). (b) is the Stimulation Collar, which contains two sets of stimulation sources S1 and S2 – these are 890nm and 940nm diodes respectively. (c) is the Sample Drawer, which is capable of housing samples up to 50mm in diameter. (d) is the Pulsed Photon Counting Control Board with an onboard microcontroller. (e) is the control computer.

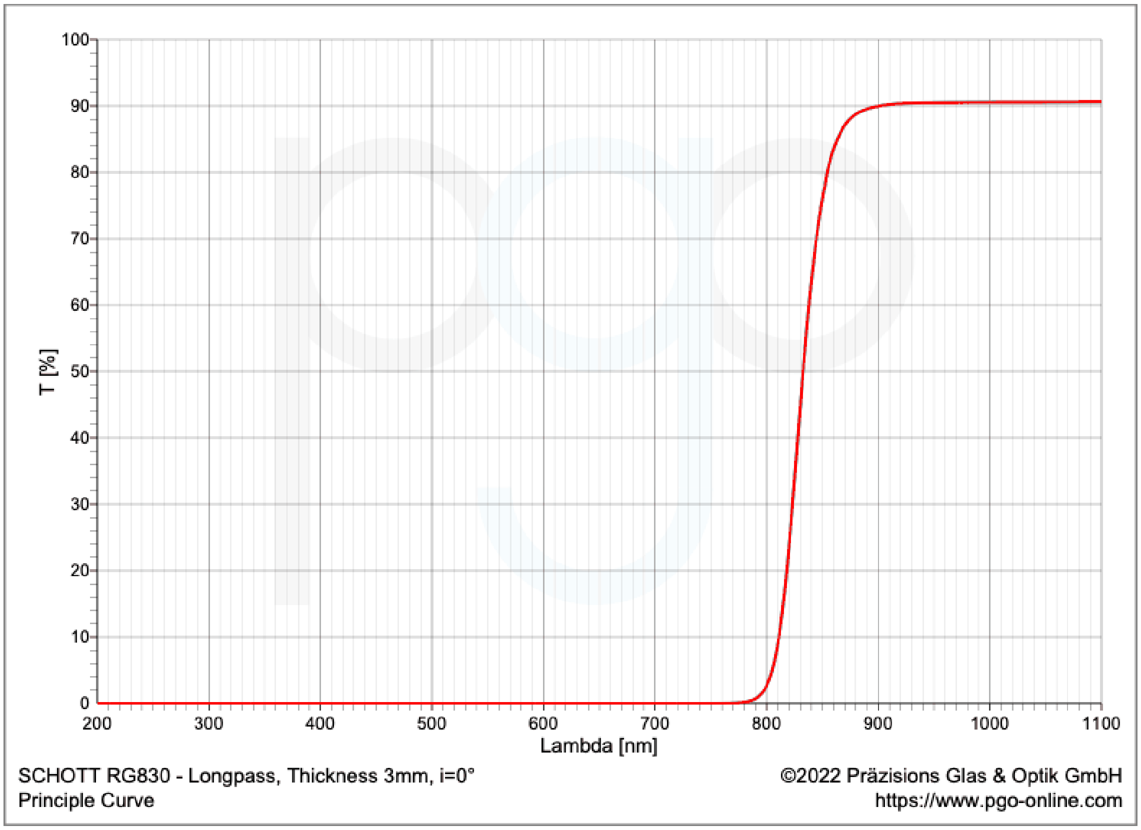

Figure 3.4 – The transmittance spectrum of the RG830 filter used in the portable OSL reader.

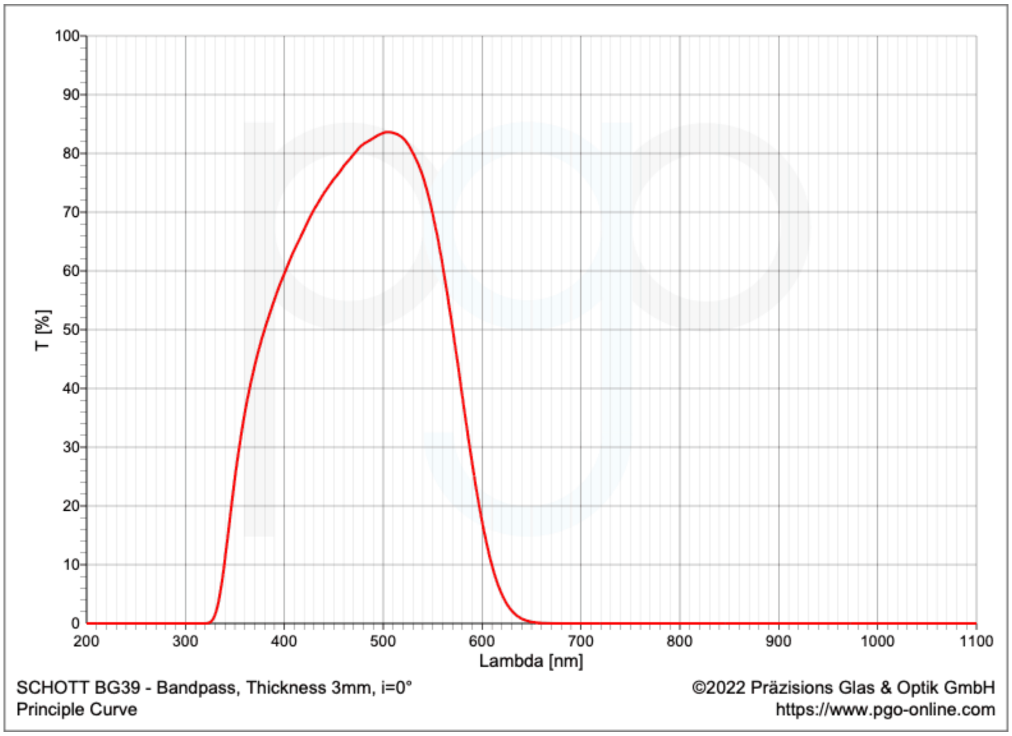

Figure 3.5 - The transmittance spectrum of the BG39 filter used in the portable OSL reader.

The modified portable OSL instrument has been used in this thesis to examine the absolute and relative responses of different feldspars to stimulation in two IR wavebands within the excitation bands from a series of feldspars samples of known composition.

3.4 TL Reader

The TL reader used in this thesis is a custom built SUERC instrument consisting of a single photon counting photomultiplier tube mounted atop a sealed sample chamber (Figure 3.6). This chamber can be purged with oxygen-free dry-nitrogen to help remove spurious signals upon heating and prevent any oxidisation of the sample plate. This device is a manual system which can hold a single sample at a time in the sealed aluminium sample chamber for measurement. The chamber itself contains a sample aliquot holder that consists of a heating plate controlled by a modular control unit (MCU). The shape of this plate differs from heater plate designs which were employed in other readers built in the same time period (Bøtter-

Jensen and Bungaard, 1978; Bøtter-Jensen, 1988; Galloway,1991). This sample holder was selected for the design as the area of heater plate material within the light path from the sample to the PMT is smaller, resulting in a smaller background signal due to less blackbody incandescence during heating (Spencer, 1996). The 'top-hat' shape of the heater plate also maintains a constant thermal contact area with the sample during heating over many cycles without distorting.

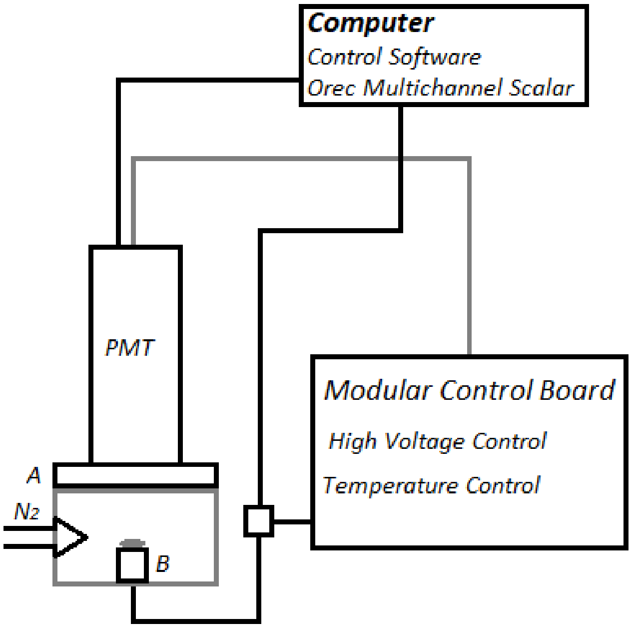

Figure 3.6 - The setup of the TL reader. The PMT has a 3mm BG39 filter contained within a holder between the PMT and the sample chamber (A). The heating unit (B) in the sample chamber can be controlled manually from the modular control board or automatically from the computer.

The plate can be heated resistively in a linear fashion up to 800°C with the temperature being measured by a Chromel-Alumel (Type K) thermocouple that is spot-welded to the underside of the heater plate. This MCU is capable of manual or computer-controlled temperature ramp and hold procedures. In the case of manual heating, the temperature of the heater plate could be raised by switching the reference to an internal voltage supply which can be varied using a 10-turn potentiometer set with a front panel mounted dial on the error detector module. The signals from the photomultiplier are then passed through an amplifier and then a discriminator before being recorded via an Ortec MCS card (Spencer, 1996).

3.5 Risø I, Risø III Reader

Two variants of Risø automatic TL/OSL readers (DTU Nutech, 2015) were used in work described in this thesis. The modern Risø automatic TL/OSL readers are continuations of earlier work conducted in the 1980s on automatic devices which could work through dozens of samples using a turntable design (Bøtter-jensen and Medjahl, 1983). These modern Risø readers incorporate the turntable design with single photon counting PMTs, diode or laser stimulation capabilities, TL heaters and onboard irradiation capability using either a beta source, an alpha source, or an X-ray generator (Markey et al. 1997; Bøtter-Jensen et al. 2000; Spooner and Allsop, 2000; Kadereit and Kreutzer, 2013).

One reader used in this investigation was a DA-15 automatic reader equipped with a laser light source emitting at 830 nm (designated as Risø I), the second reader was a DA-20 automatic reader equipped with a LED array emitting at 870nm (designated as Risø III). The readers also differ in their secondary stimulation sources, both of which stimulate in the optical region, but these are not relevant to this investigation.

The IRSL signals were detected using a 3mm BG39 filter in combination with 3mm BG3 filter front of the photomultiplier tube. This results in an observable detection window for emitted photons between the wavelengths of 325nm and 475nm (DTU,2015).

3.6 Time Resolved Stimulation Spectrometer

3.6.1 First TRS Spectrometer System

The TRS spectrometer was a modification of a pre-exciting excitation spectrometer. The original design concept of the initial spectrometer was as a research tool which could flexibly generate both excitation and emission spectra simultaneously (Sanderson et al. 1988; Sanderson, 1991; Sanderson et al. 1991). The main spectrometric components, such as the light source, monochromator, and beam production optics of the TRS spectrometer were constructed by Applied Photophysics. Other components such as the photon counting system, sample chamber and cooling coil were built on-site at the Scottish Universities Reactor Research Centre (SURRC). The excitation spectrometer was used in the doctoral work of Clark (1992) and is described in further detail there.

The instrument has full temperature control from ~-100°C to ~+500°C and has a modular design for easy reconfiguration depending upon the research requirements as it could be used as a TL reader and an excitation spectrometer. This system uses the same control modules and readout system as the TL readers, however there are differences in the design of the sample chamber (Figure 3.7). As the spectrometer was initially designed to be used with a side mounted xenon lamp as the excitation source (Sanderson et al. 1988; Clark, 1992), which is not used in this investigation, the aliquot discs are mounted on a 45° plate.

For this work it was necessary to add a collar to mount the two arrays of three TSHF6410 890nm and three TSAL6400 940nm LEDs as used in the modified pOSL system which would be used as the stimulation source (Figure 3.8). The primary contribution of this project to the spectrometer involved tweaking of the system to function as a time resolved stimulation spectrometer which used LEDs as a stimulation source rather than a xenon lamp.

The heating unit and the cryogenic units were both used in this investigation for above room temperature and cryogenic temperature stimulations.

With regards to the sample heater plate, its specifications remain unchanged when compared with the heating plating found in the TL reader and can heat an aliquot from room temperature to around 600°C using a phase angle trigger unit within the modular control board. Cooling of the sample in the variations of the spectrometer shown in Figures 3.7 and 3.8 is achieved by passing nitrogen through a copper coil suspended in liquid nitrogen to cool it to near liquid nitrogen temperatures. This gas is then passed through a cooling coil made from capillary tubing that is then soldered to the back of the sample plate and then vented to the lab. This indirectly allows the cooling of the sample to occur without direct contact between the nitrogen gas and the sample aliquot, thus preventing possible contamination as a result of sample grain dispersion throughout the chamber. The temperature of the sample plate is monitored by a thermocouple which is welded to the back of the sample plate. This gives the heating plate extra mass and imposes limitations on the top temperature.

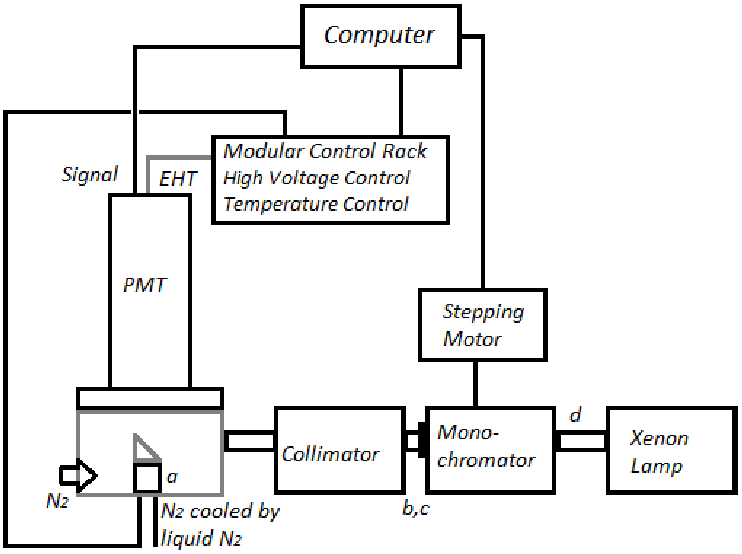

Figure 3.7 - The spectrometer design as described in Sanderson et al (1988) and Clark (1992). Within the sample chamber a is the cooling cell where nitrogen gas cooled by exposure to liquid nitrogen is used to cool the sample to cryogenic temperatures. Within the excitation unit itself, b is a filter holder before the optical shutter, c, and d is a spacer unit between the monochromator and the Xenon lamp with another filter holder.

The sample cooling rate at cryogenic temperatures is controlled by the flow rate of the cooled gas through the cooling coil - it is possible to cool the sample plate to approximately -140°C within a reasonable timescale of several minutes (Clark, 1992). The output of the thermocouple is amplified by a linear thermocouple amplifier chip, the nonlinearity of this chip at the temperature extremes has been investigated and recorded (Analog Devices Inc, 1999).

Like the TL reader described in Section 3.3, the sample chamber can be purged with oxygen free dry nitrogen to help remove irregular signals during sample heating and prevent oxidisation of the sample plate.

During and following stimulation using the LED arrays, the resulting luminescence is detected using a fast photon counting photomultiplier. Pulses from the photomultiplier are then converted to TTL logic pulses and recorded using an Ortec ACE™ MCS card with more than 4000 channels. The first spectrometer system is equipped with a MCS card which could record up to 4000 channels and dwell times as short as 2 microseconds. The MCS cards were evaluated daily using a source of known intensity to ensure that all channels had an equal input from the photomultiplier tube.

Control electronics, including high voltage supply, thermocouple amplifier, heater phase angle trigger and error detector, temperature reference and power supplies are contained in a modular control board rack unit with which allows computer control of heating rates and PSL scan speeds through a control program.

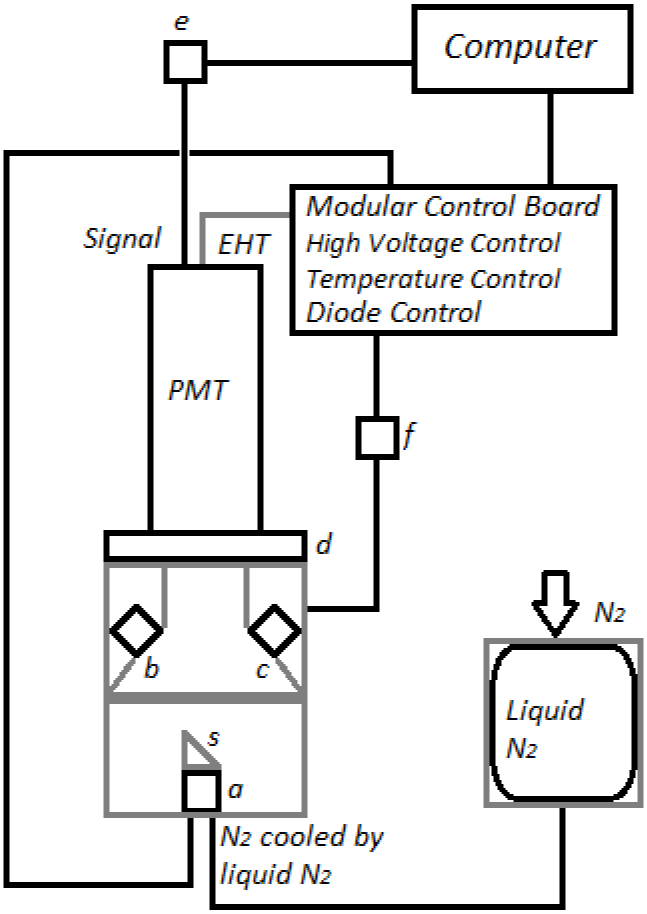

Figure 3.8 - The spectrometer as used for time resolved and cryogenic investigations. Within the sample chamber, the cooling cell (a) beneath the sample holder (s) is unchanged from the system shown in Figure 3.6. The newly added collar contains mountings for arrays of 890nm and 940nm diodes (b and c respectively). The PMT filters are contained within a holder (d). The signals from the PMT are sent through an amplifier and ECL to TTL discriminator (e) before being received at the computer, which runs the control software for the spectrometer, and stored using an Ortec MCS. The diode pulses were generated in the diode control section within the MCR, with diode selection between the 890nm and 940nm arrays occurring using switch (f).

3.6.2 Second TRS Spectrometer System

A key drawback of the first time resolved stimulation spectrometer system was that because of the added collar which contained the diode arrays, the resulting luminescence intensity which was detected from the sample was greatly diminished due to the increased distance between the sample and the PMT – particularly at microsecond timescales (Sanderson and Clark, 1994; Alexander, 2007). Furthermore, several features of spectra obtained using the first TRS spectrometer were unusual (discussed in Chapter 4), but reproducible – as such it could not be concluded if these features were representative of genuine phenomena or system artefacts.

The development of a second system was therefore needed and a schematic of this second system is shown in Figure 3.9. The specifications of this system were to improve the detectable luminescence intensity and to incorporate a more advanced Ortec Turbo MCS with 16000 channels and dwell times down to 5ns. The MCS cards were evaluated daily using a source of known intensity to ensure that all channels had an equal input from the photomultiplier tube.

The key design change was the compression of the collar design to reduce the distance between the diodes and the sample heater plate, and from the sample to the PMT, resulting in greater detectable luminescence signal. This also meant that the sample heater plate did not have to be aligned at 45 degrees as there was no longer an adjacent xenon lamp and collimator, further allowing greater illumination by either diode array. The new collar was also directly connected with the filter housing and the PMT, as opposed to them being separately attached as was the case with the first system. The compressed diode array and PMT mounting collar was secured to the sample chamber by three guide pins at the bottom of the collar which interlocked with three guide holes at the top of the sample chamber. Both of these changes provided a very secure fit and greatly reduced the light leaks when compared with the first system.

A new trigger system for the pulse generator was also developed, allowing shorter pulses to be generated with shorter delays between pulses. This, in combination with the more advanced MCS, made this system also capable of operating at nanosecond timescales. However, for the purposes of the work presented in this thesis microsecond timescales were chosen for comparative purposes but the shortest LED stimulation pulses could have been as low as 0.3-0.5ns using the system's available MCR.

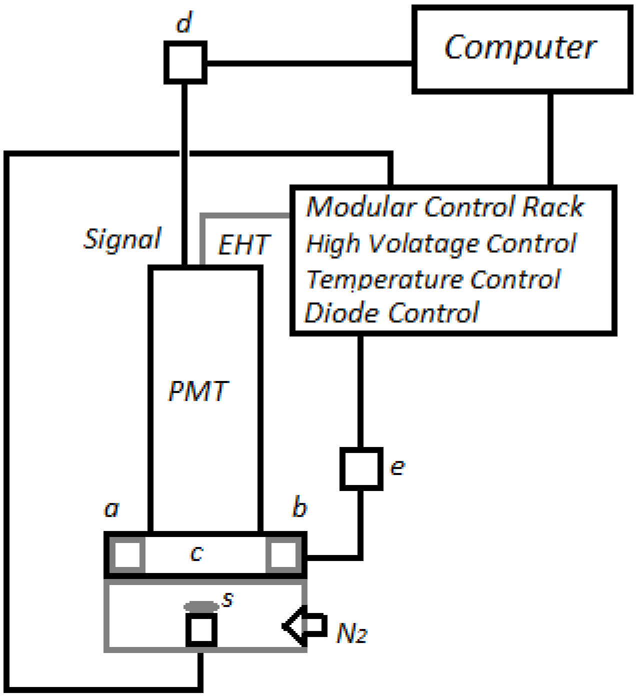

Figure 3.9 - The second TRS system used in this thesis. Contained within the specially designed collar mount are 890nm and 940nm LED arrays (a and b respectively). The PMT filters are also contained within the collar mount (c) above the sample mount (s). The signals from the PMT are sent through an amplifier and ECL to TTL discriminator (d) before being received at the computer, which runs the control software for the spectrometer, and stored using an Ortec MCS. The diode pulses were generated in the diode control section within the MCR, with diode selection between the 890nm and 940nm arrays occurring with a switch (e).

3.7 Summary

This section expanded and detailed the experimental apparatus used over the course of this thesis and made comments on their use. Further comments were made on the modification of the first TRS spectrometer modification when compared with the design used in Sanderson et al. (1988) and (Clark (1992) over the course of the project.

4 Experimental Outline and Results

The previous section discussed the experimental apparatus used over the course of this thesis. This section will discuss the experimental set-up for each investigation within this thesis before discussing the results and conclusions.

It is important to identify and understand the nature of the trapping sites and the charge transport mechanisms. Knowledge of the phosphorescence decay processes can provide very useful information, especially for modelling charge movement through the lattice. Thus, the work presented uses different approaches to identify the movement of charges through the band-tail states of various feldspar samples and their response to variations in temperature, stimulation time and wavelength. The information resulting from this approach can be combined to optimise the models used to predict the behaviour of charge movement through a relaxing complex lattice structure and provide indications on the nature of the charge storage sites. This optimisation will allow decay curves to be constructed as a step towards the development of an encompassing model for the investigation of charge storage, recombination and release mechanisms.

This thesis reports three different major investigations, which will be split up into different sections for the purpose of proper discussion. Section 4.1 will provide a description of the sample set used over the course of this thesis. Section 4.2 will lay out the expansion of the investigation into the phenomenon of PSP from a previous study (Fitzgerald, 2020; Fitzgerald et al. 2022) using the SUERC portable OSL reader detailed in Section 3. Section 4.3 will detail the time resolved PSP investigation using the time resolved stimulation spectrometers detailed in Chapter 3. Section 4.4 describes the investigation into the phenomenon of PTTL using the TRS spectrometers, Risø readers and the modified SUERC portable OSL reader. Finally, Section 4.5 will summarise the discussions contained within this section.

4.1 Description of Sample Set

4.1.1 R. J. Clark's samples

The samples used in this investigation are the same samples used in a previous study (Fitzgerald, 2020; Fitzgerald et al. 2022), which were a selected subset of the samples used in

Clark and Sanderson (1994). A list of these samples is provided in Table 4.1. All chosen samples are of a known geological origin as recorded and used by previous studies (Clark, 1992; Clark and Sanderson, 1994; Van Breeman et al. 1974; Pidgeon and Raheim, 1972; Pidgeon and Hopgood, 1975; Van Breeman et al. 1979; Van Breeman and Bowden, 1973). They were further investigated and had their mineralogical descriptions confirmed with the use of a scanning electron microscope in a previous study (Fitzgerald, 2020). The IAEA reference material F1 was also used (IAEA, 1999).

This geological variance in the sample set was used to observe any variations between the stimulated luminescence occurring in different feldspar minerals, as well as any variations within a single mineral family. Clark (1992) reported that the geologically sourced samples were obtained from the SURRC geology department (now SUERC), with many of them being previously used for geological research. These minerals had been separated for geological dating and a total of 22 samples, including four albite, two microcline, two plagioclase and potassium feldspar (K-Feldspar) are used here.

As noted by a previous study (Fitzgerald, 2020), three 1mg aliquots were prepared from each sample, one control aliquot with the natural geological signal and two aliquots with their low temperature geological signals removed. Further, a stub of each sample was also prepared for SEM analysis, the results of which are reported by Fitzgerald, 2020, and detailed in Table 4.1. Work conducted in Fitzgerald (2020) confirmed the original compositional families of these samples as well as provided evidence of microstructures on the grains of the K-feldspars.

For work involving the time resolved stimulation spectrometers, each sample was given a dose of 1 kGy after being thermally cleared by a TL heat to 500°C to remove any residual geological signal. Similarly, samples investigated with the Risø readers and the SUERC portable reader were given 100Gy doses after a thermal clear out to 500°C. Samples were then stored for two days before measurements were conducted to reduce the impact of room temperature phosphorescence on the measured signal.

Sample No.	Reference No.	Mineral*	Location	Summary of SEM analyses	Published Reference
PL016	RC167	K-Feldspar	S. Harris	All of the examined grains show peaks for K, Al, Si and O, with small Na peaks in some instances, consistent with K-feldspar, without other minerals present in significant quantities.	
PL017	RC174	K-Feldspar	Greenland		Van Breeman et al. (1974)
PL018	RC72	K-Feldspar	Norway		Pidgeon and Raheim (1972)
PL019	RC64	K-Feldspar	Norway		Pidgeon and Raheim (1972)
PL020	RC81	K-Feldspar	Norway		Pidgeon and Raheim (1972)
PL021	RC485	K-Feldspar	Greenland		Pidgeon and Hopgood (1975)
PL022	RC484	K-Feldspar	Greenland		Pidgeon and Hopgood (1975)
PL023	RC491	K-Feldspar	Greenland		Pidgeon and Hopgood (1975)
PL024	RC503	K-Feldspar	Greenland		Pidgeon and Hopgood (1975)
F1	F1	K-Feldspar	-		IAEA, 1999
PL025	RC1396C	K-Feldspar	Assynt		Van Breeman et al. (1979)
PL026	RC389	K-Feldspar	Nigeria		Van Breeman and Bowden (1973)
PL027	RC456	K-Feldspar	Nigeria		Van Breeman and Bowden (1973)
PL028	RC683B	K-Feldspar	Aberdeen		
PL029	RC630	Microcline	S. Harris	All the grains examined show x-ray peaks for K, Al, Si and O consistent with these being microcline ($KAlSi_3O_8$), without other minerals present in significant quantities.	
PL030	RC165	Microcline	S. Harris		
PL031	RC246	Plagioclase	Greenland	Contains quartz alongside plagioclase feldspars with varying calcium and sodium concentrations.	
PL032	RC659	Plagioclase	N. Harris		
PL003	RC14	Albite	S. Harris	All of the examined grains show x-ray peaks for Na, Al, Si and O consistent with the samples being albite ($NaAlSi_3O_8$), without other minerals present in significant quantities.	
PL004	RC168	Albite	S. Harris		
PL005	RC169	Albite	S. Harris		
PL006	RC164	Albite	S. Harris		

Table 4.1 - A list of samples used in this investigation as used in Fitzgerald, 2020, the published references have been attached as included in Clark and Sanderson (1994). Comments relating to the SEM analysis relating to sample mineralogy conducted in Fitzgerald, 2020, have been included for ease of access

4.2 Feldspar Investigation I – IRSL PSP Decay

4.2.1 Experimental Procedure

Fitzgerald (2020) reported the existence of PSP across the sample set used in the work presented in this thesis following stimulation with IR wavelength diodes. Follow-up exploratory work in Fitzgerald (2020) with a sub-set of five samples and measurement times which were greater than ten minutes noted that the measured PSP declined over different timescales depending on the sample. Fitzgerald et al. (2022) contains both the PSP results in this thesis and the early exploratory work on IRSL and TL from Fitzgerald (2020).

The existence of PSP following IRSL has been noted by several studies as being an indicator of charge mobility (eg Guralnik et al. (2015)). PSP could therefore be used as a probe to investigate how charge is transported through the local lattice environment, which is an important indicator for a distributed trap system (Li and Li, (2013)).

The purpose of this investigation was to conduct an experiment using long timescales for observing the decay of PSP in a range of feldspar samples after 890nm and 940nm exposure. The SUERC portable reader was used for IRSL exposure and a long non-stimulating readout. The measured decaying PSP was then analysed to determine:

- If there are numerous exponential factors at work in the decay.
- If these exponents vary across feldspar samples.
- If these exponents vary between stimulation wavelengths.
- If these exponents correspond to the activation energies of shallow traps.

Two aliquots/disk of each sample were given a 100Gy dose from the Elsec irradiator unit. This was followed by a fifteen minute preheat at 100°C in an oven to remove the low temperature luminescence components prior to any measurements and were stored in the dark when not being used.

To conduct the measurement, the control software for the portable reader was used to create a pair of custom sequences (Figure 4.1). One of these sequences consisted of a 600 second pre-stimulation background count, a sixty second stimulation period with the 890nm diodes, a 600 second count with no stimulation source active, another sixty second stimulation period with the 940nm diodes, and then a final two separate 600 second counts with no stimulation source active. Aliquot one of each sample was measured using this sequence. For the second aliquot an alternate measurement sequence was also programmed so that the 940nm diodes were used before the 890nm diodes. The temperature of the room while the measurements were ongoing was also recorded using an electronic thermometer.

Each decay curve was normalised to the first 1s channel of the PSP (C or E) to account for any differences in aliquot grain content and sample dose so that the relative rates of decay could be determined for each sample.

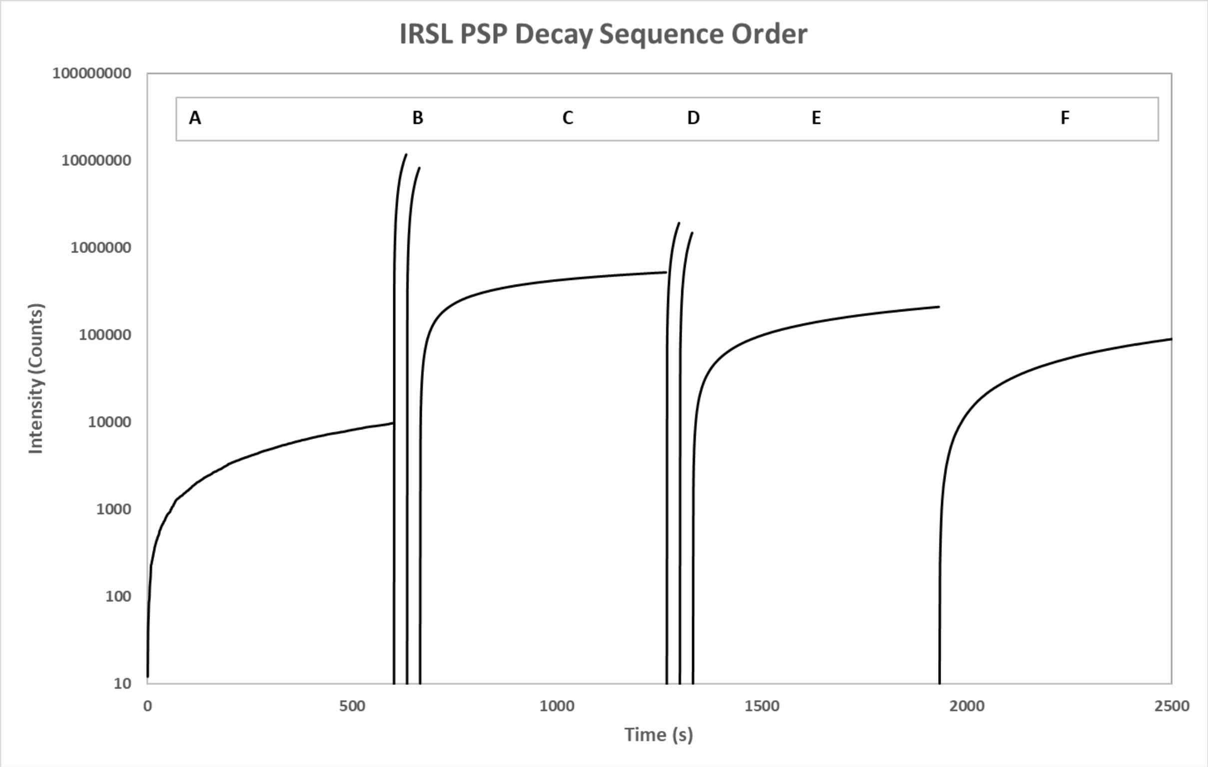

Figure 4.1 – The recorded counts for the sample RC168. The measurement sequence order is visible: A pre-stimulation dark count for 600s (A). The first stimulation sequence, either 890nm for aliquot 1 or 940nm for aliquot 2 (B). A post-stimulation count for 600s (C). The second stimulation sequence, either 890nm for aliquot 2 or 890nm for aliquot 2 (D). Two sequential post-stimulation counts for 600s each (E and F respectively).

4.2.2 Results

IRSL Profile

The IRSL depletion index represents the rate at which charge is evicted from charge storing sites as the mineral Is stimulated and charge is freed over the course of a stimulation sequence. The IRSL depletion for each feldspar sample investigated in this experiment was calculated by taking the counts recorded during the initial 30 seconds after accounting for the instrument background and dividing this by the counts detected during the latter 30 seconds after accounting for the instrument background (Sanderson and Murphy, 2010).

The IRSL depletion index (the ratio of the counts recording during first 30 seconds of stimulation with the counts recorded during the final 30 seconds of stimulation) observed across the sample set varied from 1.65 to 1.15.

Figure 4.2 shows the IRSL depletion obtained for each aliquot stimulation using both wavelengths. As shown by this graph there are clear trends across the dataset, with the 890nm stimulation resulting in a greater depletion index than the 940nm stimulation (with an increase of up to 40%). This indicates that the 890nm stimulation results in a faster decaying signal, which is in addition to it producing more detected counts per stimulation sequence as discussed in previous sections. One key feature that this investigation noted was that as a result of the stimulation of each sample’s aliquot two, where the 940nm stimulation occurred before the 890nm stimulation, the difference in the depletion indices for each wavelength reduced considerably.

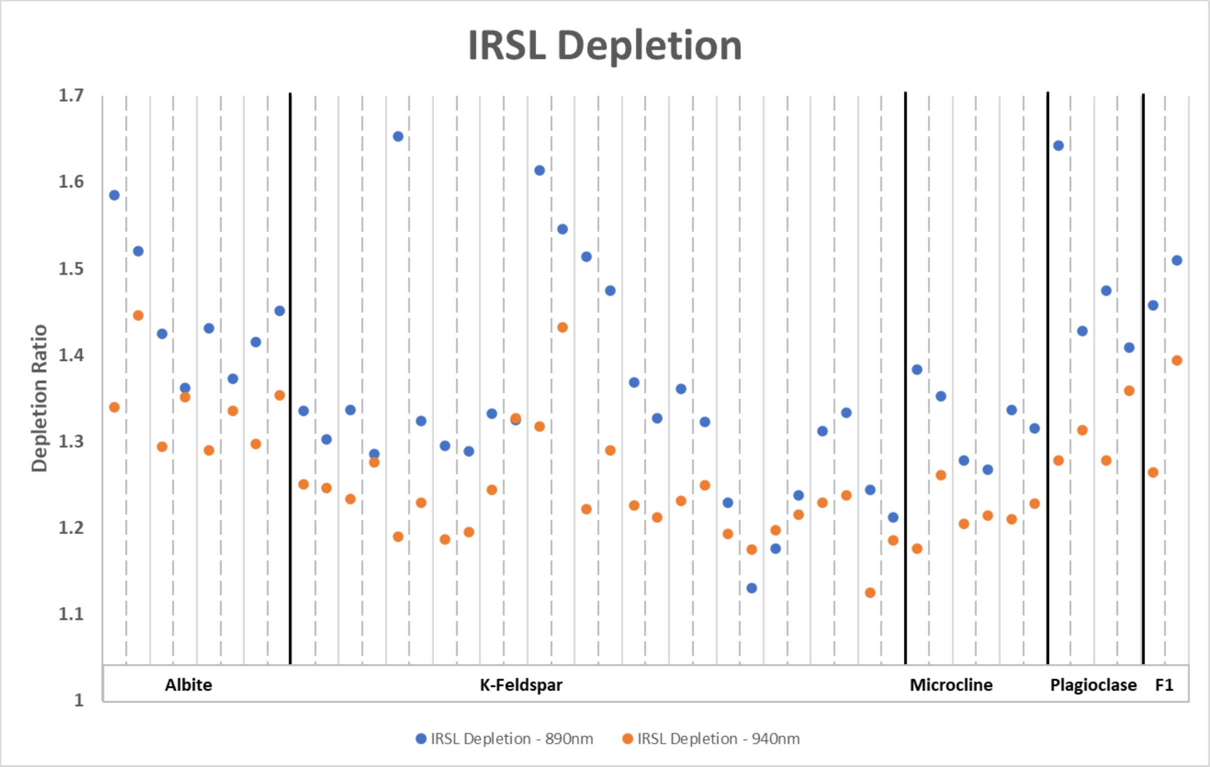

Figure 4.2 – The calculated IRSL depletion for each sample aliquot investigated in this experiment. The data is arranged such that a graph vertical subdivision contains each sequence for a specific aliquot and the major vertical divisions represent each mineral, the bolder major divisions represent each mineral family.

Also visible in Figure 4.2 is a clustering in depletion index values along mineral group lines, with albites and plagioclases having higher depletion indices than microclines for both stimulation wavelengths, and the K-Feldspars having broadly the lowest 940nm index.

Figure 4.3 shows the 940/890nm stimulation ratio obtained for each feldspar sample investigated in this experiment. The 940/890nm stimulation ratio represents the comparative intensity of detected counts following 940nm stimulation and 890nm stimulation. A 940/890nm stimulation ratio of less than 1 indicates that there is a lower number of detected counts during 940nm stimulation than there is for 890nm stimulation. The opposite case would be true for a 940/890nm stimulation ratio greater than 1. This was calculated by taking the counts recorded during the 940nm stimulation and dividing this by the counts detected during the 890nm stimulation, and accounting for the instrument background as well as any PSP following stimulation.

From Figure 4.3, the 940nm signal relative to the 890nm is more dominant in the second 30s compared with the first 30s. This suggests that the 890nm stimulation has a faster decay rate than 940nm as a consequence of being closer to the excitation band maximum. The albites, one of the K-Feldspars (RC485), both plagioclases and F1 are also differentiated from the other samples, particularly for the 940/890 ratio on the second aliquot.

The results show that the 940nm/890nm stimulation ratio varies from 0.1 to 0.42 across the sample set. As shown in Figure 4.2 this variance is dominated by two factors: the order of stimulation, and the stimulated mineral.

The variation in the stimulation ratio across mineral families is noticeable when comparing the values calculated for aliquot one of each sample and has been noted by previous studies (Fitzgerald et al. 2022; Clark and Sanderson, 1994). As noted by these previous studies, a clustering of a mineral group around a ratio value is observed, however there are slight differences in this ratio even within families, with the most obvious difference being between the two plagioclase samples. Once again it can be noted that the albites and plagioclases have a greater calculated 940/890 stimulation ratio, with the K-Feldspars having the greatest overall range in this calculated value – having both the largest and the smallest calculated stimulation ratio.

When comparing these calculated ratios with those calculated for the second sample aliquot with the stimulation order reversed, an immediate trend is noted. The values calculated for the 940nm/890nm stimulation ratio are up to a factor of four larger than those obtained for aliquot one. Further, the differences between the mineral groups noted in the above paragraph are more prominent, with clear differences observable the albite and plagioclase samples, and the rest of the sample group by a factor of two.

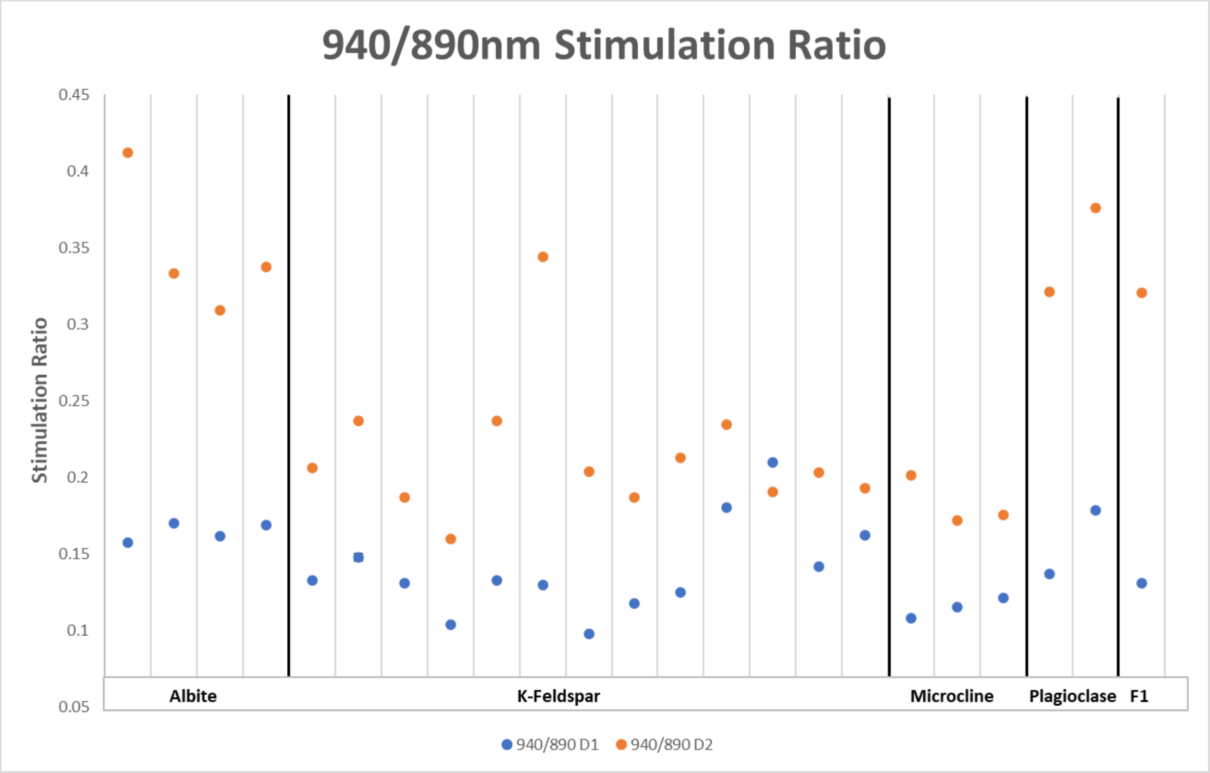

Figure 4.3 – The calculated 940/890nm stimulation ratio for each sample aliquot investigated in this experiment. The data is arranged in the order of stimulation, with divisions separating the major mineral family groups.

Figure 4.4 shows the PSP depletion obtained for each feldspar sample investigated in this experiment. The PSP depletion is a parameter which represents the rate at which charge is released from retrapping sites after the mineral has been stimulated and the lattice is allowed to begin relaxing. It is calculated by taking the net counts recorded following 600s after the end of stimulation and dividing it by the net counts recorded from the next 600s. A high PSP depletion ratio indicates that the decay following stimulation is primarily composed of fast components, whereas a lower PSP depletion ratio suggests that a mineral may have longer lived decay components. An outlier to this would be minerals with a depletion ratio of approximately 1, as this indicates little to no PSP detections above the expected background over the course of the measurement.

The PSP depletion observed across the sample set varied from 1.2 to 3.95. Figure 4.4 shows the PSP depletion obtained for each aliquot stimulation using both wavelengths. As shown by this graph there are clear trends across the dataset, with the 890nm stimulation resulting in a greater PSP depletion index than the 940nm stimulation (with an increase of up to a magnitude of 2). This indicates that the 940nm stimulation results in a proportionally larger signal which has a slower decay.

Also visible in Figure 4.4 is a clustering in PSP depletion index values along mineral group lines, with albites having higher depletion indices than K-Feldspars for both stimulation wavelengths. The microcline and plagioclase samples saw the largest differences within mineral families for the detected PSP depletion index, with the post-890nm depletion index for RC659 being a magnitude of two greater than RC246.

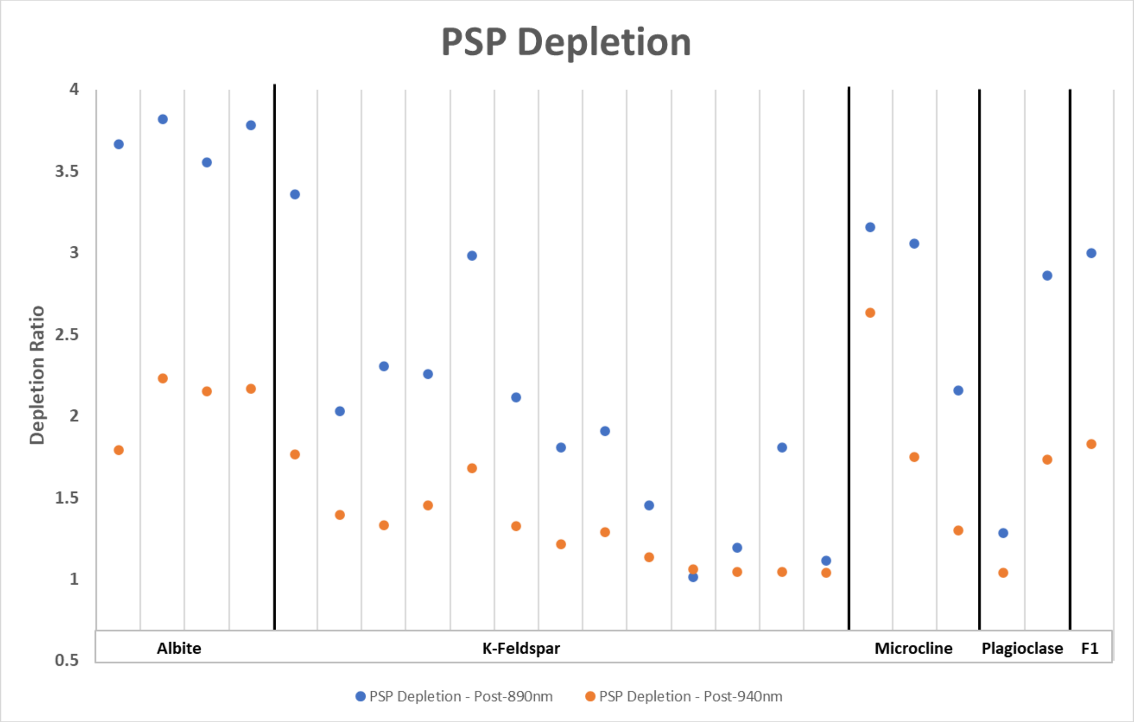

Figure 4.4 – The calculated PSP depletion for each sample aliquot investigated in this experiment. The data is arranged in the order of stimulation, with divisions separating the major mineral family groups.

Albites

The albites were the first mineral group which were investigated as part of this experiment. Overall, the collection of albite samples investigated in this experiment exhibited similar behaviour following stimulation with 890nm and 940nm LEDs once their respective decays were normalised.

The total counts per sequence observed from all albite aliquots during stimulation with 890nm and 940nm varied by an order of magnitude, the net counts recorded during the phosphorescence decay varied by factors of 2-4. The PSP depletion (the ratio of the first sequence of 600 seconds readout after the final stimulation wavelength used over the second sequence of 600 seconds) can be seen to vary across wavelengths in a consistent way across the sample set (Figure 4.4), with the post-890nm PSP decaying faster when comparted to the post-940nm PSP.

Figure 4.5 shows that the post-940nm PSP to stimulation count ratio is consistently higher than that seen after 890nm stimulation across all albite samples – with this difference increasing when the 940nm is the second stimulation wavelength used. This suggests that the processes responsible for post-IRSL emission in albites may be wavelength dependant, with a higher energy (shorter wavelength) resulting in larger signals during stimulation, but proportionally lower counts during the following period of isothermal phosphorescence decay.

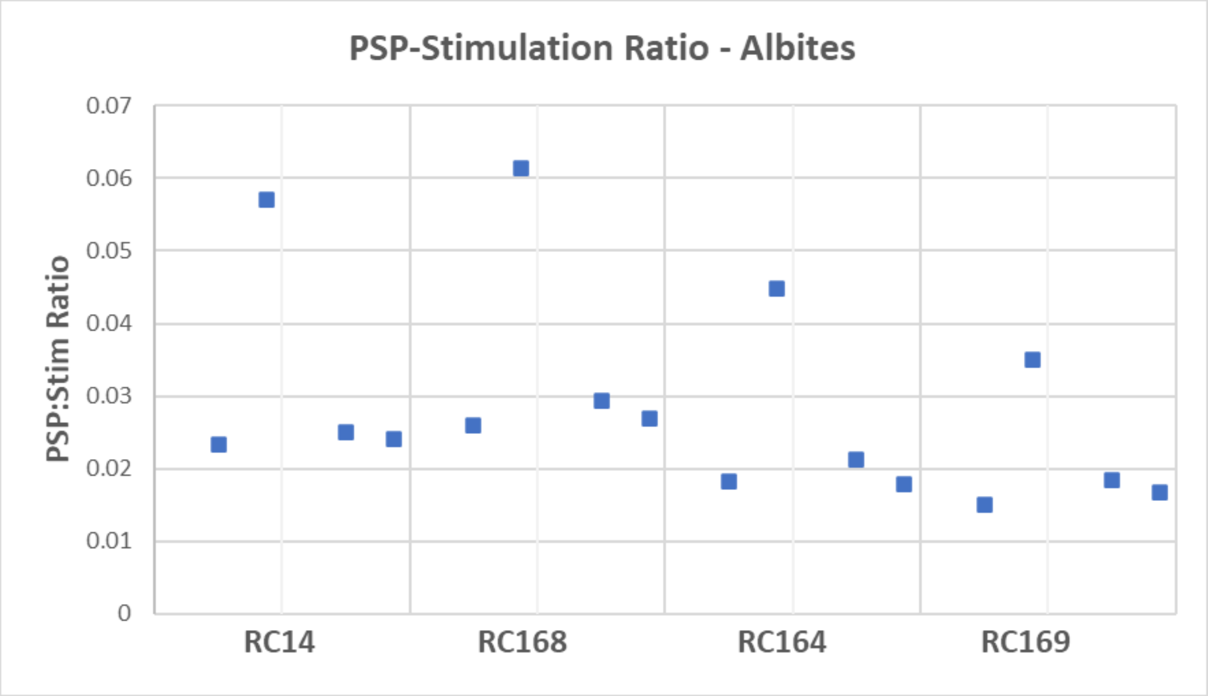

Figure 4.5 – The ratio of the PSP counts to the counts during the stimulation which preceded it. The data is arranged such that a graph vertical subdivision contains each sequence for a specific aliquot and the major vertical divisions represent each mineral.

Figure 4.6 shows the normalised PSP decay curves for RC14, the albite sample with the largest 890nm signal. The post-890nm phosphorescence (aliquot one) and the post-940nm phosphorescence (aliquot two) are very similar once normalised, despite the maximum of a factor of three difference in the PSP:Stim ratio (Figure 4.5). The post-940nm phosphorescence for aliquot one demonstrates a much slower decay rate than all the other PSP decay curves for this sample, particularly when compared with the post-890nm phosphorescence decay curve for aliquot two. Table 4.2 shows the average values of these decay components for RC14 from the decays measured.

Most PSP decays were found to adhere to the following equation:

$$f = y_0 + ae^{(-bx)} + ce^{(-dx)} + ge^{(-hx)} \tag{4.1}$$

Where f is the number of normalised counts at time x; y_0 is the normalised background; a, c, g are scaling components; and b, d, h are components representing the rate of decay over different time intervals. The averaged decay components for each sample are found in Appendix A.

RC14 PSP Decay Components	**Avg Value**	**Avg Uncertainty**
y0	0.047225	0.001075
a	0.43715	0.008825
b	0.232725	0.01
c	0.40135	0.006975
d	0.034525	0.001125
g	0.1996	0.0042
h	0.005369	0.00015
Avg R^2	0.8461	

Table 4.2 – The average PSP decay components and their uncertainties for RC14.

These trends are also seen in varying degrees across the rest of the albite samples, as shown by Figures 4.7, 4.8 and 4.9 which contain the decay curves for RC168, RC164 and RC169 respectively. RC168 had the greatest net count difference between the 890nm and 940nm signal of the albite samples used across both aliquots (Figure 4.3). The decays for this sample following both post-890nm stimulations and the post-940nm stimulation for aliquot two are very similar once normalised, despite their order of magnitude differences in net counts. The post-890nm decay for aliquot one has a faster decay rate. The post-940nm stimulation for aliquot one demonstrates a much slower decay rate than all the other PSP decay curves for this sample in a similar way as was seen for RC14.

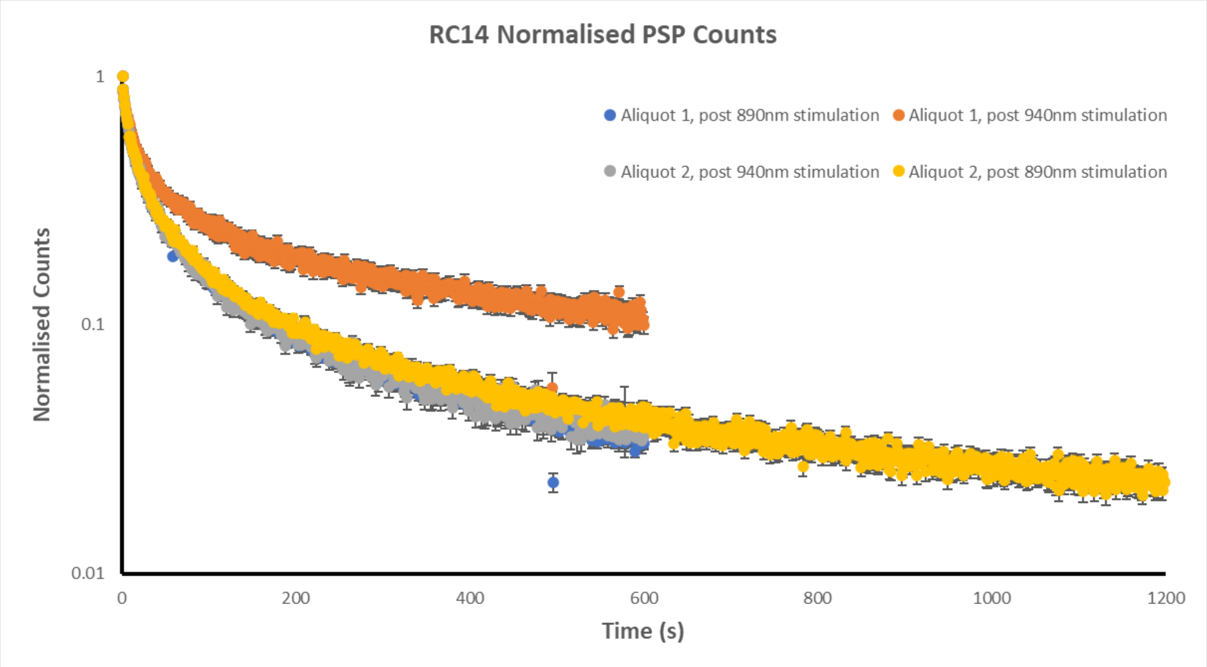

Figure 4.6 – The normalised PSP decay observed from both aliquots of RC14 after stimulation with 890nm and 940nm.

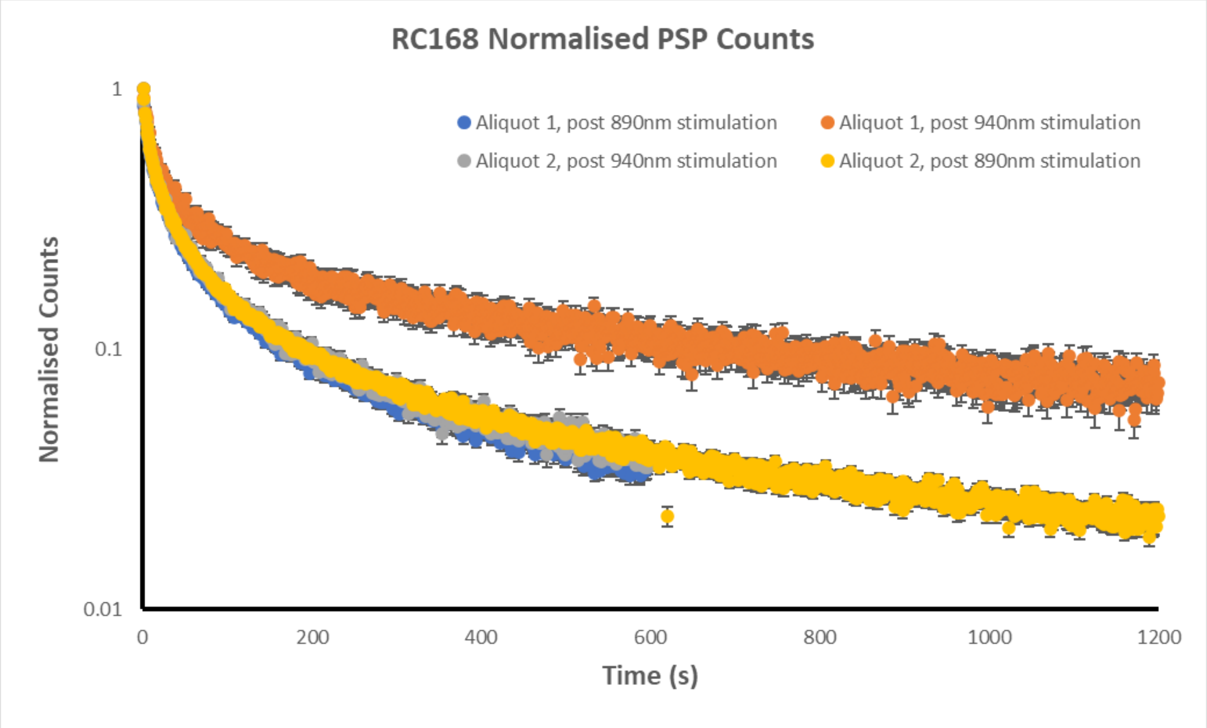

Figure 4.7 – The normalised PSP decay observed from both aliquots of RC168 after stimulation with 890nm and 940nm.

For the samples RC164 and RC169, both samples yielded lower PSP emission after 940nm stimulation than 890nm stimulation, resulting in larger uncertainties in the measurement.

The decays for these samples display similar characteristics once normalised and are different in several ways when compared with the decays seen across the RC14 and RC168 sample aliquots.

Regarding the decay curves for RC164, both decay curves after 890nm stimulation are very similar in terms of decay rate up until 200 seconds of each measurement, where the post-890nm decay for aliquot two begins to diverge due to having slower decay components (Table 4.3). The post-940nm decay for aliquot two has a slightly slower decay rate than either of the post-890nm measurements, resulting in a similar decay curve for the first 100 seconds of measurement until the decays diverge. Like previous samples, the post-940nm decay for RC164's aliquot one is considerably different from all other decays and has the slowest decay rate.

RC164	**Aliquot 1, post 890**	**Aliquot 1, post 940**	**Aliquot 2, post 940**	**Aliquot 2, post 890**
y_0	0.0349	0.074	0.0446	0.0238
unc y_0	0.0013	0.0021	0.0015	0.0005
A	0.4281	0.4379	0.3992	0.4956
unc a	0.0112	0.0144	0.0170	0.0065
b	0.2247	0.1658	0.2541	0.1559
unc b	0.0112	0.0110	0.0209	0.0040
c	0.419	0.3419	0.4305	0.3777
unc c	0.0089	0.0103	0.0141	0.0052
d	0.0352	0.0209	0.0408	0.0228
unc d	0.0014	0.0011	0.0022	0.0005
g	0.2134	0.2046	0.2367	0.1472
unc g	0.0064	0.0048	0.0081	0.0030
h	5.83E-03	2.51E-03	6.39E-03	3.46E-03
unc h	0.0002	0.0001	0.0003	0.0001

Table 4.3 – The PSP decay components calculated for RC164, as well as their uncertainties.

The final albite sample investigated, RC169, had the lowest ratios of PSP counts to counts recorded during stimulation with both sets of LEDs of the albite samples used across both aliquots. The decays for this sample showed little difference between the decays of the post-890nm stimulations and the post-940nm stimulation for aliquot two (Figure 4.9), however the post-890nm decay for aliquot two does have a slower decay on average than that seen for aliquot one.

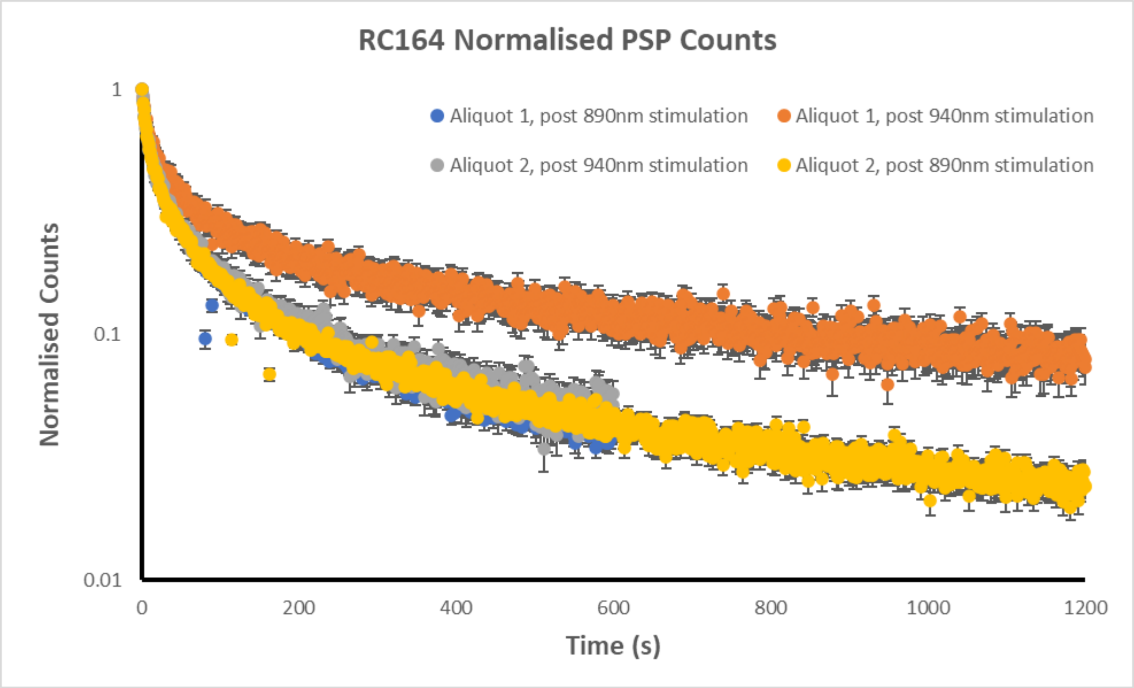

Figure 4.8 – The normalised PSP decay observed from both aliquots of RC164 after stimulation with 890nm and 940nm.

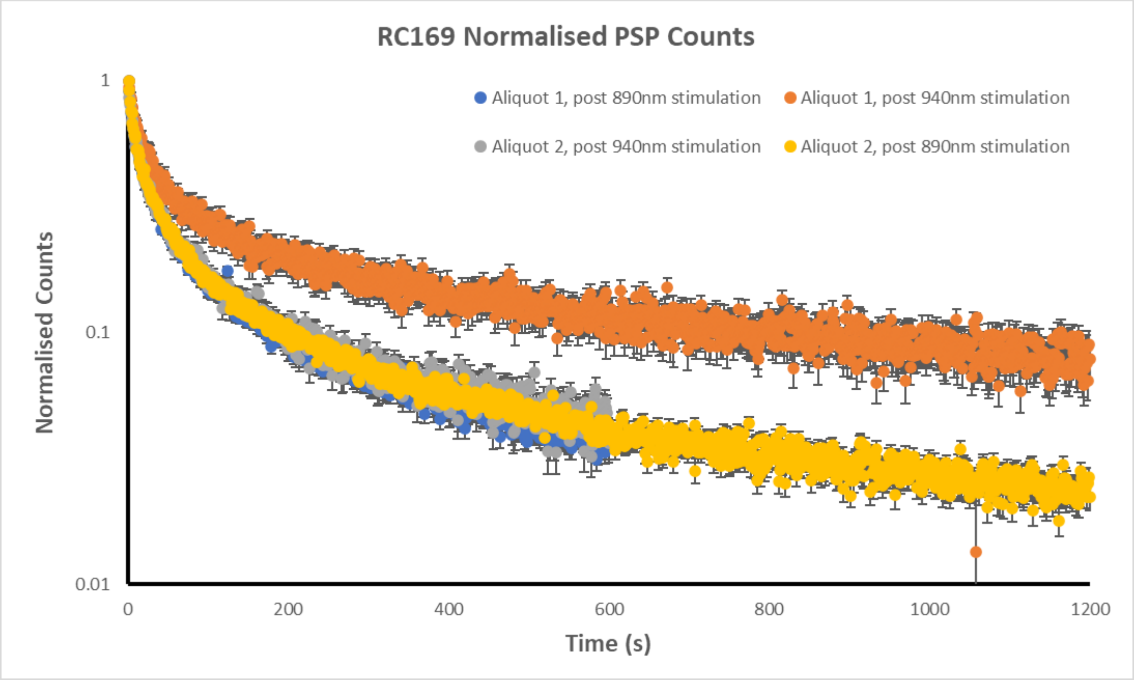

Figure 4.9 – The normalised PSP decay observed from both aliquots of RC169 after stimulation with 890nm and 940nm.

Microclines

Two microcline samples were investigated as part of this experiment.

The PSP depletion (the ratio of the first sequence of 600 seconds readout after the final stimulation wavelength used over the second sequence of 600 seconds) can be seen to vary across wavelengths in a consistent way across the sample set (Figure 4.4), with the post-890nm PSP decaying faster when comparted to the post-940nm PSP.

The measurement for RC630 was repeated due to spurious counts which were noticed during the post-940nm readout for aliquot one, resulting in much larger total sequence counts than expected. This anomaly resulted in aliquot one of RC630 being re-irradiated and the measurement repeated, with no further cases of spurious counts during the decay sequences. The spurious counts were a system artefact which occurred during that specific measurement sequence. This repeat of RC630 is what will be referenced in this investigation when the decay rates of PSP observed in RC630 are discussed.

Further, the ratio of counts recorded during 940nm stimulation to counts recorded during 890nm stimulation for aliquot one of each sample is consistent with those reported in previous studies (Clark and Sanderson, 1994; Fitzgerald et al. 2022) which observed these same albite samples. However, a key difference is apparent when comparing each aliquot for each mineral, the same ratio is an order of two to three times greater for the second aliquot than the ratio obtained for the first aliquot.

Figure 4.10 shows that the post-940nm PSP to stimulation count ratio is consistently higher than that seen after 890nm stimulation across both microcline samples – with this difference increasing when the 940nm is the second stimulation wavelength used.

Figure 4.11 shows the normalised PSP decay curves for RC630. This microcline sample was the first that was investigated. Between the two investigated microcline samples, RC630 had the greatest detected signal during stimulation of the two microcline samples, substantially greater detected phosphorescence after stimulation across both aliquots, and the fastest decaying PSP of the two microclines (Figure 4.4). There is a clear spread in the decay rates following each stimulation between both post-940nm decays; however, the post-890nm decay for aliquot one and the post-890nm decay for aliquot two have extremely similar decay rates once normalised (Table 4.4 shows the average decay components of both microclines and their uncertainties).

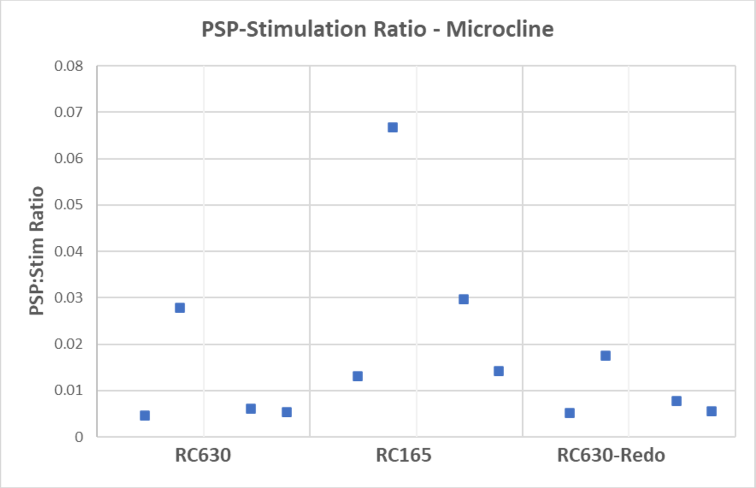

Figure 4.10 – The ratio of the PSP counts to the counts during the stimulation which preceded it. The data is arranged such that a graph vertical subdivision contains each sequence for a specific aliquot and the major vertical divisions represent each mineral.

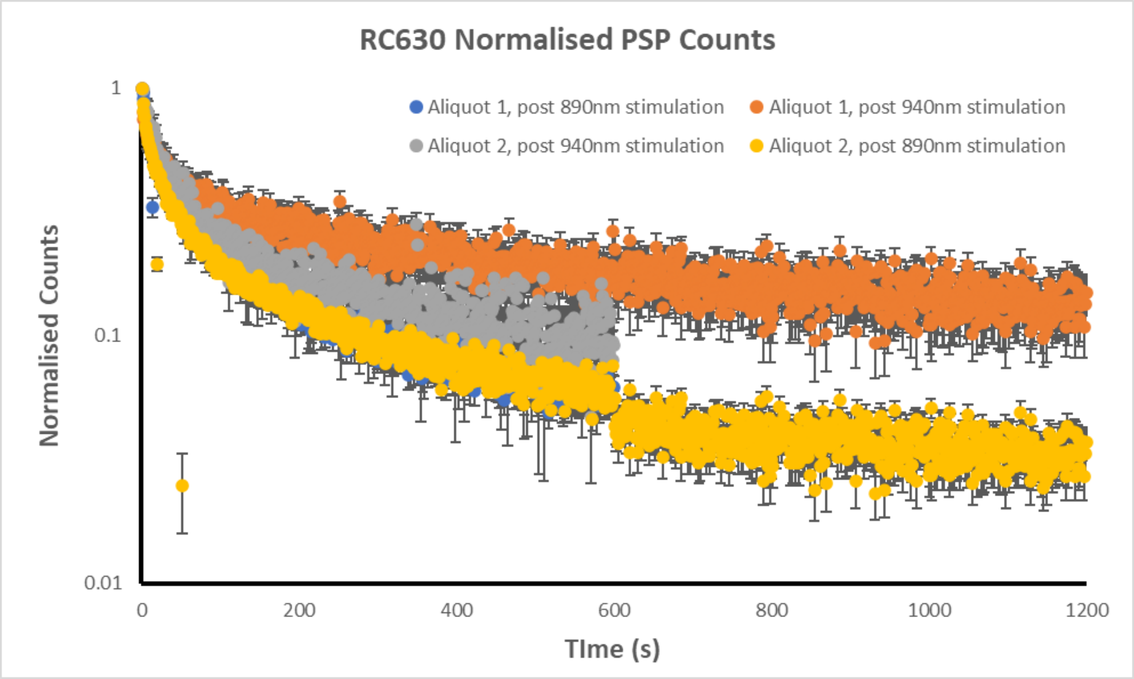

Figure 4.11 – The normalised PSP decay observed from both aliquots of RC630 after stimulation with 890nm and 940nm.

PSP Decay Components	RC630 (redo) Avg Values with Uncertainties	RC165 Avg Values with Uncertainties
y0	0.07635±0.005405	0.14755±0.003423
a	0.433725±0.049449	0.655675±0.02182
b	0.364425±0.075851	0.44735±0.036366
c	0.40365±0.066241	0.33575±0.030997
d	0.03235±0.009698	0.0232±0.004491
g	0.235675±0.036645	0.148825±0.017399
h	0.00467±0.001237	0.003736±0.000573
Avg R^2	0.8446	0.7293

Table 4.4 – The average values of the PSP decay components for RC630 and RC165, along with their respective uncertainties.

The same trend is also seen to a varying extent in the other microcline sample investigated, RC165, as shown by Figure 4.12. Sample RC165 had an order of magnitude less detected signal than that seen from RC630. There was a high degree of scattering observed during each decay curve for this sample, however similar trends continue:

- Post-890nm PSP counts have a similar decay curve regardless of the order of stimulation.
- The post-890nm counts detected for aliquot one had slightly slower decay after 400 seconds.
- The post-940nm PSP measurements follow similar decay curves but ultimately start to diverge after 200 seconds.

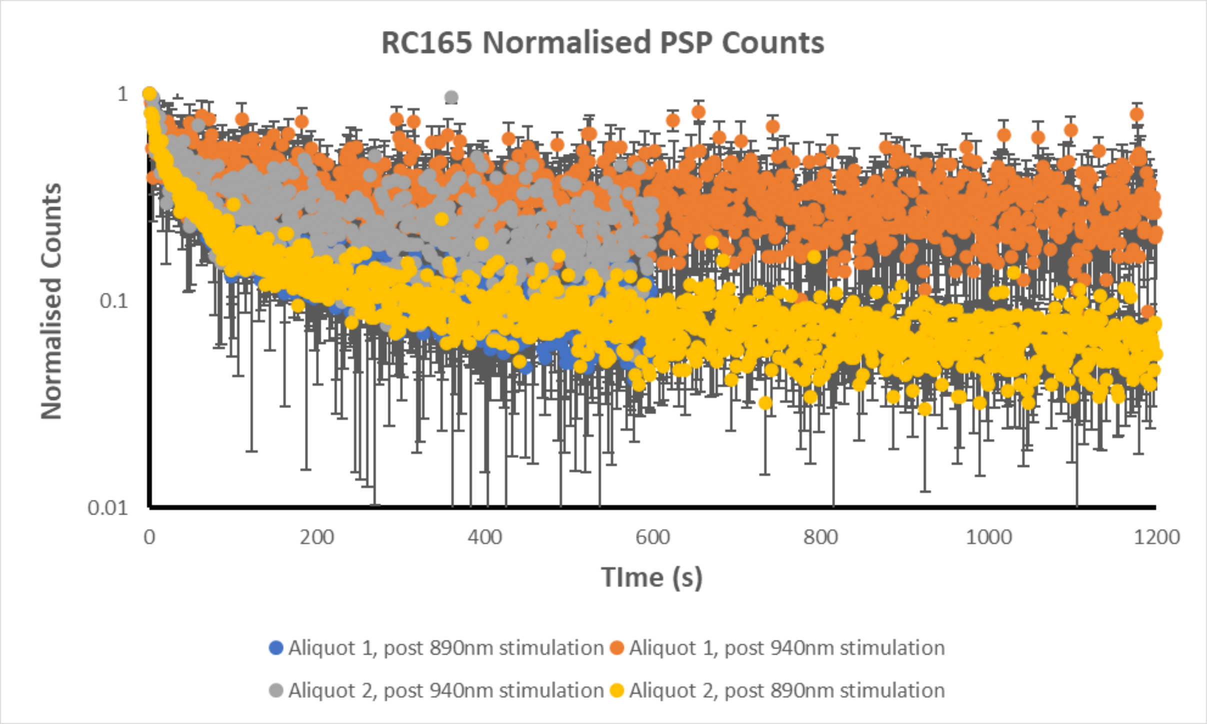

Figure 4.12 – The normalised PSP decay observed from both aliquots of RC165 after stimulation with 890nm and 940nm.

Plagioclases

Like the microcline samples, the plagioclase mineral group was investigated using two samples as part of this experiment. These samples varied considerably in terms of stimulation response, with RC659 releasing two orders of magnitude more detected counts than RC246 when stimulated with either wavelength. Due to the orders of magnitude in signal intensity between the two samples, normalisation was a key component in establishing trends.

Figure 4.13 shows the normalised PSP decay curves for RC246. This plagioclase sample had no response when stimulated with 890nm or 940nm LEDs for both aliquots regardless of the stimulation order. The 890nm stimulation wavelength did result in some PSP emission counts that returned to the numbers expected of the instrument's background count within the measurement timescale.

This behaviour was not seen in RC659, the other plagioclase sample investigated in this experiment, which, as shown by Figure 4.14, had distinct decay rates after each stimulation across both aliquots. The post-940nm PSP decay curves followed a similar decay curve until

80 to 100 seconds into the measurement, at which point they diverged due to the post-940nm decay for aliquot one having a longer decay lifetime.

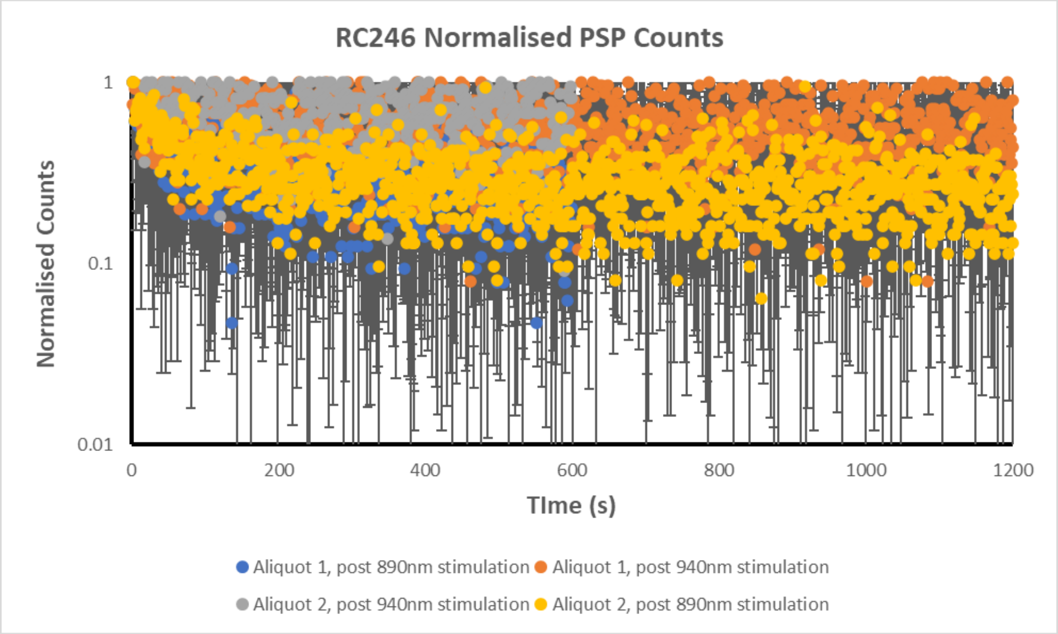

Figure 4.13 – The normalised PSP decay observed from both aliquots of RC246 after stimulation with 890nm and 940nm.

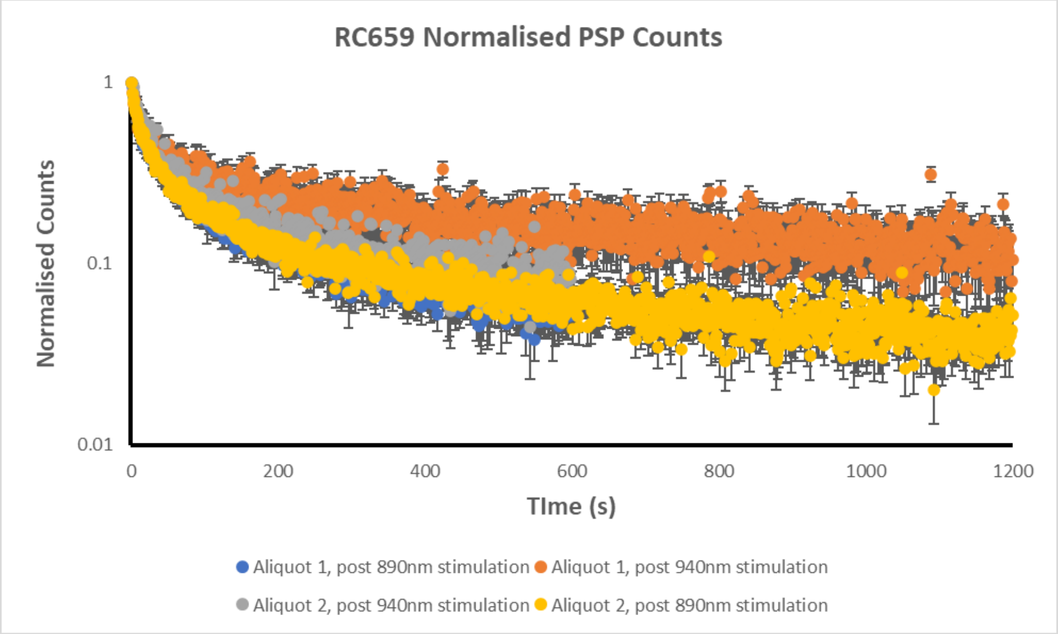

Figure 4.14 – The normalised PSP decay observed from both aliquots of RC659 after stimulation with 890nm and 940nm.

The post-940nm PSP ratio calculated for the first aliquot of RC246, while expectedly greater than that seen when compared to the post-890 PSP ratio, is erroneously high due to the extremely low signal during the 940nm stimulation of this aliquot (Figure 4.13 and Figure 4.15). Aside from this, the plagioclase samples follow the trend of the post-940nm PSP to stimulation count ratio being consistently higher than that seen after 890nm.

The PSP depletion (the ratio of the first sequence of 600 seconds readout after the final stimulation wavelength used over the second sequence of 600 seconds) can be seen to vary across wavelengths in a consistent way across the sample set (Figure 4.4), with the post-890nm PSP decaying faster when comparted to the post-940nm PSP.

Further, the ratio of counts recorded during 940nm stimulation to counts recorded during 890nm stimulation for aliquot one of each sample is broadly consistent once normalised with those reported in previous studies (Clark and Sanderson, 1994; Fitzgerald et al. 2022) which observed these same albite samples. However, a key difference is apparent when comparing each aliquot for each mineral, the same ratio is an order of two to three times greater for the second aliquot than the ratio obtained for the first aliquot.

Overall, the two plagioclase samples investigated in this experiment exhibited different behaviour following stimulation with 890nm and 940nm.

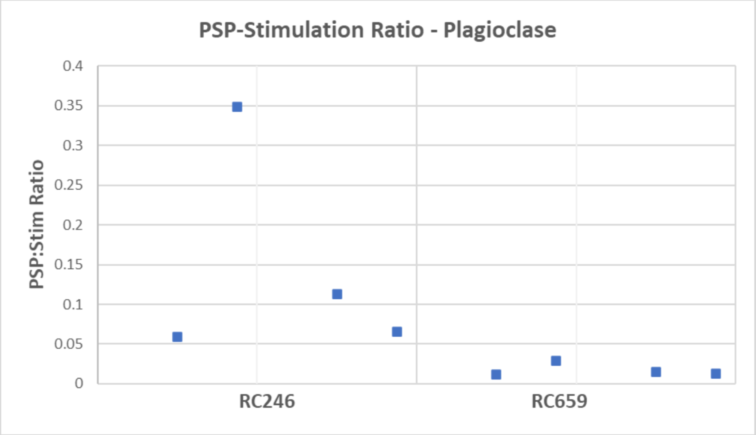

Figure 4.15 – The ratio of the PSP counts to the counts during the stimulation which preceded it.

K-Feldspar

The K-Feldspars were the most geologically diverse mineral group which were investigated as part of this experiment (Table 4.1). Fourteen K-Feldspar samples of known geological origin, as well as the IAEA reference material F1, were investigated, the largest number of any feldspar mineral grouping.

There were two distinct patterns of behaviour observed across the K-Feldspars used in this experiment: low detected counts of IRSL followed by low detected counts of PSP, and high detected counts of IRSL followed by high detected counts of PSP.

Sample response to stimulation varied by several orders of magnitude across the K-Feldspars used, particularly in response to 940nm stimulation with some samples showing no PSP after 940nm stimulation whereas others showed hundreds of thousands of counts over the measurement period. The PSP depletion can be seen to vary across wavelengths in a consistent way across the sample set, with the post-890nm PSP decaying faster when comparted to the post-940nm PSP (Figure 4.4).

The PSP ratio calculated for all K-Feldspar aliquots is shown in Figure 4.16. While the post-940nm PSP is greater than that seen when compared to the post-890 PSP ratio (Fitzgerald et al. 2022), the figures obtained for RC1396C, RC389, RC456 and RC683B are erroneously high due to the extremely low signal during the LED stimulation of these sample aliquots. Aside from this, the K-Feldspar samples follow the trend of the post-940nm PSP to stimulation count ratio being consistently higher than that seen after 890nm which were discussed in previous sections, as well as noting that the post-890nm PSP decays have a faster initial decay.

The range in the detected counts per sequence during IRSL varied across three orders of magnitude, however the range in the detected PSP counts per sequence varied across less than two orders of magnitude. This is a similar pattern in response to stimulation which was observed in the other feldspar minerals examined in this experiment.

RC167 was the first K-Feldspar sample investigated and had one of the highest numbers of detected counts across all sequences. All decay curves after stimulation for both aliquots were very similar in terms of decay rate up to 50 seconds of each measurement (Table 4.5), where the post-890nm decay for aliquot two begins to diverge due to having slower decay components. The post-940nm decay for aliquot two has a slightly slower decay rate than either of the post-890nm measurements after 100 seconds, resulting in a similar decay curve for the measurement until the decays diverge. Like previous samples, the post-940nm decay for RC167's aliquot one is considerably different than all other decays and has the slowest decay rate.

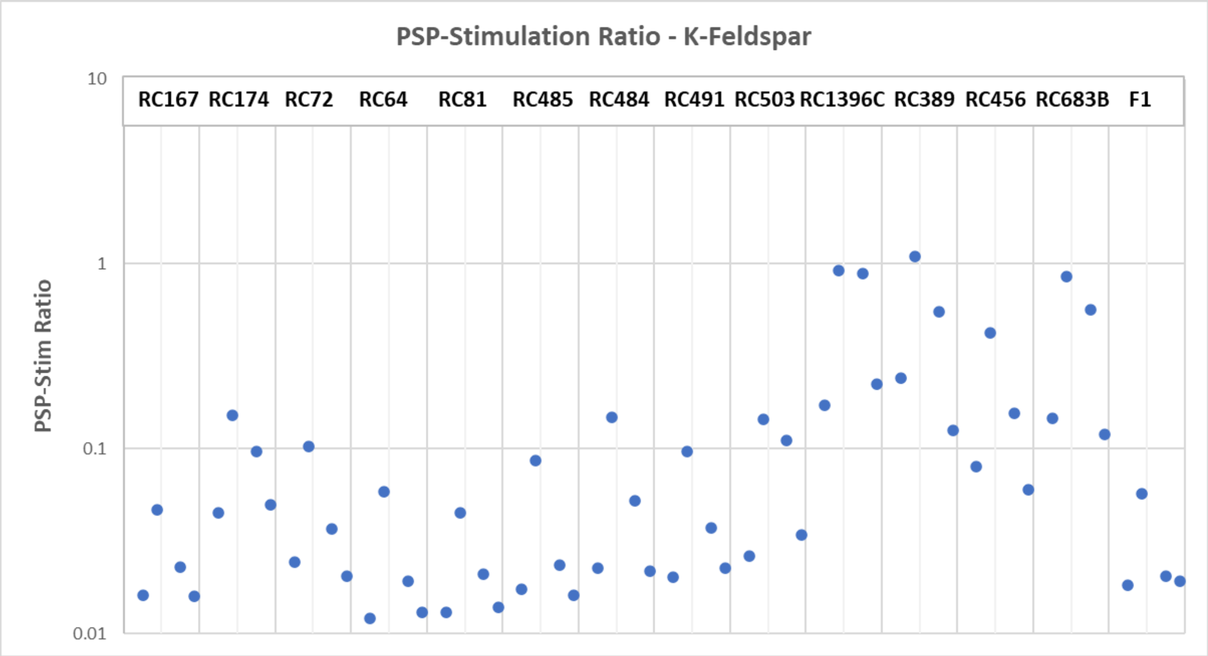

Figure 4.16 – The ratio of the PSP counts to the counts during the stimulation which preceded it.

Run (RC167)	Aliquot 1, Post-890nm	Aliquot 1, Post-940nm	Aliquot 2, Post-940nm	Aliquot 2, Post-890nm
y_0	0.0351	0.113	0.0656	0.0286
unc y_0	0.0080	0.0137	0.0121	0.0051
a	0.4769	0.4171	0.4777	0.6362
unc a	0.0080	0.0137	0.0121	0.0051
b	0.2108	0.1135	0.2276	0.3254
unc b	0.0088	0.0120	0.0146	0.0034
c	0.3873	0.2806	0.3526	0.3917
unc c	0.0063	0.0104	0.0098	0.0040
d	0.0307	0.0177	0.0288	0.0254
unc d	0.0010	0.0013	0.0016	0.0004
g	0.1897	0.1729	0.18	0.1579
unc g	0.0044	0.0048	0.0062	0.0022
h	6.23E-03	2.42E-03	5.93E-03	4.77E-03
unc h	0.0001	0.0001	0.0002	0.0001

Table 4.5 – The PSP decay components for both aliquots of RC167 and their uncertainties.

RC174 had an order of magnitude lower detected signal than that seen from RC167. There was a high degree of scattering observed during each decay curve for this sample, however similar trends continue. Both post-890nm PSP counts have a similar decay curve regardless of the order of stimulation with the post-890nm counts detected for aliquot one having a slightly slower decay after 300 seconds. The post-940nm PSP measurements follow similar decay curves initially but ultimately start to diverge after 60 seconds.

These trends are also seen in varying degrees across the rest of the K-Feldspar samples, as shown by Figures 4.17, 4.18, 4.19 and 4.20 which contain the decay curves for RC72, RC81, RC491 and F1, respectively. RC72 had the greatest net count difference between the 890nm and 940nm signal of the K-Feldspar samples used across both aliquots. All aliquots showed PSP after stimulation from either wavelength (Figure 4.17). The post-890nm PSP decay counts followed a similar decay curve, with the post-890nm decay curve for aliquot one having a slightly faster decay rate. The post-940nm PSP decay curves also followed a similar decay curve until 80 to 100 seconds into the measurement, at which point they diverged due to the post-940nm PSP decay count for aliquot one’s measurement having a longer decay time.

RC64 had one of the lowest ratios of PSP counts to counts recorded during stimulation with both sets of LEDs of the albite samples used across both aliquots (Figure 4.18). The decays for this sample showed little difference between the decays of the post-890nm stimulations and the post-940nm stimulation for aliquot two, however the post-890nm decay for aliquot two does have a slower decay on average than that seen for aliquot one with a divergence after 200 seconds post-stimulation. The decay of the post-940nm stimulation line is considerably slower than the other decays and diverges from the other decays after 40 seconds.

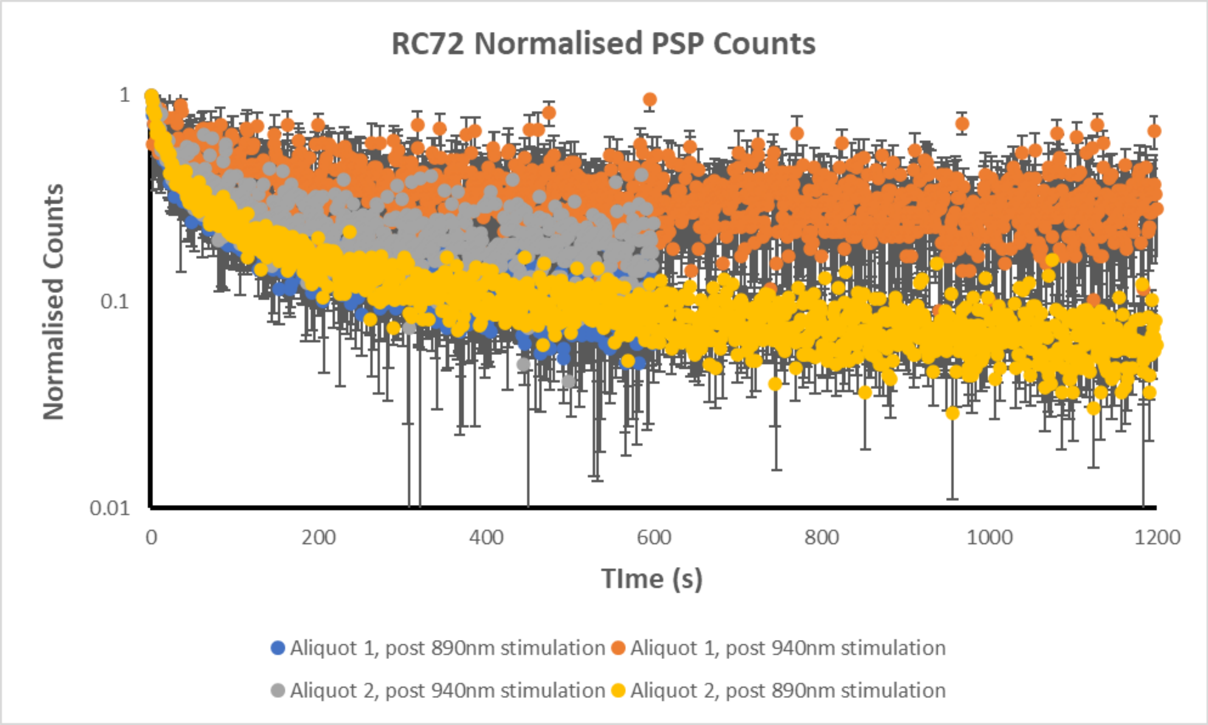

Figure 4.17 – The normalised PSP decay observed from both aliquots of RC72 after stimulation with 890nm and 940nm.

Regarding the decay curves for RC81, Figure 4.18 shows that all aliquots showed PSP after stimulation from either wavelength. The post-890nm PSP decay counts followed a similar decay curve, with the post-890nm decay curve for aliquot one having a slightly faster decay rate initially. The post-940nm decay curve for aliquot two followed a similar decay curve as the post-890nm decays, however the post-940nm decay curve for aliquot one had a considerably slower decay time.

RC485 was another K-Feldspar sample investigated in this experiment, which had similar decay rates after each stimulation across both aliquots. The post-890nm PSP decay counts followed a similar decay curve for the entire measurement cycle. Additionally, the post-940nm decay curve for aliquot two had a slightly faster decay rate. The post-940nm PSP decay curve for aliquot one was the most different of the decays measured for RC485 and followed a similar decay curve until 60 seconds into the measurement, at which point it diverged due to the post-940nm decay for aliquot one having a longer decay time than the measurement. This specific decay also included significantly more scatter due to the low number of counts.

The next trio of K-Feldspars investigated were RC484, RC491, and RC503. These samples behaved in similar ways, with Figure 4.19 showing the normalised PSP decay curves for RC491. These three K-Feldspar samples had the clearest difference between the post-890nm and post-940nm PSP. Importantly, there was no difference in the observed normalised PSP emission following 940nm stimulation of both aliquots for these samples regardless of the stimulation order, with both normalised decay curves decaying at identical rates and returning to the PMT's background count within the measurement timescale. However, the 890nm stimulation wavelength resulted in PSP emission which did not return to the numbers expected of the PMT within the measurement timescale. Further, both samples had lower PSP emission after 940nm stimulation than 890nm stimulation, resulting in larger errors in the measurement.

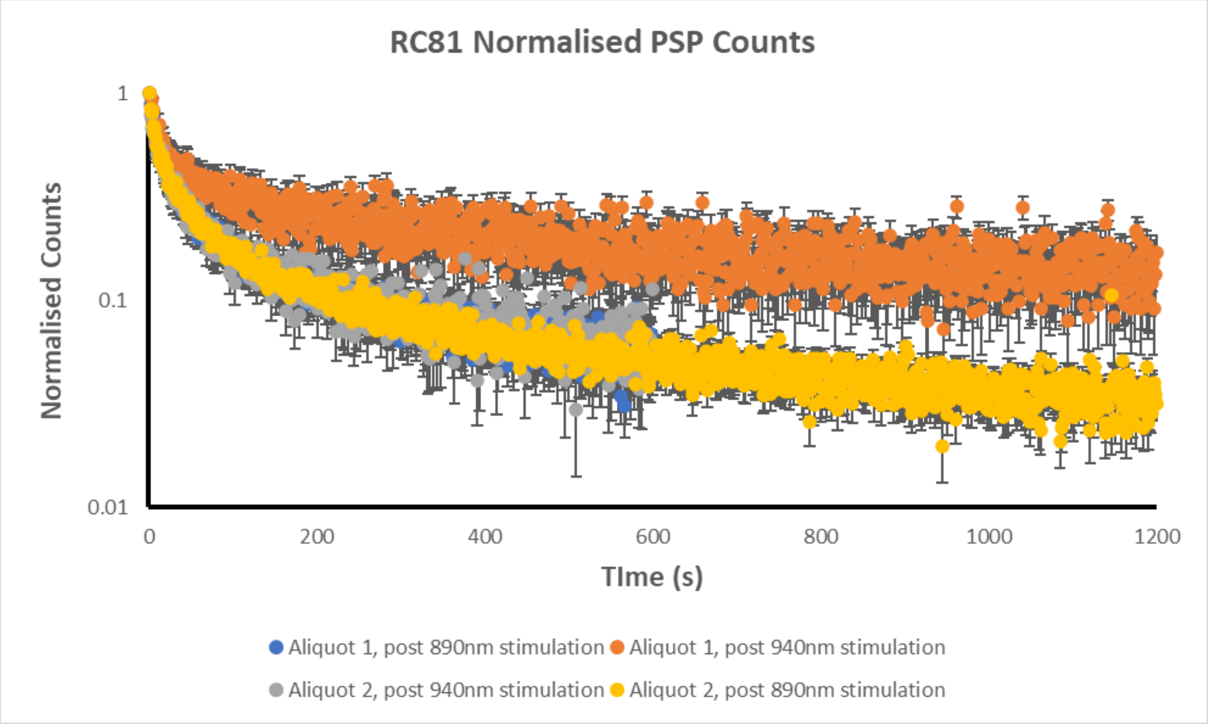

Figure 4.18 – The normalised PSP decay observed from both aliquots of RC81 after stimulation with 890nm and 940nm.

The next four K-Feldspar samples, RC1396C, RC389, RC456 and RC683B had little detected PSP following stimulation with either wavelength, with the sequences recorded following each stimulation returning similar count numbers to the instrument's background. The counts recorded during stimulation between these samples varied by more than an order of magnitude. RC456 had IRSL intensity in line with the previously discussed RC503, however RC456 only had a detected PSP decay after 890nm stimulation for both aliquots which returned to counts expected of the instrument background within 60 seconds of the end of stimulation. The other samples had no measurable PSP or PSP decay.

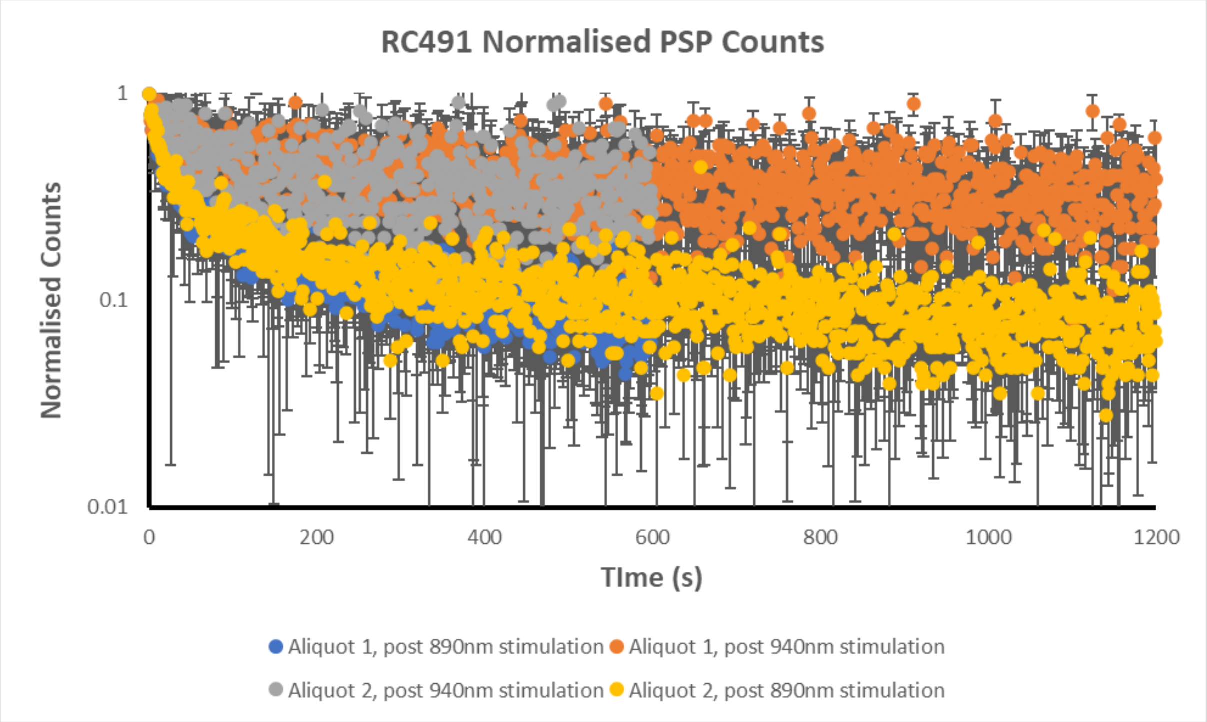

Figure 4.19 – The normalised PSP decay observed from both aliquots of RC491 after stimulation with 890nm and 940nm.

The final K-Feldspar sample investigated was the IAEA reference material F1. This sample returned the most counts per sequence during stimulation and following stimulation for both wavelengths. All aliquots showed PSP after stimulation following stimulation with either wavelength. The post-890nm PSP decay counts followed a similar decay curve with the emission of PSP continuing even 20 minutes after stimulation. The post-940nm decay for aliquot two followed a similar decay curve as the post-890nm decays, differing from the post-940nm PSP decay for aliquot one with regards to both decay time and total counts as shown by Figure 4.20.

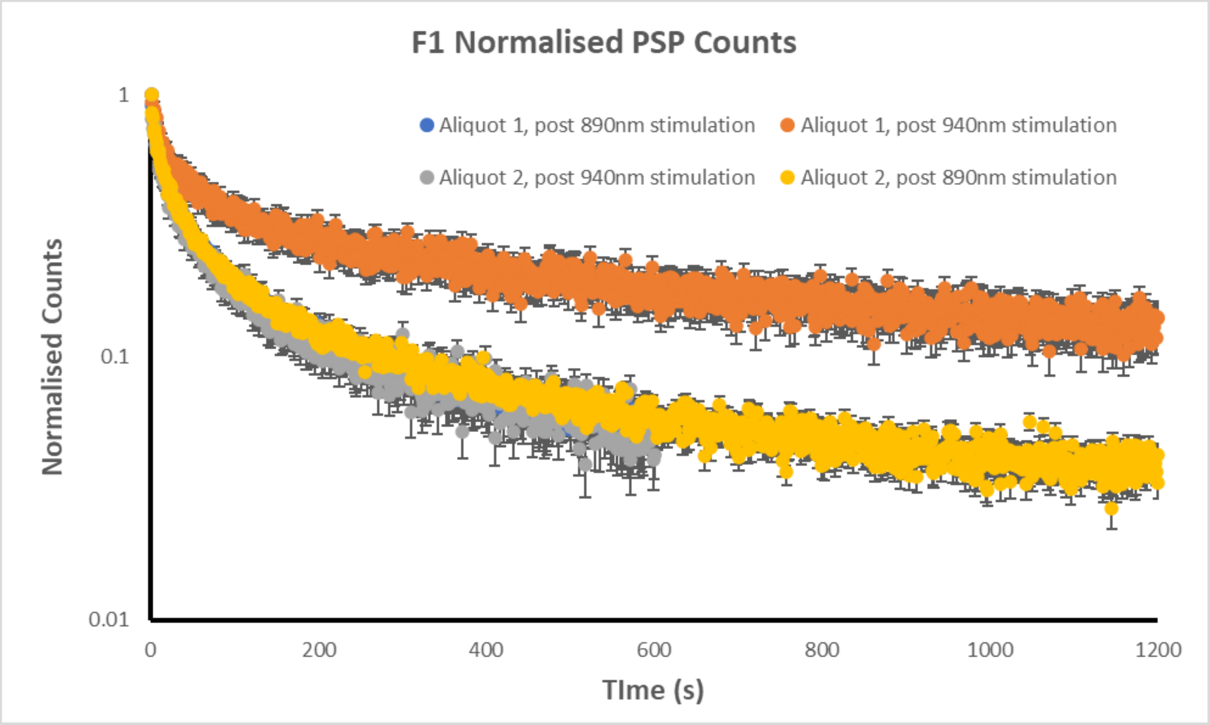

Figure 4.20 – The normalised PSP decay observed from both aliquots of F1 after stimulation with 890nm and 940nm.

4.2.3 Summary

A key observation made throughout Section 4.2.2, and in both Fitzgerald (2020) and Fitzgerald et al. (2022), was the measurement of proportionally higher PSP emission following 940nm stimulation when compared with the PSP measured after 890nm stimulation. Figure 4.21 shows the normalised PSP measured for both aliquots of each sample. The data is normalised to the IRSL counts which preceded the PSP. It is evident from Figure 4.21 that there is more PSP emitted following 940nm stimulation, however this difference between the post-940nm and the post-890nm PSP increases when 890nm is the first stimulation wavelength used. Figure 4.21 also shows that the albites have broadly similar PSP characteristics following stimulation from either wavelength. This is further supported by the similarities of the albite’s PSP depletion observed in Figure 4.4.

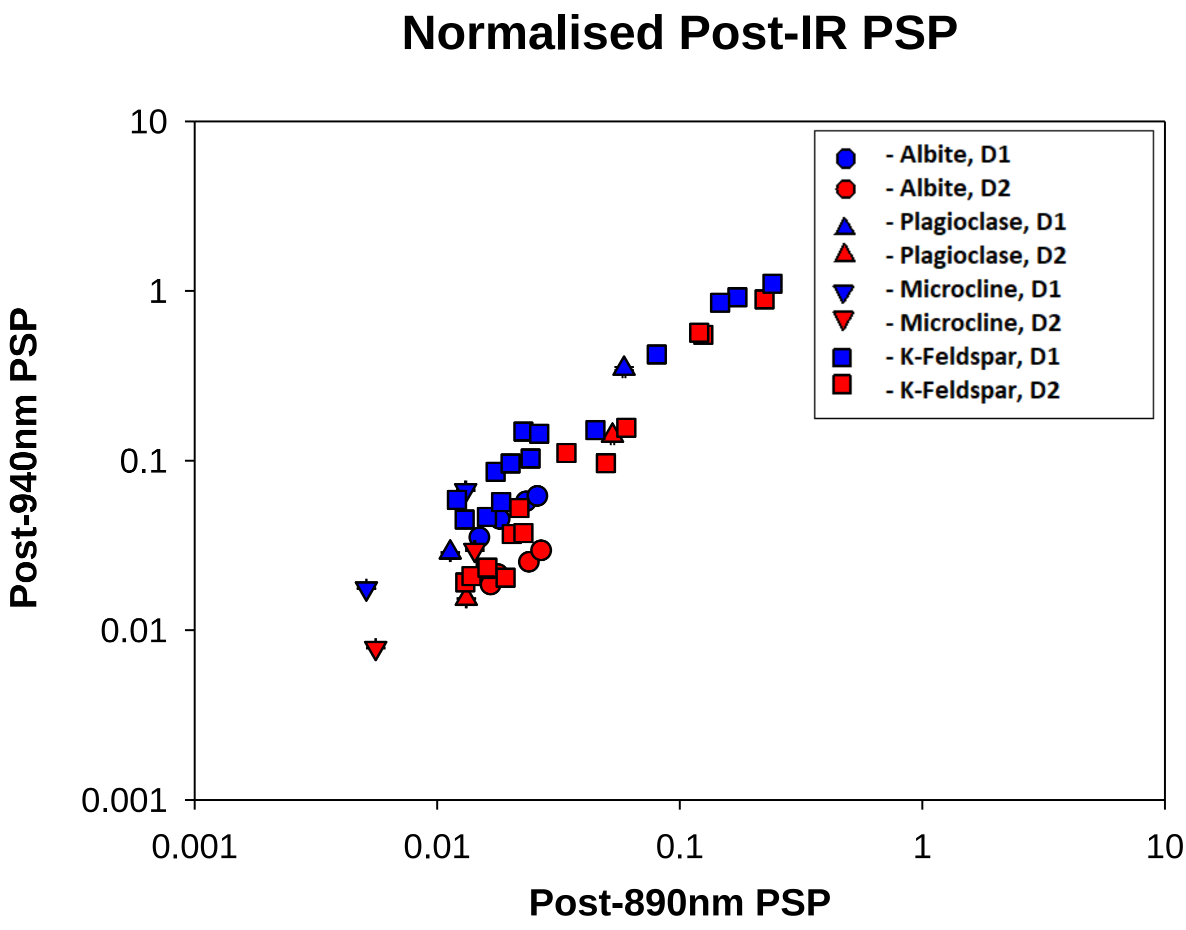

Figure 4.21 – The normalised post-IR PSP for both aliquots of each sample following 890nm and 940nm stimulation. D1/D2 represent disk/aliquot 1/2 respectively. Each point represents the total PSP counts following 890nm and 940nm stimulation which have been normalised to the net IRSL counts which respectively preceded it. For both disks, proportionally more PSP is observed following 940nm stimulation than is observed following 890nm stimulation. Proportionally more PSP is also observed following 940nm when 890nm is the first stimulation wavelength used.

While the PSP depletion index in Figure 4.4 gives an overall view regarding the decay of each sample's detected PSP, it does not give detailed information regarding charge transport processes. For more detailed information regarding these processes, a regression-based method must be employed using the normalised detected PSP data.

Each decay curve was evaluated using SigmaPlot's regression fitter to extract relevant decay components, with different numbers of desired components selected for each attempt. The number of desired components varied from 3 to 7 for each decay. This was repeated for each decay until a relationship that best fitted each decay curve was calculated. This best fit was determined using the largest R_0^2 value, with a value of 1 being a perfect fit.

The components computed for each PSP decay showed a variance between aliquots of the same sample, as well as showing a similar variance to that noted in Fitzgerald, 2020. To ascertain the mineralogical effects on these decay components across the sample set an average value of each component was calculated for both PSP decays for both aliquots of each sample. Then an average of all the samples within a particular mineral family were calculated. The results of this are shown in Figure 4.22.

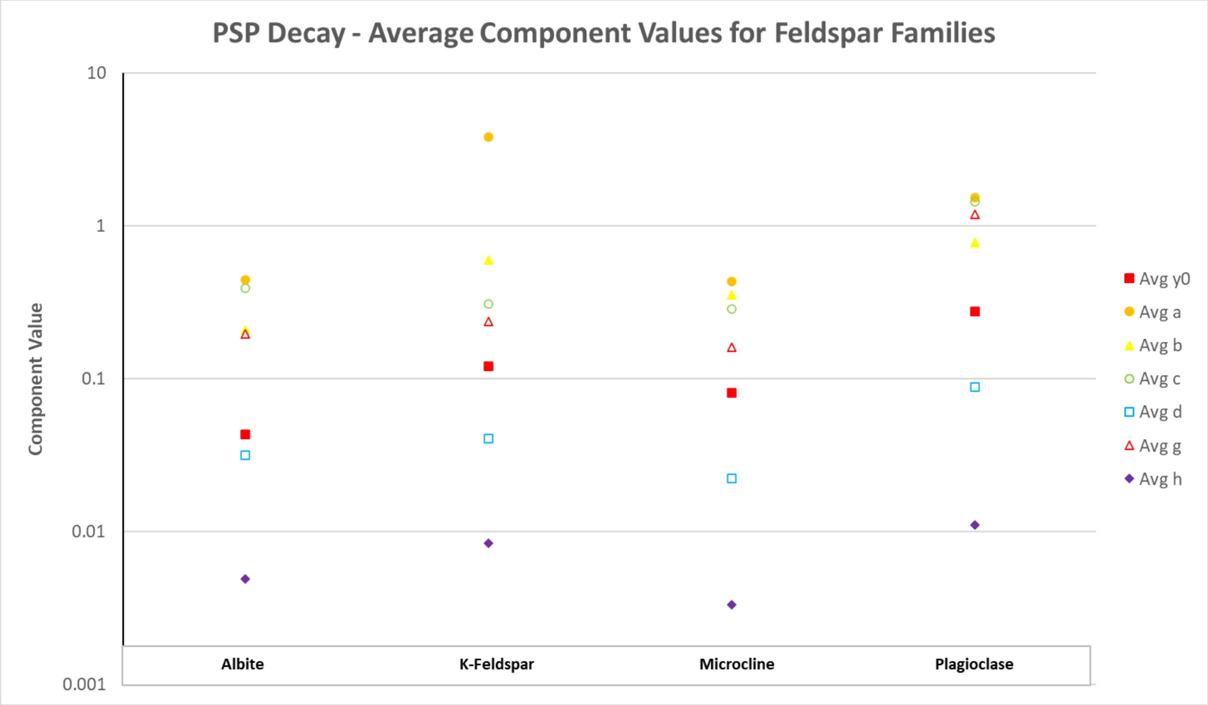

Figure 4.22 – A plot demonstrating the variance of the average decay component values by feldspar mineral family. The values y0, a, b, c, d, g, and h represent the same components which were discussed above.

Regarding the component “y_0”, which represents the normalised PSP intensity relative to the instrument’s expected background, as such a value close to 0 is desirable and values close to 1 indicate that no PSP was detected during the measurement sequence. All albite samples used in this investigation had a calculated y_0 of less than 0.1 and had the least variance in this value across the mineral group. The K-Feldspars saw the greatest variation in this value of all the mineral groups, with nearly two orders of magnitude difference between the lowest and the greatest value for y_0.

Regarding the component “a”, which represents the scaling factor for the fastest decay component “b”, all samples share similar values for this component. A key difference emerges in the form of higher values of a for the post-890nm decay – particularly when the 890nm stimulation occurs second.

Regarding the component “b”, which represents the fastest exponential decay component, each family aside from the albites showed a great deal of variance in this value as shown in Figure 4.23. This indicates that this component is related to an unstable process that is comprised of even faster components which have already mostly decayed by the start of the measurement. Despite this, there is a degree of overlap in the values obtained for the albites, plagioclases and the F1 reference sample which indicates that this component is related to a component with a lifetime of less than a second.

Regarding the component “c”, which represents the scaling factor for the second decay component “d”, the albites have the least variance whereas the K-Feldspars see a large spread across two orders of magnitude. All samples share similar values for this component, with a key difference emerging in the form of much lower values of c for the post-940nm decay when the 940nm stimulation occurs second.

Regarding the component “d”, which represents the “medium” exponential decay component, all samples shared similar values for this component. It was noted that the albites had the least variance and some of the K-Feldspars seeing a large spread in the d value for their decays. The overlap in the obtained value for this component indicates that this component’s process has a lifetime of between 50 seconds to 2 minutes depending on the mineral family.

Regarding the component “g”, which represents the scaling factor for the slowest decay component “h”, a key feature in the distribution of this component’s value across the sample set is that the post-890nm decays had considerably lower values if the 890nm stimulation occurred second. The post-940nm decays also tend to have a lower value if the 940nm stimulation occurred second. Both decays for each exposure tended to have similar values for both wavelengths if they were used first.

Regarding the component “h”, which represents the slowest exponential decay component, the value of this component remained similar for the decays resulting from the first stimulation wavelength used. The values for this decay component varied considerably for the decays resulting from the second stimulation wavelength. The K-Feldspars saw a variance across three orders of magnitude, and both the microclines and plagioclases seeing a two order of magnitude variance. This component is the longest-lived component that this experiment is capable of measuring, with lifetimes up to 10 minutes and some even beyond 10 minutes.

Figure 4.23 shows the lifetimes of each sample’s exponential decay components averaged across both aliquots. For the majority of samples there are three observed decay components which are broadly consistent and separated by an order of magnitude. This plot highlights the range in lifetimes which were calculated for each component across mineralogical families of feldspars. The stability of values seen in the albite, microcline and plagioclase samples can be directly contrasted with the wide range in values seen in the K-Feldspars. This could suggest that the mineralogical differences seen in each feldspar family can contribute to different recombination pathways for PSP, with some being inherently more unstable than others.

Now that lifetimes for these components have been established, Equation [2.10] can be used to compute possible activation energies for the localised electron states associated with the PSP decays. The measurement temperature was noted as being ambient temperature (~20°C), so by assuming a range of values for the frequency factor (s), it possible to calculate a range of possible activation energies given the decay component lifetimes. The results of this are outlined in Table 4.6 and give a range of activation energy values between 0.58eV and 0.95eV for the decay component lifetimes calculated from this experiment depending on the frequency factors of the involved states.

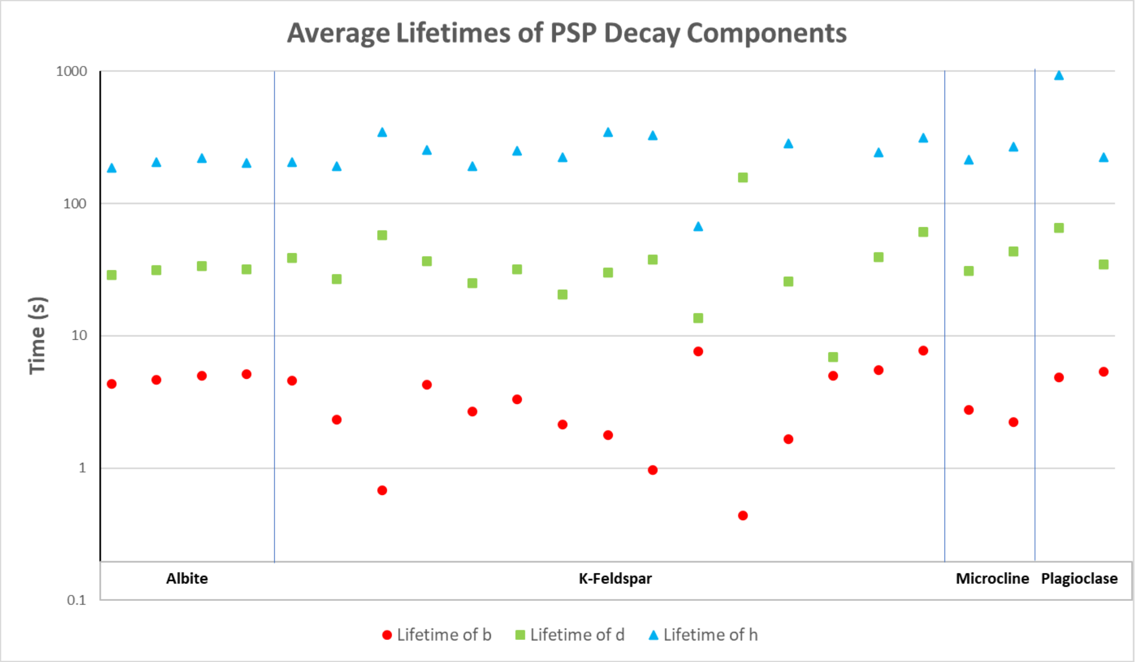

Figure 4.23 – The average lifetime for the PSP exponential decay components which were computed for each sample. Each point represents the decay components from both PSP decays measured for both aliquots. The averaged decay components for each sample are found in Appendix A.

Lifetime (s)	E/eV (10)	E/eV (11)	E/eV (12)	E/eV (13)	E/eV (14)
1.00	0.58	0.64	0.70	0.76	0.81
2.00	0.60	0.66	0.72	0.77	0.83
4.00	0.62	0.67	0.73	0.79	0.85
5.00	0.62	0.68	0.74	0.80	0.85
6.00	0.63	0.68	0.74	0.80	0.86
8.00	0.63	0.69	0.75	0.81	0.87
10.00	0.64	0.70	0.76	0.81	0.87
15.00	0.65	0.71	0.77	0.82	0.88
20.00	0.66	0.72	0.77	0.83	0.89
50.00	0.68	0.74	0.80	0.85	0.91
100.00	0.70	0.76	0.81	0.87	0.93
150.00	0.71	0.77	0.82	0.88	0.94
200.00	0.72	0.77	0.83	0.89	0.95

Table 4.6 – The activation energy (in eV) for a state with a lifetime (s) given a supposed frequency factor range of 10^{10} – 10^{14} and a sample temperature of 293K.

4.3. Feldspar Investigation II – Time Resolved PSP

4.3.1 Experimental Procedure

This experiment aimed to probe the mechanisms responsible for the faster components within the post-IRSL decay that were noted in Section 4.1.3. These components are closely related to charge mobility within the feldspar lattice structure following stimulation. As such understanding how these faster components decay at much shorter timescales would be desirable for exploring charge movement through the lattice after stimulation as they would allow the estimation of the activation energies of these localised electron states.

This experiment aimed to look at the microsecond time components in the post-IRSL decay from across the sample set at a range of temperatures using time resolved spectrometers with fast Ortec MCS cards which could record dwell times of microsecond order and faster (Figures 3.8 and 3.9). The diode control board on the first system was configured to generate 60µs pulses, either once every 10ms for 30,000 cycles with 2 µs dwell time or once every 100ms for 3000 cycles with a 20 µs dwell time. For the second system measurements consisted of 9000 cycles with pulse widths of 5 µs once every 100 ms. These cycles were summed together by a computer connected to the MCS card. Once the desired dwell time and number of measurement cycles had been selected on the computer, the start of the measurement sweep was synchronised to the diode control switches in the module control board such that a trigger pulse from the diode control board initiated the start of the MCS sweep. This was done so that each measurement could be completed in five minutes. This ensured an acceptable throughput of samples. To reduce the likelihood of input errors, the diode control was not adjusted until every measurement with the selected dwell time had been completed. The lifetimes of the decay components for this part of the investigation are detailed in Appendix C.

The second system followed an identical set up, with the only difference being that the pulse generated was 20µs long and repeated every 100ms for 9,000 cycles, allowing a complete measurement every fifteen minutes.

Each sample was given a 1kGy dose and left for two days before being given a two minute preheat at 130°C using the spectrometer's temperature control to remove the low temperature luminescence components prior to any measurements and were stored in the dark when not being used. A measurement was then taken of the sample chamber without the sample being stimulated to record a background for each sample and was followed by stimulated measurements.

A range of temperatures was used in this section of the investigation. Initial experiments were conducted from room temperature up to 100°C. A further set of experiments within the temperature region of 80°C down to cryogenic temperatures of -95°C were also conducted. For the initial measurements at cryogenic temperatures, afterpulses were noted from the photomultiplier that were recorded by the MCS, causing errors in the PSP decay fits. This was investigated and resolved by reducing the pressure of the cooled nitrogen gas to reduce the "sputtering" as the cooled nitrogen gas entered the sample chamber (Akgun et al. 2008). The lifetimes of the decay components for this part of the investigation are detailed in Appendix C.

The next section will break down the results of these investigations by mineral group, commenting on observed behaviours and trends.

4.3.2 Results

F1

Each decay curve was normalised to the initial PSP counts to account for any differences in aliquot grain content and sample dose so that the relative rates of decay could be determined for each sample. F1 was used as a test sample for each of the experimental runs in this section of the investigation due to its established large intensities during stimulation and large PSP counts following stimulation, which have been noted in 4.1.

Figure 4.24 shows the normalised net PSP decay curves for F1 following stimulation at room temperature with 890nm diodes. As a result of the difference in observation timescales between this investigation and that described in Section 4.1, the decay components computed describe different processes which act over very short timescales. Due to the large volume of data points per measurement, a trendline using the equation obtained by the regression best-fit has been imposed on each plot. Appendix B contains the calculated decay components for each sample used during the elevated temperature section of this investigation, Appendix C contains the decay components for each sample used during the cryogenic section.

Following first exploration of time-resolved spectrometry with F1, computation revealed that there were three separate components in the decay, with two separate components acting on microsecond timescales of values between 3-5µs, and one component acting on a timescale of tens of microseconds of values between 30-60µs (Table 4.7A). As such, the normalised net decay for observed PSP following IR stimulation at microsecond timescales results in decays which can be still described by Equation 4.1. The decay components calculated showed a slight variance between the two temperatures investigated. The 80°C decay components had lifetimes which were nearly two times shorter than those computed for the room temperature decay.

F1	*Post-890nm Ambient*	*Post-940nm Ambient*	*Post-890nm 80°C*	*Post-940nm 80°C*
y0	3.66E-03	5.11E-03	-4.09E-04	-5.96E-04
a	0.9694	1.1006	0.8618	1.0406
b	310995.6	364456.3	226311.7	299961.9
c	0.4651	0.7581	0.6218	0.5698
d	315762.3	365046.3	203187.4	196562.1
g	0.2739	0.1263	0.0579	0.0617
h	32533.15	25828.92	17680.93	16865.09

Table 4.7A – Decay components calculated from the PSP decays from the preliminary investigation using F1.

Figure 4.25 shows the normalised net PSP decay curves for F1 following stimulation at room temperature, 40°C and 80°C with 890nm and 940nm diodes using a 20µs dwell time on the MCS. Computation revealed that there were three separate components in the decay, with separate components acting on the tens of microseconds, hundreds of microseconds, and millisecond timescales. The decay components calculated showed a temperature dependence, particularly with respect to the tens of microseconds and millisecond timescale components. The 80°C decay components had lifetimes which were nearly two times shorter lived than those computed for the room temperature. Further, a slow rise towards a delayed intensity peak 7000-12000 microseconds following stimulation was observed and can be seen in Figure 4.24 and 4.27. This is not expected behaviour as it is expected that the signal intensity would decay to the instrumentation background over time. To investigate whether this late rise was the result of a system artefact, such as the next pulse sweep occasionally triggering too early, a second time resolved stimulation system was developed to investigate this delayed peak.

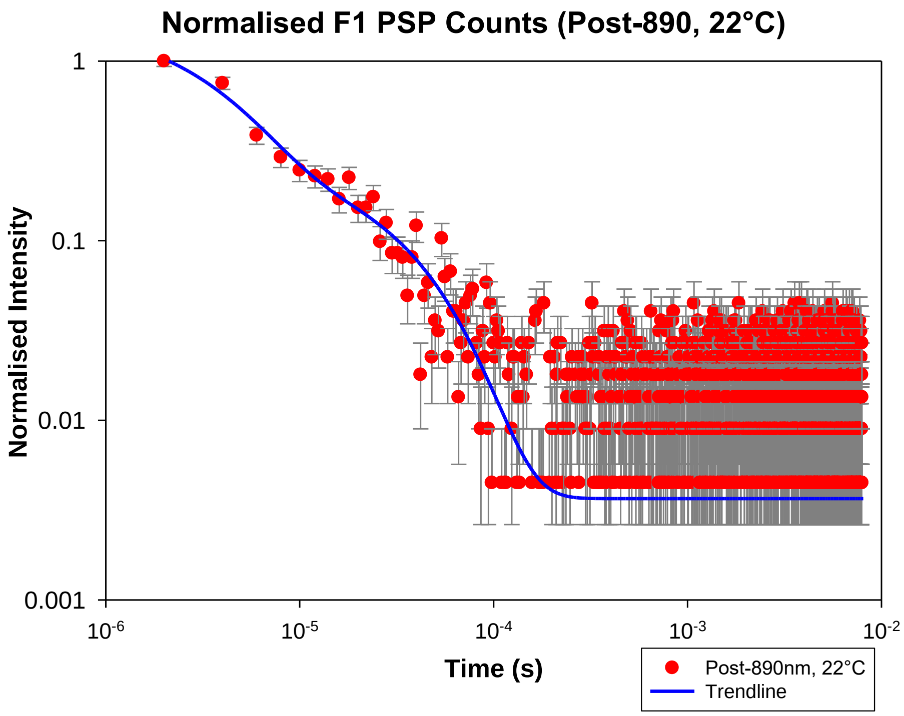

Figure 4.24 – The normalised net decay of a sample of F1 following stimulation by 890nm at room temperature using a 2μs dwell time. The trendline (blue) represents the equation obtained by regression calculations of the data (red dots).

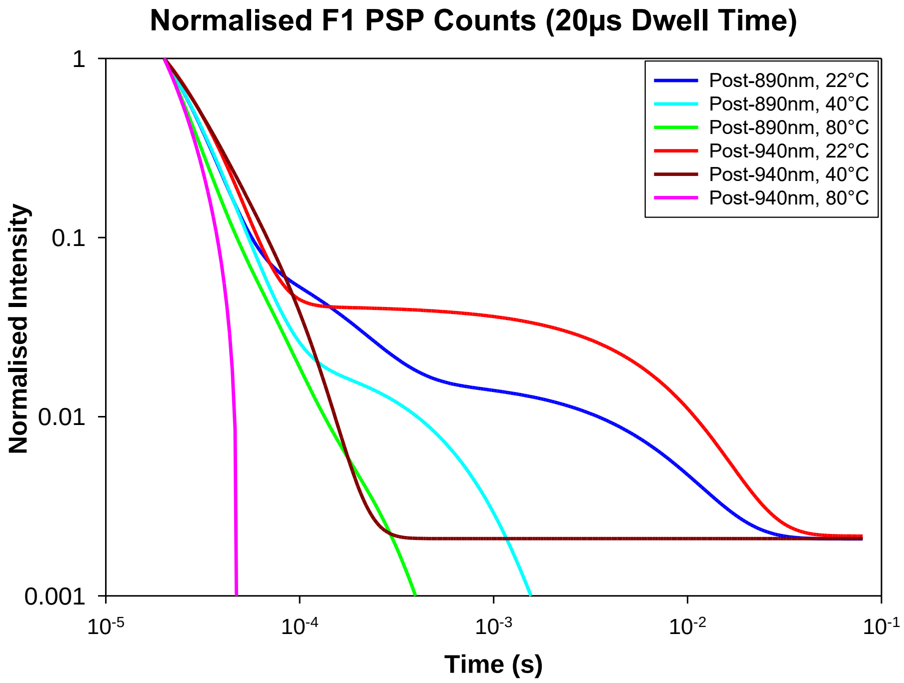

Figure 4.25 – The normalised net decay of a sample of F1 following stimulation by 890nm and 940nm diodes at room temperature, 40°C and 80°C using a 20μs dwell time.

Figure 4.26 shows the normalised net PSP decay curves for a sample of F1 following stimulation by 890nm diodes at room temperature and 80°C using 0.5µs, 2µs and 5µs dwell times on the MCS of the second TRS system. Computation of this decay revealed components of nanosecond and microsecond order, contained in Table 4.7B. The delayed rise noted on the first system is also seen on the second system during several room temperature measurements but with a normalised net peak intensity similar to the background and is not seen at all during the elevated temperature measurement. This suggests that the delayed rise is likely to be an artefact of instrument background which has an artificially high normalised net intensity due to a PSP:background ratio close to 1. For the 80°C decay components, the second TRS system also had lifetimes which were nearly two times shorter lived than those computed for the room temperature decay and ten times shorter for the millisecond timescale component, indicating a strong temperature dependence in the decay lifetimes consistent across both instruments.

F1	***Post-890nm 22°C (2us)***	***Post-890nm 22°C (5us)***	***Post-890nm 80°C (5us)***	***Post-890nm 22°C (0.5us)***
y0	0.0005	0.0004	0.0001	0.0012
a	6.7676	1.826	99.5955	0.8506
b	1489456	167657.3	1069074	780526.7
c	0.7262	0.2326	98.7025	0.4034
d	55552.82	25726.52	1071306	77154.57
g	0.0057	0.0053	0.0877	0.0334
h	296.119	197.7789	79889.68	14715.52

Table 4.7B – The decay components for the PSP decays measured on the second TRS system, which are graphed in Figure 4.26.

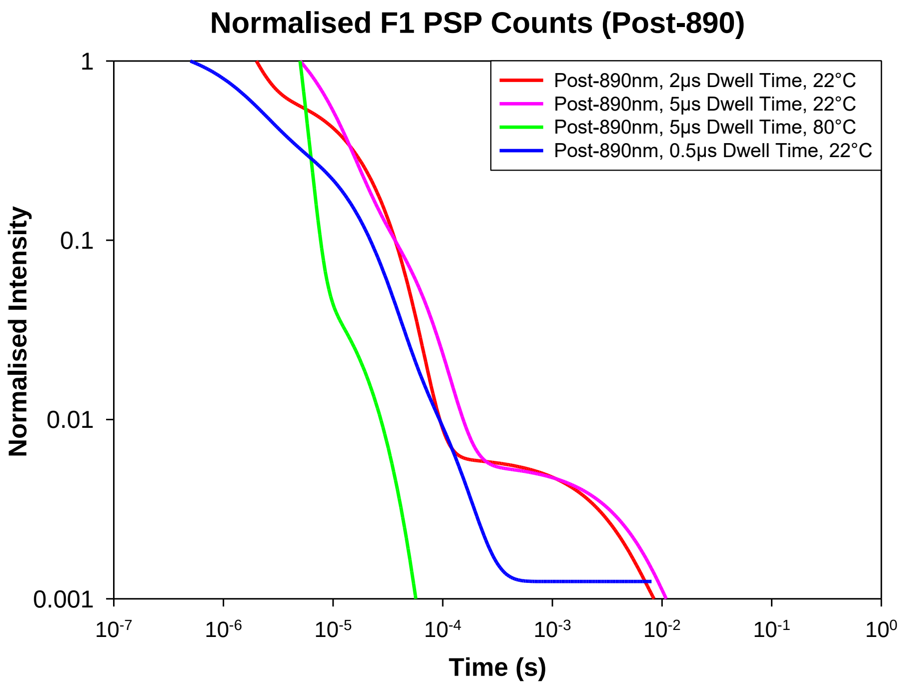

Figure 4.26 – The normalised net decay of a sample of F1 following stimulation by 890nm diodes at room temperature and 80°C using 0.5µs, 2µs and 5µs dwell time.

Further investigations were conducted to investigate this temperature dependent decay over different timescales following 890nm and 940nm stimulation. Figure 4.27 shows the normalised net PSP decay curves for F1 following stimulation at room temperature, 50°C and 100°C with both stimulation wavelengths using a 2µs dwell time on the MCS. Further, Figure 4.28 shows the normalised net PSP decay curves for F1 following stimulation at room temperature, 50°C and 100°C with 890nm diodes using a 20µs dwell time on the MCS. Computation over these two timescales identified four separate components in the PSP decay, with components acting on the microsecond, tens of microseconds, hundreds of microseconds, and millisecond timescales (Table 4.8). For each temperature investigated there was a clear difference in decay behaviour noted. This is a clear indicator of different recombination pathways within the lattice structure of the F1 sample being utilised at different measurement temperatures. For example, Figure 4.27 demonstrates that as the temperature increases, so too does the log-log linearity of the decay, with lower temperatures featuring a clear separation between the dominating components in the decay over time. The key difference between the decays at room temperature and 50°C was that while the room temperature decay had two microsecond order components and one component acting on the timescale of tens of microseconds, the 50°C decay had only one microsecond timescale component, a component which acted on the timescale of tens of microseconds, and final one which acted on the millisecond timescale. This indicates that the IR-50°C PSP-decay has a faster initial decay followed by a more stable decay over longer time periods.

Temperature	Dwell Time	Wavelength	b lifetime (s)	d lifetime (s)	h lifetime (s)
22°C	2µs	890nm	2.74E-06	2.74E-06	3.87E-05
22°C	20µs	890nm	4.42E-06	4.92E-06	5.66E-05
50°C	2µs	890nm	3.33E-06	5.09E-06	5.93E-05
50°C	20µs	890nm	0.000116	1.08E-05	0.006012
100°C	2µs	890nm	0.000465	2.04E-05	9.34E-06
100°C	20µs	890nm	1.12E-05	1.05E-05	3.46E-05
22°C	2µs	890nm	0.002903	1.47E-05	1.47E-05
22°C	20µs	890nm	1.08E-05	3.69E-06	0.000366
22°C	2µs	940nm	4.99E-05	9.53E-06	9.5E-06
22°C	20µs	940nm	2.34E-05	6.39E-06	0.006672
50°C	2µs	940nm	4.91E-06	2.65E-05	0.001649
50°C	20µs	940nm	1.94E-05	5.87E-06	0.000276
100°C	2µs	940nm	1.24E-05	0.000118	0.000588
100°C	20µs	940nm	2.17E-06	2.24E-06	0.000366
22°C	2µs	940nm	3.22E-06	3.17E-06	3.07E-05
22°C	20µs	940nm	3.55E-06	3.57E-06	2.86E-05

Table 4.8 – The room temperature and elevated temperature PSP decay components following 890nm and 940nm stimulation for F1.

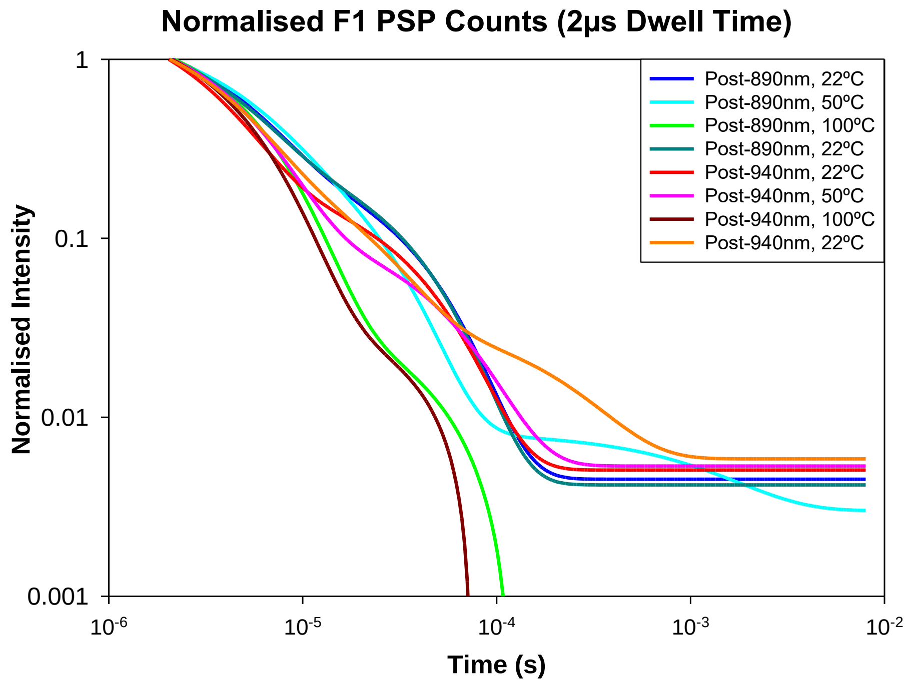

Figure 4.27 – The normalised net decay of a sample of F1 following stimulation by 890nm and 940nm diodes at room temperature, 50°C and 100°C using 2µs dwell time.

Figure 4.28 shows the normalised net PSP decay curves for F1 following stimulation at room temperature, 50°C and 100°C with 890nm and 940nm using a 20µs dwell time. Four separate components were identified in the PSP decay, with components acting on the microsecond, tens of microseconds, hundreds of microseconds, and millisecond timescales. The decay components for each temperature were evaluated and it was noted that each post-940nm decay had similar values acting for each dwell time. This is clear indicator of the same recombination pathways within the lattice structure of the F1 sample being utilised at different measurement temperatures following 940nm stimulation. However, following 890nm stimulation, a temperature dependence on the decay time is observed. As both wavelengths result in different temperature dependant behaviours following stimulation, it is reasonable to propose that the mechanisms responsible for charge relaxation at these timescales is complex, involving different recombination pathways which are accessed differently by different stimulation energies. While the post 940nm PSP could be described by an athermal tunnelling model, the post 890nm PSP is incompatible with such a model. Thus, athermal tunnelling pathways cannot be the only mechanism involved in the relaxation of stimulated charge.

A final experiment was conducted with F1 to probe how these mechanisms behaved when cooled, rather than heated. Figure 4.29 shows the normalised net PSP decay curves for F1 following stimulation at room temperature, -60°C and -78°C with 890nm and 940nm diodes using a 2µs dwell time on the MCS. The counts recorded both during stimulation and following stimulation by both wavelengths at cryogenic temperatures were two orders of magnitude lower than that seen for the room temperature measurements, and three-four orders of magnitude smaller than those observed at elevated temperatures (Table 4.9).

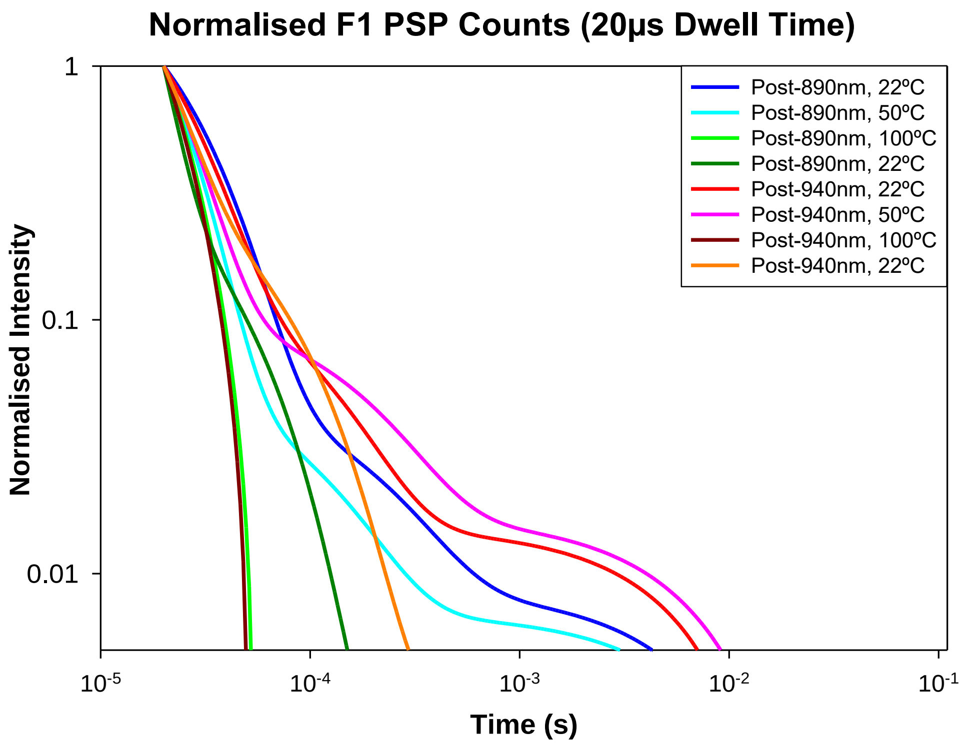

Figure 4.28 – The normalised net decay of a sample of F1 following stimulation by 890nm and 940nm diodes at room temperature, 50°C and 100°C using 20µs dwell time.

Temperature	*b lifetime (s)*	*d lifetime (s)*	*h lifetime (s)*	*Wavelength (nm)*	*F1*
22°C	2.95E-06	2.96E-06	2.78E-05	890	K-Feldspar
-60°C	2.4E-06	2.44E-06	2.7E-05	890	
-78°C	3.09E-06	3.12E-06	3.19E-05	890	
22°C	3.17E-06	1.42E-05	8.29E-05	940	
-60°C	6.03E-06	2.53E-05	0.104	940	
-78°C	4.38E-06	2.14E-05	2.08E-05	940	

Table 4.9 – The lifetime of the decay components calculated for the PSP decay for F1 at ambient and cryogenic temperatures following IRSL.

Computation revealed that there were three separate components in the decay, acting on two different timescales, with separate components acting on the timescales of microseconds and tens of microseconds. The decay components calculated showed no variance between the temperatures investigated but did have a variance based on the stimulation wavelength. The post-890nm decay components had lifetimes which had two components acting on the microsecond timescale with values of 2.4-3.2 with uncertainties of around 0.08µs and one component acting on the tens of microsecond timescale with values of 27.8-31.2 with uncertainties of around 0.04µs. Whereas the post-940nm decay components had lifetimes which had two components acting on the tens of microseconds timescale with values of 14.2-82.9 with uncertainties of around 3.9µs and one component acting on the microsecond timescale with values of 3.17-6.04 with uncertainties of around 1.68µs.

It was decided that since the net counts from the F1 following 940nm stimulation at cryogenic temperatures were so small, that further work at cryogenic temperatures using other samples would only use 890nm stimulation. To also increase the signal intensity using the same sample throughput time, two back-to-back measurements would be performed at each temperature with 890nm stimulation.

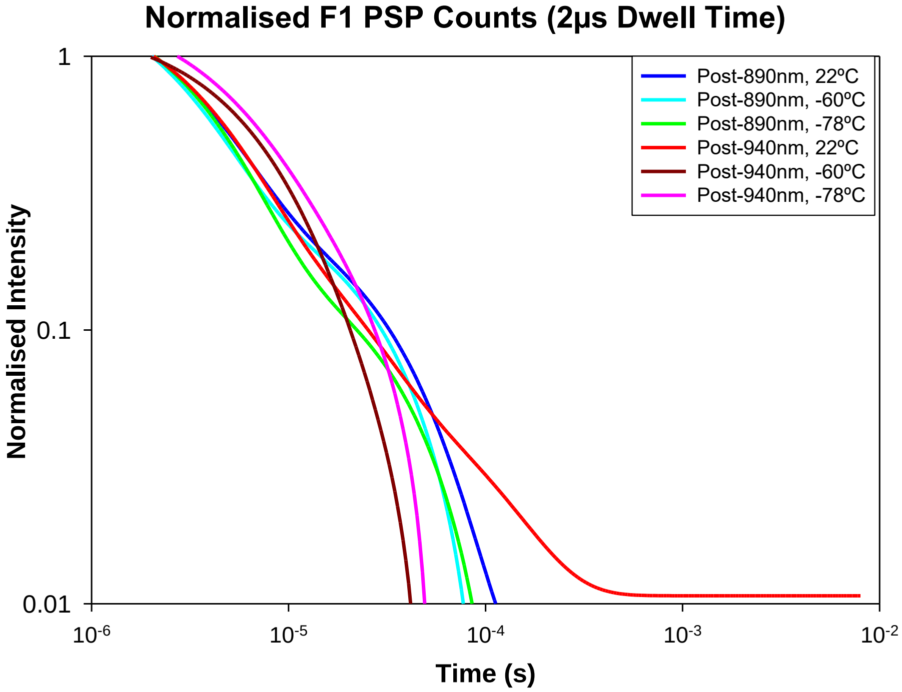

Figure 4.29 – The normalised net decay of a sample of F1 following stimulation by 890nm and 940nm diodes at room temperature, -60°C and -78°C using 2µs dwell time.

Overall, the initial work with F1 indicated that at microsecond timescales, multiple exponents still contribute to the signal decay.

For room and elevated temperatures, very similar normalised net decay rates were computed, however there were subtle differences at different temperatures depending on the stimulation wavelength used. This result indicates that different recombination pathways were accessed which were dependent on both the stimulation wavelength and the stimulation temperature. These different recombination pathways have distinct recombination lifetimes, indicating differing recombination efficiency.

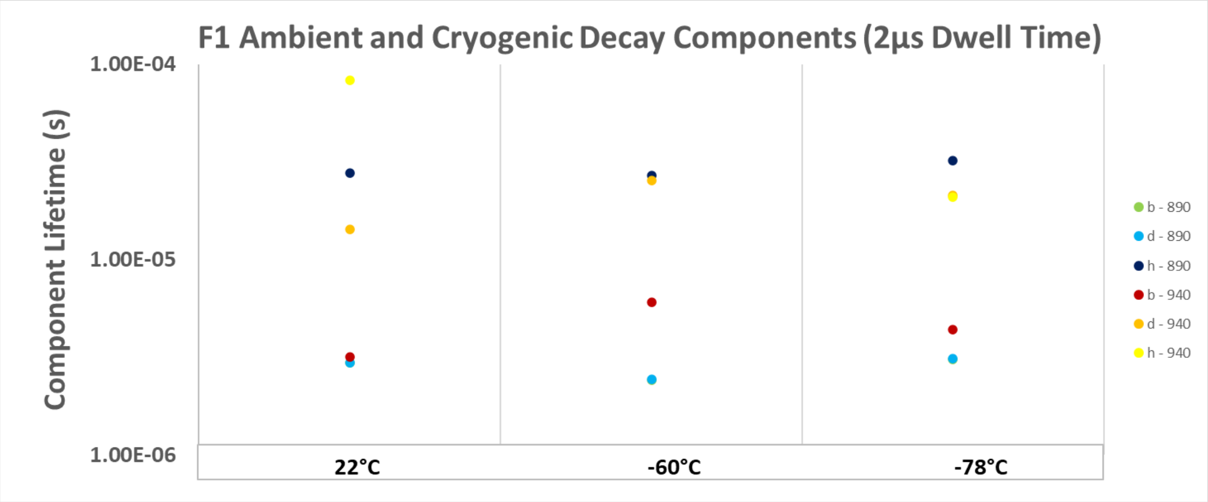

Figure 4.30 – The component lifetimes of the decays plotted in Figure 4.29 for F1 following stimulation by 890nm and 940nm diodes at room temperature, -60°C and -78°C using 2µs dwell time.

This does not describe decays seen at cryogenic temperatures, suggesting the participation of different states during post IR decay at lower temperatures as there is no thermal variance in the decays. Further, there was a clear wavelength variance in the decay components. Overall indicating the existence of band tail states with different recombination efficiencies at cryogenic temperatures.

Albites

Following on from the earlier investigative work using F1, a selection of four albite samples were used to further investigate the behaviours reported in 4.2.2.A. This allowed the investigation of the effect of mineralogical variation on the reported behaviours. The samples used were RC14, RC164, RC168 and RC169. These samples have a known geological history and were collected from South Harris, Scotland.

Figure 4.31 and Figure 4.32 show the normalised net PSP decay curves for RC14 following stimulation at room temperature, 50°C and 100°C with 890nm and 940nm diodes using 2µs and 20µs dwell times on the MCS, respectively. Computation revealed that there were three separate components in the decay, with components acting on microsecond, tens of microseconds and a final component which acted on the timescales of hundreds of microseconds and longer (Appendix B). The normalised net decay component lifetimes showed a temperature variation of a factor of two between the room temperature decays and the decays at 100°C, much less than that seen for F1. The h-component within the normalised net decay was the most unstable and had a variance across two orders of magnitude, due to this instability the presence of this component in the RC14 decays were determined to be a system artefact. The decays observed for RC14 did not show a variance relating to wavelength at 22°C or 50°C, with the main difference to decay component lifetime being driven by increasing the temperature to 100°C. This suggests that the dominate charge transport mechanisms within the RC14 lattice are not athermal in nature.

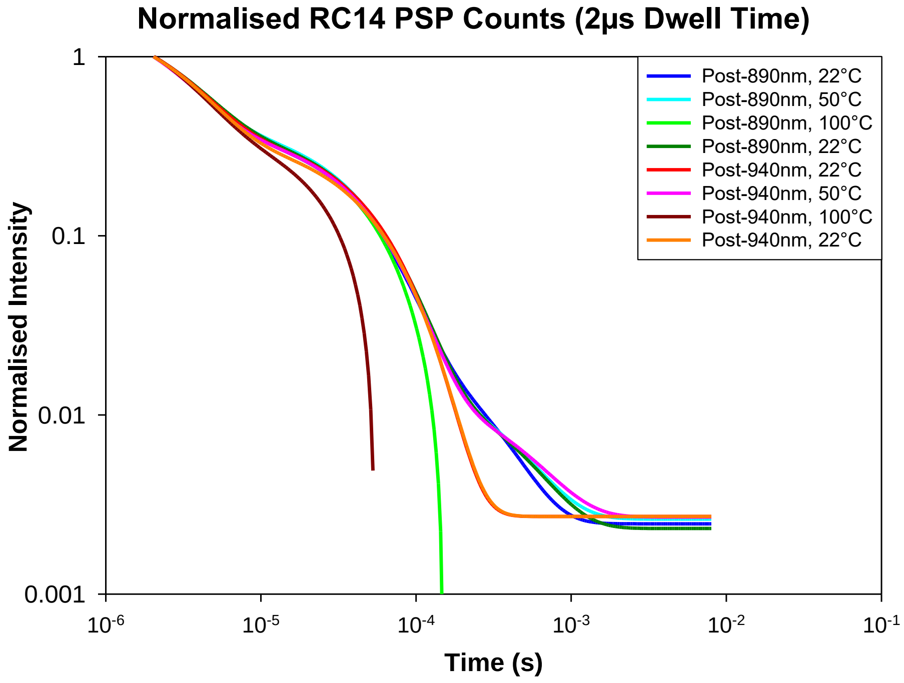

Figure 4.31 – The normalised net decay of a sample of RC14 following stimulation by 890nm and 940nm diodes at room temperature, 50°C and 100°C using a dwell time of 2µs.

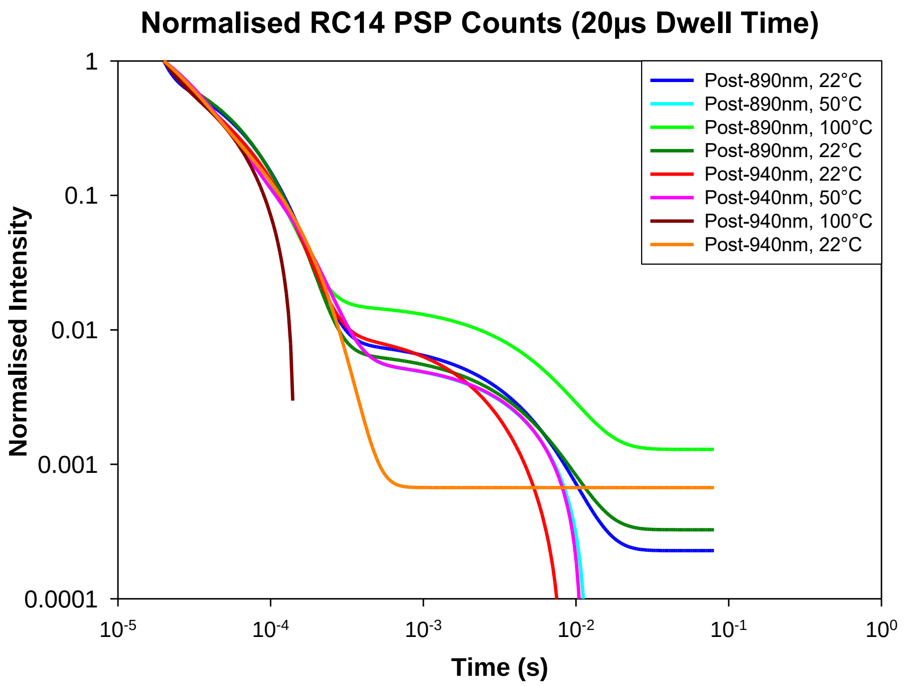

Figure 4.32 – The normalised net decay of a sample of RC14 following stimulation by 890nm and 940nm diodes at room temperature, 50°C and 100°C using a dwell time of 20µs.

Figure 4.33 and Figure 4.34 show the normalised net PSP decay curves for RC169 following stimulation at room temperature, 50°C and 100°C with 890nm and 940nm diodes using 2µs and 20µs dwell times on the MCS, respectively. Computation revealed that there were three separate components in the decay which acted across two timescales (Appendix B). Two components acted on the microsecond timescale and one component acted on the tens of microsecond timescale. The three decay components (b,d,h) had stable values between stimulation at ambient temperature, at 50°C and at 100°C. This indicates the existence of an athermal recombination process following stimulation within this sample.

The other albites, RC168 and RC164, showed similar behaviours to RC14 and RC169, respectively. RC168 was noted to have thermally variable components which acted across three orders of magnitude. RC164 was noted to have three stable components which acted across two orders of magnitude. All albites shared similar characteristics in their decay rates, particularly when stimulated at ambient temperatures and 50°C. As the geological nature of all albite samples are similar (Table 4.1) the characteristics of these pathways may be sample dependent.

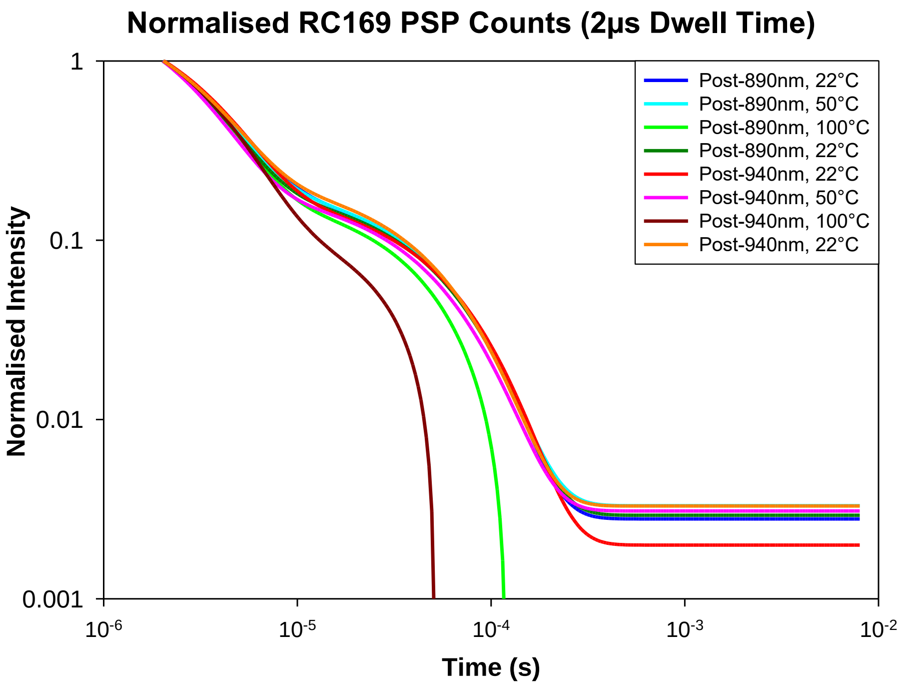

Figure 4.33 – The normalised net decay of a sample of RC169 following stimulation by 890nm and 940nm diodes at room temperature, 50°C and 100°C using a dwell time of 2µs.

The second TRS system was also used to evaluate the PSP decay across the albite samples, Figure 4.35 shows the normalised net PSP decay curves for RC14 following 890nm stimulation using this second TRS system. A 5µs dwell time was used for this measurement as it offered a way to probe decay components which contributed to the decay curves seen on the first TRS system in the 2µs and 20µs decays. A pronounced temperature driven difference was noted in the decay components (Table 4.10), with the 80°C PSP decaying entirely 100µs after the end of stimulation. The two 22°C decays showed very similar decay components across microsecond and tens of microsecond order. The post-890nm decay at room temperature following the elevated temperature measurement was computed to have a more stable component at this timescale than the decay recorded before the elevated temperature measurement by a factor of ~3. This may have implications regarding the stability of the band-tail states in the lattice following a fluctuation in stimulation temperatures.

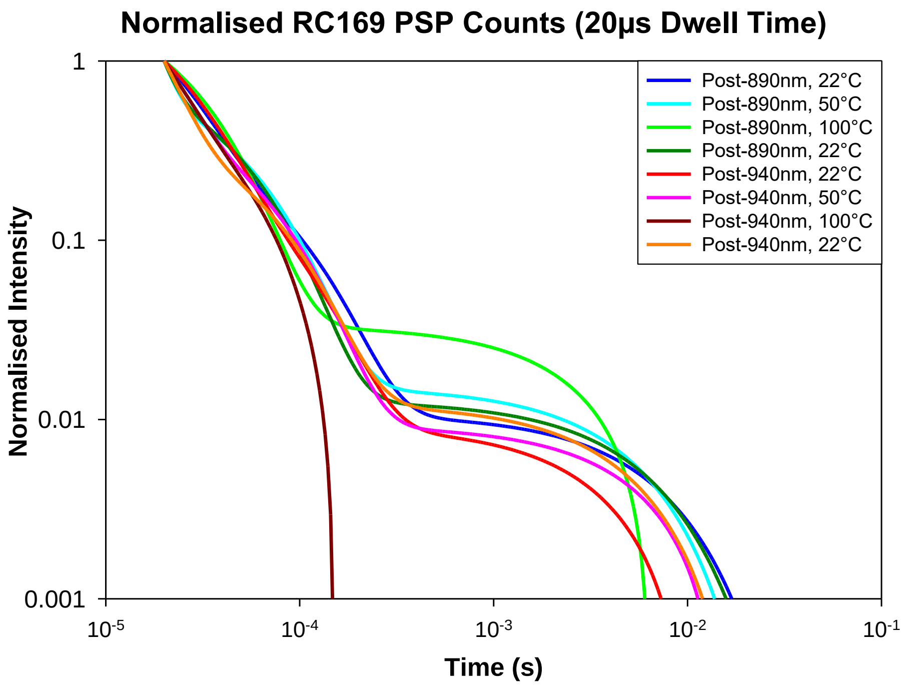

Figure 4.34 – The normalised net decay of a sample of RC169 following stimulation by 890nm and 940nm diodes at room temperature, 50°C and 100°C using a dwell time of 20µs.

RC14	***Post-890nm 22°C (5us)***	***Post-890nm 80°C (5us)***	***Post-890nm 22°C (5us)***
y0	0.0002	-0.0554	0.0001
a	0.5279	0.5095	0.9218
b	33897.28	49471.37	33704.05
c	0.45	0.7286	0.2152
d	34127.69	21229.9	12259.74
g	0.2196	0.019	0.002
h	11396.99	2599.517	236.2455

Table 4.10 – The room temperature and elevated temperature PSP exponential decay components following 890nm stimulation for RC14 on the second TRS system.

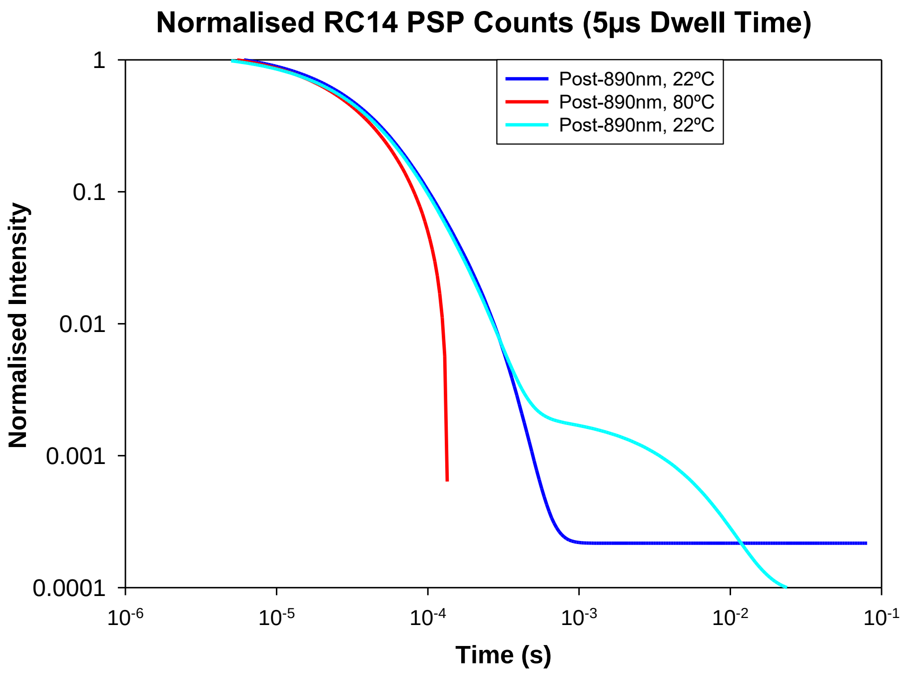

Figure 4.35 – The normalised net decay of a sample of RC14 following stimulation by 890nm diodes at room temperature and 80°C using a dwell time of 5µs.

As with F1 in the previous section, a further investigation was conducted using the albite samples at stimulation temperatures of -40°C, ambient, and 80°C using 890nm diodes. 940nm diodes were not used in this part of the investigation as the signal intensity measured during and following stimulation at -40°C was near background and to attain an acceptable level of signal-to-noise ratio would prevent the practical throughput of samples within the experimentation time window. The use of 890nm alone still allows the probing of mineralogical and temperature related influences on the mechanics of charge movement through the lattice structure following stimulation.

Figure 4.36 and Figure 4.37 show the normalised net PSP decay curves for RC168 and RC164, respectively, following stimulation at room temperature, 80°C and -40°C with 890nm diodes using a 2µs dwell time on the MCS. The computed decay components for RC168 could be described by three components which acted over two timescales following stimulation at ambient and 80°C. However, following stimulation at -40°C, the three decay components instead acted over three timescales (Appendix C). These components varied by up to an order of magnitude between the decays at 80°C and -40°C, indicating that PSP decays at these timescales are not dominated by athermal processes.

Three distinct components were noted in the decay curves for RC164 which acted across three timescales. One component acted on the microsecond timescale and one component acted on the tens of microsecond timescale, and a final component acted on the millisecond timescale. These components showed a strong variance as the temperature was adjusted, with a drop in temperature to -40°C showing an increase in the lifetime of each component. This can be interpreted as thermal processes being the dominant mechanism for charge transport following IR stimulation in the lattice of RC164.

RC14 demonstrated a greater temperature variance than RC164, with an order of magnitude variance in the lifetime of the shortest-lived decay component (~10^{-6} to 10^{-5}s) and a factor of 7 variance in the lifetime of the medium component (~$1x10^{-5}$ to $7x10^{-5}$s) and a variance of three orders of magnitude for the lifetime of the longest-lived decay component. This indicates that RC14's lattice structure which is highly sensitive to temperature changes, with athermal processes such as tunnelling being dominated by thermally driven recombination mechanisms. This result agrees with the temperature variance noted from RC14 following the elevated temperature decays represented in Figures 4.31, 4.32 and 4.35.

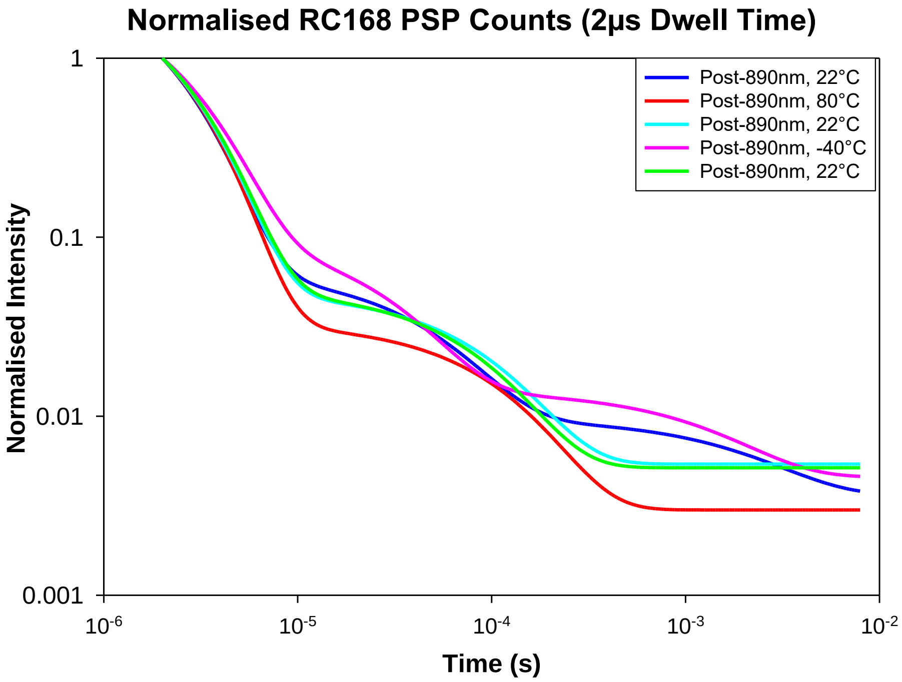

Figure 4.36 – The normalised net decay of a sample of RC168 following stimulation by 890nm diodes at room temperature, 80°C and -40°C using 2µs dwell time.

RC169 was similar to RC168 in that there was a noted stability in the value of the decay components at each stimulation temperature (Appendix C). Suggesting that charge transport mechanisms in this sample are dominated by athermal processes.

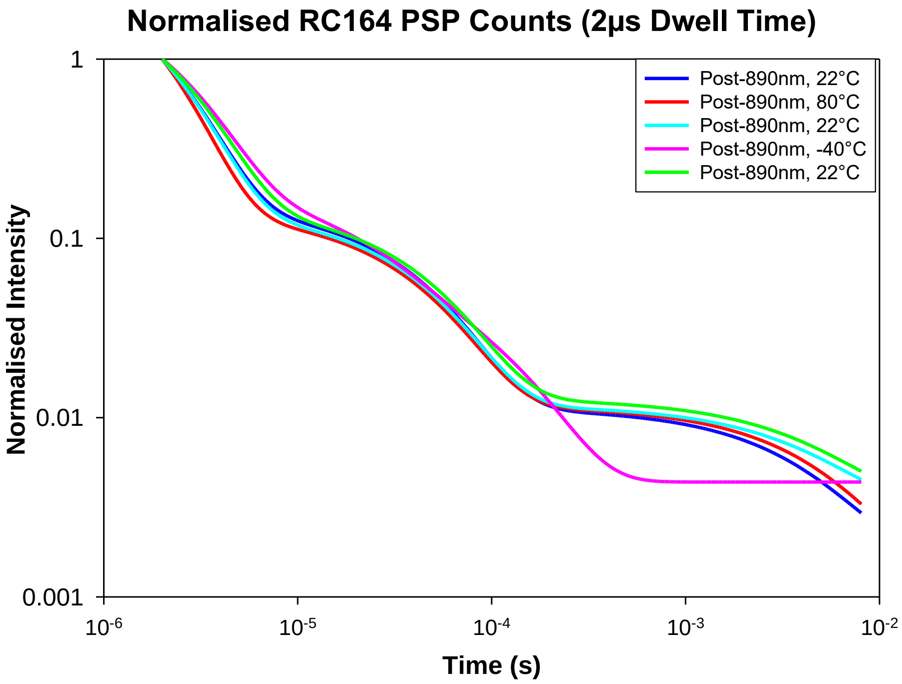

Figure 4.37 – The normalised net decay of a sample of RC164 following stimulation by 890nm diodes at room temperature, 80°C and -40°C using 2µs dwell time.

Overall, the investigations of the albite samples using time resolved spectrometry indicated that at microsecond timescales there are multiple components which contribute to the signal decay. These components have a complex variance across the mineral family that is dependent on numerous factors such as temperature and mineralogy.

For each sample at ambient temperatures, very similar normalised net decay rates were computed across the albite samples, however there were considerable differences observed when the temperatures were raised or lowered. Longer decay times were generally observed for the normalised decays seen at cryogenic temperatures than those which were measured at ambient and elevated temperatures, suggesting the participation of different states during post IR decay at lower temperatures as there is a thermally driven variance in the decays. However, samples such as RC164 and RC169 showed stable component lifetimes when investigated at different temperatures, suggesting that for these samples an athermal mechanism dominates the charge transport process following stimulation. Further, there was a clear wavelength variance in the decay components in RC168.

This result indicates that different recombination pathways were accessed which were dependent on both the stimulation wavelength and the stimulation temperature, as well as subtle differences in sample mineralogy. These different recombination pathways have distinct recombination lifetimes, indicating differing recombination efficiency across the albite samples.

Microclines

Following on from the earlier investigative work using F1 and the albite samples, a selection of two microcline samples was used to further investigate the behaviours reported in 4.2.2. This allowed the investigation of the effect of mineralogical variation on the reported behaviours. The samples used were RC165 and RC630. These samples have a known geological history and were also collected from South Harris, Scotland.

Figure 4.38 and Figure 4.39 show the normalised net PSP decay curves for RC165 following stimulation at room temperature, 50°C and 100°C with 890nm and 940nm diodes using 2µs and 20µs dwell time on the MCS, respectively. The normalised net decay components (Appendix B) varied by a factor of two across both wavelengths and by a factor of six between the room temperature decays and the decays at 100°C, suggesting complex charge transport mechanisms in the RC165 lattice following stimulation. The h component within the normalised net decay was the most unstable across the stimulation wavelengths and temperature range, varying across two orders of magnitude.

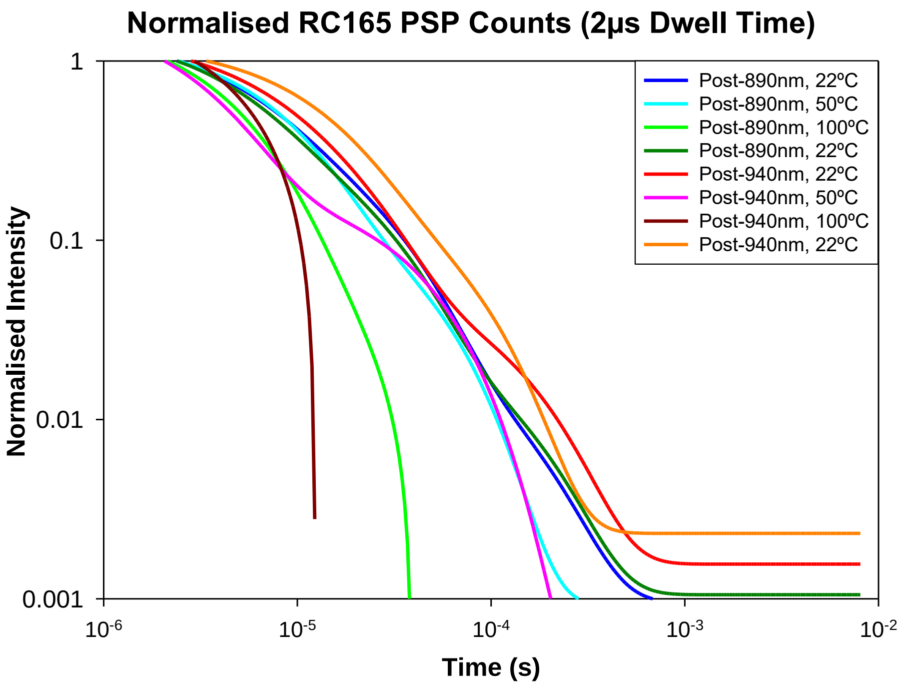

Figure 4.38 – The normalised net decay of a sample of RC165 following stimulation by 890nm and 940nm diodes at room temperature, 50°C and 100°C with a 2µs dwell time.

Figure 4.40 and Figure 4.41 show the normalised net PSP decay curves for RC630 following stimulation at room temperature, 40°C and 80°C with 890nm and 940nm diodes using 2µs and 20µs dwell times on the MCS, respectively. The decays for this sample showed key differences when compared with RC165, particularly regarding their stability across stimulation wavelengths. The PSP decay for RC630 was noted to contain three components which acted over two timescales, microseconds and tens of microseconds. At all stimulation temperature ranges the decay components obtained for the microsecond component of each decay following stimulation with both 890nm and 940nm agreed with each other within a standard error. The value obtained for the component which acted on the order of tens of microseconds showed some stability across the stimulation wavelengths but varied by up to a factor of ten across the temperature range. The decays at 100°C reached background levels tens of microseconds after the end of stimulation. Stimulation at 50°C and ambient temperature had total decay times on the order of hundreds of microseconds, with the 50°C decays having a slightly faster decay time to background.

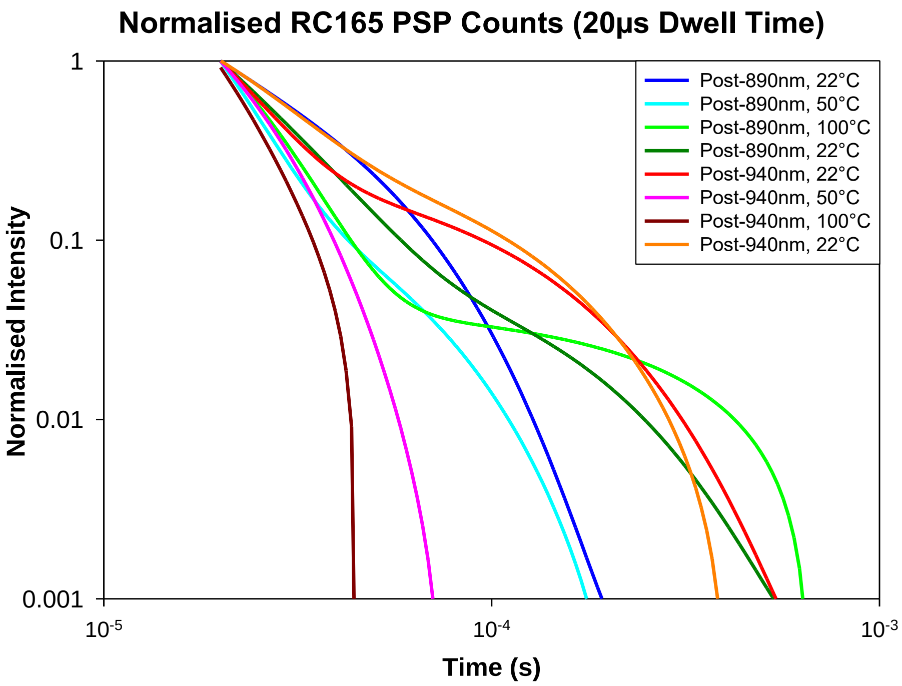

Figure 4.39 – The normalised net decay of a sample of RC165 following stimulation by 890nm and 940nm diodes at room temperature, 50°C and 100°C with a 20µs dwell time.

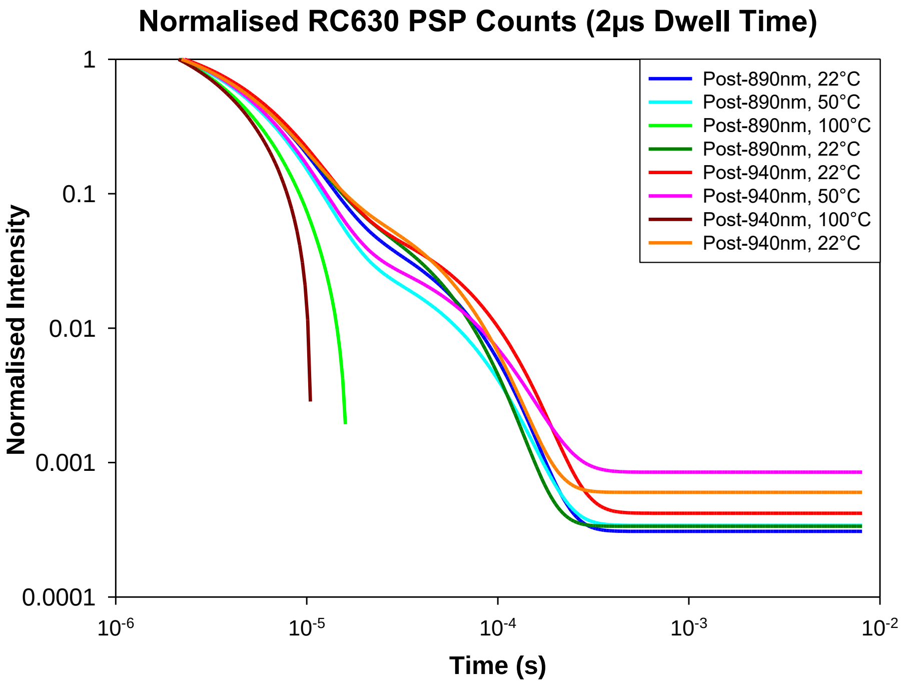

Figure 4.40 – The normalised net decay of a sample of RC630 following stimulation by 890nm and 940nm at room temperature, 50°C and 100°C with a 2µs dwell time.

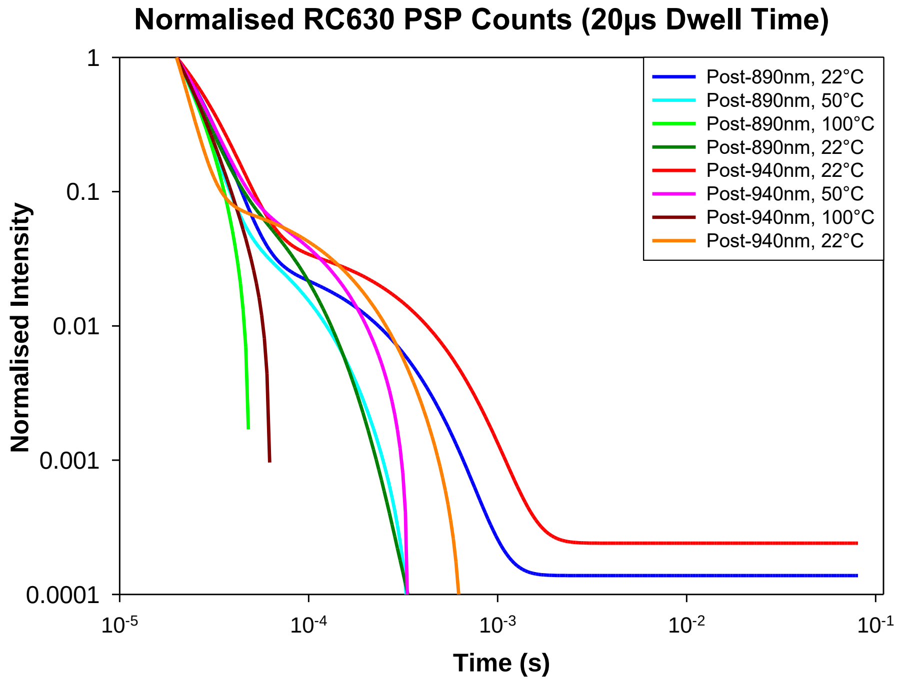

Figure 4.41 – The normalised net decay of a sample of RC630 following stimulation by 890nm and 940nm diodes at room temperature, 50°C and 100°C with a 20µs dwell time.

Figure 4.42 shows the normalised net PSP decay curves for the sample of RC630 following stimulation by 890nm diodes at room temperature and 80°C using 5µs dwell times on the MCS of the second TRS system. Computation of this decay revealed components of microsecond and tens of microsecond order (Table 4.11). The components for the ambient temperature decay showed uniformity within a standard error rather than the slight scatter in the values obtained for these components which was observed using the first TRS system. For the 80°C decay components, the second TRS system also had lifetimes which were shorter lived than those computed for the room temperature decay, with lifetimes of the longest components ranging from 17µs at 80°C to ~20µs at ambient temperature; the two microsecond order components also varied from 2.4µs lifetimes at 80°C to ~3.3µs lifetimes at ambient temperatures, indicating a temperature variance in the decay lifetimes. This indicates a strong temperature variance in the decay times which is consistent across both instruments and indicates that the charge transport mechanisms in RC630 for microsecond timescale decay following stimulation is not dominated by athermal processes.

RC630	*Post-890nm 22°C (5us)*	*Post-890nm 80°C (5us)*	*Post-890nm 22°C (5us)*
y0	0	-0.0003	0
a	0.0882	0.0432	0.108
b	45979.61	58370.63	51954.93
c	2.1305	3.6799	2.2376
d	298863.2	412877.6	306528.5
g	2.0133	3.9807	2.0135
h	298785.2	414469.4	307160.9

Table 4.11 - The room temperature and elevated temperature PSP exponential decay components following 890nm stimulation for RC630 on the second TRS system.

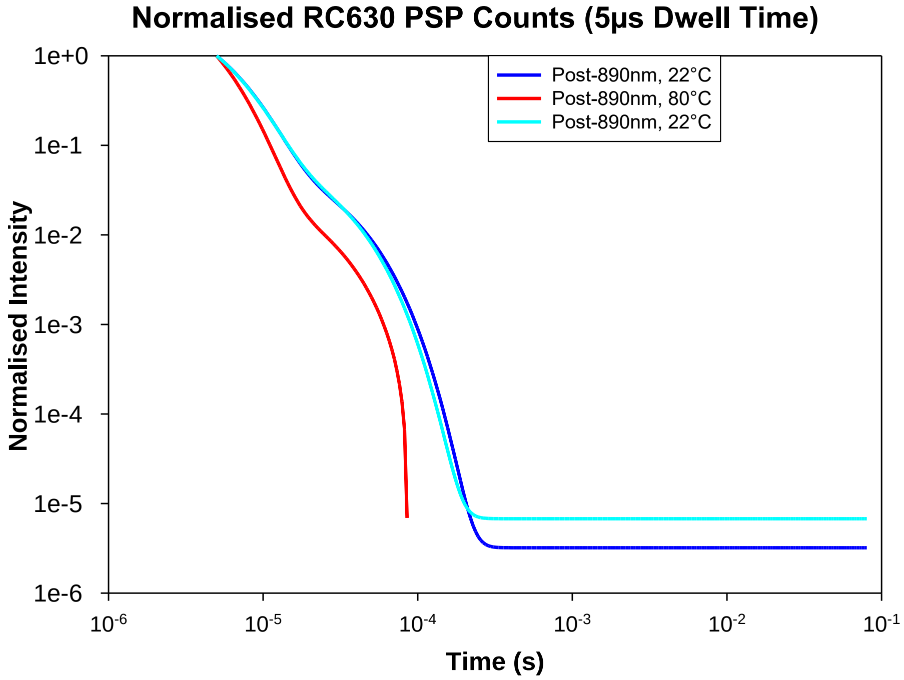

Figure 4.42 – The normalised net decay of a sample of RC630 following stimulation by 890nm diodes at room temperature and 80°C using 5μs dwell time.

Figure 4.43 shows the normalised net PSP decay curves for RC165 following stimulation at room temperature, 80°C and -40°C with 890nm diodes using a 2μs dwell time on the MCS. For two of the three ambient temperature decays, there was one component acting on the order of microseconds, one component acting on the order of tens of microseconds and one component acting on the order of hundreds of microseconds (Appendix C). For the ambient decay which followed the elevated temperature decay, which contained two microsecond order components and one tens of microsecond order component, there were two components acting on the order of tens of microseconds and one component which acted on the order of hundreds of nanoseconds. The decay observed at -40°C contained three components across two orders of magnitude, one component of microsecond order and two of tens of microsecond order. This indicated that thermally driven processes dominate the charge transport mechanisms in RC165 following stimulation.

Figure 4.44 shows the normalised net PSP decay curves for RC630 following stimulation at room temperature, 80°C and -40°C with 890nm diodes using a 2µs dwell time on the MCS. All three ambient temperature decays for RC630 contained components which were between a standard error of each other, with there being two microsecond order components and one tens of microsecond order component present in each decay. This indicates that the charge transport mechanisms of RC630 are dominated by athermal processes. For the decay observed at 80°C, there were also three decay components computed, two of microsecond order and one of tens of microsecond order. The microsecond order components for the elevated temperature decay were evaluated to have shorter lifespans than the microsecond order components computed for the ambient decay (2.6µs lifespan for the elevated decay, average of 3.1µs for the ambient decays), however the tens of microsecond order component had a value within a standard error. This resulted in a slightly faster decay to background at elevated temperatures. For the decay measured at -40°C, three components were computed that acted across three orders of magnitude, from microsecond up to hundreds of microsecond order. This resulted in the decay to background at cryogenic temperatures taking ten times longer than the decays at ambient and elevated temperatures.

This suggests that RC630 has broadly the same recombination efficiency at ambient and elevated temperatures, however at cryogenic temperatures this pathway becomes less efficient, resulting in longer lasting PSP. This indicates that the PSP decay observed in RC630 is a thermally driven process, rather than being dominated by nearest neighbour tunnelling.

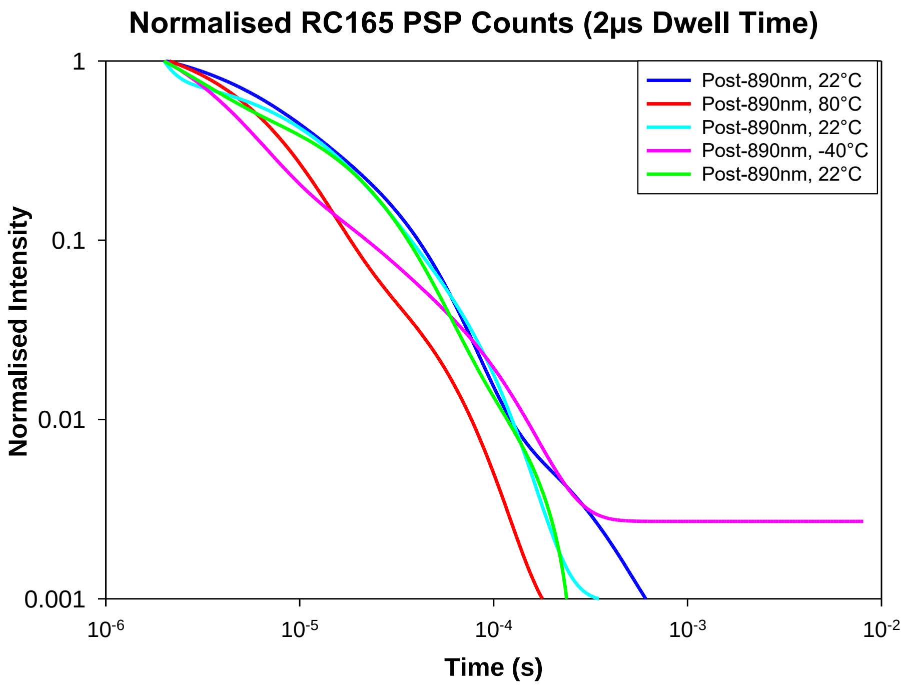

Figure 4.43 – The normalised net decay of a sample of RC165 following stimulation by 890nm diodes at room temperature, 80°C and -40°C using 2µs dwell time.

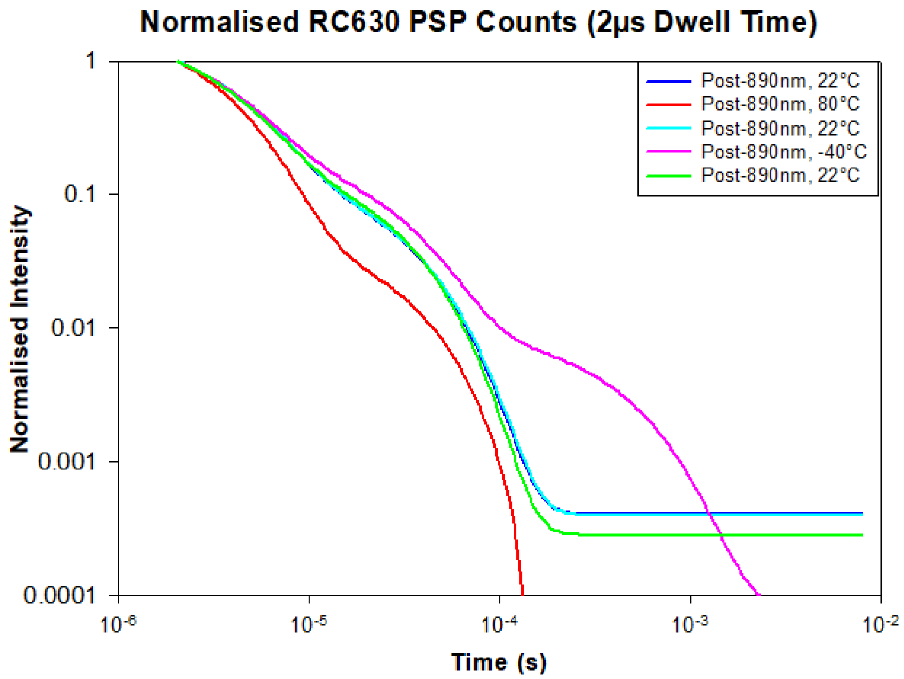

Figure 4.44 – The normalised net decay of a sample of RC630 following stimulation by 890nm diodes at room temperature, 80°C and -40°C using 2µs dwell time.

Overall, the investigations of the microcline samples using time resolved spectrometry indicated that at microsecond timescales there are multiple components which contribute to the signal decay within microcline samples. These components had a complex variance between both samples which varied on numerous factors.

For each sample at ambient temperatures, very similar normalised net decay rates were computed across the microcline samples, however there were considerable differences observed when the temperatures were raised or lowered. For the normalised decays seen at cryogenic temperatures longer decay times were noted for RC630 when compared to the other temperature ranges, suggesting the participation of different states during post IR decay at lower temperatures. There was a scatter in the thermal response observed in the decays from RC165, with the elevated and cryogenic temperatures having similar decay times. Further, there was a clear wavelength variance in the decay components for RC165, whereas similar decays were observed between the two stimulation wavelengths used for RC630. This points to the recombination pathways having different recombination efficiencies, particularly at cryogenic temperatures.

This result indicates that different recombination pathways were accessed which were dependent on both the stimulation wavelength and the stimulation temperature, though the degree to which this was measurable did vary between both samples due to subtle differences in sample mineralogy. These different recombination pathways have distinct recombination lifetimes, indicating differing recombination efficiency across the microcline samples.

Plagioclases

Following on from the earlier investigative work using various feldspar samples, a selection of two plagioclase samples were used to further investigate the behaviours reported in 4.2.2.A-C. This allowed the investigation of the effect of mineralogical variation on the reported behaviours. The samples used were RC246 and RC659. These samples have a known geological history and were collected from North Harris, Scotland, and Greenland.

Figure 4.45 and Figure 4.46 show the normalised net PSP decay curves for RC246 following stimulation at room temperature, 50°C and 100°C with 890nm and 940nm diodes using 2µs and 20µs dwell times on the MCS, respectively. RC246 has a low intensity IR signal from both 890nm and 940nm at ambient temperatures, resulting in larger uncertainties in any obtained decay components due to the large amount of scatter. Computation revealed that there were up to four separate components in the decay across four orders of magnitude when both timescales are considered, with components acting on sub-microsecond, microsecond, tens of microseconds and a final component which acted on the timescales of hundreds of microseconds and longer (Appendix B). Of these obtained components, only the ones obtained at ambient temperatures had any significance following error propagation, with the decay components describing the decays at 50°C and 100°C having uncertainties of similar value or greater than the obtained values. The normalised net decay components at ambient temperature across both dwell times showed a clear variation by stimulation wavelength and stimulation temperature, with the microsecond components of the post-890nm decay having lifetimes which were 70% of the lifetime obtained for the comparable component from the post-940nm decay (3.3±0.5µs for lifetime of the shortest component in the post-890nm decay vs 1.97±0.6µs for the lifetime of the shortest component in the post-940nm decay), the tens of microsecond order components for both decays had values of 30±4µs. This variance in the shortest order components for these decays, when considered with the low IRSL intensity seen for both wavelengths, implies that the PSP recombination and emission efficiency of the RC246 lattice is inefficient and unstable.

Figure 4.47 and 4.49 shows the normalised net PSP decay curves for RC659 following stimulation at room temperature, 40°C and 80°C with 890nm and 940nm diodes using 2µs and 20µs dwell times on the MCS, respectively. The PSP decay for RC659 was noted to contain four components which acted over four timescales: microsecond, tens of microsecond, hundreds of microsecond and millisecond. At all stimulation temperature ranges the decay components obtained for the microsecond order component of each decay following stimulation with both 890nm and 940nm agreed with each other within a standard error, indicating that there was no wavelength driven variance in decay component lifetime. The post-890nm decay at ambient temperature following the decays after elevated temperature stimulation was also observed to have a faster initial decay than the ambient temperature post-890nm decay measured before heating. This could be an indication that the lattice of RC659 sees changes in the lattice structure when it is heated and cooled which allow more efficient recombination and emission for charge which has been freed by stimulation.

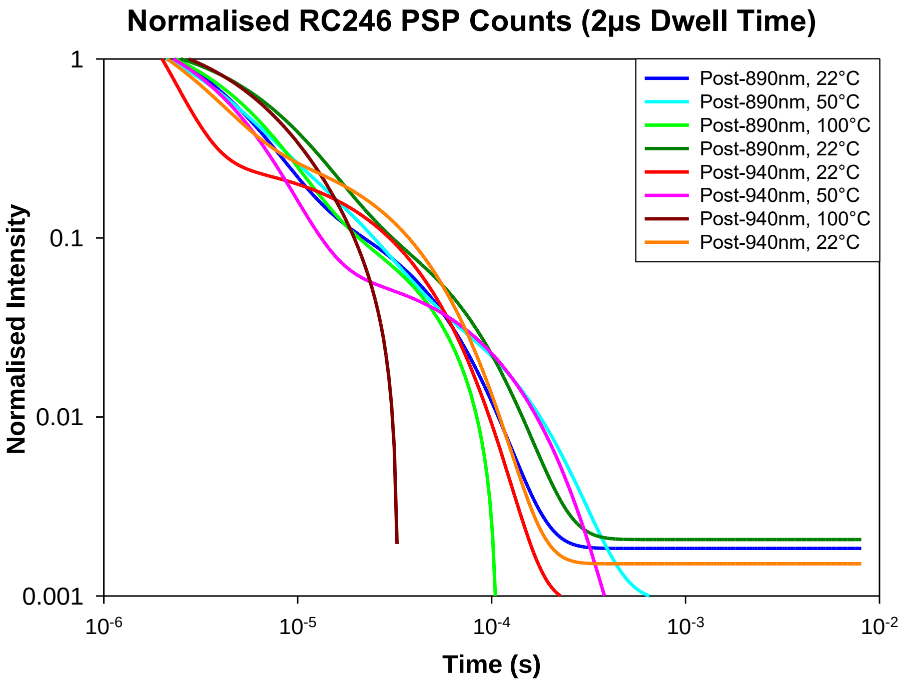

Figure 4.45 – The normalised net decay of a sample of RC246 following stimulation by 890nm and 940nm diodes at room temperature, 50°C and 100°C using 2µs dwell time.

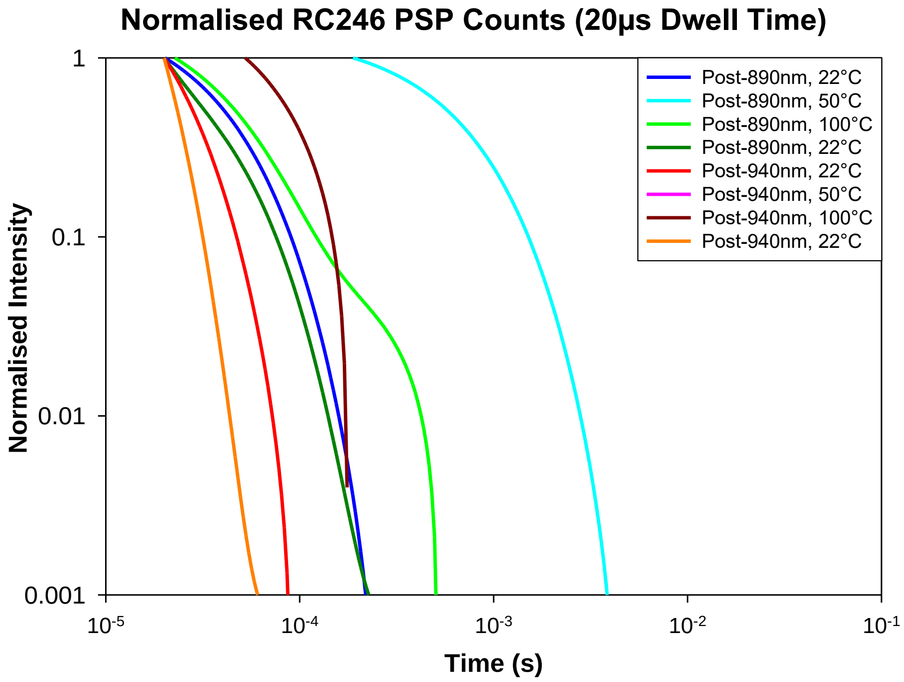

Figure 4.46 – The normalised net decay of a sample of RC246 following stimulation by 890nm and 940nm at room temperature, 50°C and 100°C using 20µs dwell time.

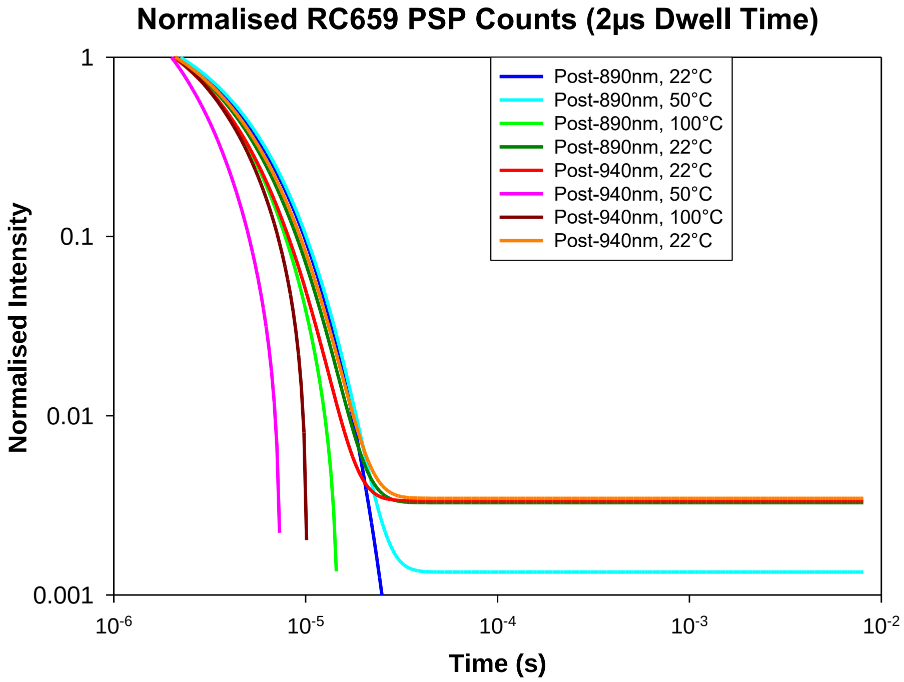

Figure 4.47 – The normalised net decay of a sample of RC659 following stimulation by 890nm and 940nm at room temperature, 50°C and 100°C using 2µs dwell time.

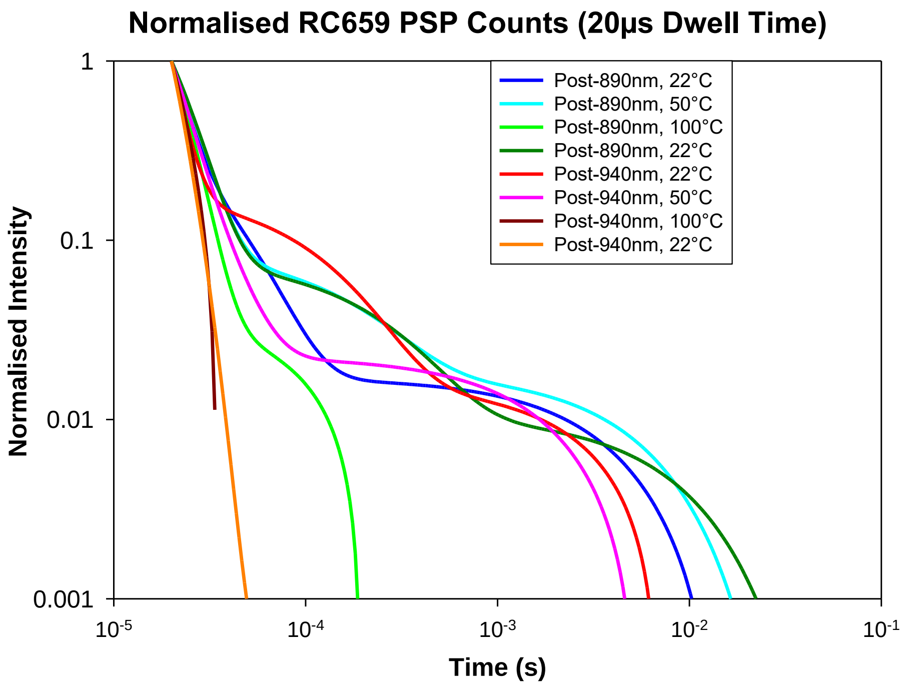

Figure 4.48 – The normalised net decay of a sample of RC659 following stimulation by 890nm and 940nm diodes at room temperature, 50°C and 100°C using 20µs dwell time.

Figure 4.49 shows the normalised net PSP decay curves for the sample of RC659 following stimulation by 890nm diodes at room temperature and 80°C using 5µs dwell times on the MCS of the second TRS system. Computation of this decay revealed components of microsecond and tens of microsecond order (Table 4.12). The components for the initial ambient and elevated temperature both contained two microsecond order components of 3.4±0.3µs and 3.8±0.2µs, with a tens of microsecond order components that ranged from 17.7±4µs to 24±6µs. However, the second ambient decay had three decay components which acted across two orders of magnitude; two microsecond order components with lifetimes of 1.1±0.2µs and a component which acted on the order of hundreds of microseconds (0.6±0.04ms lifetime). This indicates that the recombination pathways used for PSP in plagioclases change for when the sample is heated and cooled, suggesting pathway instability at the lattice level over a temperature range. The earlier observation that the ambient temperature decay recorded for RC659 following IR stimulation at elevated temperatures had a faster initial decay than the ambient temperature measurement which preceded the heating was repeated. This indicates a strong temperature variance in the decay times which is consistent across both instruments and indicates that the relaxation mechanism for microsecond timescale decay following stimulation is not driven by athermal processes.

RC659	***Post-890nm 22°C (5us)***	***Post-890nm 80°C (5us)***	***Post-890nm 22°C (5us)***
y0	-0.1214	-0.0305	0.0008
a	4.1929	2.1127	57.0714
b	290587.4	291399.7	964555.7
c	0.0274	1.6383	57.0533
d	0	266805.8	964615
g	0.0949	0.1566	0.0676
h	0.1835	56632.31	1669.039

Table 4.12 - The room temperature and elevated temperature PSP exponential decay components following 890nm stimulation for RC659 on the second TRS system.

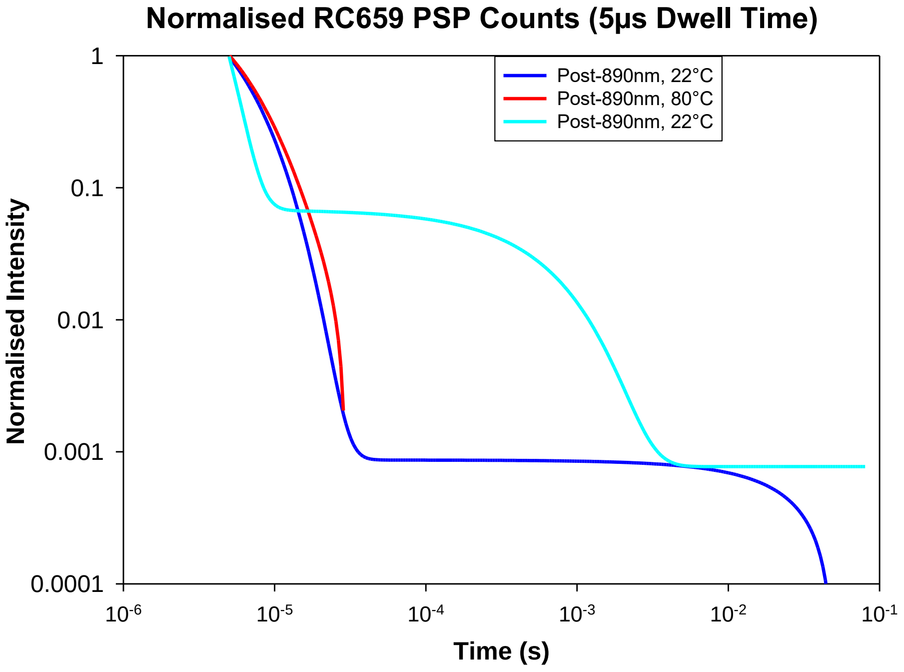

Figure 4.49 – The normalised net decay of a sample of RC659 following stimulation by 890nm diodes at room temperature and 80°C using 5μs dwell time.

Figure 4.50 shows the normalised net PSP decay curves for RC246 following stimulation at room temperature, 80°C and -40°C with 890nm diodes using a 2μs dwell time on the MCS. The computed decay components for RC246 for the first ambient temperature decay and the elevated temperature decay consisted of three separate components which acted across two orders of magnitude (Appendix C). The second ambient decay for RC246 was computed to contain longer lived components than the first ambient and elevated temperature decays, with the lifetimes longer for all components. The decay observed at -40°C and the final ambient temperature decay were described by decays with microsecond and tens of microsecond order components which were within error of the first ambient and elevated temperature decays.

Figure 4.51 shows the normalised net PSP decay curves for RC659 following stimulation at room temperature, 80°C and -40°C with 890nm diodes using a 2μs dwell time on the MCS. All three ambient temperature decays for RC630 contained components which were between a standard error of each other (Appendix C). The PSP decay measured after stimulation at 80°C consisted of components with a shorter lifespan than those calculated for the decays measured at ambient temperature. In particular, the microsecond order components for the elevated temperature decay were evaluated to have shorter lifespans than the microsecond order components computed for the ambient decay (1.6±0.1μs lifespan for the elevated decay, average of 1.8±0.2μs for the ambient decays). For the decay measured at -40°C, three components were computed that acted across two orders of magnitude, with two microsecond order components and one of tens of microsecond order. This resulted in the decay to background at cryogenic temperatures having a slower total decay time when compared with the ambient and elevated temperature PSP decays. This indicates that the PSP decay observed in RC659 is a thermally driven process, rather than being dominated by athermal processes like nearest neighbour tunnelling.

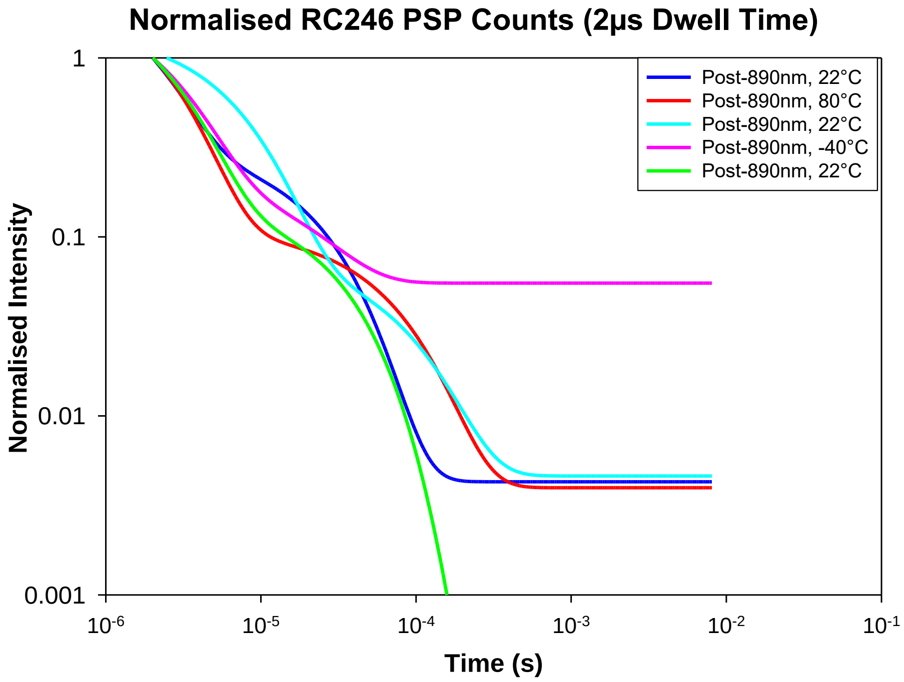

Figure 4.50 – The normalised net decay of a sample of RC246 following stimulation by 890nm diodes at room temperature, 80°C and -40°C using 2µs dwell time.

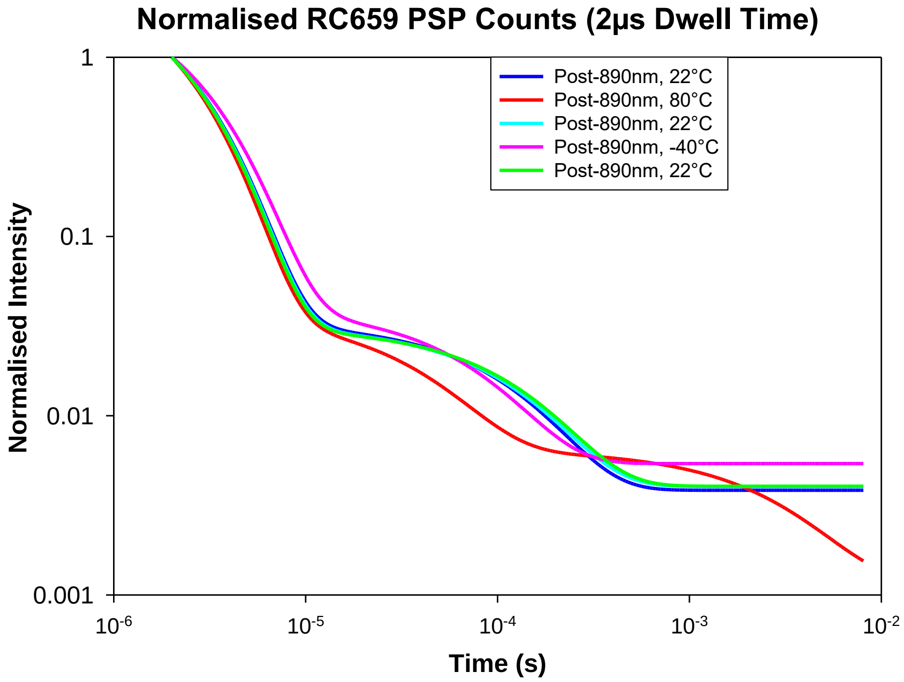

Figure 4.51 – The normalised net decay of a sample of RC659 following stimulation by 890nm diodes at room temperature, 80°C and -40°C using 2µs dwell time.

Overall, the investigations of the plagioclase samples using time resolved spectrometry indicated that at microsecond timescales there are multiple components which contribute to the signal decay within plagioclase samples.

For each sample at ambient temperatures, very similar normalised net decay rates were computed across the plagioclase samples (Appendix B/C), however subtle differences arose at cryogenic temperatures, as well as when the sample was cooled after being heated. For the normalised decays seen at cryogenic temperatures longer initial decay times were noted for both samples when compared to the other temperature ranges. This indicates that for decays at cryogenic temperatures the recombination efficiency is not the same as for decays at ambient and elevated temperatures.

These results suggest that sample conditions can result in different recombination pathways being accessed which were dependent on the specific sample mineralogy, the stimulation wavelength, and the stimulation temperature. These different recombination pathways have distinct recombination lifetimes, indicating differing recombination efficiency across the plagioclase samples.

K-Feldspar

Following on from the earlier investigative work using various feldspar samples, a selection of thirteen K-Feldspar samples were used to further investigate the behaviours reported in 4.2.2. This allowed the investigation of the effect of mineralogical variation on the reported behaviours. The samples used were RC64, RC72, RC81, RC167, RC174, RC389, RC456, RC484, RC485, RC491, RC503, RC683B and RC1396C. These samples have a known geological history and were collected from Greenland, Nigeria, Norway, and Scotland (Table 4.1).

Figure 4.52 and Figure 4.53 show the normalised net PSP decay curves for RC81 following stimulation at room temperature, 50°C and 100°C with 890nm and 940nm diodes using 2µs and 20µs dwell time on the MCS, respectively. Computation revealed that there were three separate components in the decay across both dwell times, with components acting on microsecond, tens of microseconds and a final component which acted on the timescale of milliseconds (Appendix B). The normalised net decay components showed a clear variation by temperature, with the microsecond and tens of microsecond components in the post-890nm and the post-940nm decays at ambient temperatures remaining within a standard error of each other (3.7±0.4µs, 21.7±6µs, respectively). These ambient temperature decays returned to background levels of the photomultiplier after several hundred microseconds. The decays observed following stimulation with either wavelength at 100°C have total decay lifetimes which were an order of magnitude shorter than those computed for either the ambient temperature or the 50°C decays, returning to background levels after only 20µs to 30µs. The decays observed for RC81 did not show a wavelength driven variance across the temperature range. However, a temperature driven variance was noted, with decay components following stimulation at 100°C having a shorter lifespan than those calculated for decays after stimulation at ambient temperatures or 50°C. This indicates that RC81's recombination pathways are dominated by thermal processes.

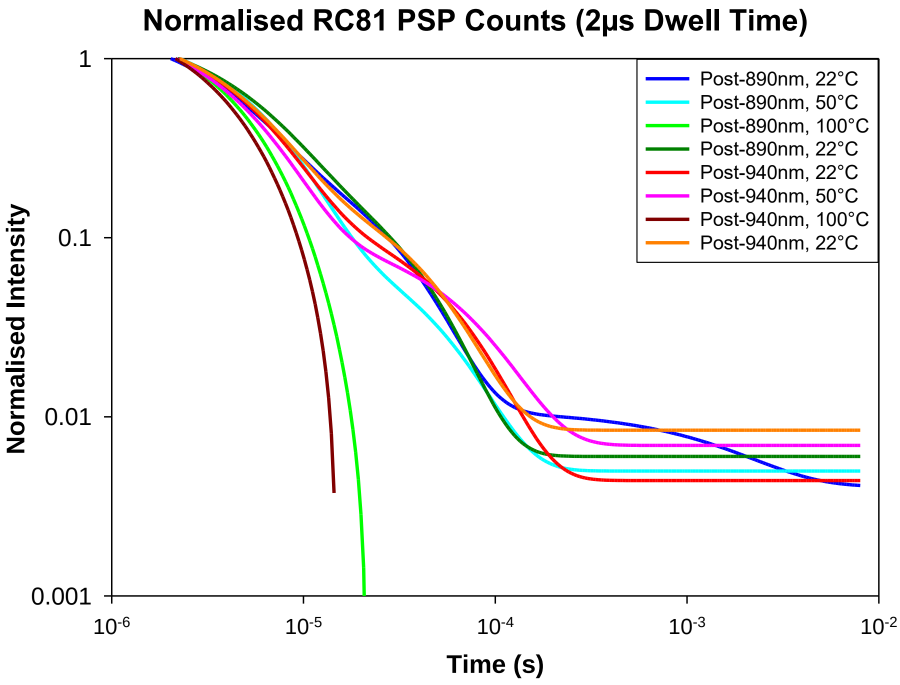

Figure 4.52 – The normalised net decay of a sample of RC81 following stimulation by 890nm and 940nm diodes at room temperature, 50°C and 100°C with a 2µs dwell time.

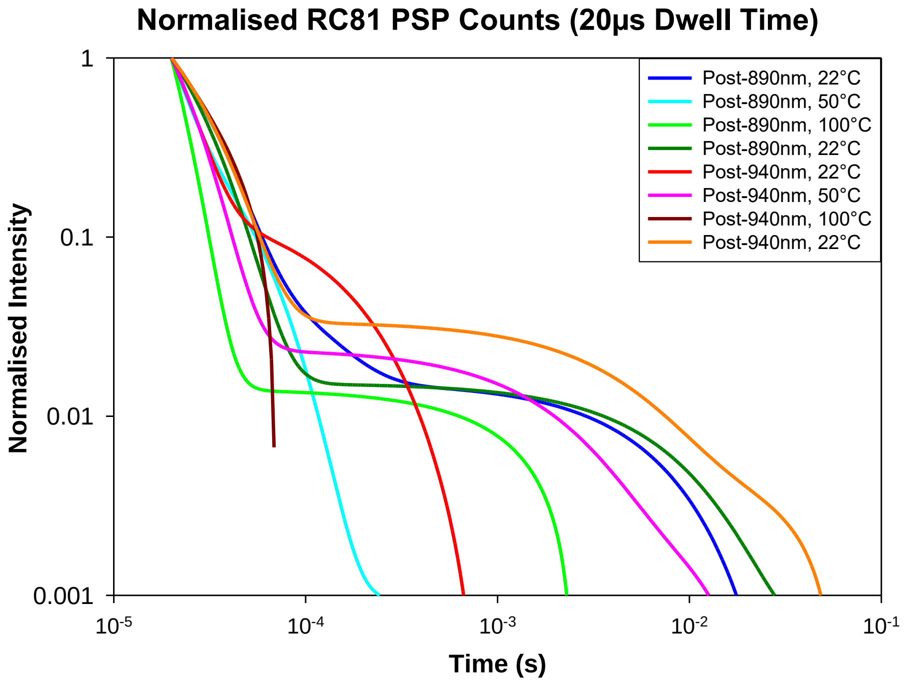

Figure 4.53 – The normalised net decay of a sample of RC81 following stimulation by 890nm and 940nm diodes at room temperature, 50°C and 100°C with a 20µs dwell time.

Figures 4.54 and 4.55 show the normalised net PSP decay curves for RC167 following stimulation at room temperature, 50°C and 100°C with 890nm and 940nm diodes using 2µs and 20µs dwell time on the MCS, respectively. Computation revealed that there were three separate components in the decay which acted across three orders of magnitude (Appendix B). These components were stable between stimulation wavelengths. However, a difference in decay lifetimes was noted between stimulation at ambient temperature and stimulation at 100°C. This indicates the existence of an additional thermally assisted recombination pathway for freed charge when RC167 is stimulated at 100°C.

The other K-Feldspars used in this part of the TRS investigation, RC683B and RC1396C, showed similar behaviours to RC167 but suffered from lowest IR stimulation response of the samples investigated. RC683B was noted to have more variable components across wavelengths and also had a large thermally driven variance from decays at 100°C when compared to the decay observed at 50°C. However, the post-940nm decay for RC683B was dominated by the instrument background at ambient temperatures for much of the measurement. The decay lifetimes from this sample varied from 4.58±2µs at 50°C for both post-IR decays to 2.3±0.7µs.

RC1396C was noted to have three stable components which acted across two orders of magnitude for the ambient decays following 890nm stimulation, however a greater variance across a further two orders of magnitude was noted for the longest living component for the decays at 50°C (which varied from ~64±10µs at ambient temperatures to millisecond order) and the decay observed at 100°C decayed too quickly to be measured. The post-940 decay observed for this sample across all temperature regions was dominated by background over the measurement timescale, resulting in a large amount of scatter which gave the trendline fits for the decay component values which were either approximately the same or smaller than the associated errors (Appendix B).

This preliminary investigation of RC683B and RC1396C indicate that both samples have a low emission and recombination efficiency for IR stimulation, even when heated to improve thermal assistance. The observation that 940nm stimulation resulted both in negligible IR emission and PSP points to the recombination pathways in these samples being either too unstable, or that these pathways need stimulation wavelengths of much higher energies to be efficient.

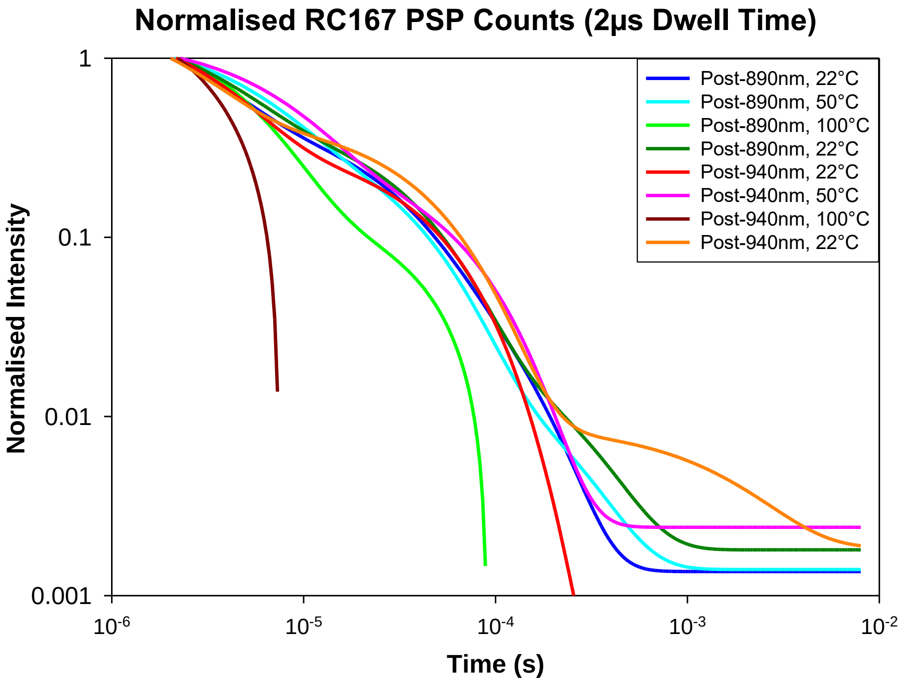

Figure 4.54 – The normalised net decay of a sample of RC167 following stimulation by 890nm diodes at room temperature, 50°C and 100°C using 2µs dwell time.

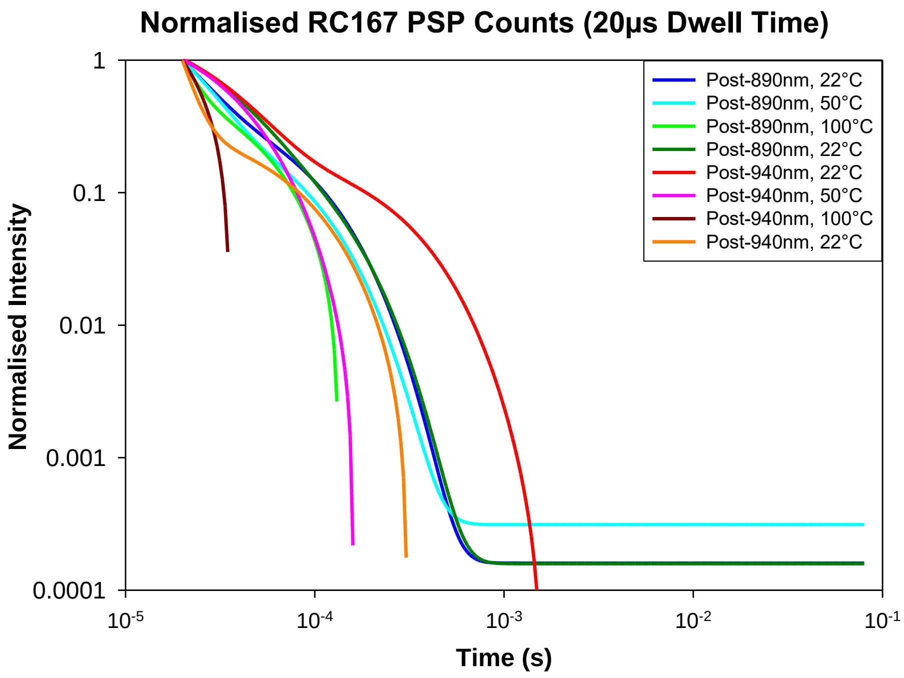

Figure 4.55 – The normalised net decay of a sample of RC167 following stimulation by 890nm and 940nm diodes at room temperature, 50°C and 100°C using 20µs dwell time.

The second TRS system was also used to evaluate the PSP decay across the K-Feldspar samples to compare the observed decays across two separate instruments. Figure 4.56 shows the normalised net PSP decay curves for RC484 following 890nm stimulation using this second TRS system. A pronounced temperature driven difference was noted in the decay components, with the 80°C PSP decaying entirely 100µs after the end of stimulation (Table 4.13). The two 22°C decays showed very similar decay components across microsecond and tens of microsecond order and were observed to decay entirely after 10ms. This decay pattern and variation was nearly identical to the decays observed on the first TRS system, indicating that the behaviour could be repeated. A key difference was observed regarding the value of the decay component of hundreds of microsecond order, as the post-890nm decay at room temperature following the elevated temperature measurement was computed to have a more stable component at this timescale than the decay recorded before the elevated temperature measurement by ~3 orders of magnitude. This may have implications regarding the stability of the band-tail states in the lattice following a fluctuation in stimulation temperatures.

RC484	*Post-890nm 22°C (5us)*	*Post-890nm 80°C (5us)*	*Post-890nm 22°C (5us)*
y0	-0.0001	-0.0002	0
a	0.3223	0.0593	0.2965
b	49968.31	40727.35	48088.38
c	3.716	3.2539	3.6218
d	320706.7	245920.1	310852.9
g	0.0013	0.0005	0.0013
h	203.8227	153.2542	200.1486

Table 4.13 - The room temperature and elevated temperature PSP exponential decay components following 890nm stimulation for RC484 on the second TRS system.

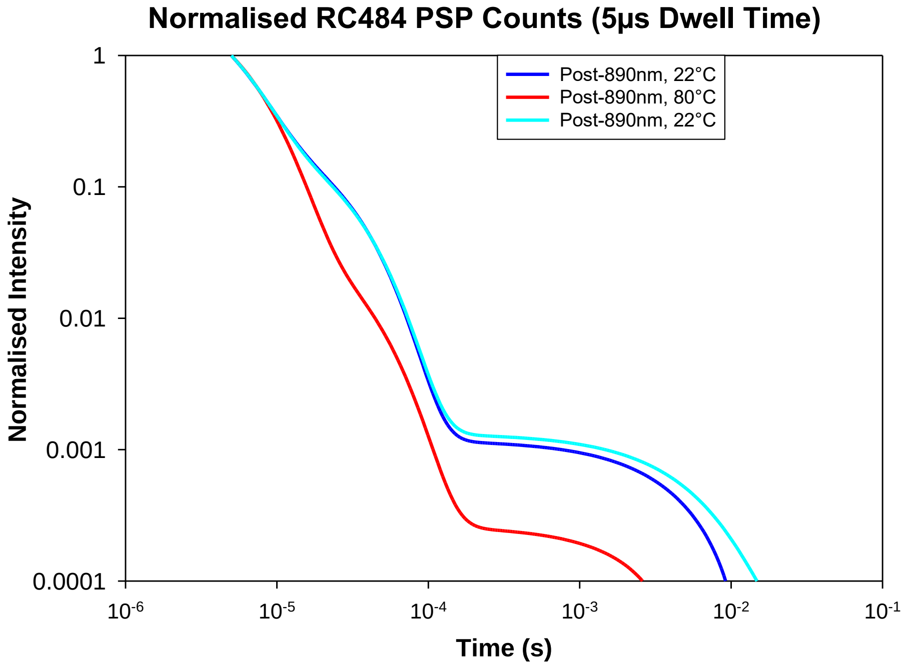

Figure 4.56 – The normalised net decay of a sample of RC484 following stimulation by 890nm diodes at room temperature and 80°C using 5µs dwell time.

A further investigation was conducted using the K-Feldspar samples at stimulation temperatures of -40°C, ambient, and 80°C using 890nm diodes.

Figure 4.57 shows the normalised net PSP decay curves for RC72 following stimulation at room temperature, 80°C and -40°C with 890nm diodes using a 2µs dwell time on the MCS. For ambient temperature and above there existed three components which acted over three timescales (Appendix C). However, following stimulation at -40°C, the three decay components instead acted over two timescales, with two acting on microsecond order and a third acting on the order of hundreds of microseconds. This resulted in the cryogenic temperature decay having the slowest time to decay to the instrument background. For the decay components acting at ambient and elevated temperatures, components acted on the orders of microseconds, tens of microseconds and hundreds of microseconds. However, the decay measured at ambient temperatures following the elevated temperature measurement had a slower decay than the two ambient temperature measurements and took a factor of two longer to decay to background (~115±30µs for the first and third ambient temperature decays, 267±57µs for the second ambient temperature decay). As there exists a measurable thermally driven variation in the decay times for RC72, it can be stated that the lattice structure of RC72 has a series of thermally related recombination pathways which differ in efficiency. This pathway is more stable at lower temperatures, particularly cryogenic temperatures, where the PSP decay can be extended for several orders of magnitude relative to PSP decays at ambient and elevated temperatures.

Figure 4.58 shows the normalised net PSP decay curves for RC491 following stimulation at room temperature, 80°C and -40°C with 890nm diodes using a 2µs dwell time on the MCS. The computed decay components for RC491 showed a clear temperature driven variance, with pronounced differences between the ambient temperature, elevated temperature, and cryogenic temperature decays (Appendix C). The decay measured at -40°C had a longer PSP decay time when compared with PSP measured following stimulation at elevated temperature. As there exists a measurable thermally driven variation in the decay times for RC491, it can be stated that charge movement through the lattice structure of RC491 is dominated by thermally driven mechanisms. These pathways are most efficient at recombining freed charge at elevated temperatures, resulting in shorter decay lifetimes and greater amounts of PSP produced. This pathway is more stable at cryogenic temperatures. This is not behaviour expected from a charge transport mechanism which is dominated by an athermal process.

RC81 was similar to RC491 in that the decay components varied by comparable amounts across the temperature range of this investigation, with the components acting on microsecond and tens of microsecond order having a shorter lifespan at higher temperatures and an order of magnitude longer lifespan at cryogenic temperatures. The PSP measured for RC81 following cryogenic stimulation did not return to the instrument background within the measurement timescale, whereas RC491's PSP had fully decayed within the measurement timescale.

RC389 had no decay component lifetime variation with temperature following stimulation at ambient and elevated temperatures (Appendix C). However, stimulation at cryogenic temperatures resulted in PSP decay components which had lifetimes 2-3 orders of magnitude longer than those calculated for decays at higher temperatures. More PSP than expected was also noted for this sample during the final ambient temperature measurement, with the microsecond order decay component for this measurement having a longer lifetime by a factor of 4.

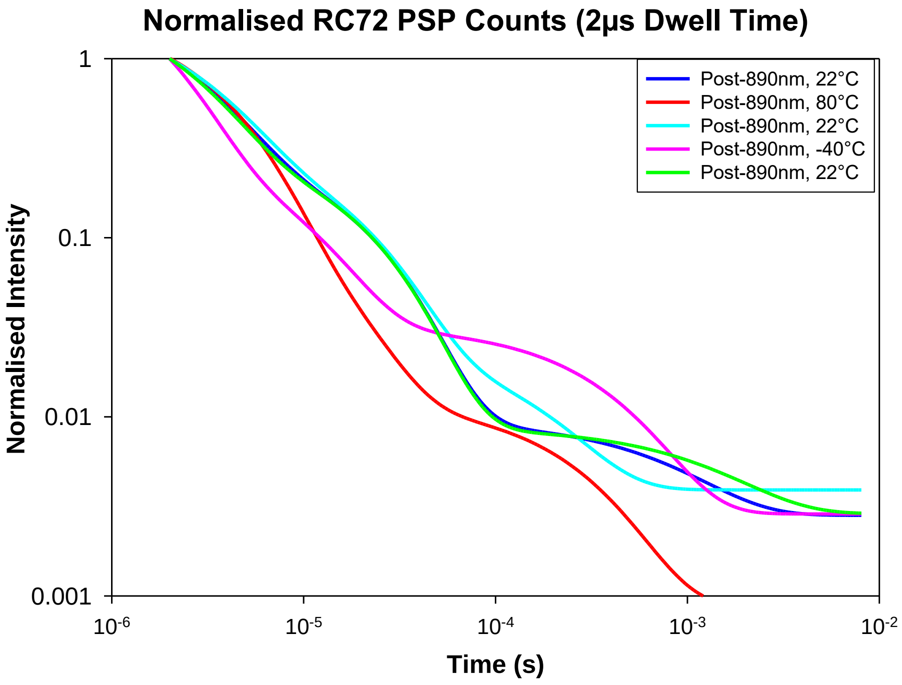

Figure 4.57 – The normalised net decay of a sample of RC72 following stimulation by 890nm diodes at room temperature, 80°C and -40°C using 2µs dwell time.

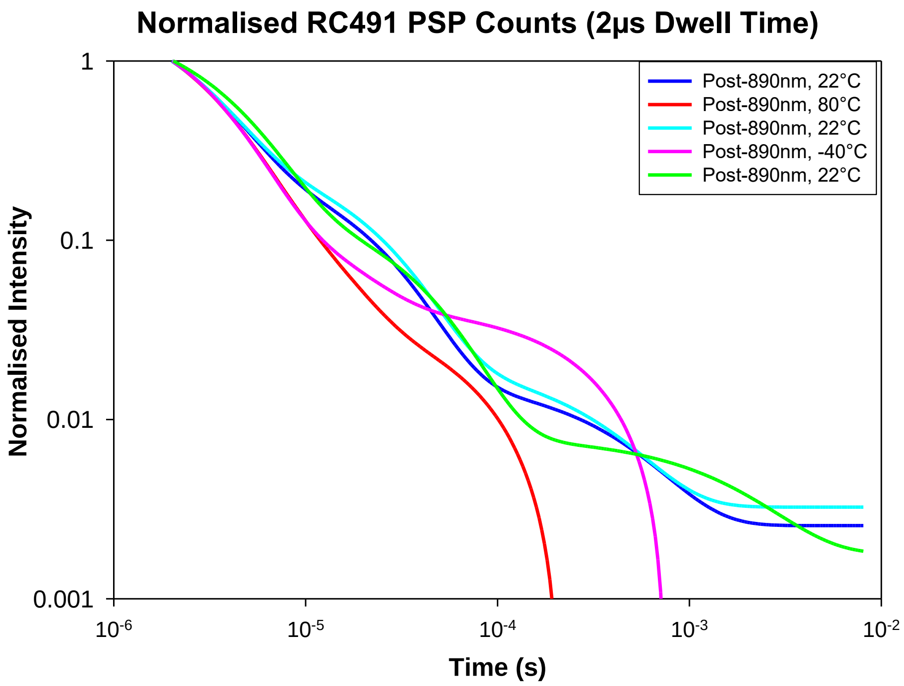

Figure 4.58 – The normalised net decay of a sample of RC491 following stimulation by 890nm diodes at room temperature, 80°C and -40°C using 2µs dwell time.

Overall, the investigations of the K-Feldspar samples using time resolved spectrometry indicated that at microsecond timescales there are multiple components which contribute to the signal decay. These components have a substantially complex variance across this mineral family that is dependent on numerous factors.

For each sample at ambient temperatures, very similar initial normalised net decay rates were computed across the K-Feldspar samples, however there were considerable differences observed when the temperatures were raised or lowered as well as when subsequent ambient decays were measured following these temperature changes. For the normalised decays seen at cryogenic temperatures longer decay times were generally observed than those which were measured at ambient and elevated temperatures, suggesting the participation of different states during post IR decay at lower temperatures. This complex behaviour indicates that different recombination pathways were accessed which were dependent on both the stimulation wavelength and the stimulation temperature, as well as subtle differences in sample mineralogy. These different recombination pathways have distinct recombination lifetimes, indicating differing recombination efficiency across the K-Feldspar samples.

4.3.3 Discussion

Appendices B and C detail the computed lifetimes of each decay measured in this section of the investigation, the results of which are plotted in Figures 4.59 and 4.60, respectively, in the same order of mineral as they appear in Appendices B and C. As can be seen from both figures there is a structured complexity to the lifetimes of the decays seen in feldspars, with mineralogically driven variations apparent – particularly within Figure 4.59 where the stability of the measured decay components can be seen for the albite samples RC14, RC164, and RC169.

The effect of varying the stimulation wavelength can be extrapolated from Figure 4.59, with a clear difference in decay component lifetime visible for several samples. The most obvious variance can be noted as occurring for RC14, RC165, RC169, RC659, and RC683B in Figures 4.59 and 4.60 and RC81, RC169, RC485, and RC630 in Figure 4.61.

This difference in decay component behaviour being driven by variations in the stimulation wavelength implies that the decay process is driven by pathways which freed charges need to have a certain initial energy to access. The additional result that the combination of varied temperature and stimulation wavelengths do not necessarily result in similar decay lifetimes also indicates a complex relaxation mechanism for freed charge to navigate through the lattice to recombination centres.

The effect of varied temperature measurements can also be determined from both graphs, with longer lived decay components observed at lower stimulation temperatures. The varied ambient temperature decays following elevated or lowered temperatures are represented on the graph, with an obvious increase in decay component lifetime seen in Figures 4.59, 4.60 and 4.61 following elevated or lowered temperatures for RC165, RC246, RC491, RC659, and RC683B.

This temperature driven variance in the decay component lifetime has implications for the driving process behind this decay mechanism. As this variance is seen across three distinct regions of temperature, from cryogenic to ambient to elevated it is clear that this process is not athermal and as such cannot be described using a simple single trap model for charge recombination within the feldspar lattice. This also indicates the existence of band tail states with different recombination efficiencies even at cryogenic temperatures.

As these recombination centres continue to release freed charges as detectable photons for many orders of magnitude longer than the stimulation itself, it should be possible to use TL to gain a measurement of the charge population of these unstable, decaying centres. The next section will detail the use of the phototransferred thermoluminescence phenomenon to characterise these centres for the purposes of further modelling.

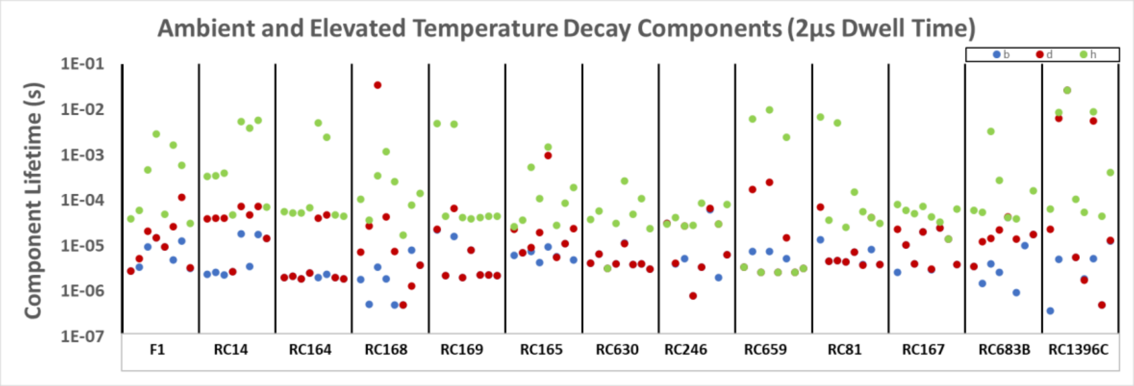

Figure 4.59 – The lifetimes of each of the exponential decay components computed for each sample used in the ambient and elevated decay experiment which used both the 890nm and 940nm diode arrays and a 2µs dwell time on the MCS. Eight sets of three points per sample are organised in the following order: post-890nm decay at ambient temperature, post-890nm decay at 50°C, post-890nm decay at 100°C, post-890nm decay at ambient temperature, post-940nm decay at ambient temperature, post-940nm decay at 50°C, post-940nm decay at 100°C, and post-940nm decay at ambient temperature. Figure data contained within Appendix B.

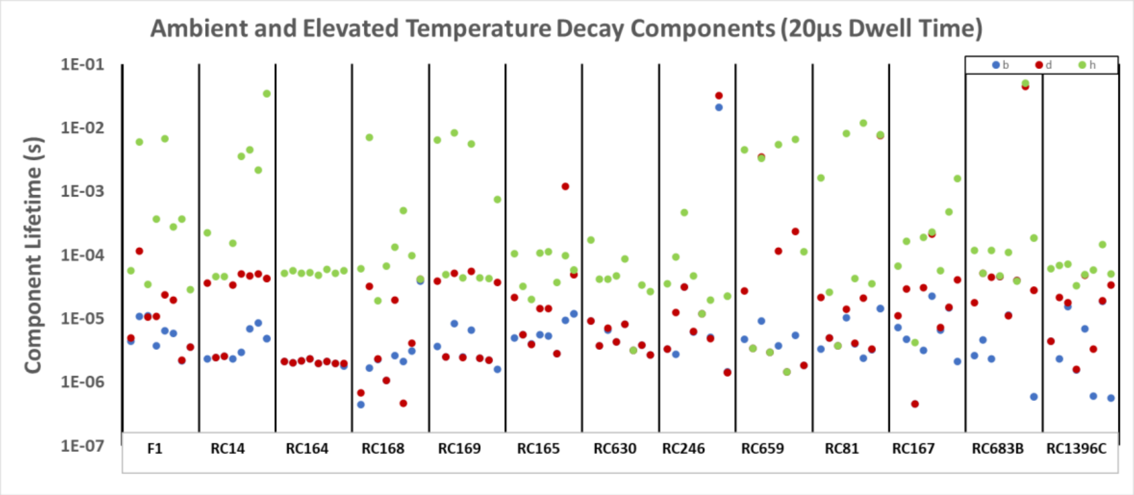

Figure 4.60 – The lifetimes of each of the exponential decay components computed for each sample used in the ambient and elevated decay experiment which used both the 890nm and 940nm diode arrays and a 20µs dwell time on the MCS. Eight sets of three points per sample are organised in the following order: post-890nm decay at ambient temperature, post-890nm decay at 50°C, post-890nm decay at 100°C, post-890nm decay at ambient temperature, post-940nm decay at ambient temperature, post-940nm decay at 50°C, post-940nm decay at 100°C, and post-940nm decay at ambient temperature. Figure data contained within Appendix B.

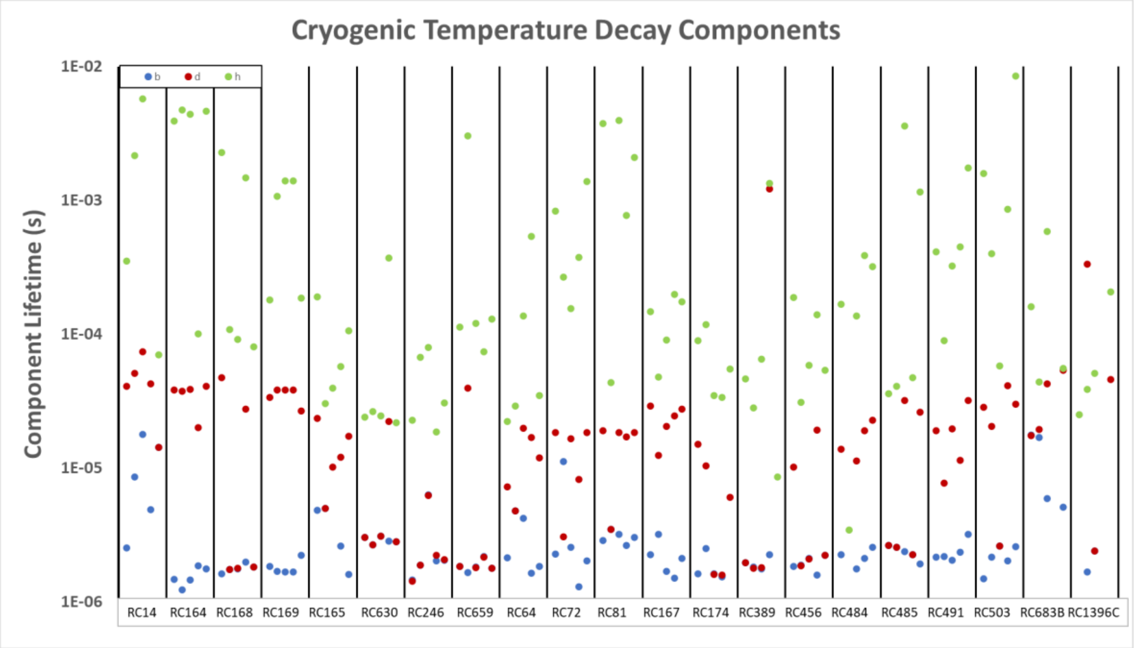

Figure 4.61 – The lifetimes of each of the exponential decay components computed for each sample used in the cryogenic experiment which used the 890nm array and 2μs dwell times on the MCS. Each sample's components are arranged in order of measurement: room temperature, 80°C, room temperature, -40°C, room temperature. Figure data contained within Appendix C.

Similar to Section 4.2 using Equation [2.10], it is possible to compute activation energies for the localised electron states with lifetimes equal to the PSP decay component lifetimes calculated from this experiment. Table 4.14 contains a range of possible activation energies for these states assuming frequency factors of 10^{10}-$10^{14}s^{-1}$. Additionally, activation energies have been calculated to account for the range of temperatures used in this experiment, from 233K to 353K. As can be seen from the table, the range of values for the states responsible for the PSP decay at this timescale, if they exist, have activation energies which suggest that they are separate states than those which were measured in Section 4.2.

Lifetime (μs)	E/eV (10^{10})	E/eV (10^{11})	E/eV (10^{12})	E/eV (10^{13})	E/eV (10^{14})	E/eV (10^{12} at 353K)	E/eV (10^{12} at 233K)
1.00	0.23	0.29	0.35	0.41	0.47	0.42	0.28
2.00	0.25	0.31	0.37	0.42	0.48	0.44	0.29
4.00	0.27	0.33	0.38	0.44	0.50	0.46	0.31
5.00	0.27	0.33	0.39	0.45	0.51	0.47	0.31
6.00	0.28	0.34	0.39	0.45	0.51	0.47	0.31
8.00	0.29	0.34	0.40	0.46	0.52	0.48	0.32
10.00	0.29	0.35	0.41	0.47	0.52	0.49	0.32
15.00	0.30	0.36	0.42	0.48	0.53	0.50	0.33
20.00	0.31	0.37	0.42	0.48	0.54	0.51	0.34
50.00	0.33	0.39	0.45	0.51	0.56	0.54	0.36
100.00	0.35	0.41	0.47	0.52	0.58	0.56	0.37
150.00	0.36	0.42	0.48	0.53	0.59	0.57	0.38
200.00	0.37	0.42	0.48	0.54	0.60	0.58	0.38

Table 4.14 – The activation energy (in eV) for a state with a lifetime (μs) given a supposed frequency factor range of 10^{10} – 10^{14} and a sample temperature of 293K. Two additional columns illustrate the temperature driven effect on the activation energy by showing the activation energy with associated PSP decay lifetimes at 353K and 233K for a frequency factor of 10^{12}.

4.4 Feldspar Investigation III – PTTL

4.4.1 Experimental Procedure

The storage sites responsible for the delayed post-IRSL recombination of freed charge that results in the detectable PSP decay that were noted in Sections 4.1 and 4.2 are of interest for the purposes of modelling how charge populations are affected by IR exposure. These storage sites are closely related to charge mobility within the feldspar lattice structure as the lattice relaxes following stimulation and must be more unstable than the main IRSL recombination centres at room temperature to account for the post-IR PSP lifetimes. A previous study using these samples used limited TL studies following stimulation and showed that for some feldspar samples that low temperature trapping sites existed with activation energies of ~1eV and peak temperatures of 100-120°C (Fitzgerald, 2020). As such, to understand how these unstable trapping environments decay following IR exposure this investigation will expand on this previous work and probe these short-lived trapping sites using PTTL.

As with previous sections of this project, twenty-two feldspar samples were used in this section of the investigation. As three separate TL readers are used across two different stimulation temperatures for each sample, efforts were taken during sample preparation to minimise the variation for each sample between measurements to ensure that each measurement was as closely comparable to each other as possible. Ensuring similar sample properties to those used in previous sections of this project was also a priority to ensure that any PSP which was detected could be assumed to be decaying via similar mechanisms to those which have been previously discussed in Sections 4.1 and 4.2. To this end, before each measurement every sample was thermally cleared by a TL ramp up to 400°C at 5°C, followed by a reheat to ensure that no freed charge remained in the temperature region of interest to this study. The Elsec irradiator described in Section 3 was then used to give each sample a 100Gy dose, each sample was then left overnight.

The apparatus used for sample measurement included the SUERC portable IRSL (pIRSL) reader (using its 890nm LED array) and TL instruments which were described in Section 3, Risø 1 (using its 830nm LASER) and Risø 3 (using its 870nm LED).

As a result of the difference in photomultiplier filters used in the instruments, the observable detection window for emitted photons is between the wavelengths of 325nm and 475nm for Risø 1 and 3. It is constrained to include primarily photons of wavelengths shorter than 350nm and longer than 650nm for the SUERC TL reader, though there is some breakthrough due to a variable T% for the BG39 filter (Figure 3.5).

A difference in the temperature scale was noted between the measurements of Risø 1 and the SUERC TL reader, with the Risø 1 TL plot having the same characteristics as the SUERC TL reader plot but with a 10°C to 20°C delay and resulting in the figures derived via Arrhenius plots of the Risø 1 data giving erroneously high values for the activation energy of the PTTL recombination site, differing by several standard errors. The temperature scale was corrected with regards to this temperature delay and the activation energies computed from the Risø 1 TL plots then gave activation energies which were within 5 standard errors of the values obtained from the SUERC TL reader plots. Any further variation in the activation energies obtained using the Risø 1 TL plots can likely be attributed to the recombination centre having lost more recombining freed charge due to the longer time it takes for Risø 1 to conduct the TL ramp following stimulation.

A similar difference in the temperate scale was noted between the measurements of Risø 3 to that of Risø 1 when compared with the SUERC TL reader, with the Risø 3 TL plot having the same characteristics as the SUERC TL reader plot but with a 10°C to 20°C delay and resulting in the figures derived via Arrhenius plots of the Risø 3 data giving higher values for the activation energy of the PTTL recombination site, differing by 10 standard errors (with most of them initially being above 1.4eV). The temperature scale was corrected with regards to this temperature delay and the activation energies computed from the Risø 3 TL plots then gave activation energies which were within 5 standard errors of the values obtained from the SUERC TL reader plots. Any further variation in the activation energies obtained using the Risø 3 TL plots can likely be attributed to the recombination centre having lost more recombining freed charge due to the higher holding temperature of 50°C while the sample was raised and lowered between the 870nm stimulation and the TL ramp whereas the changeover between the SUERC pIRSL reader and the TL reader occurred at ambient temperatures.

The measurement cycle for each sample consisted of several steps, starting with an initial TL ramp up to 200°C at 5°C/s to fully clear any remaining low temp signal. This was followed by 60 seconds of stimulation from the IR-source being used which was bracketed by a 15 second non-stimulating measurement, and then a TL ramp up to 200°C at 5°C/s as soon as possible. A second TL ramp up to 200°C at 5°C/s was then recorded to attain a net signal. There was a cooling period of sixty seconds between TL ramps. The measurements recorded with the SUERC portable IRSL and TL readers, as well as Risø 1, were conducted at ambient temperature (22°C). The measurements recorded using Risø 3 were conducted at 50°C. The time between IR stimulation and TL ramps varied across the instruments, with a manual change over from the SUERC pIRSL instrument to the TL reader taking a timed 15 seconds. The two Risø readers took slightly different times for the sample to be raised, lowered, and raised again between the IR stimulation and the TL ramp. Risø 1 took 25 seconds to complete this process and Risø 3 took 15 seconds. Each sample was measured on each instrument up to three times to confirm reproducibility of the results and allow for confident cross-comparison.

To attain the value of the activation energies of sites populated by phototransfer, Arrhenius plots of the logarithm of the net TL count against 1/kT were produced, where k is Boltzmann's constant and T is temperature in degrees Kelvin. The gradient of the trendline at the rising edge of PTTL peaks on this plot equals the activation energy of the recombination centre (Bouscary and King, 2022). The peak temperature was also noted.

4.4.2 Room Temperature Investigation

This section will break down the results of this experiment following ambient temperature stimulation and TL, commenting on observed behaviours and trends as well as comparing the two instrumental approaches used (SUERC pIRSL and TL vs Risø 1).

Appendix D contains the activation energies of all PTTL peaks examined over the course of this thesis. The activation energies obtained from the SUERC pIRSL TL measurement varied from 0.56±0.04eV to 0.84±0.02eV; the Risø 1 measurements returned PTTL peaks with activation energies from 0.55±0.02 to 0.72±0.02. Table 4.15 shows the average activation energies for the PTTL peaks measured for the each of the feldspars following room temperature 890nm stimulation.

SAMPLE	SUERC TL	UNCERT	RISØ I	UNCERT
RC167	0.691	0.123	0.546	0.145
RC174	0.700	0.049	0.615	0.085
RC72	0.709	0.052	0.606	0.081
RC64	0.702	0.013	0.592	0.036
RC81	0.686	0.075	0.661	0.116
RC485	0.693	0.113	0.567	0.080
RC484	0.632	0.083	0.524	0.003
RC491	0.671	0.248	0.555	0.022
RC503	0.670	0.202	0.593	0.101
F1	0.689	0.018	0.577	0.089
RC1396C	0.817	0.455	0.620	0.290
RC389	0.642	0.415	0.720	0.346
RC456	0.718	0.186	0.605	0.162
RC683B	0.699	0.332	0.575	0.280
RC630	0.711	0.104	0.614	0.254
RC165	0.701	0.089	0.577	0.120
RC246	0.682	0.366	0.675	0.122
RC659	0.643	0.085	0.624	0.222
RC14	0.739	0.111	0.629	0.059
RC168	0.620	0.085	0.624	0.135
RC169	0.689	0.186	0.570	0.126
RC164	0.612	0.096	0.549	0.091

Table 4.15 – The average activation energies and uncertainties calculated for each of the feldspars following room temperature 890nm stimulation using the SUERC pIRSL reader and 830nm stimulation using Risø 1. Samples are arranged by mineralogy in the following order: K-Feldspars, Microclines, Plagioclases, Albites.

Figures 4.62 and 4.63 show a net PTTL curve for F1 recorded on the SUERC TL reader and Risø 1 reader, respectively. The activation energies obtained for the PTTL peaks for the TL ramps conducted on the SUERC TL reader are 0.68±0.03eV and 0.70±0.03eV, the values obtained for the PTTL peaks for the TL ramps conducted on Risø 1 are 0.58±0.03eV and 0.57±0.02eV. These values are within 5 standard errors of each other, suggesting that the approximate value of the activation energy for the PTTL recombination centres is likely somewhere within these values, or there is an unquantified uncertainty which has not been accounted for and propagated.

The activation energies obtained for the PTTL peaks for the TL ramps conducted on the SUERC TL reader for RC81 are 0.69±0.07eV and 0.68±0.02eV, the values obtained for the PTTL peaks for the TL ramps conducted on Risø 1 are 0.64±0.05eV and 0.67±0.03eV. These values are within a standard error of each other, highlighting a good agreement in the value of this recombination centre's activation energy.

The activation energies obtained for the PTTL peaks for the TL ramps conducted on the SUERC TL reader for RC1396C are 0.60±0.31eV and 1.03±0.42eV, the values obtained for the PTTL peaks for the TL ramps conducted on Risø 1 are 0.58±0.37eV and 0.61±0.30eV. The scatter observed in these values for the activation energy of the PTTL peaks for this sample is partly a result of the lower recorded net counts during the TL ramp and is reflected by the higher uncertainties.

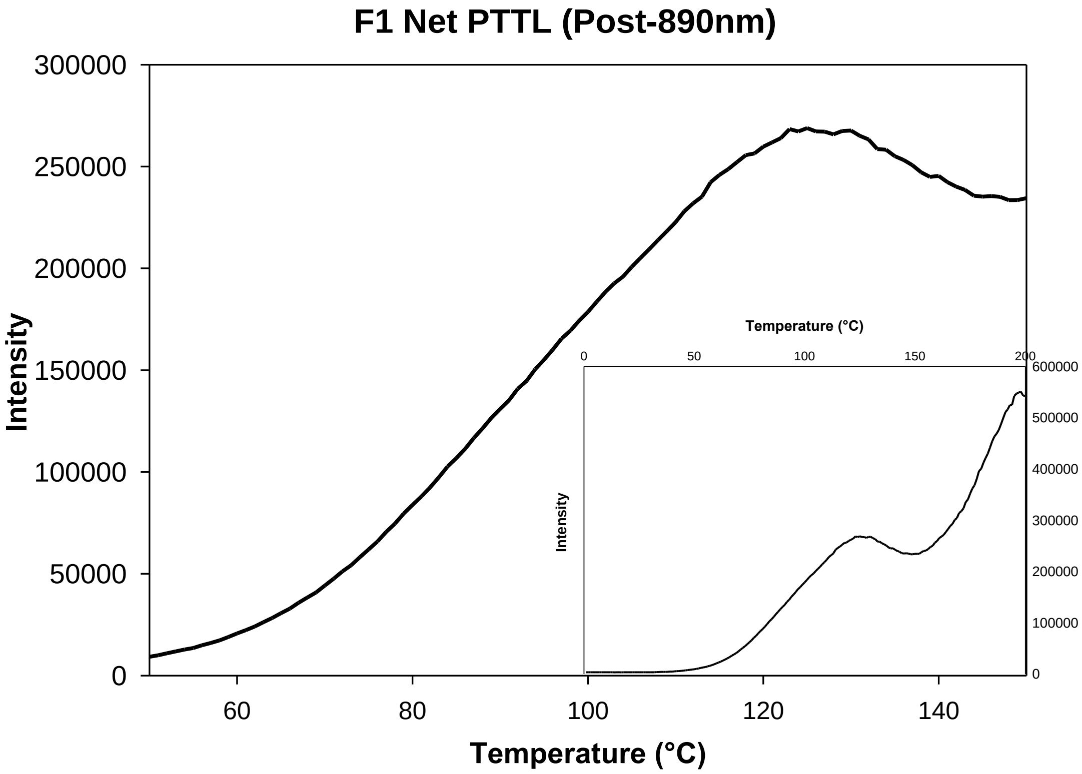

Figure 4.62 – The net counts recorded using the SUERC TL reader for aliquot A of the sample F1. A PTTL peak at ~125°C is apparent, with a rise towards it starting at ~55°C. The major plot shows the PTTL peak in more detail, the inset plot shows the complete TL ramp up to 200°C.

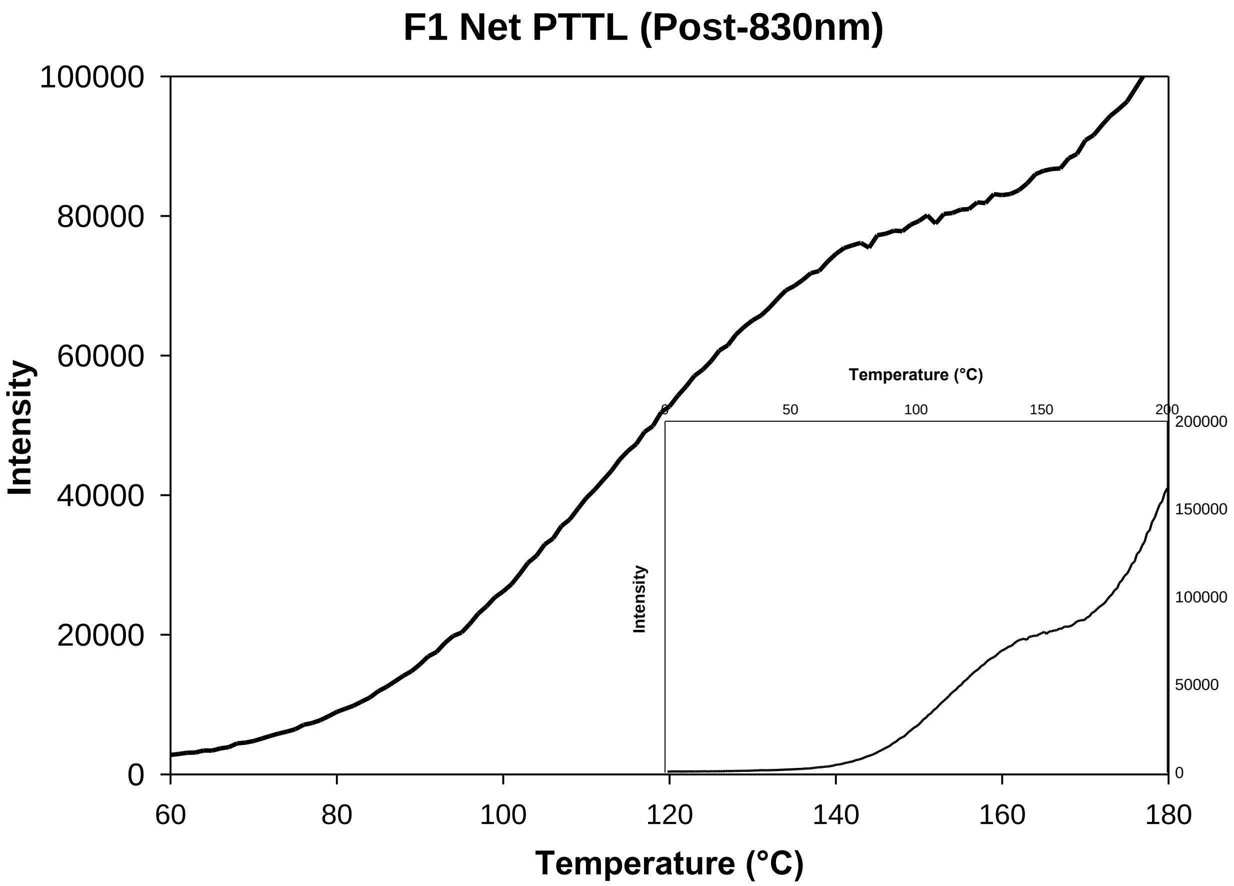

Figure 4.63 – The net counts recorded using the Risø 1 reader for aliquot A of the sample F1. A PTTL shoulder at ~145°C is apparent, with a rise towards it starting at ~70°C. The major plot shows the PTTL peak in more detail, the inset plot shows the complete TL ramp up to 200°C.

Figures 4.64 and 4.65 show a net PTTL curve for RC14 recorded on the SUERC TL reader and Risø 1 reader, respectively. The activation energies obtained for the PTTL peaks for the TL ramps conducted on the SUERC TL reader are 0.75±0.03eV and 0.72±0.04eV, the values obtained for the PTTL peaks for the TL ramps conducted on Risø 1 are 0.65±0.02eV and 0.61±0.02eV. These values are within 5 standard errors of each other, suggesting that the approximate value of the activation energy for the PTTL recombination centres is likely somewhere within these values, or there is an unquantified uncertainty which has not been accounted for and propagated.

The activation energies obtained for the PTTL peaks for the TL ramps conducted on the SUERC TL reader for RC164 are 0.69±0.07eV and 0.68±0.02eV, the values obtained for the

PTTL peaks for the TL ramps conducted on Risø 1 are 0.64±0.05eV and 0.67±0.03eV. These values are within a standard error of each other, highlighting a good agreement in the value of this recombination centre's activation energy.

The activation energies obtained for the PTTL peaks for the TL ramps conducted on the SUERC TL reader for RC169 are 0.63±0.06eV and 0.77±0.04eV, the values obtained for the PTTL peaks for the TL ramps conducted on Risø 1 are 0.55±0.04eV and 0.59±0.10eV. The scatter observed in these values for the activation energy of the PTTL peaks for this sample is partly a result of the temperature delay in Risø 1's TL ramp when compared with the SUERC TL reader that resulted in elongated PTTL shoulders instead of defined peaks which caused difficulties with the Arrhenius plot trendline fit.

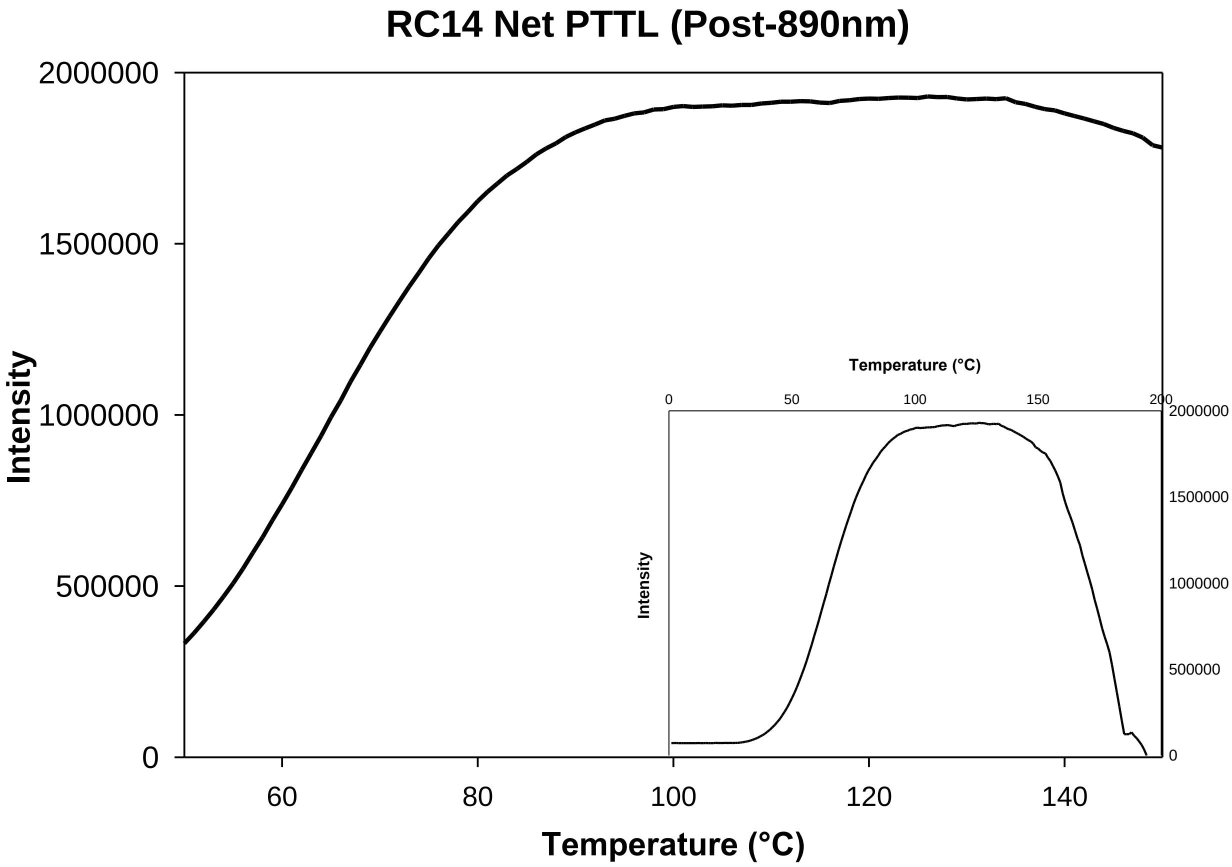

Figure 4.64 – The net counts recorded using the SUERC TL reader for aliquot A of the sample RC14. A PTTL peak at ~120°C is apparent, with a rise towards it starting at ~40°C. The major plot shows the PTTL peak in more detail, the inset plot shows the complete TL ramp up to 200°C.

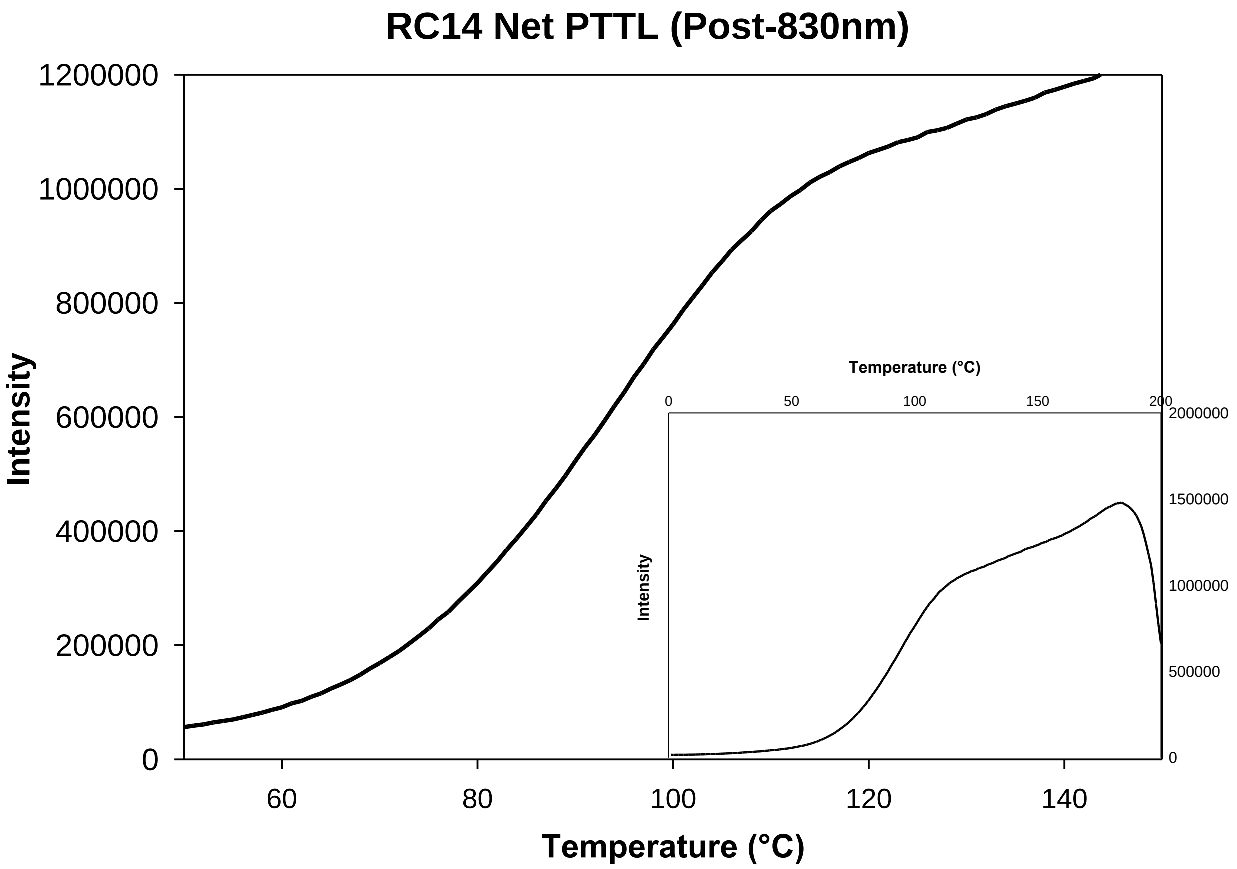

Figure 4.65 – The net counts recorded using the Risø 1 reader for aliquot A of the sample RC14. A PTTL shoulder at ~110°C is apparent, with a rise towards it starting at ~55°C. The major plot shows the PTTL peak in more detail, the inset plot shows the complete TL ramp up to 200°C.

Figures 4.66 and 4.67 show a net PTTL curve for RC165 recorded on the SUERC TL reader and Risø 1 reader, respectively. The activation energies obtained for the PTTL peaks for the TL ramps conducted on the SUERC TL reader are 0.70±0.04eV and 0.70±0.05eV, the values obtained for the PTTL peaks for the TL ramps conducted on Risø 1 are 0.59±0.06eV and 0.56±0.03eV. These values are within 2 standard errors of each other, suggesting that the approximate value of the activation energy for the PTTL recombination centres is likely somewhere within these values, with the difference likely dominated by the increased time it takes Risø 1 to raise and lower the sample between the 830nm stimulation and the TL ramp.

The activation energies obtained for the PTTL peaks for the TL ramps conducted on the SUERC TL reader for RC630 are 0.74±0.06eV and 0.68±0.03eV, the values obtained for the

PTTL peaks for the TL ramps conducted on Risø 1 are 0.64±0.03eV and 0.59±0.05eV. With the exception of the final result, these values are within a standard error of each other, highlighting a good agreement in the value of this recombination centre's activation energy. The activation energy calculated from the Risø 1 TL ramp is still within two standard errors of the other calculated values for the recombination centre's activation energy and suggests the variance is due to an unquantified uncertainty rather than instrumental differences.

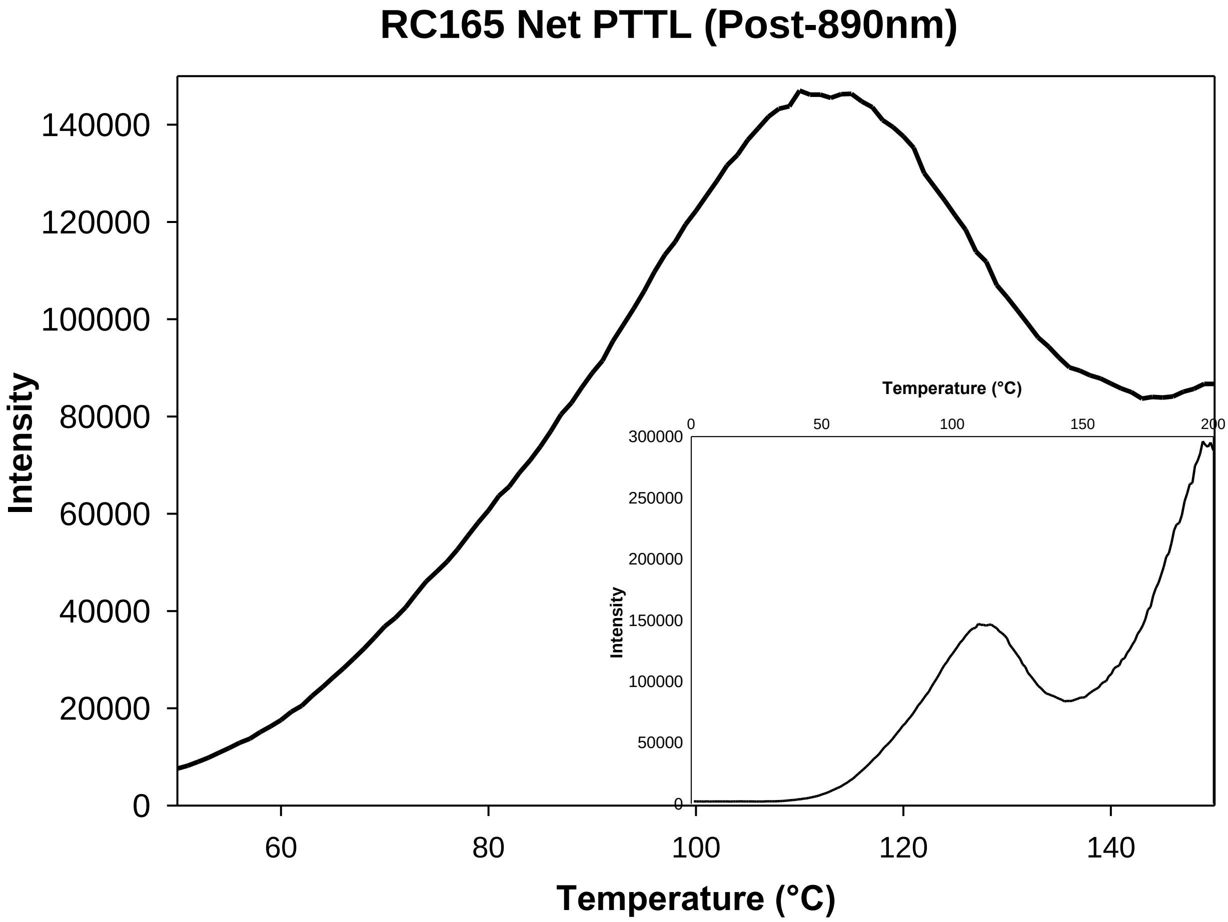

Figure 4.66 – The net counts recorded using the SUERC TL reader for aliquot A of the sample RC165. A PTTL peak at ~115°C is apparent, with a rise towards it starting at ~50°C. The major plot shows the PTTL peak in more detail, the inset plot shows the complete TL ramp up to 200°C.

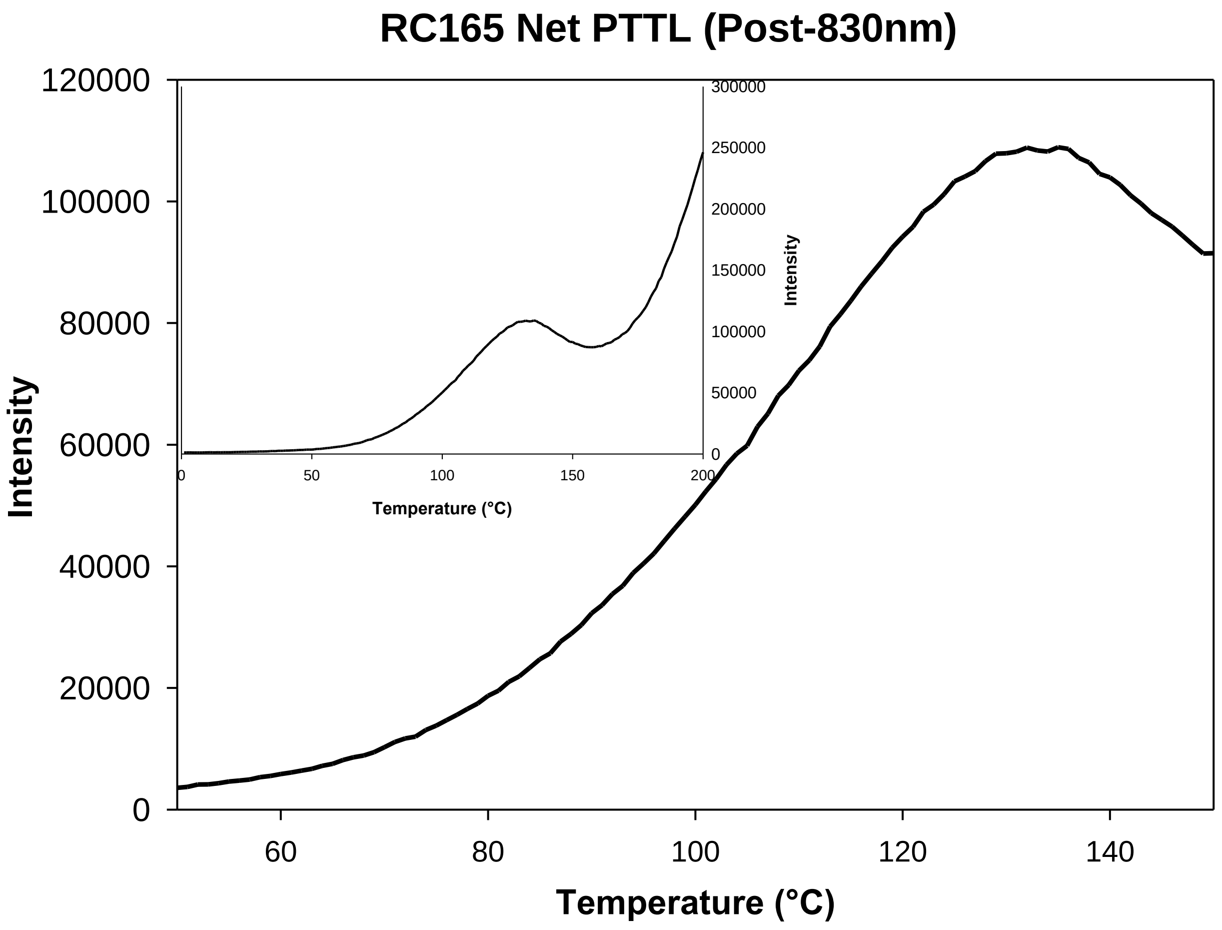

Figure 4.67 – The net counts recorded using the Risø 1 reader for aliquot A of the sample RC165. A PTTL peak at ~125°C is apparent, with a rise towards it starting at ~55°C. The major plot shows the PTTL peak in more detail, the inset plot shows the complete TL ramp up to 200°C.

Figures 4.68 and 4.69 show a net PTTL curve for RC484 recorded on the SUERC TL reader and Risø 1 reader, respectively. The activation energies obtained for the PTTL peaks for the TL ramps conducted on the SUERC TL reader are 0.61±0.10eV and 0.65±0.05eV, the value obtained for the PTTL peak for the TL ramp conducted on Risø 1 is 0.52±0.05eV. These values are within 2 standard errors of each other, suggesting that the approximate value of the activation energy for the PTTL recombination centres is likely somewhere within these values, with the difference likely dominated by the increased time it takes Risø 1 to raise and lower the sample between the 830nm stimulation and the TL ramp as well as a lower IR response from the sample.

The activation energies obtained for the PTTL peaks for the TL ramps conducted on the SUERC TL reader for RC72 are 0.72±0.17eV and 0.70±0.06eV, the value obtained for the PTTL peak for the TL ramp conducted on Risø 1 is 0.61±0.03eV. These values are within a standard error of each other, highlighting a good agreement in the value of this recombination centre's activation energy. The activation energy calculated from the Risø 1b TL ramp is still within two standard errors of the other calculated values for the recombination centre's activation energy.

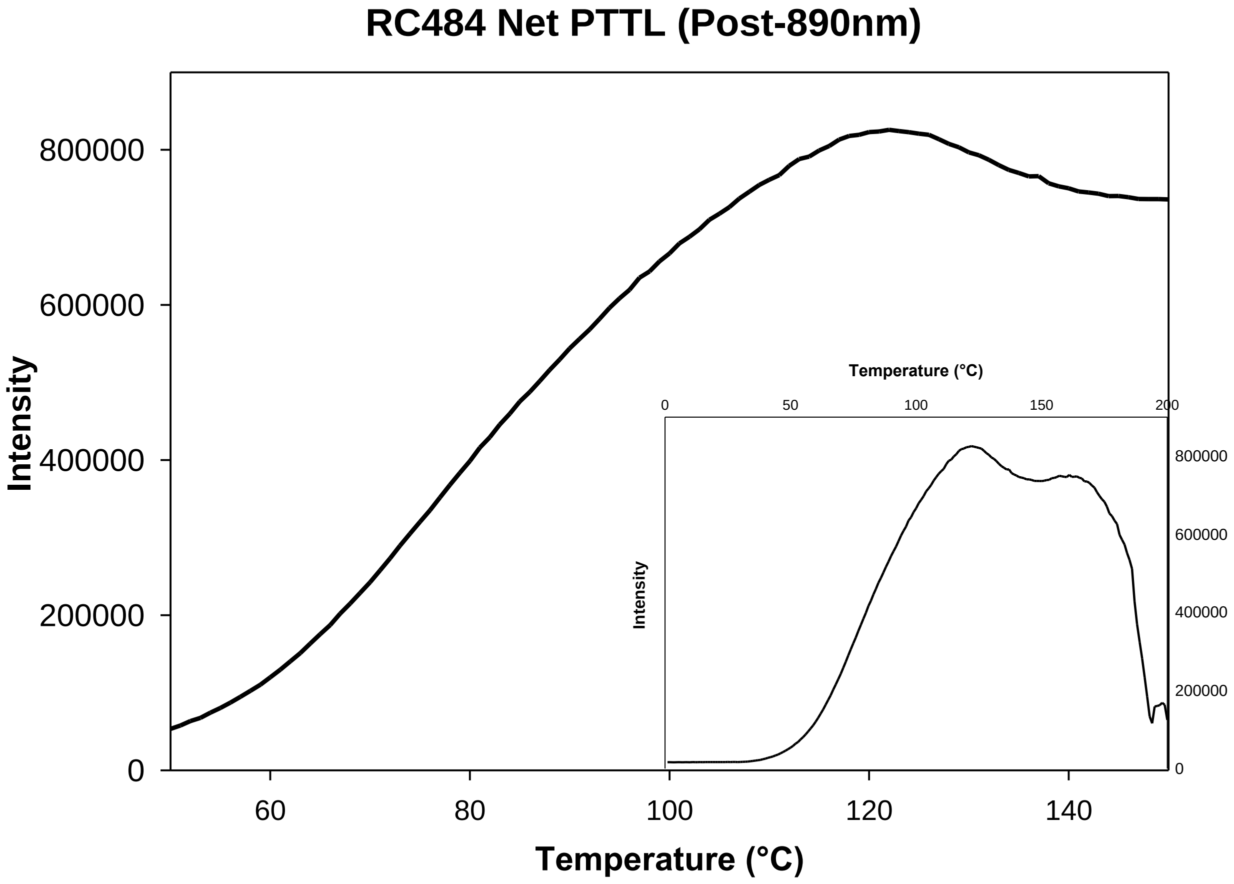

Figure 4.68 – The net counts recorded using the SUERC TL reader for aliquot A of the sample RC484. A PTTL peak at ~120°C is apparent, with a rise towards it starting at ~50°C. The major plot shows the PTTL peak in more detail, the inset plot shows the complete TL ramp up to 200°C.

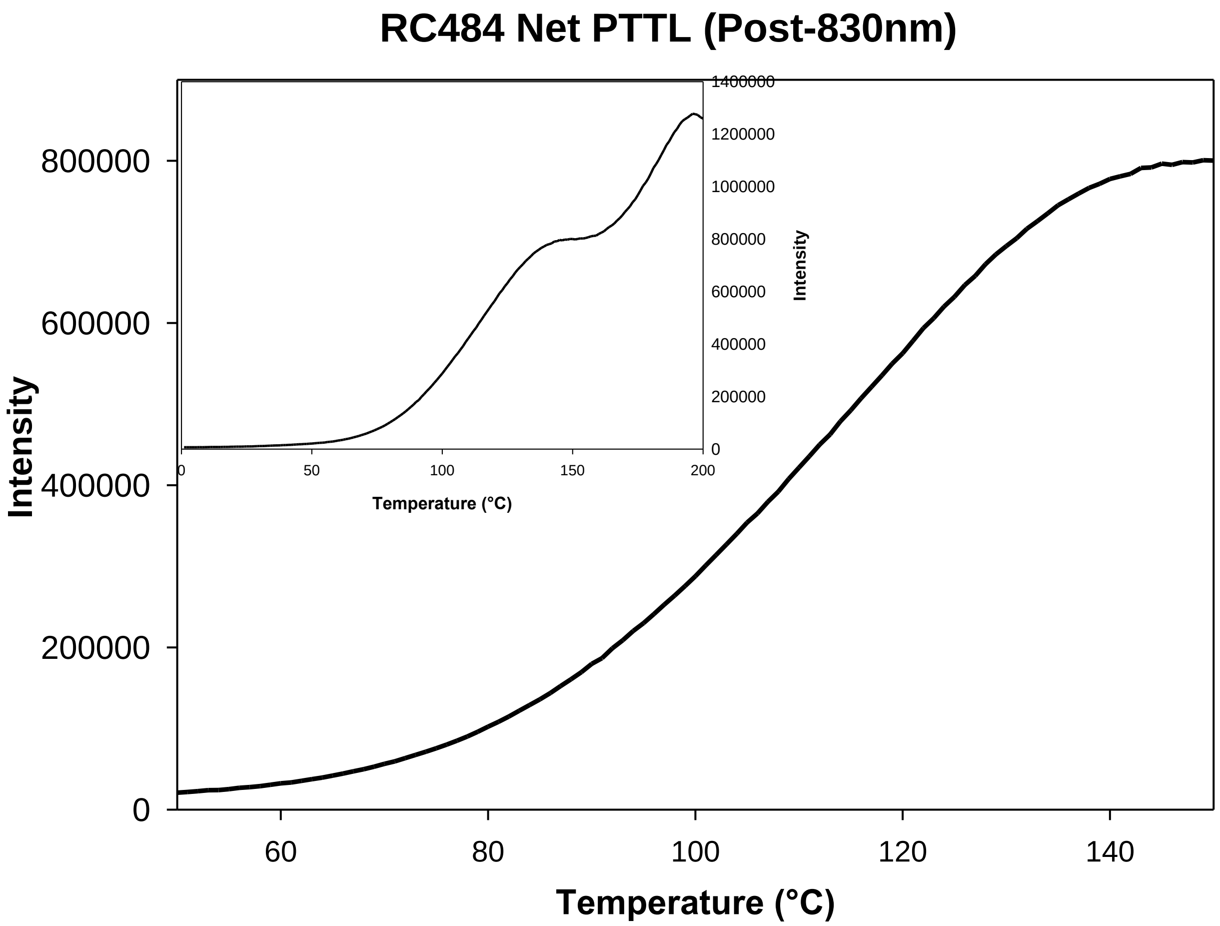

Figure 4.69 – The net counts recorded using the Risø reader for aliquot A of the sample RC484. A PTTL peak at ~140°C is apparent, with a rise towards it starting at ~60°C. The major plot shows the PTTL peak in more detail, the inset plot shows the complete TL ramp up to 200°C.

Figures 4.70 and 4.71 show a net PTTL curve for RC659 recorded on the SUERC TL reader and Risø 1 reader, respectively. The activation energies obtained for the PTTL shoulders for the TL ramps conducted on the SUERC TL reader are 0.73±0.22eV and 0.55±0.28eV, the value obtained for the PTTL peak for the TL ramp conducted on Risø 1 is 0.62±0.14eV. While these results are within two standard errors of each other, there was a noted low net intensity of PTTL noted in the TL ramp plots which resulted in much larger errors for this sample than for most of the other feldspars examined.

This low intensity was also seen in the other plagioclase sample, with the activation energies obtained for the PTTL peaks for the TL ramps conducted on the SUERC TL reader for RC246 being 0.66±0.20eV and 0.70±0.15eV, the value obtained for the PTTL shoulder for the TL ramp conducted on Risø 1 is 0.67±0.39eV. As with RC659, the PTTL observed in RC246 had a very low intensity which, while still above background, made fitting a trendline for the PTTL shoulder difficult and resulted in errors which were a considerable fraction of the computed value of the shoulder's activation energy.

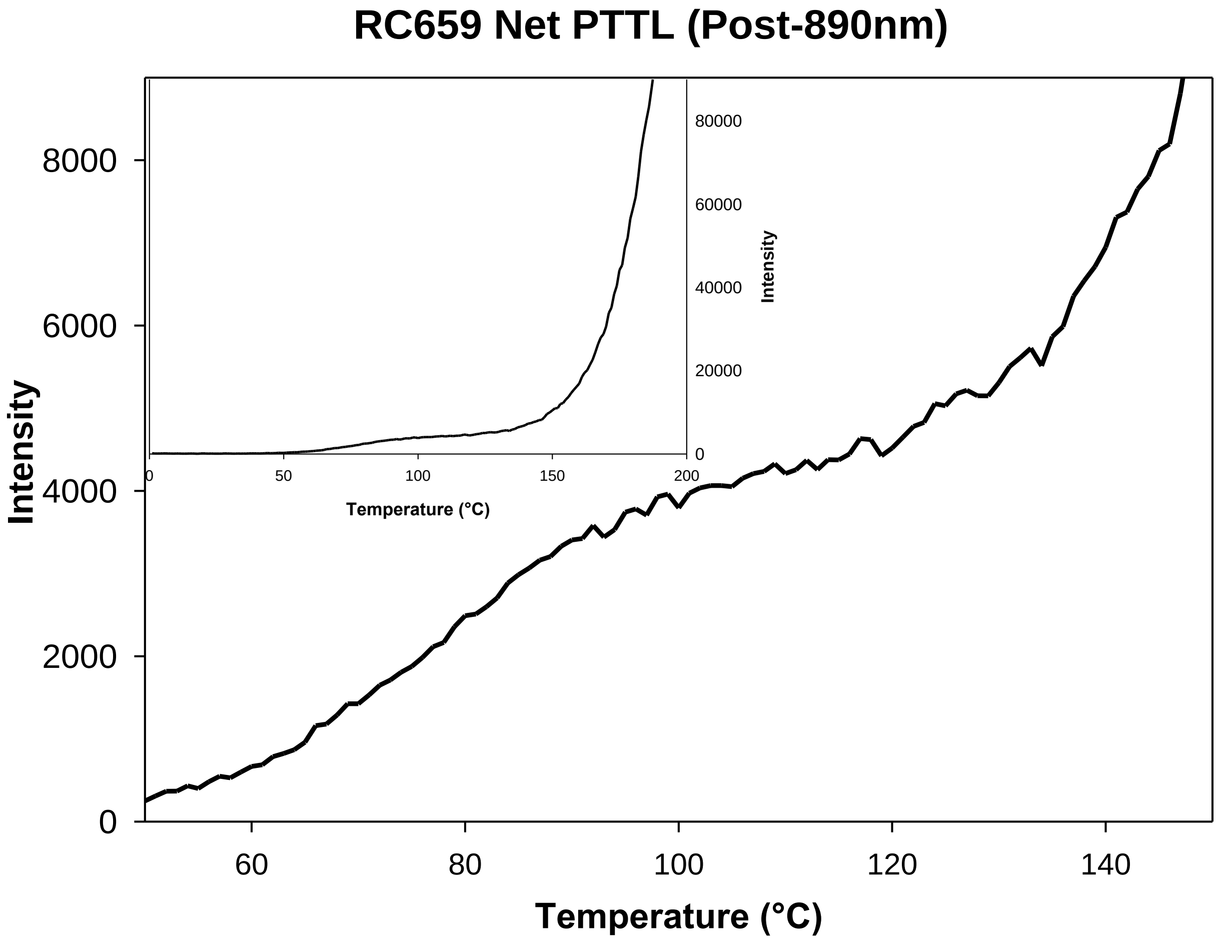

Figure 4.70 – The net counts recorded using the SUERC TL reader for aliquot A of the sample RC659. A PTTL shoulder at ~110°C is apparent, with a rise towards it starting at ~50°C. The major plot shows the PTTL peak in more detail, the inset plot shows the complete TL ramp up to 200°C.

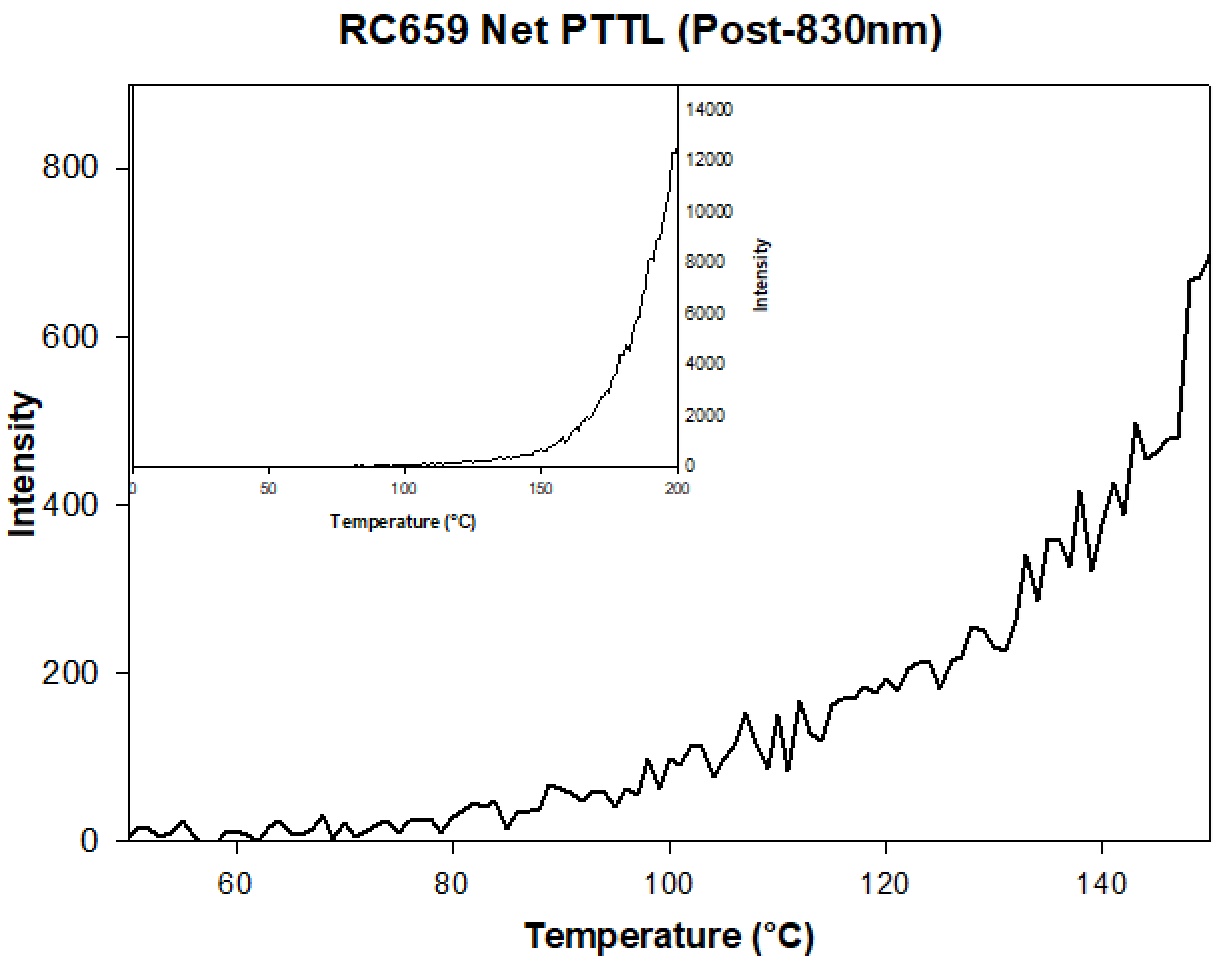

Figure 4.71 – The net counts recorded using the Risø 1 reader for aliquot A of the sample RC659. A PTTL peak at ~115°C is apparent, with a rise towards it starting at ~50°C. The major plot shows the PTTL peak in more detail, the inset plot shows the complete TL ramp up to 200°C.

4.4.3 Elevated Temperature Investigation

Table 4.16 shows the average activation energies for the PTTL peaks measured for the each of the feldspars following 890nm stimulation at 50°C using Risø 3. The measurements returned PTTL peaks with activation energies from 0.80±0.03 to 0.92±0.08.

Sample	*RISØ III*	*Uncert*
RC167	0.850	0.120
RC174	0.760	0.053
RC72	0.875	0.029
RC64	0.802	0.116
RC81	0.763	0.125
RC485	0.739	0.096
RC484	0.742	0.070
RC491	0.745	0.189
RC503	0.718	0.116
F1	0.814	0.078
RC1396C	0.828	0.332
RC389	0.757	0.267
RC456	0.818	0.251
RC683B	0.831	0.326
RC630	0.882	0.062
RC165	0.888	0.14699
RC246	0.643	0.196
RC659	0.876	0.108
RC14	0.855	0.118
RC168	0.911	0.096
RC169	0.759	0.136
RC164	0.753	0.028

Table 4.16 - The average activation energies and uncertainties calculated for each of the feldspars following 870nm stimulation at 50°C. Samples are arranged by mineralogy in the following order: K-Feldspars, Microclines, Plagioclases, Albites.

Figure 4.72 shows a net PTTL curve for F1 recorded on the Risø 3 reader. The activation energies obtained for the PTTL peaks for the TL ramps conducted on the Risø 3 reader are 0.80±0.03eV, 0.91±0.07eV and 0.83±0.05eV. These values are within 2 standard errors of each other, suggesting that the approximate value of the activation energy for the PTTL recombination centres at this elevated stimulation temperature is likely somewhere within these values, or there is an unquantified uncertainty which has not been accounted for and propagated.

Figure 4.73 shows a net PTTL curve for RC14 recorded on the Risø 3 reader. The activation energies obtained for the PTTL peaks for the TL ramps conducted on the Risø 3 reader are 0.8±0.05eV, 0.91±0.02eV and 0.85±0.08eV. These values are within a standard error of each other, suggesting that the approximate value of the activation energy for the PTTL recombination centres at this elevated stimulation temperature is likely somewhere within these values.

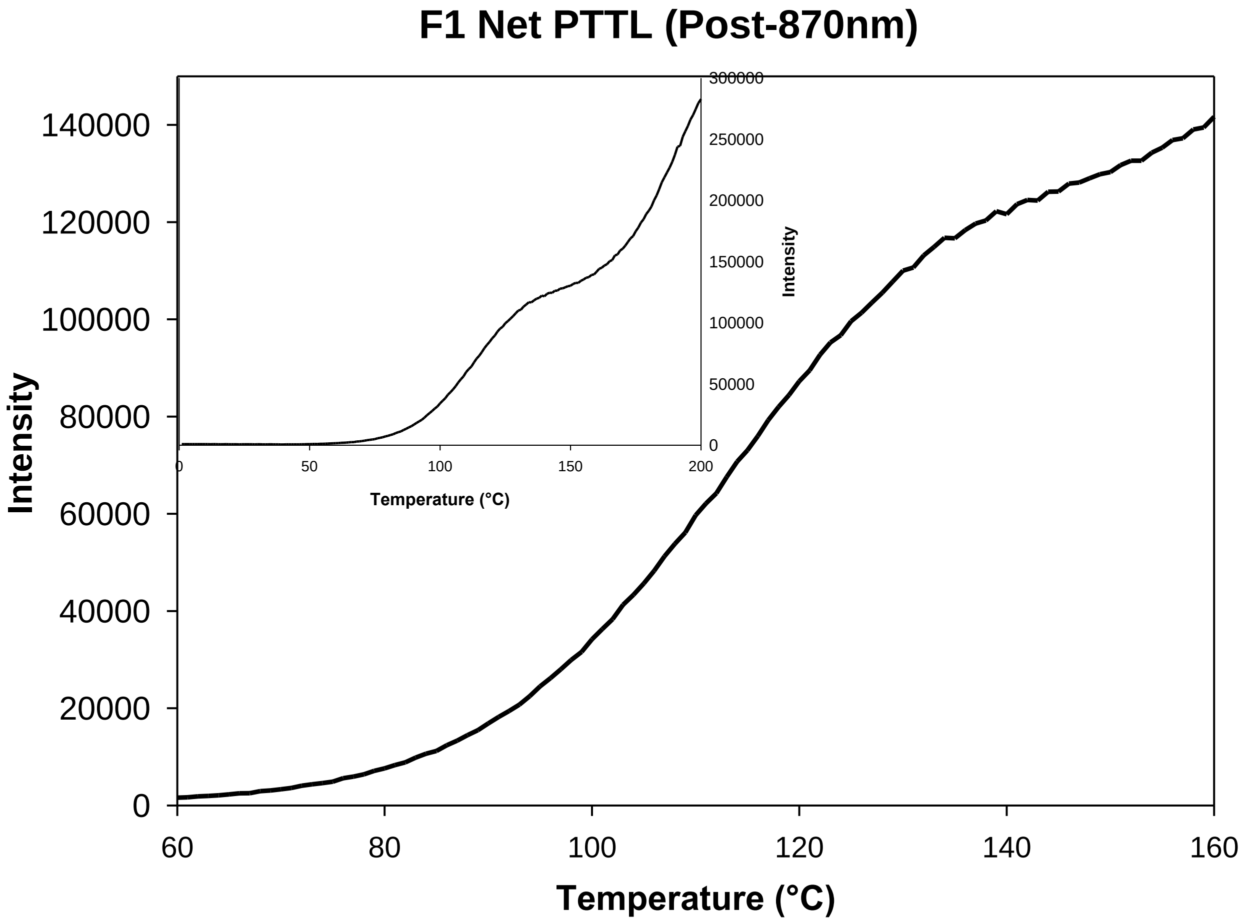

Figure 4.72 – The net counts recorded using the Risø 3 reader for aliquot B of the sample F1. A PTTL shoulder at ~125°C is apparent, with a rise towards it starting at ~70°C. The major plot shows the PTTL peak in more detail, the inset plot shows the complete TL ramp up to 200°C.

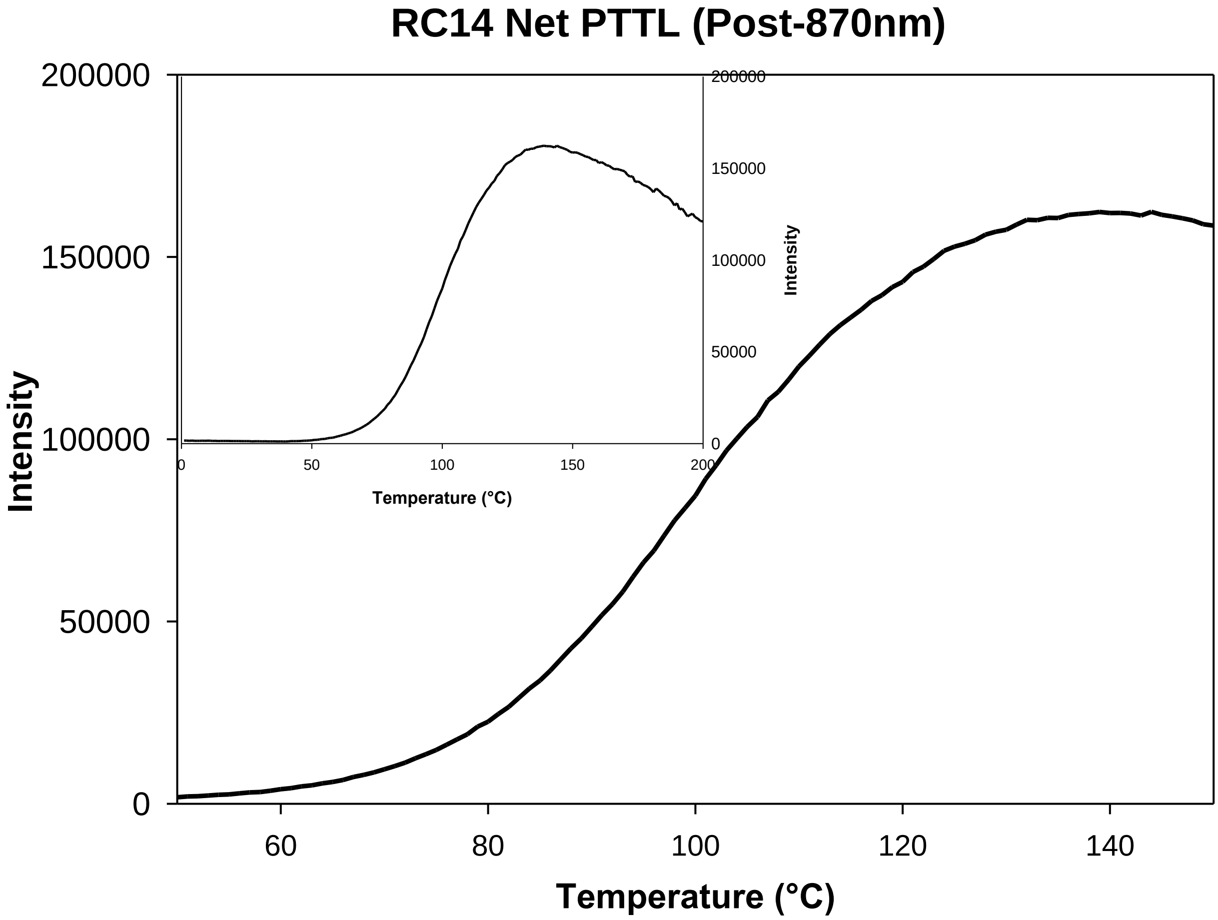

Figure 4.73 – The net counts recorded using the Risø 3 reader for aliquot A of the sample RC14. A PTTL peak at ~135°C is apparent, with a rise towards it starting at ~60°C. The major plot shows the PTTL peak in more detail, the inset plot shows the complete TL ramp up to 200°C.

Figure 4.74 shows a net PTTL curve for RC165 recorded on the Risø 3 reader. The activation energies obtained for the PTTL peaks for the TL ramps conducted on the Risø 3 reader are 0.90±0.05eV and 0.88±0.05eV. These values are within a standard error of each other, suggesting that the approximate value of the activation energy for the PTTL recombination centres at this elevated stimulation temperature is likely somewhere within these values.

Figure 4.75 shows a net PTTL curve for RC484 recorded on the Risø 3 reader. The activation energy obtained for the PTTL shoulder for the TL ramp conducted on the Risø 3 reader is 0.74±0.06eV. This shoulder was similar to that seen in the Risø 1 plots, however due to the thermal lag both of appeared as shoulders rather than the defined peaks seen in the SUERC TL plots.

Another K-Feldspar sample, RC456 had activation energies obtained for the PTTL shoulder for the TL ramp conducted on the Risø 3 reader with values of 0.82±0.07eV and 0.82±0.05eV. Disregarding decimal values which fall into error range, the values for the activation energy of the PTTL recombination centre for this sample had identical values for both TL ramps, indicating that is close to, if not equal to, the true activation energy of this centre for this stimulation temperature.

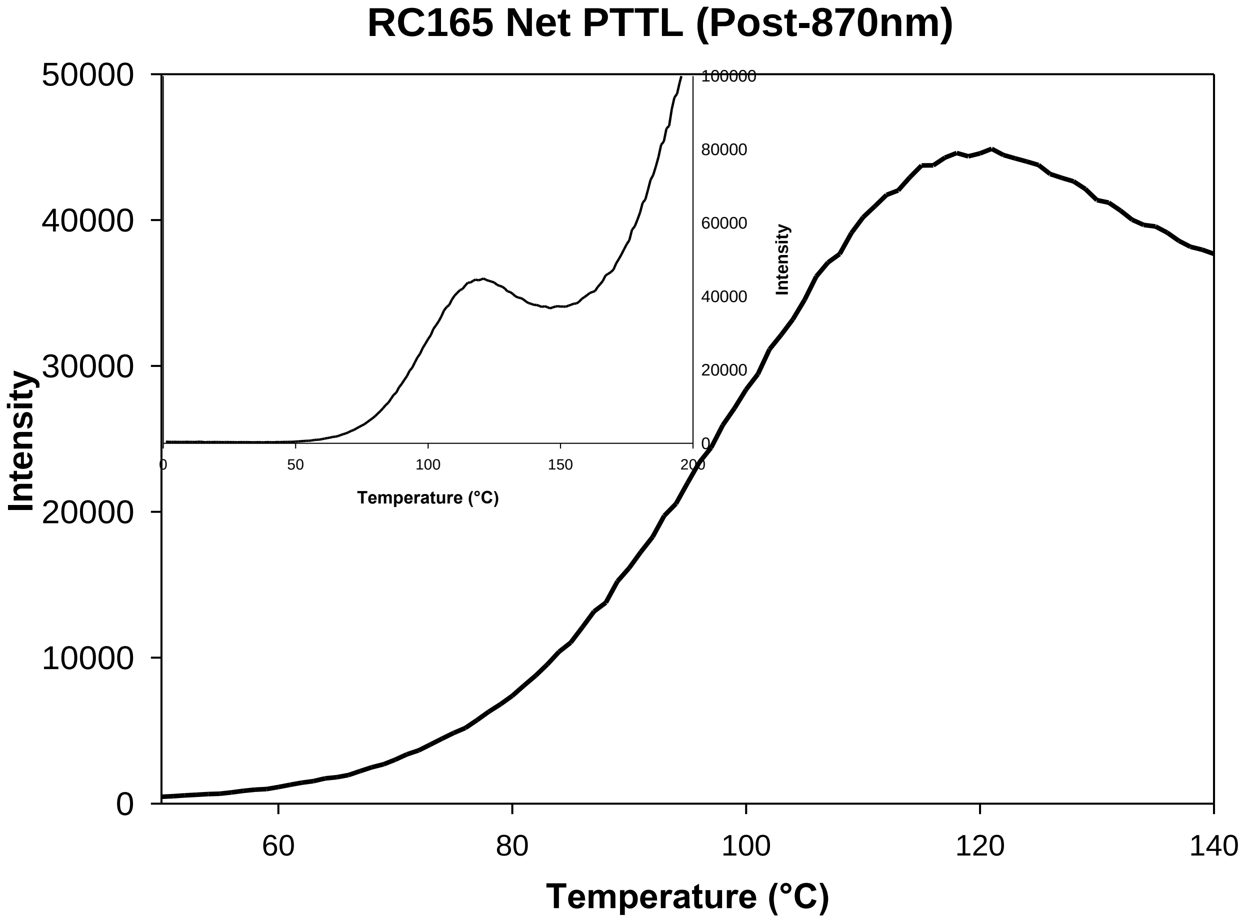

Figure 4.74 – The net counts recorded using the Risø 3 reader for aliquot A of the sample RC165. A PTTL peak at ~120°C is apparent, with a rise towards it starting at ~60°C. The major plot shows the PTTL peak in more detail, the inset plot shows the complete TL ramp up to 200°C.

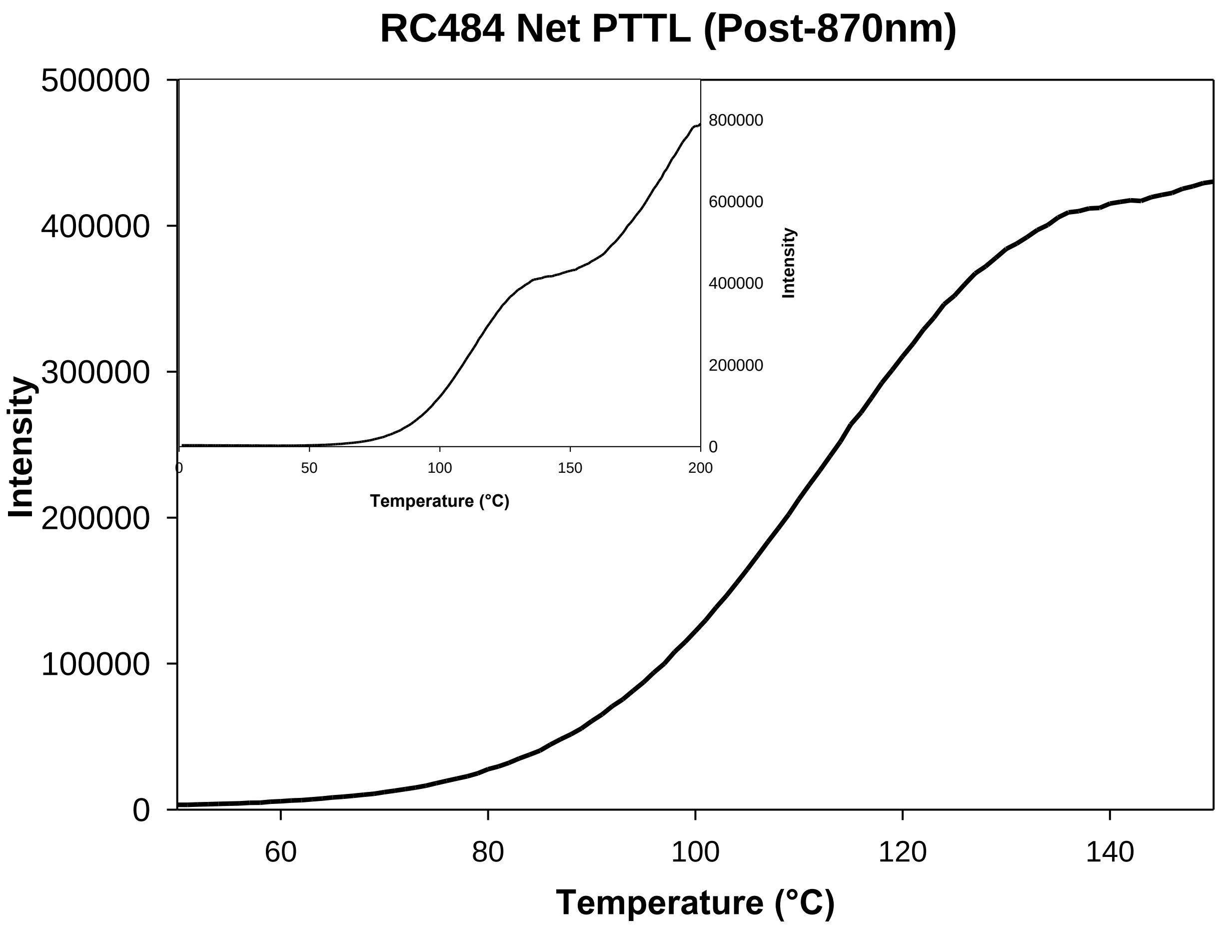

Figure 4.75 – The net counts recorded using the Risø 3 reader for aliquot A of the sample RC484. A PTTL shoulder at ~135°C is apparent, with a rise towards it starting at ~70°C. The major plot shows the PTTL peak in more detail, the inset plot shows the complete TL ramp up to 200°C.

Figure 4.76 shows a net PTTL curve for RC659 recorded on the Risø 3 reader. The activation energy obtained for the PTTL shoulder for the TL ramp conducted on the Risø 3 reader is 0.88±0.35eV. As can be seen in the figure, the net intensity of this PTTL shoulder is very low, resulting in large errors when computing the activation energy of this recombination centre. A possible cause for this is that at this stimulation temperature the recombination centre responsible for PSP emission is highly unstable and does not have a long lifetime. This is broadly supported by the results of Section 4.2, which showed that RC659 had a rapidly decaying PSP signal at elevated temperatures.

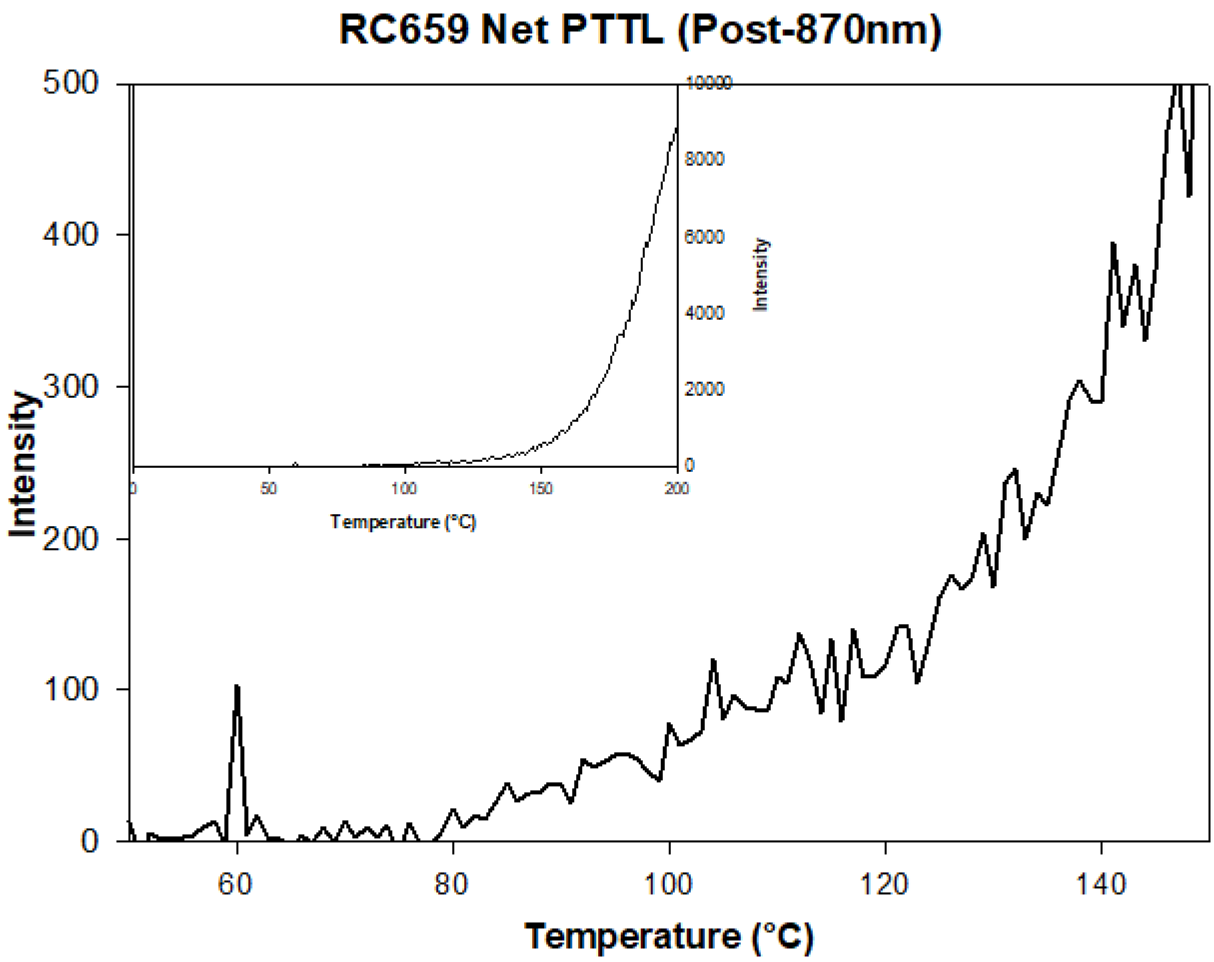

Figure 4.76 – The net counts recorded using the Risø 3 reader for aliquot A of the sample RC659. A slight PTTL shoulder at ~115°C is visible, with a rise towards it starting at ~80°C. The major plot shows the PTTL peak in more detail, the inset plot shows the complete TL ramp up to 200°C.

4.4.4 Discussion

The activation energies obtained from the TL ramps following stimulation with 890nm via the SUERC pIRSL, 830nm via Risø 1, and 870nm via Risø 3 are shown in Figure 4.77. Following a review of the data, several conclusions can be drawn which will be expanded upon in the next section.

There is a mineralogically induced variation in the stability of the recombination centre responsible for PSP, represented by the large uncertainties associated with the samples which showed low intensity net PTTL signals associated with PSP. The plagioclase samples were noted as having the lowest intensities for all three readers. A handful of K-Feldspar samples, which have also been noted in previous sections as having a low IR-response, such as RC1396C, RC456 and RC683B also had low net PTTL signals across all three readers.

There was also a temperature variation noted, with the activation energies obtained from the Risø 3 TL ramps having higher computed values for the recombination sites responsible for the post IR-PSP. In all but a handful of cases, such as the Risø 3b TL ramp for RC389 and the Risø 3a TL ramp for RC169, the values obtained for the activation energies of these sites were 0.2-0.3eV higher than those obtained following stimulation at ambient temperatures. There could be several explanations for this.

The first possible explanation is that the recombination sites following ambient temperature stimulation have been decaying longer by the time the temperature on the TL ramp reaches the peak temperature compared with the TL ramp following IR stimulation at 50°C, resulting in an underestimation in the activation energy.

Another branch of reasoning as to this variation is that the recombination centres exist as a distribution in the lattice of each sample. This would imply that a higher temperature stimulation would disregard the recombination centres with lower activation energies, which would be too unstable to accept any freed charge at the higher temperatures, resulting in a more clearly defined peak or shoulder around the more stable recombination centres.

It is also possible that the slight difference in stimulation wavelength between the three instruments results in the lattice structure of each sample relaxing in slightly different ways following stimulation, creating recombination centres with slightly different decay characteristics and activation energies that would allow for the several standard errors in activation energy variation seen across the measurements.

Of key importance is that the range of activation energies computed for the PTTL peaks observed in this experiment is identical to the range of hypothetical activation energies computed in Section 4.2 in Table 4.6. This similarity could be interpreted as the measured PTTL peaks being the localised electron states responsible for the PSP decays which were observed in Section 4.2.

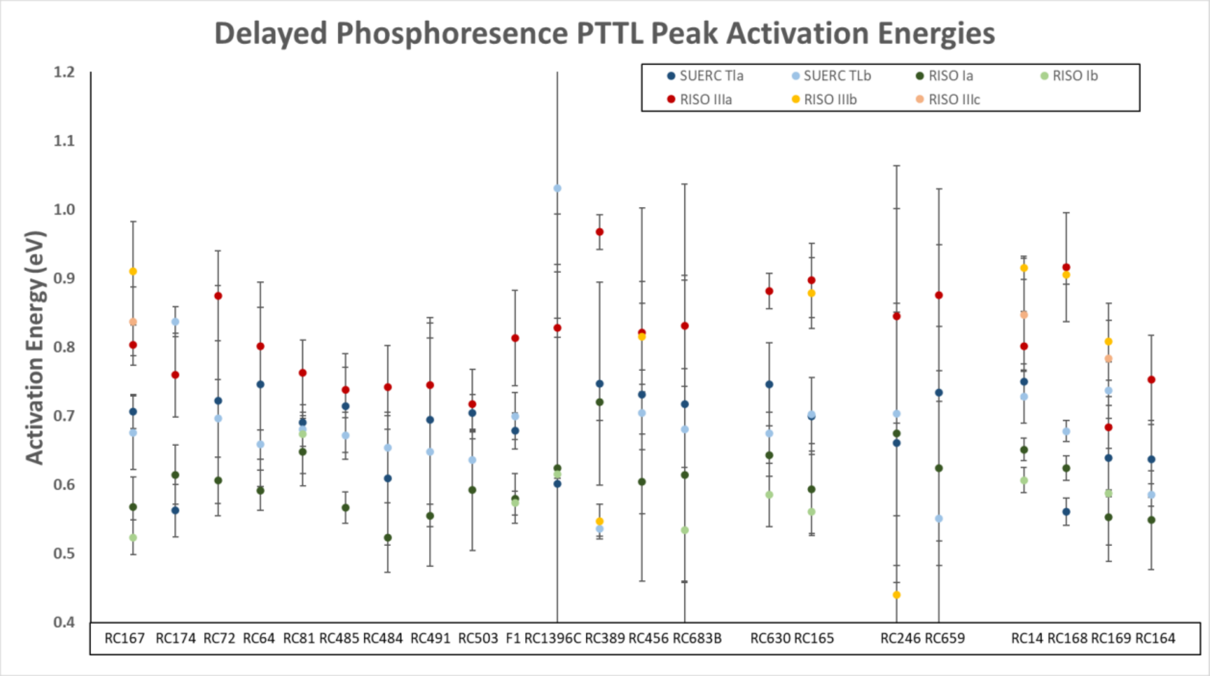

Figure 4.77 – The computed activation energies for each sample for each measurement taken. They are ordered by feldspar mineral sub-family; K-Feldspar, Microcline, Plagioclase, Albite.

The next section will further explore this PTTL data, while considering the results of previous sections, to establish a way of modelling the charge storage environment of the feldspar samples used in this experiment to predict the existence of additional recombination sites which could have shorter decay times than is possible to measure with ambient and elevated temperature stimulation and TL.

5 Modelling and Additional Work

This section will relate the results discussed in the Experimental Outline and Results section to published theory. The results relating to the computed PSP decay lifetimes and PTTL peak activation energies will be used alongside a Python program to examine what these results reveal regarding charge transport and storage through the lattices of feldspars. This will be followed by a limited investigation on predicted cryogenic TL peaks in the feldspar samples used in this investigation.

5.1 Theoretical Implications of Results

The results detailed in Section 4 had several key implications about the nature of charge storage and transport mechanisms within feldspars. One of these implications is that PSP was observed to occur at both second and microsecond timescales, in both cases having decays with multiple components at room temperature that ranged across six orders of magnitude. It should be stated that for a single first order trap the curve should be exponential in nature and thus the log plots should be linear, a factor which is obviously not the case as shown in Section 4.3. This result echoes the findings detailed in an earlier study which reported the observation of multiple components in the post-IR phosphorescence decays of orthoclase feldspars across different timescales (Ankjærgaard and Jain, 2010).

However, this earlier study conducted its investigation using only a single aliquot of orthoclase feldspar and did not calculate the net counts for each measurement before normalising. This may have resulted in a greater background count rate for the higher temperature measurements than the results reported in this thesis. When directly comparing results between this investigation and the Ankjærgaard and Jain paper, the difference in preheat temperatures used may cause a discrepancy as Ankjærgaard and Jain used preheat temperatures from 270-410°C, whereas the work described in this thesis used preheat temperatures of 100°C for the PSP and PTTL investigations and 130°C for the time-resolved investigation. This variance would result in differences in the charge population of the IRSL traps, as well as the band-tail states. The common result of multiple decay components, however, is a strong result and indicates that charge movement through the band-tail states following stimulation while the lattice relaxes is not strongly affected by the preheat temperature is more strongly related to the stimulation temperature and the stimulation wavelength.

An investigation described in Alexander (2007) also noted post-IR PSP at sub-second timescales. That investigation used MCS dwell times of 200ns and IR stimulation times of 1µs, which are an order of magnitude smaller than the time-resolved work detailed in Section 4. Alexander used a similar preheat temperature as that described in Section 4, 135°C, but had a much longer preheat time of 16 hours, as opposed to the 2 minutes used during the TR investigation. This was undertaken to stabilise the longer decay time components and yielded mixed results. Regardless, the observation of multiple decay time components in Alexander (2007) for the aliquots of F1 used strongly agree with the results described in Section 4.

Separate microsecond order post-stimulation decay components were also noted in Tsukamoto et al (2010) and Sanderson and Clark (1994) following blue stimulation of K-Feldspar at various temperatures using microsecond order stimulation.

The results explored in Section 4 also consistently indicate that post-IRSL PSP decay component lifetimes are affected by variations in stimulation temperature. The effect of stimulation temperature on the IRSL or OSL emission is documented in the literature (Schmidt et al. 2011). These results provide clear evidence that the post-IR decay components are thermally unstable, and decay lifetimes have clear temperature dependences. This result is echoed in the literature, as studies such as Clark, 1992 noted that the infra-red component of the excitation spectrum is thermally less stable than other components such as the green or blue. Murray et al. (2009) also noted that the IR signal and post-IR PTTL signal were detectably reduced by a low temperature preheat and indicated that this result was indicative of a distribution of IR sensitive traps. Further, while the specific trap defect responsible for IRSL has not been determined, the Fe^{3+} site substituting for Al^{3+} within the lattice is broadly attributed as the driving defect responsible for “deep” red emission that is seen in IRSL and post-IR TL. This defect has been reported as being thermally unstable with regards to charge emission (Kumar et al. 2018; Riedesel, 2020; Riedesel et al. 2021).

A key result of note from Section 4 is that post-IRSL PSP decays can be probed by TL, with the range of the calculated activation energies of the PTTL peaks being identical to the range of possible activation energies computed from PSP decay component lifetimes. Within the literature there was a consideration given in Qin et al. (2015) (which examined PTTL signals at higher temperatures in K-Feldspars and compared them with post-IR IRSL measurements) that the PTTL process was a considerable factor in post-IR signals even at elevated temperatures.

A related result was noted in Section 4 that suggests that the measured activation energies of the PTTL peaks showed a subtle variation with stimulation temperature. If the trapping sites responsible for the IR and post-IR PTTL signals, as well as the band-tail states, are best described by a model which characterises charge storage sites as a continuum then it should be possible to “peel” away these storage sites through a process of stimulating samples and measuring TL ramps at higher and higher temperatures (Sanderson et al. 1988). While the work described in this thesis did not attempt a thorough study of this phenomenon, the difference noted between the ambient temperature stimulations followed by TL with the IR50 followed by TL does indicate that this should be possible to do with these samples.

This behaviour is not to be expected if the infra-red stimulation peak is totally thermally assisted, and these assisted components could be due to the presence of shallow trapped charge carriers with a thermal lifetime at room temperature of a few days (Clark, 1992; Sakurai and Gartia, 1997). If the PSP decay components computed in Section 4 represent the lifetimes of various PTTL traps, then this suggests that there exists a close association of trap and emission components (Townsend et al. 2021).

This would imply that the existence of multiple decay exponents indicates the existence of multiple PTTL peaks. As such, it should be possible to deconvolve these PTTL peaks to their component parts (Kirsh et al. 1987).

5.2 Deconvolving PTTL Peaks

Peaks observed in Section 4 were not of a uniform shape across the sample set despite a constant experimental procedure. This is expected as the glow peak should be built up from component glow peaks which have maxima at different temperatures corresponding to different values (Randall and Wilkins, 1945b; Horowitz and Yossian, 1995). Most peaks which were observed were complex in shape. A python program derived from a peak deconvolution program detailed by Pagonis (2022) was developed and was used to deconvolve these PTTL peaks to characterise each of their lifetimes, frequency factors and activation energies. Appendix E contains the python code used for this analysis.

To determine if multiple peaks were necessary to describe the PTTL curves which were measured, an initial attempt was made to describe these curves using a single TL peak with an activation energy which was computed using an Arrhenius plot of the net-TL counts from the TL ramp. Figure 5.1 shows the resulting output of mapping the TL peak corresponding to the activation energy obtained from the Arrhenius plot for RC64 on the Risø 3 TL reader which was plotted in Section 4. The plotted TL peak does not describe the obtained TL glow curve with any degree of accuracy, as such it was clear that to properly describe this TL glow curve it will need to be deconvolved to find the number of component curves.

The python program detailed in Appendix E was then used to deconvolve the Risø 3 TL data for RC64. The program works by importing the TL data and then sequentially fitting more TL peaks with a given frequency factor and activation energy, allowing a pre-set variance in these values (within an order of magnitude of the given value), with a sum trendline being plotted for each, until five combinations of TL peaks were fitted against the data. These trendlines were then evaluated with a Figure of Merit Score (FOMS) to determine their accuracy, with the value closest to zero judged to be the most accurate fit.

Figure 5.2 contains the results of this program using the same TL data for RC64 which was used in Figure 5.1. The program returned that the best fits for the measured net PTTL peaks were obtained using 4 or 5 composite TL peaks. However, given that the plots for two of the five peaks were virtually identical with no real increase in the accuracy of the plot, the best fit was determined to be the result of 4 composite peaks. This result reinforces the supposition made for this section, with a strong implication that the PTTL peak which was measured represents a complex system with multiple components.

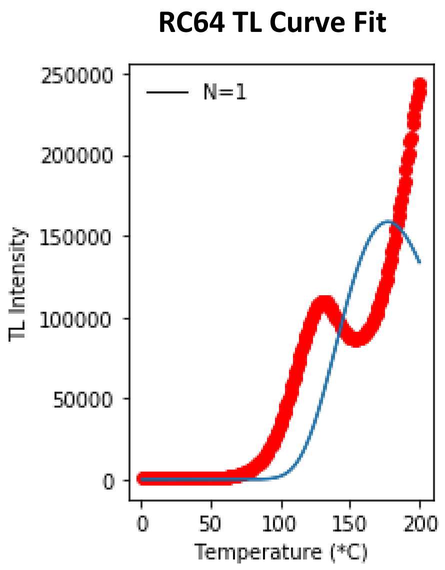

Figure 5.1 – Figure shows a PTTL peak obtained from RC64 on the Risø 3 TL data. The red plot are the measured counts and the blue line is a computation of the TL peak corresponding to the activation energy obtained from the measured data (0.8018±0.0565)eV.

Additional PTTL peaks were examined in this manner in order to determine if expressing these PTTL peaks as complex mechanisms with component peaks was the most accurate representation of the data. Figure 5.3 shows the plots obtained by analysing the F1 SUERC TL data with the python program and Figure 5.4 shows the plots obtained by analysing the SUERC TL data for RC165.

In the case of the F1 glow curve, the PTTL peak is best described with the inclusion of 4-5 component peaks, with a slightly increased accuracy for the 5 component peaks plot. Curiously, both of these plots imply the existence of a component peak which is low temperature (peak temperature of less than 100°C). The separated nature of these components, when compared to the peaks seen in the deconvolved plot for RC64 in Figure 5.2 would imply that it should be possible to "peel" away these component peaks with a carefully heating and stimulation regime in a separate experiment. This conceptual experiment unfortunately fell outside the experimental time constraints of this thesis but an expansion of this idea is discussed further in Section 6.

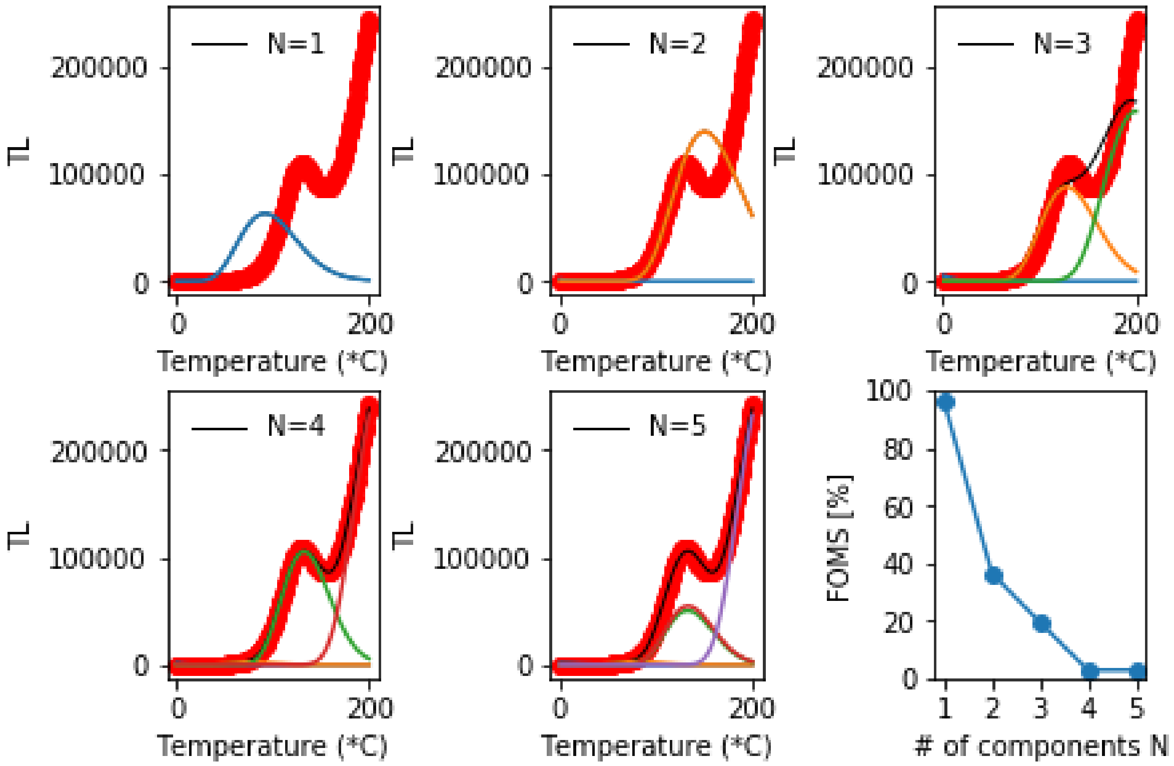

Figure 5.2 – A summary of the deconvoluted TL peaks evaluated for the RC64 Risø 3 TL data. Blue represents a TL peak of activation energy 0.6eV, orange represents a TL peak of activation energy 0.7eV, green represents a TL peak of activation energy 0.8eV, red represents a TL peak of activation energy 0.9eV, and purple represents a TL peak of activation energy 1eV. The given frequency factor was of the order of x10^{11}. The black trendline is the sum of the deconvoluted peaks. The FOMS for each plot in order from N=1 to N=5 are 96.30, 36.40, 19.39, 2.79, 2.79.

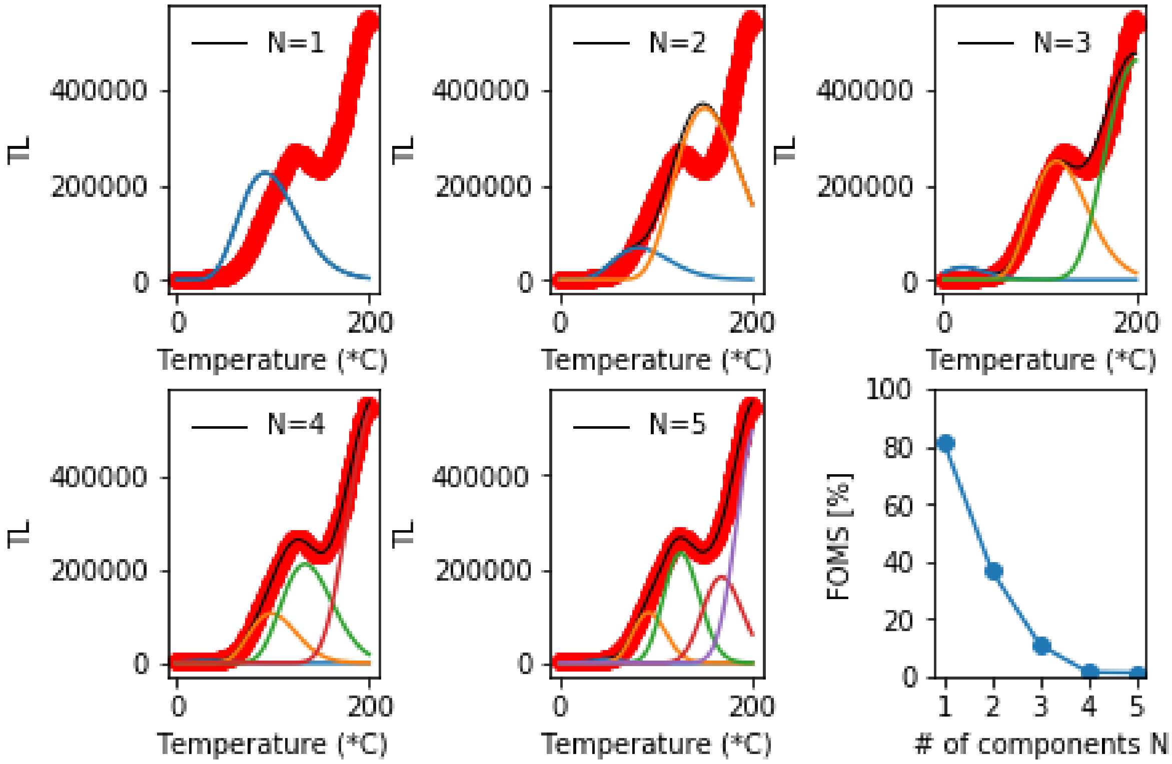

Figure 5.3 – A summary of the deconvoluted TL peaks evaluated for the F1 SUERC TL reader data. Blue represents a TL peak of activation energy 0.6eV, orange represents a TL peak of activation energy 0.7eV, green represents a TL peak of activation energy 0.8eV, red represents a TL peak of activation energy 0.9eV, and purple represents a TL peak of activation energy 1eV. The given frequency factor was of the order of x10^{11}. The black trendline is the sum of the deconvoluted peaks. The FOMS for each plot in order from N=1 to N=5 are 81.36, 36.61, 10.95, 1.42, 1.20.

The component peaks seen in Figure 5.4 assign the best FOMS to the 5 component peaks plot, with the trendline clearly following the measured TL plots and the component peaks having a distinguishable peak temperature variance. Similar to the previous discussion regarding the deconvolved peaks for the SUERC TL data for F1, this result implies the existence of peaks with lower activation energies and temperatures than this experiment could reasonably detect.

This is particularly the case when the lifetimes of these peaks are considered, as high frequency factor peaks with lower activation energies will rapidly decay even at room temperature. These charge storage sites have lifetimes which are comparable to the shortest living PSP decay components which were measured at second order. Since the results of Section 4 demonstrated a clear relationship between PSP and PTTL, it may be appropriate to consider the lifetimes of these unstable states to be analogous to the various lifetimes which were computed for the post-IRSL PSP decays.

This assumption would give the sites corresponding to the PTTL peaks approximate lifetimes of up to 2.0s at room temperature, as lifetimes above this would have been measured and included in the PTTL peaks. While this is a broad range of lifetimes it is helpful for estimating the likelihood of designing an experiment to detect these low energy (0.6eV) PTTL peaks by allowing the limiting of both frequency factor values and peak temperatures.

As such, to investigate these thermally unstable peaks it is necessary to conduct a PTTL investigation at cryogenic temperatures. This will allow the possibility of detecting charge storage sites following IRSL from sites which would normally have decayed before measurement could occur.

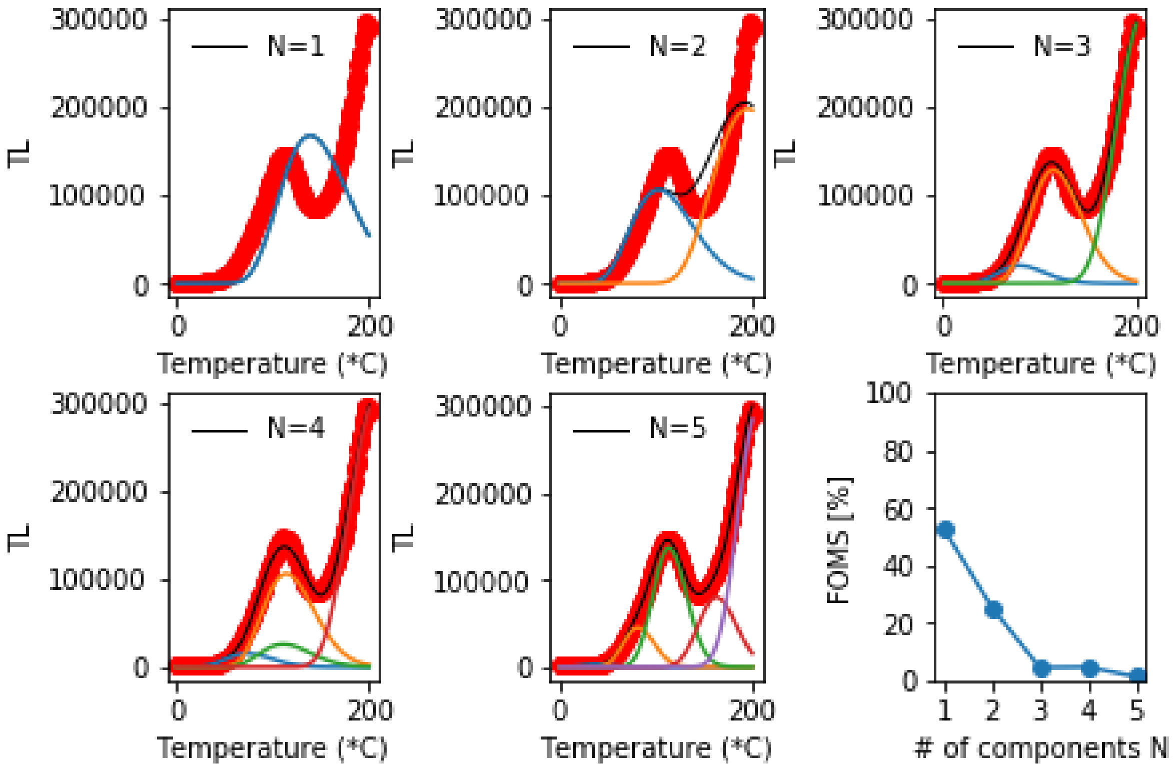

Figure 5.4 – A summary of the deconvoluted TL peaks evaluated for the RC165 SUERC TL reader data. Blue represents a TL peak of activation energy 0.7eV, orange represents a TL peak of activation energy 0.8eV, green represents a TL peak of activation energy 0.9eV, red represents a TL peak of activation energy 1.0eV, and purple represents a TL peak of activation energy 1.1eV. The given frequency factor was of the order of x10^{11}. The black trendline is the sum of the deconvoluted peaks. The FOMS for each plot in order from N=1 to N=5 are 52.54, 25.29, 4.42, 4.57, 1.27.

5.3 Cryogenic PTTL Investigation

Having determined that the observed PTTL peaks consisted of multiple component TL peaks with varying activation energies, a comparison with the PSP decays at second, and sub-second, order timescales noted a similar variation in lifetimes of the decay components. If these components which are shorter lived (with lifetimes of microseconds or less) at room temperature are related to a TL peak(s) which is unstable and rapidly decays at room temperature, then it should be possible to stimulate samples and measure this TL peak at lower temperatures to attain an activation energy.

To this end, an experiment was conducted using the first TR system as a combined IR source and TL reader using the SUERC TL software package on the control computer and a manually timed IR-stimulation.

This follow-up experimental investigation used one aliquot from 13 of the 22 feldspar samples described in Section 4.1, taking at least two samples from each of the feldspar families. The samples were given a 1kGy dose and left overnight to remove any post-irradiation phosphorescence.

The measurement cycle itself consisted of a TL ramp up to 215°C at 1°C/s followed by cooling the sample down to as close to -100°C as possible, which typically varied from -92°C to -98°C as a result of either poor thermal contact or a flow rate issue related to the tube connection between the liquid nitrogen cooled coils and the sample chamber. The samples were then stimulated for five minutes with 890nm diodes once the temperature had stabilised. The heating cycle of the TL ramp was then started during the last three seconds of stimulation in order to minimise the delay between stimulation and PTTL measurement as much as possible. The flow rate of the cooled nitrogen gas into the chamber was manually cut after the thermocouple reading returned a temperature of ~-10°C. This TL ramp was a heating to 215°C before being cooled to a sample temperature close to -100°C and heated again to attain a net TL signal.

The heating rate was adjusted from 5°C/s to 1°C/s for this experiment as preliminary tests found that sputtering occurring when the cooled nitrogen gas interacted with the heater plate. This effect caused two simultaneous phenomena: the occurrence of microphonic induced spurious count recordings by the photomultiplier, and an inconsistent heating rate when the sample was between -80°C and -25°C, which was also the temperature of interest for this investigation. Reducing the heating rate broadly solved this issue, however occasional microphonic induced noise did still occur.

Activation energies were then computed with an Arrhenius plot using the same process described in Section 4.

5.3.1 Cryogenic PTTL Results

The results of this cryogenic investigation will be discussed by feldspar mineral group, as there was a noted variance in the results which may be mineralogically related. Of the 13 samples investigated, 8 samples had detectable PTTL peaks at cryogenic temperatures which could be used to estimate an activation energy with meaningful uncertainties.

Four albite samples were investigated as part of this follow-on experiment: RC14, RC168, RC169, and RC164. Figure 5.6 shows the net PTTL peak obtained following stimulation at cryogenic temperatures for RC14. The activation energy for this peak of this peak was computed to be (0.33±0.040)eV with a frequency factor of the order $10^9 s^{-1}$, giving an approximate trap lifetime of 8 seconds at -100°C and sub-second lifetimes at room temperature (0.1ms). While, at room temperature, this particular peak does not correspond to the PSP decay component which acted on the order of seconds, it is equivalent to the longest-lived component for the room temperature time-resolved decays recorded for RC14 (which also had decay lifetimes of ~0.1ms).

The activation energies obtained for the remaining albite samples were (0.26±0.07)eV for RC168, (0.32±0.03)eV for RC169, and (0.22±0.06)eV for RC164, with lifetimes at room temperature which were approximately equal to the lifetime computed for the RC14 cryogenic PTTL peak (~0.1ms). Of the samples used in this investigation, the albite samples had the largest TL signal intensities at cryogenic temperatures, with PTTL peaks above 1000 counts, allowing easier detection of these PTTL peaks, as well as lower activation energy errors due to a higher signal-to-noise ratio.

Of the plagioclase samples, only RC246 produced any detectable PTTL peak at cryogenic temperatures. This peak was dominated by system noise because of slight microphonics interference with the measurement during heating, resulting in a PTTL peak which was difficult to properly characterise for activation energy computation. Through manual removal of the microphonic interference from the TL data, an activation energy of (0.14±0.09)eV was calculated for this sample with a frequency factor of the order $10^9 s^{-1}$. While this result is within two standard errors of the activation energies calculated for the four albite samples, it is likely that this PTTL peak is too unstable for measurement following stimulation, even at cryogenic temperatures.

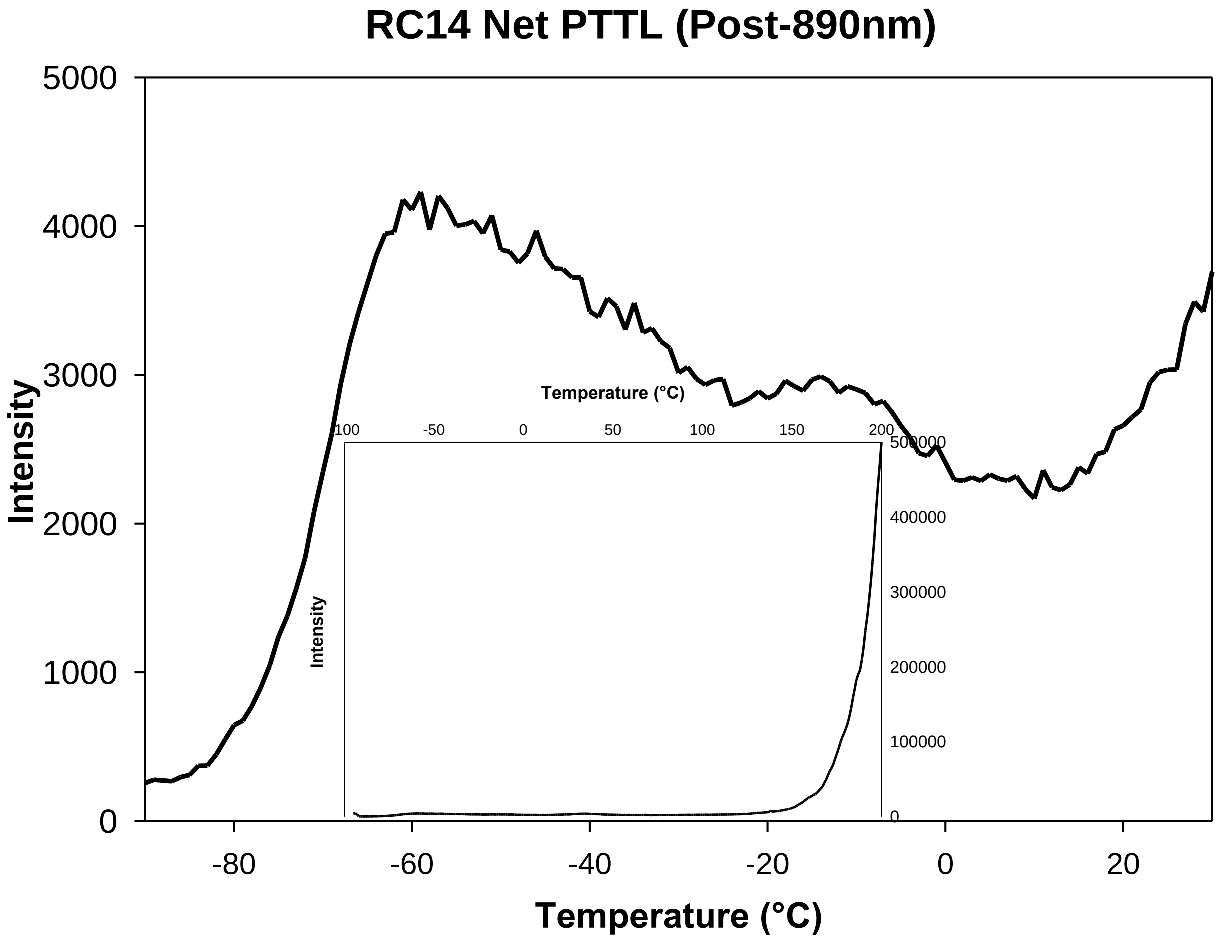

Figure 5.6 – The net TL data obtained from RC14 following stimulation at cryogenic temperatures. The sub-plot contains the complete net-TL glow curve. A TL peak at ~-60°C is apparent, as well as a further shoulder at ~-20°C.

Both microcline samples, RC165 and RC630 gave small measurable PTTL peaks. Figure 5.7 shows the small PTTL peak recorded for RC630, the recorded counts for this peak are an order of magnitude less than the PTTL peaks observed in the albite samples. This PTTL peak for RC165 was of a similar intensity, resulting in computed activation energies that had higher proportional uncertainties. The activation energies calculated for RC165 and RC630 were (0.16±0.10)eV and (0.17±0.07)eV, respectively, with both peaks having frequency factors of the order $10^9 s^{-1}$, while these activation energies are comparable to the activation energy calculated for RC246.

Five K-Feldspar samples were used for this follow-on experiment: F1, RC81, RC167, RC683B and RC1396C. While these samples had a response to IRSL at cryogenic temperatures, only RC81 had any measurable PTTL signal above instrument background. Figure 5.8 shows the glow curve for RC81, including the small PTTL peak which was observed during heating. The activation energy for this PTTL peak was computed to be (0.16±0.13)eV and a frequency factor of the order $10^9 s^{-1}$, with the high uncertainty being the result of the low intensity of the peak, as can be seen from the graph with most channels recording <100 net-counts during the TL ramp and reheat.

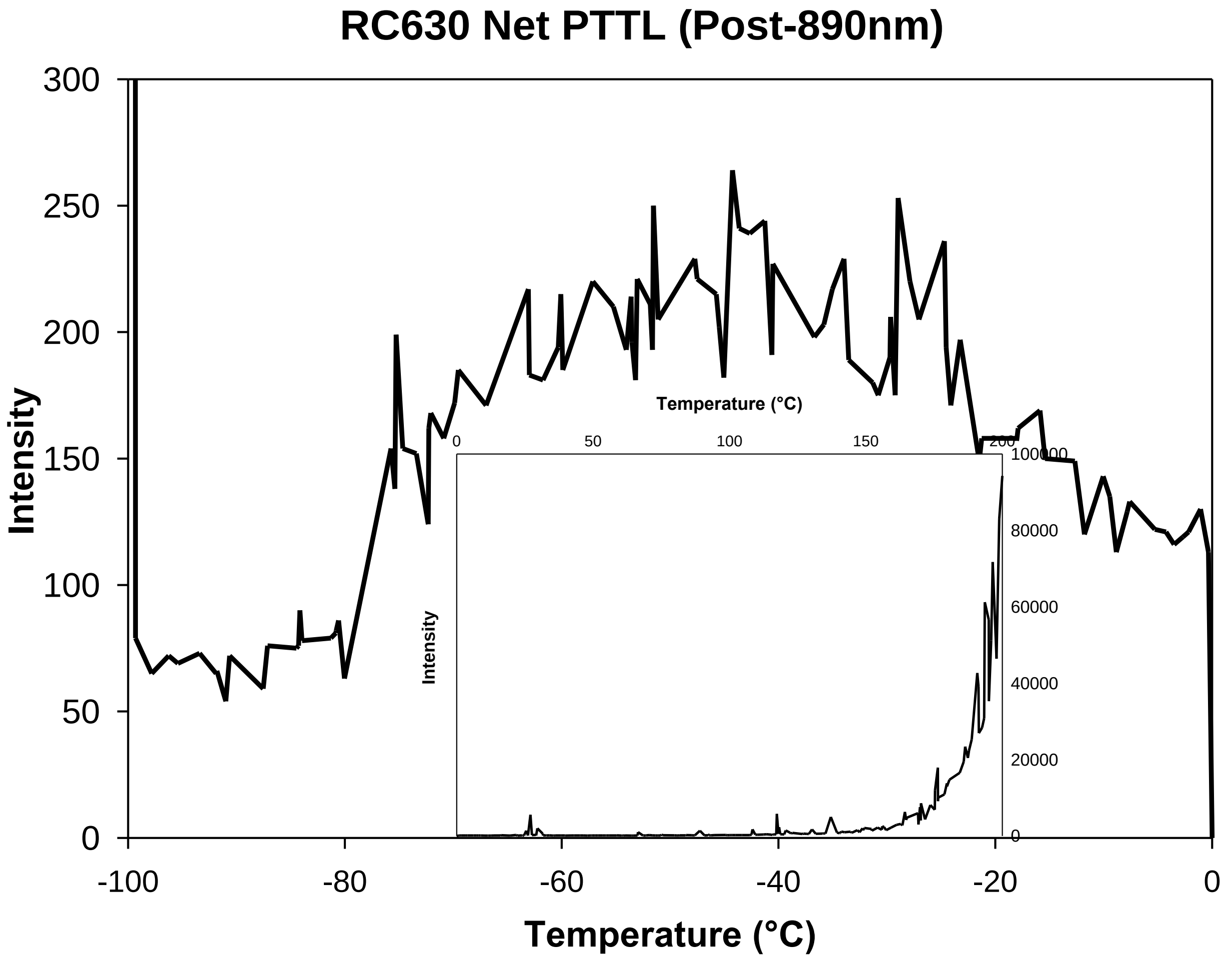

Figure 5.7 – The net TL data obtained from RC630 following stimulation at cryogenic temperatures. The sub-plot contains the complete net-TL glow curve. A TL peak at ~-50°C is apparent.

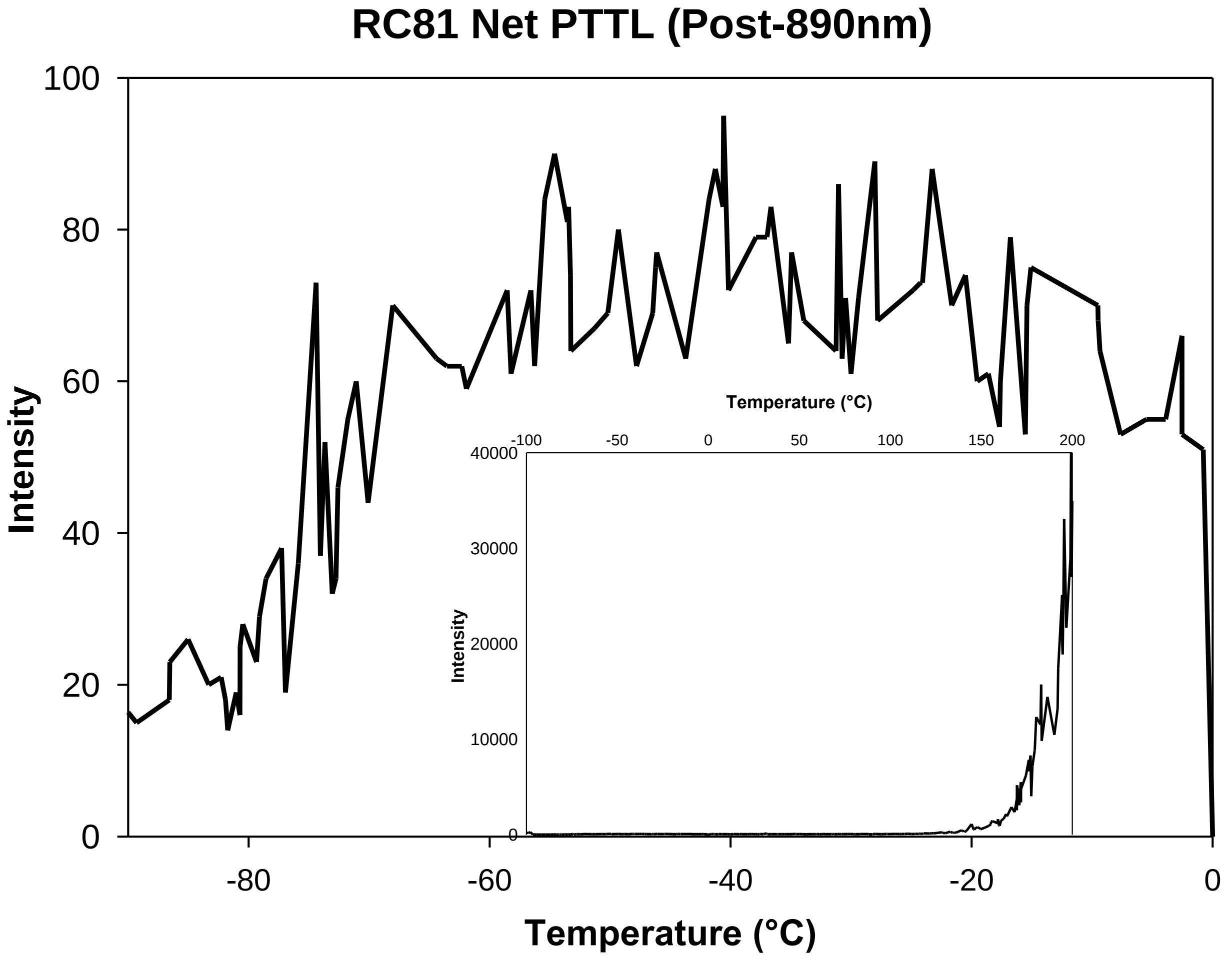

Figure 5.8 – The net TL data obtained from RC81 following stimulation at cryogenic temperatures. The sub-plot contains the complete net-TL glow curve. A small TL peak at ~-40°C is visible.

It should be noted that even at temperatures of -100°C, TL peaks with activation energies less than 0.2eV and frequency factors of the order 10^9s^{-1} should only have lifetimes on the order of milliseconds and so would have completely decayed by the time the TL ramp begins. As such, the PTTL peaks being measured do not have enough signal from the current experimental set-up to allow the rising edge to be accurately mapped to an Arrhenius plot and allow the calculation of more accurate PTTL activation energies.

While the physical characterisation of the observed cryogenic PTTL peaks could be improved through adjustments of the parameters of the experiment, the observation of clear TL peaks at cryogenic temperatures for the albite samples is the first time the phenomenon of cryogenic PTTL following IRSL is believed to have been reported in feldspars.

As can be seen in Figure 5.9, the activation energies obtained for these cryogenic PTTL peaks measured after cryogenic IRSL are distinct from the PTTL peaks which were observed following IRSL at room temperature and 50°C. This result is a strong indicator of a complex charge transport and storage mechanism which is temperature dependent, as well as possibly being mineralogically driven, which cannot be described by simple single trap models or by athermal tunnelling processes.

Fundamentally, the range of PTTL activation energies calculated for this experiment are identical to those estimated in Table 4.14 in Section 4.3. This strongly implies that these PTTL peaks are related to PSP decays of microsecond order.

This novel discovery is the direct result of using post-IR phenomena such as PSP and PTTL to model charge transport and storage within a range of feldspars.

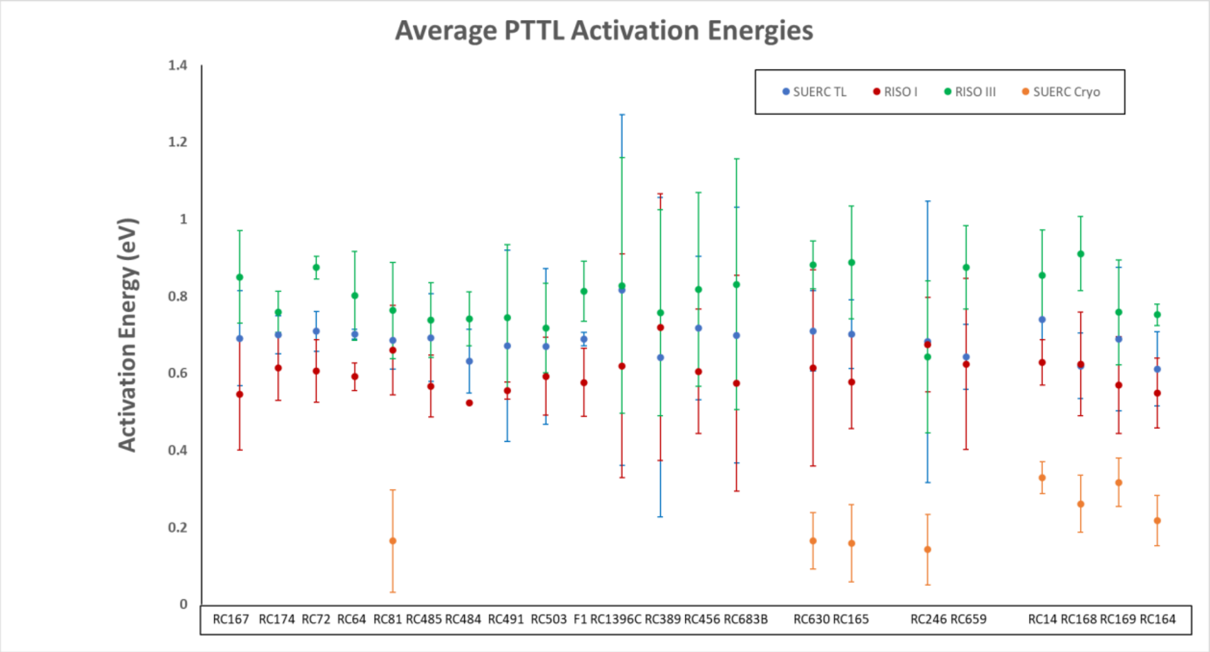

Figure 5.9 – The distribution of the computed activation energies (activation energies were averaged for the samples with more than one experimental run) of the cryogenic PTTL peaks when compared to the average TL peaks of the ambient and elevated PTTL peaks.

6 Conclusions and Future Work

6.1 Conclusions

The work described in this thesis outlines four separate investigations using 22 feldspar samples from four distinct feldspar families (including K-Feldspar, Albite, Plagioclase and Microcline samples as well as the F1 IAEA standard material) for the purposes of examining how post-IRSL phenomena can be used to describe charge storage and transportation within the material lattice of feldspars.

The investigations included the measurement of post-IR PSP at different temperatures, timescales and following different stimulation wavelengths to determine the variability in the observed phosphorescence decay lifetimes across the sample set. Post-IR PTTL was also recorded at different temperatures and following different stimulation wavelengths to determine if the states responsible for the PSP decay could be measured to characterise any variability.

The mineralogical differences in the decay components calculated in Sections 4.2 and 4.3 point to complex lattice-driven factors which are interacting with the band-tail states as the lattice relaxes following stimulation. This behaviour is in stark contrast with simple single trap models which explain any observed decay as occurring through nearest neighbour tunnelling. This tunnelling interaction does not account for the orders of magnitude difference that is observed in decay component lifetimes across the sample set. This variation is more easily explained by a model which includes a distribution of band-tail state pathways that vary, if not from sample to sample, then by mineral family to mineral family within feldspars.

PSP decay lifetimes were recorded from microsecond to minute order with noted variances with the same sample as a result of changes to the stimulation wavelength and temperature. This is an indication that the thermal assistance afforded by the increased temperature allows the use of different recombination pathways during relaxation. The observation that proportionally more PSP was emitted following 940nm stimulation than 890nm stimulation suggests that the processes responsible for post-IRSL emission in feldspars may be wavelength energy determinant, with a higher energy (shorter wavelength) resulting in more detected signal during stimulation, but proportionally lower detected counts during the following period of isothermal phosphorescence decay. This behaviour indicates that for most of the feldspar samples investigated over the course of this work, charge transport is dominated by thermally driven mechanisms which transport charge from clusters of traps following stimulation through band-tail states to the recombination centres (eg García-Guinea et al. 2003), not by athermal processes such as tunnelling (eg Andersen et al. 2012).

This observation of normalised PSP behaviour reported in 4.2 and 4.3 is compatible with those of Guérin and Visocekas (2015) who reported that charge transport within volcanic feldspar lattices can be described by a combination of thermally driven mechanisms which can operate alongside athermal mechanisms, with the dominance of each mechanism being temperature dependent.

PTTL peaks were also measured and computed to have activation energies within the ranges of 0.45-1eV, though the tails of this activation energy distribution are dominated by measurements with high uncertainties as most PTTL peaks had activation energies of 0.6-0.9eV. This corresponded to the activation energies predicted using the PSP decay components from second to minute order.

A cryogenic investigation then revealed that these predicted peaks did exist, with activation energies of the range 0.10-0.37eV and corresponding room temperature lifetimes of the order of microseconds – which aligned with the activation energies calculated using the microsecond timescale PSP decay component lifetimes. This is the first known reporting of cryogenic PTTL peaks in feldspars.

The results of this investigation indicate that the predicted activation energies attained using the post-IR PSP decay component lifetimes correspond to the lifetimes of the PTTL peaks.

Feldspars contain complex system of charge transport following stimulation to re-trapping sites which can then be probed by TL. This is not behaviour which can be easily explained with a simple principal trap model, instead indicating that a distribution of trapping systems must exist within the lattice to allow the observed variability in behaviour – particularly when multiple feldspar families are considered.

This result is a clear demonstration that not only can these post-IR phenomena be used to describe the transport and storage of charge within feldspars but that they are indicative of mechanisms which are dominated by thermally driven systems, rather than athermal tunnelling processes. This indicates that charge mobility following IRSL is moved through lattices of feldspars from a complex network of trapping sites via band-tail states towards the recombination centres.

6.2 Future Work

The results detailed in Section 4 and expanded in Section 5 reveal several avenues of future research for the investigation of charge storage and transport within feldspars using IRSL phenomena. Of particular interest are the post-IR effects, such as PSP and PTTL, which allow indirect measurement of charge storage and transport within the lattice of feldspars, to build on the results of this thesis the following steps are proposed.

An exploration of the relationship between the PSP decay lifetimes and the PTTL peak activation energies using temperature varied excitation spectroscopy by using the first TRS system as an excitation spectrometer (as described in Section 3.5), which would allow the relationship between stimulation wavelength and charge recombination mechanisms to be thoroughly explored. This would allow the deconvolution of PSP decay components by evaluating peak wavelengths for each sample individually (Godfrey-Smith and Cada, 1996). The same process could also be repeated using TL to deconvolve the components of the PTTL peaks recorded in Section 4.4 (Kirshi et al. 1987).

The modification of the current time-resolved spectrometer system at SUERC to allow stable cooling to a lower temperature than was achieved in the experiments in Section 5. This would permit further time-resolved measurements at temperatures below -100°C, as well as allowing the measurement of additional PTTL peaks with µs room temperature lifetimes.

Acknowledgements

SF would like to thank the University of Glasgow and SUERC for hosting his MSc research, as well as for allowing access to needed software and apparatus necessary for the completion of this research.

The late Dr. Lorna Carmichael for laboratory work assistance.

Professor David C.W. Sanderson, Dr. Alan J. Cresswell, and Dr. Loic Martin for providing supportive supervisorship throughout this project, all of whom gave great and thoughtful feedback and ideas as well as laboratory assistance.

7 Bibliography

Analog Devices, Monolithic Thermocouple Amplifiers with Cold Junction Compensation, AD594/AD595, 1999

A. Kadereit, S. Kreutzer, “Risø calibration quartz – A challenge for β-source calibration. An applied study with relevance for luminescence dating”, Measurement, Volume 46, Issue 7, pp 2238-2250, 2013

A.G. Wintle, “Anomalous Fading of Thermoluminescence in Mineral Samples”, Nature Vol. 245, pp 143–144, 1973

A.S. Murray, J.P. Buylaert, K.J. Thomsen, M. Jain, “The effect of preheating on the IRSL signal from feldspar”, Radiation Measurements, Volume 44, Issues 5–6, pp 554-559, 2009

A.J.J. Bos, “Theory of thermoluminescence”, Radiation Measurements 41, pp 545 – 556, 2007

A.J.J. Bos, “Thermoluminescence as a Research Tool to Investigate Luminescence Mechanisms”, Materials, 10, 1357, 2017

B. Guralnik, M. Jain, F. Herman, R.B. Paris, T.M. Harrison, A.S. Murray, P.G. Valla, E.J. Rhodes, “Effective closure temperature in leaky and/or saturating thermochronometers”, Earth and Planetary Science Letters, Volume 384, pp 209-218, 2013

B. Guralnik, B. Li, M. Jain, R. Chen, R.B. Paris, A.S. Murray, S.H. Li, V. Pagonis, P.G. Valla, F. Herman, “Radiation-induced growth and isothermal decay of infrared-stimulated luminescence from feldspar”, Radiation Measurements, Volume 81, pp 224-231, 2015

B. Li, S.H. Li, “Luminescence dating of K-feldspar from sediments: A protocol without anomalous fading correction”, Quaternary Geochronology, Volume 6, Issue 5, 2011

B. Li, S.H. Li, “The effect of band-tail states on the thermal stability of the infrared stimulated luminescence from K-feldspar”, Journal of Luminescence, Volume 136, pp 5-10, 2013

C. Ankjærgaard, M. Jain, “Optically stimulated phosphorescence in orthoclase feldspar over the millisecond to second time scale”, Journal of Luminescence, Volume 130, Issue 12, pp 2346-2355, 2010a

C. Ankjærgaard, M. Jain, “Optically stimulated phosphorescence in quartz over the millisecond to second time scale: insights into the role of shallow traps in delaying luminescent recombination”, J. Phys. D: Appl. Phys. 43 255502, 2010b

C. Bouscary, G.E. King, “Luminescence thermochronometry of feldspar minerals: Optimisation of measurement conditions for the derivation of thermal kinetic parameters using isothermal holding experiments”, Quaternary Geochronology, Volume 67, 101240, 2022

C. Schmidt, S. Kreutzer, “Optically stimulated luminescence of amorphous/microcrystalline SiO2 (silex): Basic investigations and potential in archaeological dosimetry”, Quaternary Geochronology, Volume 15, pp 1-10, 2013

D.C.W. Sanderson, “Fading of thermoluminescence in feldspars: characteristics and corrections”, Nucl. Tracks Radiat. Meas., Vol. 14, Nos 1/2, pp. 155-161, 1988

D.C.W. Sanderson, C. Slater, K. Cairns, “Development of Luminescence Tests to Identify Irradiated Foods. Project N384: Project Report 1”, Project Report, Ministry of Agriculture, Fisheries and Food, 1988

D.C.W Sanderson, R.J. Clark, “Pulsed Photostimulated luminescence of alkali feldspars”, Radiation Measurements, Vol. 23. Nos 213. pp. 633-639, 1994

D.C.W. Sanderson, P. Bishop, I. Houston, M. Boonsener, “Luminescence characterisation of quartz-rich cover sands from NE Thailand”, Quaternary Science Reviews 20, pp 893-900, 2001

D.C.W. Sanderson, S. Murphy, “Using simple portable OSL measurements and laboratory characterisation to help understand complex and heterogeneous sediment sequences for luminescence dating”, Quaternary Geochronology, Volume 5, Issues 2–3, pp 299-305, 2010

D.I. Godfrey-Smith, M. Cada, “IR Stimulation spectroscopy of plagioclase and potassium feldspars, and quartz”, Radiation protection Dosimetry, Vol. 66, Nos 1—4, pp. 379-385, 1996

D.J. Huntley, M.R. Baril, S. Haidar, “Tunnelling in plagioclase feldspars”, J. Phys. D: Appl. Phys. 40, pp 900-906, 2007

DTU Nutech, Denmark, “Guide to ‘The Risø TL/OSL Reader’”, 2015

E. Şahiner, G. Kitis, V. Pagonis, N. Meriç, G.S. Polymeris, “Tunnelling recombination in conventional, post-infrared and post-infrared multi-elevated temperature IRSL signals in microcline K-feldspar”, Journal of Luminescence, Volume 188, pp 514-523, 2017

E.D. Schmidt, A.S. Murray, F. Sirocko, S. Tsukamoto, M. Frechen, “IRSL Signals from Maar Lake Sediments Stimulated at Various Temperatures”, E&G Quaternary Sci. J., 60, 8, https://doi.org/10.3285/eg.60.1.07, 2011

E.G. Yukihara, A.C. Coleman, R.H. Biswas, R. Lambert, F. Herman, G.E. King, “Thermoluminescence analysis for particle temperature sensing and thermochronometry: Principles and fundamental challenges”, Radiation Measurements, Volume 120, pp 274-280, 2018

F. Daniels, C.A. Boyd, D.F. Saunders, “Thermoluminescence as a Research Tool,” Science117, pp 343-349, 1953

G. Bonfiglioli, P. Brovetto, and C. Cortese, “Thermoluminescence and F-Centers. I. Theory,” Phys. Rev. 114, pp 951-955, 1959

G. Guérin, R. Visocekas, “Volcanic feldspars anomalous fading: Evidence for two different mechanisms”, Radiation Measurements, Volume 81, pp 218-223, 2015

G. Hütt, I. Jaek, J. Tchonka, “Optical Dating: K-Feldspars optical response stimulation spectra”, Quaternary Science Reviews, Vol. 7, pp. 381-385, 1988

H. Gobrecht and D. Hoffmann, “Spectroscopy of traps by fractional glow technique,” J. Phys. Chem. Solids 27, pp 509-522, (1966)

H. Kim, M. C. Kim, J. Lee, I. Chang, S.K. Lee, J.L. Kim, “Dose re-evaluation in personal dosimetry using the phototransferred thermoluminescence method of LiF:Mg,Cu,Si TLD”, Radiation Measurements, Volume 118, pp 20-25, 2018

H. Young, R.A. Freedman, “University Physics with Modern Physics, 13th Edition (University of Glasgow)” Published by Pearson, 2014. ISBN 978-1-78434-107-7

I.K. Bailiff, S.G.E. Bowman, S.F. Mobbs, M.J. Aitken, “The phototransfer technique and its use in thermoluminescence dating”, Journal of Electrostatics, 3, pp 269-280, 1977

I.K. Bailiff, N.R.J. Poolton, “Studies of charge transfer mechanisms in feldspars,” Nucl. Tracks Radiat. Meas., 18, pp 111-118, 1991

I.K. Bailiff, S.M. Barnett “Characteristics of infrared stimulated luminescence from a feldspar at low temperatures,” Radiat. Meas. 23, pp 541-546, 1994

I.M.C. Anthony, D.C.W. Sanderson, G.T. Cook, D. Abernethy, R.A. Housley, “Dating a burnt mound from Kilmartin, Argyll, Scotland”, Quaternary Science Reviews 20, pp 921-925, 2001

J. Cameron, Radiation Dosimetry, Environmental Health Perspectives Vol.91, pp. 45-48, 1991

J. García-Guinea, V. Correcher, A. Delgado, L. Sanchez-Muñoz, “Cluster linkages between luminescence emission spectra and continuous trap distribution in a volcanic sanidine”, Radiation Measurements, Volume 37, Issues 4–5, pp 473-477, 2003

J. Izewska, G. Rajan, Radiation Dosimeters (PDF). International Atomic Energy Agency. p. 88, 2012

J. Prakash, “Thermoluminescence glow curve involving any extent of retrapping or any order of kinetics”, Pramana journal of physics, Vol. 81, No. 3, pp. 521-533, 2013

J. Qin, J. Chen, J.B. Salisbury, “Photon transferred TL signals from potassium feldspars and their effects on post-IR IRSL measurements”, Journal of Luminescence, Volume 160, pp 339-350, 2015

J.L. Muniz, V. Correcher and A. Delgado, “PTTL Dose re-estimation applied to quality control in TLD-100 based personal dosimetry”, Radiation Protection Dosimetry, Vol. 85, Nos. 1–4, pp 63–66, 1999

J.Q. Spencer, “The Development of Luminescence Methods to Measure Thermal Exposure in Lithic and Ceramic Materials”, PhD Thesis, University of Glasgow, 1996

J.T. Randall, M.H.F. Wilkins, “Phosphorescence and electron traps I. The study of trap distributions”, Royal Society, Volume 184, Issue 999, pp 365–389, 1945a

J.T. Randall, M.H.F. Wilkins, “Phosphorescence and electron traps II. The interpretation of long-period phosphorescence”, Royal Society, Volume 184, Issue 999, pp 390–407, 1945b

K.J. Thomsen, A.S Murray, M. Jain, “Stability of IRSL signals from sedimentary K-Feldspar samples”, Geochronometria 38, pp 1-13, 2011

M. Lamothe, L.F. Brisson, F. Hardy, “Circumvention of anomalous fading in feldspar luminescence dating using Post-Isothermal IRSL”, Quaternary Geochronology, Volume 57, 101062, 2020

M. Jain, C. Ankjærgaard, “Towards a non-fading signal in feldspar: Insight into charge transport and tunnelling from time-resolved optically stimulated luminescence”, Radiation Measurements, Volume 46, Issue 3, pp 292-309, 2011

M. Jain, R. Sohbati, B. Guralnik, A.S. Murray, M. Kook, T. Lapp, A.K. Prasad, K.J. Thomsen, J.P. Buylaert, “Kinetics of infrared stimulated luminescence from feldspars”, Radiation Measurements, Volume 81, pp 242-250, 2015

M.A. Short, “An investigation into the physics of the infrared excited luminescence of irradiated feldspars”, PhD Thesis, Simon Fraser University, 2003

M.L. Chithambo, “The analysis of time-resolved optically stimulated luminescence: II. Computer simulations and experimental results”, J. Phys. D: Appl. Phys. 40 1880, 2007

M.L. Chithambo, P. Niyonzima, J.M. Kalita, “Phototransferred thermoluminescence of synthetic quartz: Analysis of illumination-time response curves”, Journal of Luminescence, Volume 198, pp 146-154, 2018

M.R. Baril, D.J. Huntley, “Infrared stimulated luminescence and phosphorescence spectra of irradiated feldspars”, J. Phys.: Condens. Matter 15 8029, 2003

M.T. Andersen, M. Jain, P. Tidemand-Lichtenberg, “Red-IR stimulated luminescence in K-feldspar: Single or multiple trap origin?”, Journal of Applied Physics 112, 043507, 2012

N. Klasen, M. Fiebig, F. Preusser, “Applying luminescence methodology to key sites of Alpine glaciations in Southern Germany”, Quaternary International, Volume 420, pp 249-258, 2016

N.D. Brown, E.J. Rhodes, T. Mark Harrison, “Using thermoluminescence signals from feldspars for low-temperature thermochronology”, Quaternary Geochronology, Volume 42, pp 31-41, 2017

N.R.J. Poolton, J. Wallinga, A. Murray, E. Bulur, L. Botter-Jensen, “Electrons in feldspar I: on the wavefunction of electrons trapped at simple lattice defects”, Phys Chem Min 29, pp 210–216, 2002a

N.R.J. Poolton, J. Wallinga, A. Murray, E. Bulur, L. Botter-Jensen, “Electrons in feldspar II: a consideration of the influence of conduction band-tail states on luminescence processes”, Phys Chem Min 29, pp 210–216, 2002b

N.R.J. Poolton, R.H. Kars, J. Wallinga, J.J. Bos, “Direct evidence for the participation of band-tails and excited-state tunnelling in the luminescence of irradiated feldspars”, Journal of Physics: Condensed Matter, Volume 21, Number 48, pp 292-309, 2009

P. Braunlich, L.A. DeWerd, J.P. Fillard, J. Gasiot, H. Glaefeke, P.Kelly, D.V. Lang, J.Vanderschueren, “Thermally Stimulated Relaxation in Solids”, Textbook, Topics in Applied Physics, Volume 37, 1979

P. Morthekai, Jugina Thomas, M.S. Pandian, V. Balaram, A.K. Singhvi, “Variable range hopping mechanism in band-tail states of feldspars: A time-resolved IRSL study”, Radiation Measurements, Volume 47, Issue 9, pp 857-863, 2012

P.D. Townsend, Y. Wang, S.W.S. McKeever, “Spectral evidence for defect clustering: Relevance to radiation dosimetry materials”, Radiation Measurements, Volume 147, 106634, 2021

P.W. Levy, “Thermoluminescence kinetics in materials exposed to the low doses applicable to dating and dosimetry”, Nucl. Tracks, Vol 10, Nos 4-6. pp. 547-556. 1985

R. Kumar, “A new understanding of luminescence processes in feldspar using novel site-selective spectroscopic techniques”, PhD Thesis, Technical University of Denmark, 2019

R. Kumar, M. Kook, A.S. Murray, M. Jain, “Towards direct measurement of electrons in metastable states in K-feldspar: Do infrared-photoluminescence and radioluminescence probe the same trap?”, Radiation Measurements, Volume 120, pp 7-13, 2018

R. Visocekas, C. Barthou, P. Blanc, “Thermal quenching of far-red Fe3+ thermoluminescence of volcanic K-feldspars”, Radiation Measurements, Volume 61, 15650, 2014

R.H. Kars, N.R.J. Poolton, M. Jain, C. Ankjærgaard, P. Dorenbos, J. Wallinga, “On the trap depth of the IR-sensitive trap in Na- and K-feldspar”, Radiation Measurements, Volume 59, pp 103-113, 2013

R.J. Clark, “Photostimulated Luminescence as an Archaeological Dating Tool,” PhD Thesis, University of Glasgow, 1992

R.J. Clark and D.C.W. Sanderson, “Photostimulated luminescence excitation spectroscopy of feldspars and micas”, Radiation Measurements, Vol. 23, Nos 213, pp. 641-646, 1994

S. Riedesel, “Exploring variability in the luminescence properties of feldspars”, PhD Thesis, Aberystwyth University, 2020

S. Riedesel, G.E. King, A.K. Prasad, R. Kumar, A.A. Finch, M. Jain, “Optical determination of the width of the band-tail states, and the excited and ground state energies of the principal dosimetric trap in feldspar”, Radiation Measurements, Volume 125, pp 40–51, 2019

S. Riedesel, A.M.T. Bell, G.A.T. Duller, A.A. Finch, M. Jain, G.E. King, N.J. Pearce, H.M. Roberts, “Exploring sources of variation in thermoluminescence emissions and anomalous fading in alkali feldspars”, Radiation Measurements, Volume 141, 106541, 2021

S. Tsukamoto, A. Murray, C. Ankjærgaard, M. Jain.3 and T. Lapp, “Charge recombination processes in minerals studied using optically stimulated luminescence and time-resolved exo-electrons”, J. Phys. D: Appl. Phys. 43 325502, 2010

S.A. Alexander, “The Stability of the R The Stability of the Remnant Luminescence Emissions of Alkali Feldspar”, PhD Thesis, University of Glasgow, 2007

S.K. Fitzgerald, “Mechanism for Infra-Red Stimulated Luminescence in Feldspars,” Undergraduate Dissertation, University of Glasgow, 2020 – Contained in Appendix F

S.K. Fitzgerald, D.C.W. Sanderson, A.J. Cresswell, L. Martin, “Using Infra-red stimulated luminescence and phototransferred thermoluminescence to investigate electron trapping and charge transport in feldspars,” Radiation Measurements, Volume 156, 106817, 2022

T. Sakurai, “Evidence of continuous trap distribution in the glow curve of a Brown microcline”, Journal of Applied Physics 82, 5722, 1997

U. Akgun, A.S. Ayan, G. Aydin, F. Duru, J. Olson, Y. Onel, “Afterpulse timing and rate investigation of three different Hamamatsu Photomultiplier Tubes”, Journal of Instrumentation, Volume 3, 2008

V. Pagonis, “Luminescence Signal Analysis Using Python”, Textbook, Springer, ISBN 978-3-030-96797-0, 2022

V. Pagonis, C. Kulp, “Monte Carlo simulations of tunneling phenomena and nearest neighbor hopping mechanism in feldspar”, Journal of Luminescence, Volume 181, pp 114-120, 2017

W. Hoogenstraaten, “Electron Traps in Zinc-Sulphide Phosphors,” Philips Research Reports 13, pp 515-693, 1958

Y. Kirshi, S. Shoval, P.D. Townsend, “Kinetics and Emission Spectra of Thermoluminescence in the Feldspars Albite and Microcline”, Physica status solidi (a)Volume 101, Issue 1, pp 253-262, 1987

Y.S. Horowitz, D. Yossian, “Computerised Glow Curve Deconvolution Application to Thermoluminescence Dosimetry,” Radiation Protection Dosimetry, Vol. 60, No. 1, pp 345–349, 1995

Appendix A – Average PSP Decay Components for each Feldspar Sample:

RC14 PSP Decay Components	Avg Value	Avg Uncertainty
y0	0.047225	0.001075
a	0.43715	0.008825
b	0.232725	0.01
c	0.40135	0.006975
d	0.034525	0.001125
g	0.1996	0.0042
h	0.005369	0.00015
Avg R^2	0.8461	

RC168 PSP Decay Components	Avg Value	Avg Uncertainty
y0	0.038625	0.0009
a	0.4617	0.008
b	0.21635	0.007425
c	0.390275	0.00625
d	0.031725	0.00085
g	0.19255	0.003475
h	0.004841	0.000125
Avg R^2	0.7768	

RC164 PSP Decay Components	Avg Value	Avg Uncertainty
y0	0.044325	0.00135
a	0.4402	0.012275
b	0.200125	0.011775
c	0.392275	0.009625
d	0.029925	0.0013
g	0.200475	0.005575
h	0.004546	0.000175
Avg R^2	0.8264	

RC169 PSP Decay Components	Avg Value	Avg Uncertainty
y0	0.043725	0.001108
a	0.434025	0.434025
b	0.19465	0.0097
c	0.39365	0.19465
d	0.031325	0.009733
g	0.20035	0.39365

h	0.004938	0.007617
Avg R^2	0.8066	

RC167 PSP Decay Components	Avg Value	Avg Uncertainty
y0	0.060575	0.0097
a	0.0097	0.0097
b	0.501975	0.009733
c	0.0097	0.007617
d	0.219325	0.001092
g	0.009733	0.004417
h	0.35305	0.000144
Avg R^2	0.6309	

RC174 PSP Decay Components	Avg Value	Avg Uncertainty
y0	0.131875	0.012677
a	0.45045	0.032908
b	0.430075	0.038667
c	0.378725	0.027513
d	0.03735	0.003623
g	0.206175	0.017883
h	0.005201	0.000427
Avg R^2	0.7640	

RC72 PSP Decay Components	Avg Value	Avg Uncertainty
y0	0.1199	0.009538
a	21.11525	0.104794
b	1.4796	0.182379
c	0.280375	0.161315
d	0.017275	0.02374
g	0.1711	0.088585
h	0.002895	0.003022
Avg R^2	0.8907	

RC64 PSP Decay Components	Avg Value	Avg Uncertainty
y0	0.122475	0.001108
a	0.384875	0.0097
b	0.235	0.009733
c	0.338125	0.007617
d	0.0272	0.001092

g	0.22225	0.004417
h	0.003903	0.000144
Avg R^2	0.9084	

RC81 PSP Decay Components	Avg Value	Avg Uncertainty
y0	0.07055	0.005416
a	0.43735	0.033898
b	0.372175	0.053472
c	0.426675	0.046383
d	0.039725	0.006814
g	0.207575	0.025694
h	0.005222	0.000873
Avg R^2	0.7340	

RC485 PSP Decay Components	Avg Value	Avg Uncertainty
y0	0.074425	0.003595
a	0.3291	0.013788
b	0.302925	0.060128
c	0.376875	0.051015
d	0.03165	0.007386
g	0.21085	0.028826
h	0.004009	0.000929
Avg R^2	0.7233	

RC484 PSP Decay Components	Avg Value	Avg Uncertainty
y0	0.2252	0.00644
a	0.67735	0.039523
b	0.472075	0.063829
c	0.23845	0.055733
d	0.0489	0.008184
g	0.22345	0.030778
h	0.004473	0.001046
Avg R^2	0.6992	

RC491 PSP Decay Components	Avg Value	Avg Uncertainty
y0	0.1583	0.006343
a	0.606475	0.025692
b	0.56075	0.0405
c	0.36055	0.033132

d	0.033425	0.004729
g	0.197875	0.019205
h	0.002861	0.000593
Avg R^2	0.8096	

RC503 PSP Decay Components	Avg Value	Avg Uncertainty
y0	0.082725	0.002049
a	2.58965	0.006871
b	1.03815	0.014481
c	0.2019	0.018522
d	0.026525	0.001549
g	0.104	0.010571
h	0.003067	0.000299
Avg R^2	0.7118	

RC1396C PSP Decay Components	Avg Value	Avg Uncertainty
y0	0.3875	28.68611
a	0.2546	0.2546
b	0.130992	0.090722
c	0.085475	0.130992
d	0.01496	0.089383
g	0.157475	0.085475
h	0.073272	1.36631
Avg R^2	0.1564855	

RC389 PSP Decay Components	Avg Value	Avg Uncertainty
y0	0.05785	16.9876
a	24.9561	0.342011
b	2.289025	61.24848
c	0.189	68.04327
d	0.006347	13.63386
g	0.468075	48.57924
h	0.000315	0.365748
Avg R^2	0.5521	

RC456 PSP Decay Components	Avg Value	Avg Uncertainty
y0	-0.13975	1.951182
a	0.667925	0.667925
b	0.605325	0.030445

c	0.292025	0.605325
d	0.038676	0.048192
g	0.546075	0.292025
h	0.003531	0.039511
Avg R^2	0.6274	

RC683B PSP Decay Components	Avg Value	Avg Uncertainty
y0	0.289925	23.76122
a	0.19155	0.173703
b	0.144334	0.237045
c	0.435425	12.64733
d	0.201529	20.41337
g	0.22185	28.36971
h	0.000314	0.037856
Avg R^2	0.3955	

RC630 PSP Decay Components	Avg Value	Avg Uncertainty
y0	0.0003	0.005069
a	0.4712	0.021333
b	0.129502	0.027968
c	0.31915	0.022122
d	0.016381	0.003163
g	0.2301	0.013049
h	0.003193	0.000398
Avg R^2	0.6939	

RC630 (redo) PSP Decay Components	Avg Value	Avg Uncertainty
y0	0.07635	0.005405
a	0.433725	0.049449
b	0.364425	0.075851
c	0.40365	0.066241
d	0.03235	0.009698
g	0.235675	0.036645
h	0.00467	0.001237
Avg R^2	0.8446	

Sample was redone due to a readout error halfway through the measurement.

RC165 PSP Decay Components	Avg Value	Avg Uncertainty
y0	0.14755	0.003423
a	0.655675	0.02182
b	0.44735	0.036366
c	0.33575	0.030997
d	0.0232	0.004491
g	0.148825	0.017399
h	0.003736	0.000573
Avg R^2	0.7293	

RC246 PSP Decay Components	Avg Value	Avg Uncertainty
y0	0.0672	6.548
a	0.3663	20.713
b	0.206775	36.84432
c	0.33765	13.3351
d	0.015337	2.8516
g	0.395975	8.5474
h	0.00107	0.12635
Avg R^2	0.15513	

RC659 PSP Decay Components	Avg Value	Avg Uncertainty
y0	0.071475	0.003256
a	0.39985	0.0097
b	0.186475	0.009733
c	0.389325	0.007617
d	0.02885	0.001092
g	0.206075	0.004417
h	0.004464	0.000148
Avg R^2	0.7862	

F1 PSP Decay Components	Avg Value	Avg Uncertainty
y0	0.060025	0.004001
a	0.419675	0.015502
b	0.18155	0.016967
c	0.36095	0.012591
d	0.025375	0.001724
g	0.20455	0.007783
h	0.004104	0.000219
Avg R^2	0.8911	

Appendix B – Ambient and Elevated Temperature TRS Analysis of post-IRSL decay

Temperature	Dwell Time	Wavelength	b lifetime (s)	d lifetime (s)	h lifetime (s)
22°C	2µs	890nm	2.74E-06	2.74E-06	3.87E-05
22°C	20µs	890nm	4.42E-06	4.92E-06	5.66E-05
50°C	2µs	890nm	3.33E-06	5.09E-06	5.93E-05
50°C	20µs	890nm	0.000116	1.08E-05	0.006012
100°C	2µs	890nm	0.000465	2.04E-05	9.34E-06
100°C	20µs	890nm	1.12E-05	1.05E-05	3.46E-05
22°C	2µs	890nm	0.002903	1.47E-05	1.47E-05
22°C	20µs	890nm	1.08E-05	3.69E-06	0.000366
22°C	2µs	940nm	4.99E-05	9.53E-06	9.5E-06
22°C	20µs	940nm	2.34E-05	6.39E-06	0.006672
50°C	2µs	940nm	4.91E-06	2.65E-05	0.001649
50°C	20µs	940nm	1.94E-05	5.87E-06	0.000276
100°C	2µs	940nm	1.24E-05	0.000118	0.000588
100°C	20µs	940nm	2.17E-06	2.24E-06	0.000366
22°C	2µs	940nm	3.22E-06	3.17E-06	3.07E-05
22°C	20µs	940nm	3.55E-06	3.57E-06	2.86E-05

F1 – K-Feldspar

Temperature	Dwell Time	Wavelength	b lifetime (s)	d lifetime (s)	h lifetime (s)
22°C	2µs	890nm	2.34E-06	3.63E-05	0.000222
22°C	20µs	890nm	2.3E-06	3.93E-05	0.000333
50°C	2µs	890nm	2.41E-06	2.42E-06	4.54E-05
50°C	20µs	890nm	2.54E-06	4.08E-05	0.000351
100°C	2µs	890nm	2.54E-06	2.53E-06	4.57E-05
100°C	20µs	890nm	2.27E-06	4.06E-05	0.000401
22°C	2µs	890nm	2.32E-06	3.39E-05	0.000153
22°C	20µs	890nm	2.63E-06	2.68E-06	4.7E-05
22°C	2µs	940nm	2.91E-06	5.03E-05	0.003535
22°C	20µs	940nm	1.79E-05	7.38E-05	0.005347
50°C	2µs	940nm	6.88E-06	4.63E-05	0.004495
50°C	20µs	940nm	3.42E-06	4.82E-05	0.003851
100°C	2µs	940nm	8.52E-06	5.08E-05	0.002158
100°C	20µs	940nm	1.78E-05	7.36E-05	0.005767
22°C	2µs	940nm	4.86E-06	4.25E-05	0.034737
22°C	20µs	940nm	1.43E-05	1.43E-05	6.98E-05

RC14 – Albite

Temperature	Dwell Time	Wavelength	b lifetime (s)	d lifetime (s)	h lifetime (s)
22°C	2µs	890nm	(2±0.08)E-06	(2±0.13)E-06	5.65E-05

22°C	20µs	890nm	2.09E-06	2.09E-06	5.17E-05
50°C	2µs	890nm	2.14E-06	2.14E-06	5.22E-05
50°C	20µs	890nm	2.03E-06	2.03E-06	5.71E-05
100°C	2µs	890nm	1.88E-06	1.85E-06	5.22E-05
100°C	20µs	890nm	2.16E-06	2.16E-06	5.17E-05
22°C	2µs	890nm	2.48E-06	2.48E-06	6.87E-05
22°C	20µs	890nm	2.31E-06	2.31E-06	5.31E-05
22°C	2µs	940nm	1.97E-06	4.05E-05	0.005091
22°C	20µs	940nm	1.95E-06	1.95E-06	4.76E-05
50°C	2µs	940nm	2.3E-06	4.69E-05	0.002431
50°C	20µs	940nm	2.14E-06	2.14E-06	5.96E-05
100°C	2µs	940nm	1.97E-06	1.95E-06	4.73E-05
100°C	20µs	940nm	1.97E-06	1.98E-06	5.21E-05
22°C	2µs	940nm	1.85E-06	1.87E-06	4.47E-05
22°C	20µs	940nm	1.78E-06	1.97E-06	5.71E-05

RC164 – Albite

Temperature	**Dwell Time**	**Wavelength**	**b lifetime (s)**	**d lifetime (s)**	**h lifetime (s)**
22°C	2µs	890nm	6.87E-07	4.42E-07	6.05E-05
22°C	20µs	890nm	1.78E-06	7.2E-06	0.000105
50°C	2µs	890nm	1.66E-06	3.21E-05	0.00705
50°C	20µs	890nm	5.09E-07	2.68E-05	3.62E-05
100°C	2µs	890nm	2.29E-06	2.35E-06	1.91E-05
100°C	20µs	890nm	0.033963	0.000346	3.4E-06
22°C	2µs	890nm	1.08E-06	1.08E-06	6.64E-05
22°C	20µs	890nm	1.86E-06	4.37E-05	0.001188
22°C	2µs	940nm	2.59E-06	1.97E-05	0.000133
22°C	20µs	940nm	7.37E-06	4.89E-07	0.000257
50°C	2µs	940nm	2.1E-06	4.65E-07	0.000493
50°C	20µs	940nm	4.89E-07	4.88E-07	1.68E-05
100°C	2µs	940nm	3.07E-06	4.1E-06	9.65E-05
100°C	20µs	940nm	7.83E-06	1.27E-06	7.72E-05
22°C	2µs	940nm	4.18E-05	4.2E-05	3.89E-05
22°C	20µs	940nm	3.77E-06	3.73E-06	0.00014

RC168 – Albite

Temperature	**Dwell Time**	**Wavelength**	**b lifetime (s)**	**d lifetime (s)**	**h lifetime (s)**
22°C	2µs	890nm	2.2E-05	2.26E-05	0.00494
22°C	20µs	890nm	3.92E-05	3.6E-06	0.006349
50°C	2µs	890nm	2.16E-06	2.15E-06	4.48E-05
50°C	20µs	890nm	2.51E-06	2.5E-06	4.86E-05
100°C	2µs	890nm	1.59E-05	6.69E-05	0.004718
100°C	20µs	890nm	5.21E-05	8.24E-06	0.008284

22°C	2µs	890nm	1.96E-06	1.96E-06	4.18E-05
22°C	20µs	890nm	2.49E-06	2.46E-06	4.34E-05
22°C	2µs	940nm	7.88E-06	7.88E-06	3.91E-05
22°C	20µs	940nm	5.48E-05	6.65E-06	0.00561
50°C	2µs	940nm	2.28E-06	2.27E-06	4.17E-05
50°C	20µs	940nm	2.35E-06	2.36E-06	4.38E-05
100°C	2µs	940nm	2.23E-06	2.23E-06	4.37E-05
100°C	20µs	940nm	2.21E-06	2.2E-06	4.23E-05
22°C	2µs	940nm	2.16E-06	2.15E-06	4.48E-05
22°C	20µs	940nm	3.7E-05	1.58E-06	0.000738

RC169 – Albite

Temperature	Dwell Time	Wavelength	b lifetime (s)	d lifetime (s)	h lifetime (s)
22°C	2µs	890nm	4.96E-06	2.13E-05	0.000106
22°C	20µs	890nm	2.32E-05	6.15E-06	2.65E-05
50°C	2µs	890nm	3.22E-05	5.61E-06	5.64E-06
50°C	20µs	890nm	6.87E-06	6.89E-06	3.67E-05
100°C	2µs	890nm	3.97E-06	3.89E-06	2E-05
100°C	20µs	890nm	7.38E-06	8.98E-06	0.000528
22°C	2µs	890nm	1.45E-05	5.61E-06	0.000108
22°C	20µs	890nm	4.27E-06	1.93E-05	0.000109
22°C	2µs	940nm	5.26E-06	1.44E-05	0.000113
22°C	20µs	940nm	9.33E-06	0.000981	0.001477
50°C	2µs	940nm	2.8E-06	2.81E-06	3.71E-05
50°C	20µs	940nm	5.62E-06	5.45E-06	2.83E-05
100°C	2µs	940nm	9.38E-06	0.001208	9.79E-05
100°C	20µs	940nm	1.11E-05	1.1E-05	8.63E-05
22°C	2µs	940nm	1.18E-05	5.8E-05	4.92E-05
22°C	20µs	940nm	4.81E-06	2.34E-05	0.000191

RC165 – Microcline

Temperature	Dwell Time	Wavelength	b lifetime (s)	d lifetime (s)	h lifetime (s)
22°C	2µs	890nm	4.1E-06	4.1E-06	3.81E-05
22°C	20µs	890nm	0.000174	9.24E-06	9.24E-06
50°C	2µs	890nm	5.72E-05	6.44E-06	6.44E-06
50°C	20µs	890nm	3.73E-06	3.73E-06	4.13E-05
100°C	2µs	890nm	3.18E-06	3.17E-06	3.18E-06
100°C	20µs	890nm	4.15E-05	6.52E-06	7.04E-06
22°C	2µs	890nm	3.97E-06	3.97E-06	3.05E-05
22°C	20µs	890nm	4.29E-06	4.3E-06	4.71E-05
22°C	2µs	940nm	0.000265	1.13E-05	1.12E-05
22°C	20µs	940nm	8.74E-05	8.24E-06	8.23E-06
50°C	2µs	940nm	3.83E-06	3.82E-06	4.97E-05

50°C	20µs	940nm	3.18E-06	3.18E-06	3.18E-06
100°C	2µs	940nm	0.00011	3.93E-06	3.93E-06
100°C	20µs	940nm	3.84E-06	3.85E-06	3.36E-05
22°C	2µs	940nm	3.04E-06	3.04E-06	2.4E-05
22°C	20µs	940nm	2.66E-06	2.66E-06	2.64E-05

RC630 – Microcline

Temperature	**Dwell Time**	**Wavelength**	**b lifetime (s)**	**d lifetime (s)**	**h lifetime (s)**
22°C	2µs	890nm	3.33E-06	3.32E-06	3.51E-05
22°C	20µs	890nm	3.06E-05	3.04E-05	3.03E-05
50°C	2µs	890nm	2.72E-06	1.24E-05	9.37E-05
50°C	20µs	890nm	4.02E-06	4.07E-06	4.21E-05
100°C	2µs	890nm	3.16E-05	3.16E-05	0.000459
100°C	20µs	890nm	2.73E-05	5.23E-06	2.73E-05
22°C	2µs	890nm	6.19E-06	6.2E-06	4.68E-05
22°C	20µs	890nm	7.79E-07	7.87E-07	2.83E-05
22°C	2µs	940nm	1.2E-05	1.2E-05	1.2E-05
22°C	20µs	940nm	3.41E-06	3.41E-06	8.56E-05
50°C	2µs	940nm	5.11E-06	4.83E-06	1.94E-05
50°C	20µs	940nm	6.23E-05	6.63E-05	0.110753
100°C	2µs	940nm	0.031822	0.224115	0.020799
100°C	20µs	940nm	1.97E-06	2.96E-05	2.97E-05
22°C	2µs	940nm	1.46E-06	1.42E-06	2.27E-05
22°C	20µs	940nm	6.27E-06	6.26E-06	8E-05

RC246 – Plagioclase

Temperature	**Dwell Time**	**Wavelength**	**b lifetime (s)**	**d lifetime (s)**	**h lifetime (s)**
22°C	2µs	890nm	3.35E-06	3.36E-06	3.35E-06
22°C	20µs	890nm	0.004495	2.71E-05	4.75E-06
50°C	2µs	890nm	0.000175	7.38E-06	0.006076
50°C	20µs	890nm	3.39E-06	3.39E-06	3.38E-06
100°C	2µs	890nm	2.55E-06	2.56E-06	2.57E-06
100°C	20µs	890nm	9.12E-06	0.003469	0.003339
22°C	2µs	890nm	0.000245	7.55E-06	0.009808
22°C	20µs	890nm	2.95E-06	2.94E-06	2.94E-06
22°C	2µs	940nm	2.6E-06	2.6E-06	2.59E-06
22°C	20µs	940nm	3.76E-06	0.000116	0.005443
50°C	2µs	940nm	0.002441	1.49E-05	5.23E-06
50°C	20µs	940nm	1.44E-06	1.44E-06	1.45E-06
100°C	2µs	940nm	2.54E-06	2.54E-06	2.54E-06
100°C	20µs	940nm	5.46E-06	0.000237	0.006606
22°C	2µs	940nm	3.1E-06	3.1E-06	3.12E-06
22°C	20µs	940nm	1.83E-06	1.85E-06	0.000113

RC659 – Plagioclase

Temperature	Dwell Time	Wavelength	b lifetime (s)	d lifetime (s)	h lifetime (s)
22°C	2µs	890nm	3.31E-06	2.17E-05	0.001619
22°C	20µs	890nm	7.02E-05	1.34E-05	0.006776
50°C	2µs	890nm	2.58E-05	4.93E-06	4.95E-06
50°C	20µs	890nm	4.57E-06	4.58E-06	3.6E-05
100°C	2µs	890nm	3.74E-06	3.73E-06	3.76E-06
100°C	20µs	890nm	4.66E-06	4.66E-06	0.00508
22°C	2µs	890nm	0.008048	1.41E-05	1.04E-05
22°C	20µs	890nm	4.33E-06	4.36E-06	2.5E-05
22°C	2µs	940nm	4.04E-06	4.07E-06	4.28E-05
22°C	20µs	940nm	7.14E-06	7.14E-06	0.000149
50°C	2µs	940nm	2.39E-06	2.09E-05	0.01187
50°C	20µs	940nm	3.8E-06	3.76E-06	5.65E-05
100°C	2µs	940nm	3.25E-06	3.28E-06	3.51E-05
100°C	20µs	940nm	4.09E-05	4.2E-05	8.18E-06
22°C	2µs	940nm	0.00769	1.43E-05	0.007654
22°C	20µs	940nm	3.85E-06	3.87E-06	3.1E-05

RC81 – K-Feldspar

Temperature	Dwell Time	Wavelength	b lifetime (s)	d lifetime (s)	h lifetime (s)
22°C	2µs	890nm	2.54E-06	2.28E-05	7.94E-05
22°C	20µs	890nm	1.1E-05	7.23E-06	6.6E-05
50°C	2µs	890nm	1.04E-05	1.04E-05	5.99E-05
50°C	20µs	890nm	4.77E-06	2.91E-05	0.000163
100°C	2µs	890nm	3.96E-06	3.95E-06	5.14E-05
100°C	20µs	890nm	4.54E-07	4.55E-07	4.18E-06
22°C	2µs	890nm	2.04E-05	2.04E-05	7.22E-05
22°C	20µs	890nm	3.14E-06	3.06E-05	0.00019
22°C	2µs	940nm	2.98E-06	3.01E-06	4.29E-05
22°C	20µs	940nm	2.26E-05	0.000215	0.000226
50°C	2µs	940nm	2.45E-05	2.44E-05	3.27E-05
50°C	20µs	940nm	6.59E-06	7.21E-06	5.65E-05
100°C	2µs	940nm	1.38E-05	1.39E-05	1.4E-05
100°C	20µs	940nm	0.000477	1.46E-05	1.51E-05
22°C	2µs	940nm	3.87E-06	3.87E-06	6.43E-05
22°C	20µs	940nm	2.12E-06	4.09E-05	0.001606

RC167 – K-Feldspar

Temperature	Dwell Time	Wavelength	b lifetime (s)	d lifetime (s)	h lifetime (s)
22°C	2µs	890nm	2.59E-06	1.77E-05	0.000117

22°C	20µs	890nm	3.45E-06	3.45E-06	5.96E-05
50°C	2µs	890nm	4.58E-06	5.12E-05	5.11E-05
50°C	20µs	890nm	1.49E-06	1.23E-05	5.45E-05
100°C	2µs	890nm	2.33E-06	4.43E-05	0.000119
100°C	20µs	890nm	4.02E-06	1.45E-05	0.003293
22°C	2µs	890nm	4.56E-05	4.54E-05	4.64E-05
22°C	20µs	890nm	2.62E-06	2.22E-05	0.000275
22°C	2µs	940nm	1.12E-05	1.11E-05	0.000109
22°C	20µs	940nm	4.13E-05	4.23E-05	4.13E-05
50°C	2µs	940nm	3.94E-05	3.93E-05	3.85E-05
50°C	20µs	940nm	9.15E-07	1.4E-05	3.91E-05
100°C	2µs	940nm	0.044618	1.32E-07	0.050797
100°C	20µs	940nm	0.127463	9.91E-06	0.171615
22°C	2µs	940nm	5.85E-07	2.8E-05	0.000184
22°C	20µs	940nm	1.76E-05	1.75E-05	0.000161

RC683B – K-Feldspar

Temperature	**Dwell Time**	**Wavelength**	**b lifetime (s)**	**d lifetime (s)**	**h lifetime (s)**
22°C	2µs	890nm	3.7E-07	2.27E-05	6.5E-05
22°C	20µs	890nm	4.36E-06	4.38E-06	6.14E-05
50°C	2µs	890nm	5.04E-06	0.006473	0.008583
50°C	20µs	890nm	2.34E-06	2.13E-05	6.8E-05
100°C	2µs	890nm	0.026049	0.02651	0.026081
100°C	20µs	890nm	1.53E-05	1.79E-05	7.15E-05
22°C	2µs	890nm	5.58E-06	5.57E-06	0.000106
22°C	20µs	890nm	1.56E-06	1.58E-06	3.3E-05
22°C	2µs	940nm	1.83E-06	1.74E-06	5.47E-05
22°C	20µs	940nm	6.86E-06	4.85E-05	4.95E-05
50°C	2µs	940nm	5.18E-06	0.005509	0.008762
50°C	20µs	940nm	3.29E-06	5.98E-07	5.8E-05
100°C	2µs	940nm	4.94E-07	4.93E-07	4.51E-05
100°C	20µs	940nm	1.92E-05	1.88E-05	0.000147
22°C	2µs	940nm	1.28E-05	1.29E-05	0.000412
22°C	20µs	940nm	5.67E-07	5E-05	3.35E-05

RC1396C – K-Feldspar

Appendix C – Cryogenic, Ambient and Elevated Temperature post-IRSL decay lifetimes

Temperature	b lifetime (s)	d lifetime (s)	h lifetime (s)	Wavelength (nm)	F1
22°C	2.95E-06	2.96E-06	2.78E-05	890	K-Feldspar
-60°C	2.4E-06	2.44E-06	2.7E-05	890	
-78°C	3.09E-06	3.12E-06	3.19E-05	890	
22°C	3.17E-06	1.42E-05	8.29E-05	940	
-60°C	6.03E-06	2.53E-05	0.104	940	
-78°C	4.38E-06	2.14E-05	2.08E-05	940	

Temperature	b lifetime (s)	d lifetime (s)	h lifetime (s)	RC14
22°C	2.54E-06	4.08E-05	0.000351	Albite
80°C	8.52E-06	5.08E-05	0.002158	
22°C	1.78E-05	7.36E-05	0.005767	
-40°C	4.86E-06	4.25E-05	0.034737	
22°C	1.43E-05	1.43E-05	6.98E-05	

Temperature	b lifetime (s)	d lifetime (s)	h lifetime (s)	RC164
22°C	3.82E-05	1.47E-06	0.003912	Albite
80°C	1.23E-06	3.75E-05	0.004725	
22°C	1.45E-06	3.86E-05	0.004383	
-40°C	1.85E-06	1.99E-05	0.0001	
22°C	1.76E-06	4.1E-05	0.004625	

Temperature	b lifetime (s)	d lifetime (s)	h lifetime (s)	RC168
22°C	1.62E-06	4.75E-05	0.002287	Albite
80°C	1.74E-06	1.74E-06	0.000109	
22°C	1.76E-06	1.77E-06	9.12E-05	
-40°C	1.98E-06	2.76E-05	0.001472	
22°C	1.82E-06	1.83E-06	8.05E-05	

Temperature	b lifetime (s)	d lifetime (s)	h lifetime (s)	RC169
22°C	3.37E-05	1.83E-06	0.00018	Albite
80°C	3.82E-05	1.69E-06	0.001068	
22°C	3.84E-05	1.68E-06	0.001393	
-40°C	3.84E-05	1.68E-06	0.001393	
22°C	2.22E-06	2.66E-05	0.000187	

Temperature	b lifetime (s)	d lifetime (s)	h lifetime (s)	RC165
22°C	4.81E-06	2.34E-05	0.000191	Microcline
80°C	4.97E-06	4.98E-06	3.02E-05	

22°C	3.02E-07	1.01E-05	3.96E-05	
-40°C	2.6E-06	1.21E-05	5.75E-05	
22°C	1.61E-06	1.72E-05	0.000106	

Temperature	b lifetime (s)	d lifetime (s)	h lifetime (s)	RC630
22°C	3.04E-06	3.04E-06	2.4E-05	Microcline
80°C	2.66E-06	2.66E-06	2.64E-05	
22°C	3.09E-06	3.08E-06	2.46E-05	
-40°C	2.83E-06	2.23E-05	0.000371	
22°C	2.81E-06	2.81E-06	2.19E-05	

Temperature	b lifetime (s)	d lifetime (s)	h lifetime (s)	RC246
22°C	1.46E-06	1.42E-06	2.27E-05	Plagioclase
80°C	1.87E-06	1.88E-06	6.72E-05	
22°C	6.27E-06	6.26E-06	8E-05	
-40°C	2.22E-06	2.03E-06	1.85E-05	
22°C	2.06E-06	2.04E-06	3.08E-05	

Temperature	b lifetime (s)	d lifetime (s)	h lifetime (s)	RC659
22°C	1.83E-06	1.85E-06	0.000113	Plagioclase
80°C	1.66E-06	3.93E-05	0.003046	
22°C	1.81E-06	1.81E-06	0.000121	
-40°C	2.17E-06	2.17E-06	7.38E-05	
22°C	1.78E-06	1.78E-06	0.000129	

Temperature	b lifetime (s)	d lifetime (s)	h lifetime (s)	RC64
22°C	2.12E-06	7.25E-06	2.23E-05	K-Feldspar
80°C	4.76E-06	4.77E-06	2.92E-05	
22°C	4.19E-06	1.99E-05	0.000137	
-40°C	1.69E-05	1.64E-06	0.000537	
22°C	1.84E-06	1.19E-05	3.5E-05	

Temperature	b lifetime (s)	d lifetime (s)	h lifetime (s)	RC72
22°C	2.27E-06	1.85E-05	0.000834	K-Feldspar
80°C	1.12E-05	3.06E-06	0.000268	
22°C	2.55E-06	1.66E-05	0.000155	
-40°C	8.21E-06	1.29E-06	0.000376	
22°C	2.03E-06	1.84E-05	0.001384	

Temperature	b lifetime (s)	d lifetime (s)	h lifetime (s)	RC81
22°C	2.86E-06	1.89E-05	0.003761	K-Feldspar
80°C	3.47E-06	3.47E-06	4.35E-05	

22°C	3.18E-06	1.84E-05	0.003937	
-40°C	2.64E-06	1.71E-05	0.000776	
22°C	3.04E-06	1.83E-05	0.002096	

Temperature	**b lifetime (s)**	**d lifetime (s)**	**h lifetime (s)**	**RC167**
22°C	2.24E-06	2.91E-05	0.000148	K-Feldspar
80°C	3.19E-06	1.24E-05	4.77E-05	
22°C	1.68E-06	2.05E-05	9.06E-05	
-40°C	2.44E-05	1.51E-06	0.000199	
22°C	2.11E-06	2.75E-05	0.000176	

Temperature	**b lifetime (s)**	**d lifetime (s)**	**h lifetime (s)**	**RC174**
22°C	1.5E-05	1.62E-06	8.92E-05	K-Feldspar
80°C	1.04E-05	2.49E-06	0.000118	
22°C	1.62E-06	1.6E-06	3.47E-05	
-40°C	1.54E-06	1.58E-06	3.38E-05	
22°C	6.42E-07	6.06E-06	5.47E-05	

Temperature	**b lifetime (s)**	**d lifetime (s)**	**h lifetime (s)**	**RC389**
22°C	1.97E-06	1.96E-06	4.65E-05	K-Feldspar
80°C	1.82E-06	1.77E-06	2.82E-05	
22°C	1.77E-06	1.8E-06	6.51E-05	
-40°C	0.001344	2.24E-06	0.001215	
22°C	3E-07	3E-07	8.6E-06	

Temperature	**b lifetime (s)**	**d lifetime (s)**	**h lifetime (s)**	**RC456**
22°C	1.83E-06	1.02E-05	0.000187	K-Feldspar
80°C	1.88E-06	1.87E-06	3.11E-05	
22°C	2.1E-06	2.08E-06	5.83E-05	
-40°C	1.58E-06	1.92E-05	0.00014	
22°C	2.22E-06	2.23E-06	5.35E-05	

Temperature	**b lifetime (s)**	**d lifetime (s)**	**h lifetime (s)**	**RC484**
22°C	2.25E-06	1.38E-05	0.000168	K-Feldspar
80°C	0.032536	0.026056	3.45E-06	
22°C	1.76E-06	1.13E-05	0.000137	
-40°C	2.11E-06	1.9E-05	0.000385	
22°C	2.57E-06	2.29E-05	0.00032	

Temperature	**b lifetime (s)**	**d lifetime (s)**	**h lifetime (s)**	**RC485**

22°C	2.65E-06	2.65E-06	3.58E-05	K-Feldspar
80°C	2.55E-06	2.57E-06	4.08E-05	
22°C	2.37E-06	3.2E-05	0.003603	
-40°C	2.26E-06	2.24E-06	4.76E-05	
22°C	1.92E-06	2.62E-05	0.001152	

Temperature	**b lifetime (s)**	**d lifetime (s)**	**h lifetime (s)**	**RC491**
22°C	2.15E-06	1.9E-05	0.000414	K-Feldspar
80°C	2.19E-06	7.69E-06	8.93E-05	
22°C	2.04E-06	1.95E-05	0.000322	
-40°C	2.33E-06	1.14E-05	0.000451	
22°C	3.19E-06	3.21E-05	0.001745	

Temperature	**b lifetime (s)**	**d lifetime (s)**	**h lifetime (s)**	**RC503**
22°C	2.85E-05	1.48E-06	0.001584	K-Feldspar
80°C	2.17E-06	2.05E-05	0.000401	
22°C	2.6E-06	2.6E-06	5.8E-05	
-40°C	2.02E-06	4.13E-05	0.000862	
22°C	2.58E-06	3.01E-05	0.008495	

Temperature	**b lifetime (s)**	**d lifetime (s)**	**h lifetime (s)**	**RC683B**
22°C	1.76E-05	1.75E-05	0.000161	K-Feldspar
80°C	1.7E-05	1.94E-05	4.39E-05	
22°C	5.92E-06	4.25E-05	0.000587	
-40°C	2.68E-07	3.13E-07	1.06E-07	
22°C	5.09E-06	5.39E-05	5.57E-05	

Temperature	**b lifetime (s)**	**d lifetime (s)**	**h lifetime (s)**	**RC1396C**
22°C	9.8E-07	6.81E-07	2.51E-05	K-Feldspar
80°C	1.67E-06	0.000335	3.88E-05	
22°C	2.4E-06	2.39E-06	5.12E-05	
-40°C	N/A	N/A	N/A	
22°C	8.82E-07	4.58E-05	0.000208	

Appendix D – PTTL Investigation Activation Energies

Sample	*SUERC Tla*	*Uncert*	*SUERC TLb*	*Uncert*	*RISO Ia*	*Uncert*	*RISO Ib*	*Uncert*	*RISO IIIa*	*Uncert*	*RISO IIIb*	*Uncert*	*RISO IIIc*	*Uncert*	*SUERC Cryo A*	*Uncert*	*SUERC Cryo B*	*Uncert*
RC167	0.7068	0.0249	0.6756	0.0535	0.5678	0.0433	0.5237	0.0251	0.8032	0.0294	0.9103	0.0725	0.8376	0.0503				
RC174	0.5628	0.0380	0.8370	0.0217	0.6149	0.0432		0.0000	0.7596	0.0605								
RC72	0.7223	0.1669	0.6962	0.0564	0.6063	0.0337		0.0000	0.8749	0.0649								
RC64	0.7461	0.1488	0.6586	0.0215	0.5919	0.0291		0.0000	0.8018	0.0565								
RC81	0.6906	0.0741	0.6808	0.0250	0.6477	0.0491	0.6738	0.0272	0.7634	0.0470					0.1713	0.0017	0.1587	0.0007
RC485	0.7141	0.0766	0.6721	0.0254	0.5673	0.0229		0.0000	0.7386	0.0327								
RC484	0.6093	0.0967	0.6543	0.0460	0.5236	0.0506		0.0000	0.7417	0.0608								
RC491	0.6946	0.1409	0.6477	0.1657	0.5553	0.0162		0.0000	0.7447	0.0980								
RC503	0.7044	0.0273	0.6365	0.0419	0.5927	0.0877		0.0000	0.7177	0.0503								
F1	0.6785	0.0263	0.7000	0.0340	0.5803	0.0359	0.5735	0.0169	0.8137	0.0694								
RC1396C	0.6016	0.3075	1.0316	0.4222	0.6239	0.3699	0.6158	0.3047	0.8280	0.0138								
RC389	0.7472	0.1476	0.5361	0.0102	0.7201	0.0268		0.0000	0.9676	0.0253	0.5471	0.0253						
RC456	0.7314	0.2709	0.7047	0.0304	0.6050	0.0466		0.0000	0.8211	0.0745	0.8157	0.0485						
RC683B	0.7170	0.1810	0.6811	0.2234	0.6146	0.1546	0.5347	0.2080	0.8314	0.2061								
RC630	0.7460	0.0602	0.6751	0.0303	0.6436	0.0313	0.5853	0.0462	0.8818	0.0257					0.2055	0.0417	0.1258	0.0852
RC165	0.6999	0.0558	0.7030	0.0535	0.5935	0.0668	0.5608	0.0311	0.8972	0.0541	0.8788	0.0511			0.1593	0.0016		
RC246	0.6610	0.2032	0.7033	0.1482	0.6747	0.3891		0.0000	0.8454	0.2559	0.4402	0.0426			0.1430	0.0004		
RC659	0.7339	0.2153	0.5514	0.2786	0.6242	0.1415		0.0000	0.8758	0.3541								
RC14	0.7501	0.0253	0.7286	0.0384	0.6514	0.0165	0.6069	0.0184	0.8011	0.0509	0.9156	0.0166	0.8470	0.0821	0.3290	0.0646		
RC168	0.5613	0.0196	0.6782	0.0154	0.6243	0.0181		0.0000	0.9162	0.0792	0.9054	0.0141		0.0000	0.2616	0.0151		
RC169	0.6397	0.0569	0.7375	0.0409	0.5527	0.0402	0.5880	0.0989	0.6842	0.0309	0.8081	0.0560	0.7839	0.0552	0.2705	0.0156	0.3640	0.0324
RC164	0.6375	0.0559	0.5857	0.0164	0.5489	0.0720		0.0000	0.7527	0.0650				0.0000	0.2181	0.0110		

Appendix E – Python Code – TL Peak Deconvolution

```
# -*- coding: utf-8 -*-
# Finding the optimal number of components to fit
# the glow curve for Feldspar samples
from scipy import optimize
import numpy as np
import matplotlib.pyplot as plt
import tkinter as tk
from tkinter import filedialog
import os
import warnings
warnings.filterwarnings("ignore")
#Deconvolution of prompt TL with N=1-5 components using original KP-TL
#create a tkinter root widget
root=tk.Tk()
root.withdraw()

# Open a file dialog to allow the user to select multiple txt files
input_files = filedialog.askopenfilenames(filetypes=[("Text files", "*.txt")])

for input_file in input_files:
    print(input_file)
    data = np.loadtxt(input_file) # Import net TL glow curve
    x_data, y_data = data[:, 0], data[:, 1] # Assigns imported data to columns

    z, kB =1.8, 8.617E-5 #sets constants
    while True:
        try:
```

```
            s = float(input("Enter the frequency factor for this sample:")) #Prompts user to input
the frequncy factor evaluated for the net TL curve
            break
        except ValueError:
            print("Invalid input. Try again.")
            print(s)


    def TL(T, B,En ,rho, s): #Will be used to generate TL peaks
            return abs(B)* np.exp(-rho*( (np.log(1+z*s*kB*(((T+\
                                                            273)**2.0)/np.abs(En))*np.exp(-En/(kB*(T+273)))*\
                                                (1-2*kB*(T+273)/En)))**3.0))*(En**2.0-6*(kB**2.0)*\

((T+273)**2.0))*((np.log(1+z*s*kB*(((T+273)**2.0)/\
                                                                                    abs(En))*np.exp(-En/(kB*(T+273)))*(1-
2*kB*(T+273)/\
                                                                                      En)))**2.0)/(En*kB*s*((T+273)**2)*z-
2*(kB**2.0)*\

s*z*((T+273)**3.0)+np.exp(En/(kB*(T+273)))*En) #KP-TL equation for TL analysis
    def total_TL(T, *inis): #Computes KP-TL equation for dataset
        u=np.array([0 for i in range(len(x_data))])
        Bs, Ens,rho,s= inis[0:nPks], inis[nPks:2*nPks],\
            inis[-2],inis[-1]
        for i in range(nPks):
            u=u+TL(T,Bs[i],Ens[i],rho,s)
            return u


    def main(nPks,s):
        Bs=[2e17]*7
        B=Bs[0:nPks]
        lowB, highB=[0.01*x for x in B], [50*x for x in B]
```

```
    lowrho, highrho, rho= [0.005,.02,.01]#escape efficiency boundaries
    lows, highs =[1e10, 2e12]#frequency factors boundaries
    Ens=[.7,.8,.9,1.0,1.1] #energy range
    En=Ens[0:nPks] #Creats seperate plots for each energy value
    lowEn,highEn =[0.6*x for x in En],[1*x for x in En] #Energy boundaries
    inis=B+En+[rho]+[s]
    lowbnds=lowB+lowEn+[lowrho]+[lows] #Sets lower limits for plots
    highbnds=highB+highEn+[highrho]+[highs] #Sets upper limits for plots
    params, params_covariance = optimize.curve_fit(total_TL,\

x_data,y_data,p0=inis,bounds=(lowbnds,highbnds),maxfev=10000)
    plt.subplot(2,3, nPks)
    plt.scatter(x_data, y_data,c="r")
    plt.plot(x_data, total_TL(x_data,
                  *params),c="black",label="N="+str(nPks),linewidth=1)


    for i in range(0,nPks):
        plt.plot(x_data, TL(x_data,
                  params[i],params[nPks+i],params[-2],params[-1]))
        leg = plt.legend()
        leg.get_frame().set_linewidth(0.0)
        plt.ylabel("TL")
        plt.xlabel("Temperature (*C)")
        print("Activation Energies (eV): ",En)
        res=total_TL(x_data, *params)-y_data
        FOM=100*np.sum(abs(res))/np.sum(y_data)
        FOMS[nPks-1]=FOM

  FOMS = [0] * 5  # Limits FOMS plot - MUST BE EQUAL TO TOTAL PLOTS OR CODE BREAKS
```

```
    for nPks in range(1, 6, 1):
        main(nPks, s)
        plt.subplot(2, 3, nPks)
        plt.title(os.path.splitext(os.path.basename(input_file))[0] + ' - ' + str(nPks) + ' components')
        plt.savefig(os.path.splitext(input_file)[0] + '_N' + str(nPks) + '.png')
        plt.subplot(2, 3, 6)
        print("FOMS: ", FOMS)
        plt.plot(range(0, 5), FOMS, "o-")
        plt.ylabel('FOMS [%]')
        plt.xlabel('# of components N')
        plt.ylim([0, 100])
        my_xticks = [1, 2, 3, 4, 5]
        plt.xticks(range(0, 5), my_xticks)
        plt.tight_layout(pad=0.1, h_pad=0.1, w_pad=0.1, rect=None)
        plt.show()
```

Appendix F – S. Fitzgerald, 2020.

Mechanism for Infra-Red Stimulated Luminescence in Feldspars

xxxxxxxx

Kelvin Building, Department of Physics and Astronomy, University of Glasgow,
Glasgow, G12 8QQ, UK

xxxxxxxx@student.gla.ac.uk

Abstract. An investigation was conducted into a collection of twenty-three feldspar samples to investigate the mechanisms responsible for producing infra-red stimulated luminescence (IRSL) using stimulation wavelengths of 890nm and 940nm. This was done by collecting evidence for both the distributions of traps and charge mobility (as opposed to localised recombination tunnelling) in order to address questions in the literature. A series of experiments was conducted to examine the relationship between stimulation wavelength and IRSL production. Additionally, charge mobility was investigated probing the relationship between phototransferred thermoluminescence (PTTL), IRSL, and phosphorescence.

A variance in stimulation response between the two chosen wavelengths was recorded, the ratio of which groups the samples into distinct feldspar families. This indicates a distributed trap structure across feldspars.

This report has shown for the first time that IRSL does generate PTTL from shallow traps, confirming charge mobility and was used to examine the kinetics of the charge transfer process, with charge transported from a trap with activation energies 1-1.2eV to a shallower trap with energies 0.7-0.8eV. A much shallower trap with activation energies of 0.1-0.3eV was also detected in some samples.

Critically, it was noted that there were multi-exponential decay constants in post-stimulation phosphorescence that varied depending on the stimulation wavelength used. This also indicates charge movement and distributed electron traps.

1. Background

Feldspars are a family of minerals which comprise almost half of the mass of the Earth's crust. They are broadly separated into three groups; Potassium Feldspar, Calcium Feldspar, and Sodium Feldspar ($KAlSi_3O_8$, $CaAl_2Si_2O_8$, $NaAlSi_3O_8$ respectively).

Potassium and Sodium feldspars are alkaline and are widely used as geochronometers due to their property of being precise natural dosimeters when undergoing Optically Stimulated Luminescence (OSL) or Thermally Stimulated Luminescence (TL) up to as far back as 1 million years (Huntley et al. 1985). This ability to look so far back in time when compared with the other major natural dosimeters such as quartz (upper dating limit of ~250,000 years) and radiocarbon (upper dating limit of ~50,000 years), makes feldspars especially useful to examine climate cycles and geological processes over Quaternary timescales.

Over these timescales, the minerals will be exposed to ionizing radiation, which will create free electrons within the atomic structure. For insulators like feldspars, such free electrons become trapped by impurities or defects within the material lattice. The number of these trapped electrons is a measure of the radiation dose and is exploited for radiation dosimetry and for dating in both geology and archaeology.

Infra-red stimulated luminescence (IRSL) and TL are primary methods of feldspar dating and rely on the excitation of trapped electrons, which produce a measurable photon count when released. However, a curious property of feldspars is that there can be considerable leaking of dosimetry information because of rapid, time-dependent recombination from electron traps to recombination centres; this process is a commonly referred to as anomalous fading (Wintle, 1973; Visocekas, 1985; Sanderson, 1988) and various models, including quantum tunnelling, have been used to describe this process (Huntley et al. 2007; Sahiner et al. 2017; Pagonis et al. 2017).

Presently there are two main conflicting models regarding electron trapping and IRSL production in feldspars. One model uses the concept of feldspars having a fundamental trap (Andersen et al. 2012; Kumar et al. 2018; Thomsen et al. 2011). This model highlights that the observed behaviour of stimulated feldspar samples, such as photoluminescence, can be explained using both quantum tunnelling and consider the band tail states at the lower edge of the conduction band.

The other primary model hypothesises the opposite, with the proposal being that feldspars have a varied trap distribution which differs across families of feldspar (Li et al. 2011a; Li et al. 2011b; Thomsen et al. 2011; Clark et al. 1994a; Clark et al. 1994b). This model predicts that the mobility of free charge is responsible for stimulation response mechanisms, and accounts for phenomena such as phosphorescence.

The literature remains relatively split on which model is correct, and as such this report investigates a variety of feldspar samples to determine if a multi or a single trap origin for this phenomenon can be experimentally verified. This report will also investigate the properties of charge mobility within feldspars, and whether experimentally observed behaviour can be better explained using either quantum tunnelling or free charge mobility.

2. Experimental Method

For this experiment, twenty-three feldspar samples were utilised, with twenty-one being samples previously utilised in Clark and Sanderson's paper (Clark et al. 1994a). Two other samples were used, a sanidine standard provided by SUERC and the IAEA potassium feldspar standard F-1 (IAEA/RL/45). A complete sample list is shown in table 1.

For each sample, three disks and a stub were prepared, each with a total grain mass of around one gram. The disks were thermally cleared of their natural signal by heating them, with a heating rate of five degrees Celsius per second, up to 500 degrees Celsius, before cooling them and reheating them again.

2.1. Investigation of Sample Properties

In order to verify the purity of the samples used for this investigation, an examination of the twenty-three stubs taken from each sample material is required to ensure that the chosen samples had been correctly catalogued prior to selection. A Hitachi S-3400N Scanning Electron Microscope with an Oxford Instruments INCA x-ray analyser was used in this analysis.

A site of interest was selected for each stub sample, these typically encompassed between ten to fifteen grains depending on the sample. For each site, the available grains were processed using INCA, which returns the elemental composition of a selected region. It does this by first detecting the relevant grains using the atomic number contrast, which is derived from a backscattered electron image. Minerals are then identified using X-ray spectrum data and structural information from the BSE image and subsequently read out onto the user interface.

Depending on variation in surface features between grains for each sample, between fifteen and twenty-five area samples were investigated.

2.2. Sample Investigation Using Infra-Red Wavelengths

In R.J. Clark and D.C.W. Sanderson's 1994 paper (Clark et al. 1994a) it was observed that for the chosen samples, an excitation spectral survey revealed a variation in sensitivity, and in the ratio of the infrared (840nm and 900nm) to green (590nm) stimulation bands, and the ratio of the two infrared peaks in the emission spectrum from the xenon lamp used in this investigation.

Further investigation into this phenomenon which probes deeper into the infrared would be ideal as it should cast a clear light on the nature of electron traps in feldspars. As such, this will serve as the starting point for this project. As such, one of SUERC's portable OSL readers was used, and was set up with BG39 detection filters in the detection band and two main IR wavelengths from arrays of light emitting diodes – one centred on 890 nm, the other centred on 940 nm.

Two disks were taken from each of the twenty-three samples and were given a 100Gy dose. For each sample, a fifteen second dark count was first taken, followed by two stimulation periods using the 890nm laser lasting for thirty seconds each, another fifteen second measurement was taken without any stimulation, which was then followed by two further stimulation periods using the 940nm laser, and was concluded by a final fifteen second measurement with no stimulation.

This experimental setup allows for a recording of the photostimulated luminescence as it decays with continued stimulation and allows for an accurate calculation of both the depletion index for each sample at both stimulation wavelengths, and the ratio of the counts for each stimulation wavelength as described by Sanderson and Murphy (2010).

2.3. Investigation of Thermoluminescence Peaks

The question of charge mobility versus quantum tunnelling is also one that will be investigated in this project, To this end, one disk from each of the twenty-three samples were each dosed with 100Gy and used to collect a range of PTTL readings in order to determine if IRSL results in the mobility of charge to another electron trap that can be thermally probed. The TL reader used in this experiment is the same one which was used in Sanderson et al (1989).

This experiment consists of three parts. An initial heating up to 200 degrees Celsius, cooling over a period of forty seconds and then reheating to 200 degrees Celsius. A net photon count is recorded for each temperature. The sample is then placed in the same OSL reader as before and exposed to the same stimulation sequence. After this, the TL measurement was repeated after a measured thirty second wait.

2.4. Investigation of Post-Stimulation Phosphorescence

While conducting the previous two experiments it was noted that all samples showed PSP in the IRSL-PTTL run, and as such a further investigation was conducted using longer timescales for observing PSP to look at the decay constants from a subset of samples. The samples chosen were F1, RC246, RC484, RC485 and RC14. These were selected as it was noted that the measured PSP declined over different timescales depending on the sample. As such, IRSL stimulation was used in a range of samples followed by a long non-stimulating readout to determine if there are numerous exponential factors at work in the decay of post-stimulated phosphorescence across feldspar samples that are variable with stimulation wavelength.

Sample No.	Mineral	Reference No.	Location
PL003	Albite	RC14	S. Harris
PL004	Albite	RC168	S. Harris
PL005	Albite	RC169	S. Harris
PL006	Albite	RC164	S. Harris
PL016	K-Feldspar	RC167	S. Harris
PL017	K-Feldspar	RC174	Greenland
PL018	K-Feldspar	RC72	Norway
PL019	K-Feldspar	RC64	Norway
PL020	K-Feldspar	RC81	Norway
PL021	K-Feldspar	RC485	Greenland
PL022	K-Feldspar	RC484	Greenland
PL023	K-Feldspar	RC491	Greenland

PL024	K-Feldspar	RC503	Greenland
PL025	K-Feldspar	RC1396C	Assynt
PL026	K-Feldspar	RC389	Nigeria
PL027	K-Feldspar	RC456	Nigeria
PL028	K-Feldspar	RC683B	Aberdeen
PL029	Microcline	RC630	S. Harris
PL030	Microcline	RC165	S. Harris
PL031	Plagioclase	RC246	Greenland
PL032	Plagioclase	RC659	N. Harris
F1	K-Feldspar	F1	-
SAN	K-Feldspar	Sanidine	Colorado, USA

Table 1: **Complete sample list, all RC samples are from the 1994 Clark, Sanderson paper.**

3. Results and Analysis

3.1. Investigation of Sample Properties

Analysis of each sample using the scanning electron microscope revealed that for all the samples, bar the sanidine, each sample had been correctly catalogued.

Specifically, for the albite samples (RC14, RC168, RC169 and RC164 respectively) there were no substantial impurities in the grain selection which could be expected to alter experimental behaviour (See Appendix 1).

Regarding the microcline samples (RC630 and RC165), impressive homogeneity was observed in the elemental make up across the selected examination site, with no impurities recorded.

The plagioclase samples (RC246 and RC659) showed a large concentration of quartz alongside variations of either potassium or sodium concentrations. RC246 the highest quartz concentration, with over half of the selected grains containing quartz.

The SEM results for the sample labelled as sanidine (see figure A) were indicative that the supplied sample was not in fact Sanidine, as there proved to be very little potassium at all on the observed stub. As such, the origin of this specific sample was investigated, and it was discovered that the sample was composed of the waste material produced during the manufacture of SUERC’s batch of sanidine standard using material obtained in Fish Canyon Tuff, Colorado, USA - an area of keen geological research interest (M. Ort, 1997). Based on this, a high variance from disk to disk is expected.

The rest of the K-Feldspar samples only showed slight variations in the amount of sodium against the amount of potassium. There were also variations in the amount of quartz visible across the K-Feldspar samples.

As quartz does not react to IRSL it can be said that the variations in its presence across samples will have no effect in future experiments within this investigation.

Therefore, barring the sanidine, there is expected to be little variance between disks from each sample, as such the results of subsequent sections are expected to be reliable.

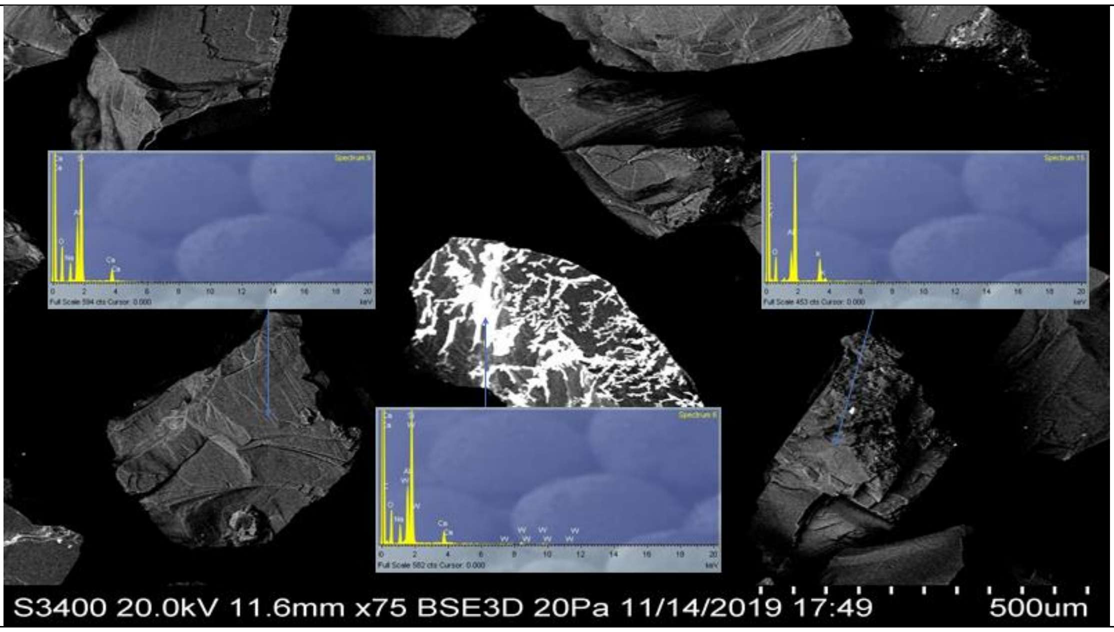

Figure A: SEM results of the sample labelled as sanidine which clearly show a tungsten infused grain alongside calcium feldspars.

3.2. Sample Investigation Using Infra-Red Wavelengths

Following the collection of data from each of the forty-six disks, Excel was used to calculate the ratio of the net total counts for each of the stimulation wavelengths for each sample. Subsequent graphs were generated using SigmaPlot.

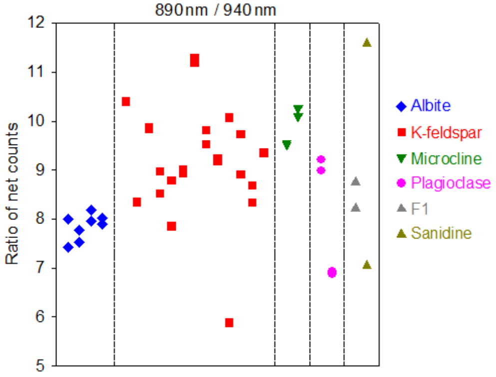

Figure B: Graph showing the ratio between the net counts for each wavelength for each sample disk.

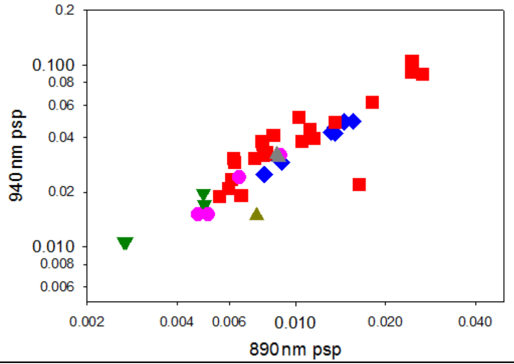

Figure C: Graph showing the seemingly linear trend between the PSP ratio for each sample disk.

The total counts for each sample at each wavelength was calculated by adding the total counts recorded during both thirty second stimulation blocks together and subtracting the dark count recorded before and after stimulation. To compensate for the fact that these dark counts were recorded for only a total of thirty seconds, compared to one minute for the stimulation, the dark count figures were doubled. The ratio of the net counts between the two wavelengths was then calculated.

As shown in their respective graphs in Appendix 2, for both wavelengths used, the Albite, Plagioclase and Microcline samples were grouped into their own clusters, whereas the more general K-Feldspars are distributed across graph. All samples aside from the sanidine have a low variance in count rate between sample disks. This is to be expected as, from section 3.1, the sanidine samples contain very little sanidine and so there may be considerable variation is content from dish to dish.

Additionally, when the ratio of these counts at both wavelengths is plotted for each sample as shown in figure B, the clustering of the feldspar families becomes even more apparent.

In order to determine a count loss rate with continuous stimulation, a depletion index was also calculated for each sample at both wavelengths. This was done by dividing the net counts recorded during the first thirty seconds of stimulation by those recorded from the second thirty second period.

The depletion indexes showed a greater response to the 890nm wavelength, with every sample having a ratio of 890nm depletion to 940nm depletion that was greater than one. While this could be attributed to the sample becoming depleted with continued stimulation, the ratio between both stimulation windows should remain unaffected and so this does lend credibility to an observation that both wavelengths have different stimulation properties for the feldspar samples.

Curiously, when the ratio of 890nm to 940nm PSP was taken it showed a rough linear trend as seen in figure C. This was taken to suggest something fundamental about its production that was closely tied to the structure of each sample and remained unchanged regardless of the choice in stimulation wavelength used.

3.3. Investigation of Thermoluminescence Peaks

As in section 3.2, Excel was used for reformatting of the raw data, while SigmaPlot was used to generate the subsequent graphs.

As shown across all graphs, showcased in Appendix 3, there is clear evidence of phototransfer as a result of the infra-red stimulation. The difference in peak location between the preheat TL measurement and the post-RISL measurement demonstrates that, depending on the sample, there is a tendency to move towards a low temperature peak centred between eighty and twenty degrees Celsius.

For some samples the post-stimulation curve contains negligible counts, most notably that of RC1396C and RC683B. This can be explained by considering that these samples have their electron traps fully cleared out by the IRSL-stimulation and so have little re-trapping occurring for the TL measurement to probe.

As seen in Figure D, the post-IRSL shows a clear shift in the peak of the detected net counts, and the formation of a clear shoulder. This is indicative of charge transport occurring.

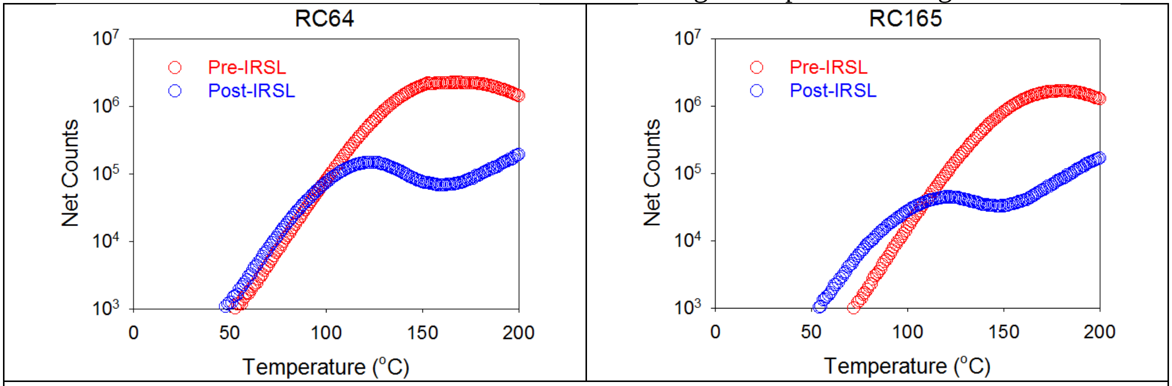

Figure D: Graphs showing the creation of a new lower temperature peak as a result of IRSL for two of the samples.

This TL data was also used to calculate the trap depth which was being probed by either measurement. To do this, each TL curve was fitted to an Arrhenius plot. This, when combined with each peak's respective temperature, gave the activation energy for each trap. This could then be applied in a one-dimensional kinetic simulation to return a mean lifetime for the trap, and its associated frequency factor.

The data in Appendix 4 clearly supports the graphic findings, with the preheats generally activating a trap with an energy range from 1-1.2eV depending on the sample, and the post-IRSL TL measurement probing much shallower traps with energies 0.7-0.8eV and one outlier which was activated at 0.5eV. In the case of some samples, a trap with energies 0.1-0.35eV was activated by the post-IRSL. This either correlates to short lived shallow traps and typically have a lifetime of less than ten minutes or suggests that these samples were completely cleared out by the IRSL sequence.

Curiously, significant PSP was measured across all samples. This led onto section 3.4, where the PSP decay for a selection of samples was investigated further.

3.4. Investigation of Post-Stimulation Phosphorescence

SigmaPlot was used for data processing and graph generation for this section of the investigation.

Investigation of the five samples revealed a common trend of the 890nm IRSL stimulation returning a higher post-stimulation phosphorescence count than the 940nm. This concurs with findings from sections 3.2 and 3.3, which both suggest that 890nm is the peak activation wavelength. The regression wizard function within SigmaPlot was then used to provide a best fit relationship for the PSP decay over time. It did this by deriving a relationship to describe the decay rate which has the form:

$f=y_0+a*exp(-b*x)+c*exp(-d*x)+g*exp(-h*x)$

Where b,d,h are time components of the decay, y_0 is the average count rate without stimulation and a,c,g are scaling constants for each time component.

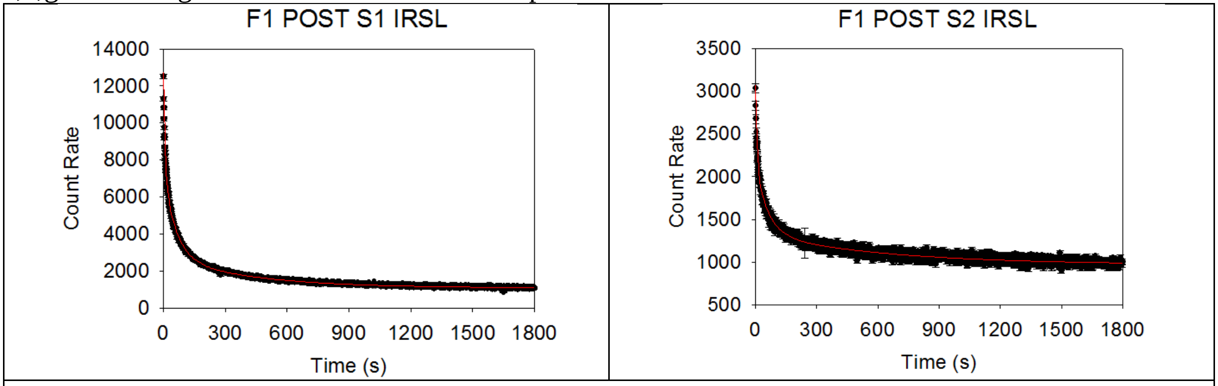

Figure E: Graphs showing the decay rate of PSP over time for the sample of F1 for both stimulation wavelengths used.

The experimental results, graphs and regression wizard calculation results are shown in Appendix 5 and an example of the resulting F1 PSP decay graphs are displayed in figure E. This data shows, critically, a variance in the time components present in the decay rate of post-stimulation phosphorescence which is both wavelength and sample dependent. As expected, the F1 PSP decay was far less turbulent than the PSP decay for RC246, and likewise the RC14 sample showed a cleaner decay curve than RC484 and RC485. Across all samples the S2 wavelength (940nm) resulted in less PSP than that seen after S1 (890nm) stimulation. RC246 showed very little PSP after S2 exposure, which poses interesting questions for trap behaviour and the properties of charge mobility within these samples.

4. Discussion

This investigation first looked at how IR excitation band in feldspars changes with wavelength. The findings of this result will be closely referenced to the paper written by Kumar et al. 2018 which included low temperature measurements. The findings of these papers interpret the IR excitation band as the product of a single trap - although even close to liquid helium temperature, the IR excitation band reported in these papers remains broad.

In Clark et al. (1994a), figure 2 shows the variations in the excitation ratio at 840 and 900nm (the experiment was conducted at room temperature, as opposed to the above Risoe paper). This corresponds to strong lines expected in the Xenon lamp spectrum which was used in that experiment.

Clark and Sanderson found variable excitation ratios across the range of feldspar samples that they used, with clear differences found between the albite and plagioclase samples in the data set. Additionally, the potassium feldspar samples used returned a varied data set.

To compare the results from that paper and this report, the same experiment has been repeated as detailed above in section 2.2. As such, whereas Clark and Sanderson probed the excitation on the short wavelength side of the main peak wavelength this report has broadened that horizon to now look at the excitation on the long wavelength side.

As previously described in section 3.2, the stimulation ratio of 890nm vs 940 nm also shows a similar layout to Clark and Sanderson's paper. This includes the tight albite and plagioclase clusters. However, compared with Clark and Sanderson's paper, the results of this experiment found that there was a greater dispersion across the potassium feldspar samples. As such, since both results complement each other, the findings of this experiment can be taken as evidence to show that the families of traps involved in IRSL production are distributed and inherently linked with their native lattice structures. However, the findings regarding the linear PSP ratio for each wavelength across the sample set does point towards the PSP having a fundamental trap from which it is emitted.

The results described in section 3.3 also compliment the findings in the 1980's that demonstrated that photo-stimulation in the 400-700nm wavelength range was accompanied by PTTL to shallower traps. This photo-transferred trap emits at about 80 degrees centigrade, which lines up with the findings detailed in section 3.3. As such, it makes sense to state that that this is also true for IR stimulation in the 890-940nm range.

This phototransfer process that gives a new TL peak after IR measurement can be shown independently using either the graphical data or the kinetic simulations data taken from the Arhenius plot. However, when these two results are used together, they show a very strong case for free charge moment. Along with the evidence of phosphorescence after IR stimulation (which went onto form the basis for further investigation that was detailed in sections 2.4 and 3.4), it can be reported that the movement of charge and re-trapping in shallow traps as a consequence of stimulation is an active phenomenon which can be observed.

Regarding the findings laid out in section 3.4, it can be stated as a result of this preliminary experiment, from which more in-depth investigations could be conducted, that the time constants of the observed post-stimulation-phosphorescence at both the 890nm and 940 nm stimulation wavelengths have a multi-exponential form.

Also of note is the difference in the time constants which arises when the excitation wavelength of 890nm is used to stimulate the samples compared with 940nm. Additionally, stimulating at the peak excitation wavelength of 890nm results in more phosphorescence than on the long wavelength tail, and this post-890nm stimulation phosphorescence contains strong components with very short decay times.

There are several interpretations which could explain this behaviour. Within a re-trapping model, stimulating the sample with a higher energy packet (such as at the peak excitation wavelength at 890nm) allows charge carriers to migrate further away from the trap, and as such they could move to regions within the sample where there are more shallow traps available to intercept the mobile charge, and, as such, delay luminescence emission. On the other hand, at 940nm, which supplies less energy to the sample, the charge carriers are unable to get close to these shallow traps and simply re-collapse back to the traps they were emitted from.

Another interpretation is based on thermally assisted tunnelling. This utilises the fundamental trap theory and can indicate that the process of thermally heating the sample will delay the charge lost during recombination as the free charges travel along the band-tail states of the sample. This is not without precedent and could be explained using a band-hopping mechanism like that proposed by Morthkai et al. (2012). This would occur during the IRSL stimulation cycle between TL heating, the sample would experience a variation in charge density as the electron trap is emptied and the charge moves to either recombine or escape. This explains the varied post-stimulation phosphorescence across the sample set, as this variance in charge density would likely result in a near binary response to IRSL and TL such that either the sample will undergo PSP or it will not, and the wavelengths used on the samples will only alter the free charge that is emitted or recombined. However, it does not account for the differences in decay time constants in this PSP which have been found, nor does it account for the differences in the response to both of the stimulation wavelengths used.

5. Conclusions

Over the course of this investigation it has been the aim of this report to answer two fundamental questions: What is the best model to describe the structure of electron traps within potassium feldspars? What is the mechanism that explains the movement of charge within feldspars?

Following investigation into the properties of each chosen sample using the methods of IRSL and TL detailed in previous sections, the experimental results – particularly those detailed in section 3.3 - it is the finding of this report that the results obtained are best described using a distributed trap model. This was decisively proven by the clear emergence of photo-transferred peaks following infrared stimulation, with the different activation energies of at least two traps being determined using kinetic calculations: one shallow, with activation energies of 1-1.2eV, and one shallow, with activation energies of 0.7-0.8eV, though another even shallower trap which is extremely short lived with activation energies 0.1-0.35eV may also exist in some samples.

This behaviour is also a clear representation of charge transport rather than quantum tunnelling from a fundamental trap to an acceptor site as it is an unmistakeable example of free charge being stimulated out of a deeper trap and moving to either escape the system or a trap with a lower activation energy. The free charges which leave the system rather than recombining into another trap do so via phosphorescence and this has been observed for nearly all samples across every experiment.

Additionally, the variance in the decay time constants of this post-stimulation phosphorescence across samples and depending on the wavelength is also evidence of both distributed electron traps and free charge movement.

As such this report finds that the experimental evidence lends far more credibility to the existence of distributed traps within feldspars which utilise charge transport, though the opposing mechanism of quantum tunnelling alongside fundamental feldspar traps cannot be ruled out entirely because it can be applied to several of the results obtained over the course of this investigation with a fair amount of plausibility.

6. Further Work

A clear start to further research would be the repeating of the experiments detailed in this report at controlled temperatures both above and below the twenty-seven degrees Celsius used over the course of this investigation to model the effect temperature has on PSP decay rate and stimulation response variance depending on the used wavelength. This would allow better comparison with the 2018 paper by Kumar et al. which looked at the phenomena at liquid helium temperatures.

A further point of interest to research would be repeating the experiment detailed in section 2.4 with a large sample collection and readout time. As this experiment was limited to five samples in this report due to time constraints, having a larger sample collection and readout time would be an excellent and thorough way to map the contribution of the decay time exponents to the PSP decay curve.

The setup of the experiment detailed in section 2.3 also contained an oversight which was only realised close to the finalisation of this report. The TL peak probed by the post-IRSL TL measurement would be probing the peak caused by the 940nm stimulation. As such, repeating this experiment but altering it so that a TL measurement was conducted after the 890nm AND 940nm stimulation is recommended. This would allow investigation into whether the TL peak itself differs depending on the stimulation wavelength used. Based on other results obtained over the course of this investigation, it would likely be the case that the 940nm TL peak would differ from the 890nm TL peak, and potentially kinetic simulations obtained from this data may point towards the existence of a different shallow trap that the charge freed by the 890nm stimulation recombine in.

Another line of investigation which could be undertaken is the use of a BG-39 filter in combination with an IRSL reader to repeat the experiments detailed in sections 2.2, 2.3 and 2.4 as to obtain readouts at other various additional stimulation wavelengths. Doing so would provide a much clearer picture as to the precise workings of how a chosen stimulation wavelength effects the properties of electron trapping, re-trapping and charge movement.

Acknowledgements

The author thanks the Scottish Universities Environment Research Centre (SUERC) for hosting this project's investigation and allowing the use of laboratory equipment which was crucial to gathering the results obtained.

The author thanks Professor D.C.W Sanderson and Doctor A. Cresswell for their assistance in helping the author familiarise themselves with the lab equipment, SigmaPlot, and being on hand to discuss specifics and technical details.

References

[1] M. Ort, "New results for the 27.8Ma Fish Canyon Tuff and the La Garita Caldera, San Juan volcanic field, Colorado," (1997)

[2] IAEA, "Report on the intercomparison run F-1 U and K (Th) in feldspar," IAEA/RL/45

[3] M. Andersen, M. Jain, P. Tldemand-Lichtenberg, "Red-IR stimulated luminescence in K-feldspar: single or multiple trap origin?" J. Appl. Phys. 112, 043507 (2012); https://doi.org/10.1063/1.4745018

[4] R. Visocekas, “Tunnelling radiative recombination in labradorite: its association with anomalous fading of thermoluminescence,” Nucl. Tracks. Vol. 10. Nos 4-6, pp. 521-529, 1985

[5] V. Pagonis, C. Kulp, “Monte Carlo simulations of tunneling phenomena and nearest neighbor hopping mechanism in feldspars,” Journal of Luminescence 181 (2017) 114–120

[6] F. Şahiner, G. Kitis, V. Pagonis, N. Meriç, G. Polymeris, “Tunnelling recombination in conventional, post-infrared and post-infrared multi-elevated temperature IRSL signals in microcline K-feldspar,” Journal of Luminescence 188 (2017) 514–523

[7] R. Kumar, M. kook, A.S. Murray, M. Jain, “Towards direct measurement of electrons in metastable states in K-feldspar: Do infrared-photoluminescence and radioluminescence probe the same trap?” Radiation Measurements 120 (2018) 7–13

[8] P. Morthkai, J. Thomas, M.S. Pandian, V. Balaram, A.K. Singvi, “Variable range hopping mechanism in band-tail states of feldspar: A time-resolved IRSL study,” Radiation Measurements 47 (2012) 857e863

[9] A.G. Wintle, “Anomalous fading of thermoluminescence in mineral samples,” J. Luminescence 15, 385-393, (1973)

[10] D.C.W. Sanderson, “Fading of thermoluminescence in feldspars: Characteristics and corrections,” Nucl. Tracks Radiat. Meaa., Vol. 14, Nos 1/2, pp. 155--161, 1988

[11] D.J. Huntley, M.R. Baril, S. Haldar, “Tunnelling in plagioclase feldspars,” J. Phys. D: Appl. Phys. 40 (2007) 900–906

[12] Huntley, D.J., Godfrey-Smith, D.I., Thewalt, M.L., "Optical dating of sediments,” 1985, Nature 313 (5998), 105–107

[13] R.J. Clark, D.C.W. Sanderson, “Photostimulated luminescence excitation spectroscopy of feldspars and micas,” Radiation Measurements Vol. 23, Nos 2/3,p p. 641-646, 1994a

[14] D.C.W. Sanderson, C. Slater, K.J. Cairns, “Thermoluminescence of foods: origins and implications for detecting irradiation,” Radiat. Phys. Chem. Vol. 34, No. 6, pp. 915-924, 1989

[15] R.J. Clark, D.C.W. Sanderson, “Pulsed photostimulated luminescence of alkali feldspars,” Radiation Measurements, Vol. 23. Nos 2/3. pp. 633-639, 1994b

[16] B. Li and S.-H. Li, “Thermal stability of infrared stimulated luminescence of sedimentary K-feldspar,” Radiat. Meas. 46(1), 29–36 (2011a)

[17] B. Li and S.-H. Li, “Luminescence dating of K-feldspar from sediments: A protocol without anomalous fading correction,” Quaternary Geochronol. 6(5), 468–479 (2011b)

[18] K. J. Thomsen, A. S. Murray, and M. Jain, “Stability of IRSL signals from sedimentary K-feldspar samples,” Geochronometria 38(1), 1–13 (2011)

[19] Sanderson, D.C.W. and Murphy, S. (2010) Using simple portable OSL measurements and laboratory characterization to help understand complex and heterogeneous sediment sequences for luminescence dating. Quaternary Geochronology, 5(2-3), pp. 299-305

Appendices

APPENDIX 1

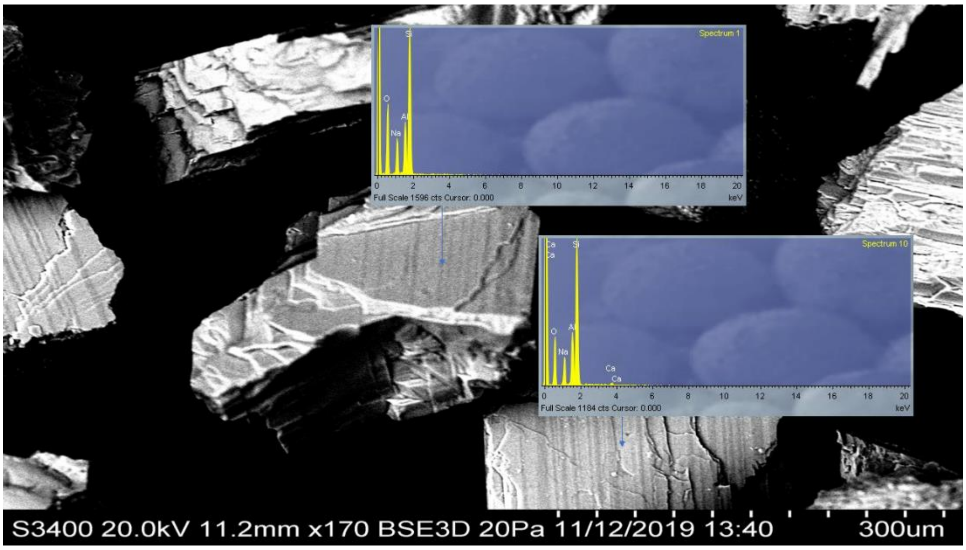

RC14

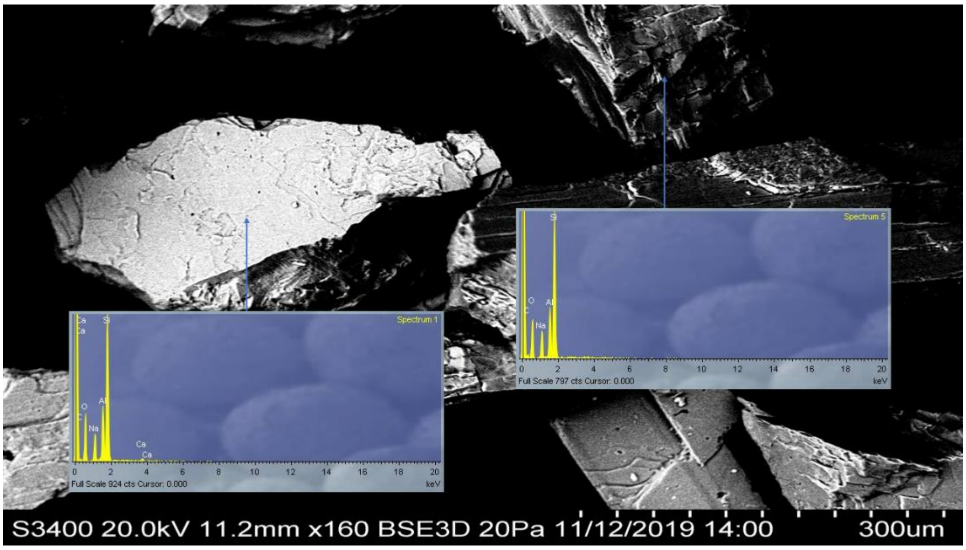

RC164

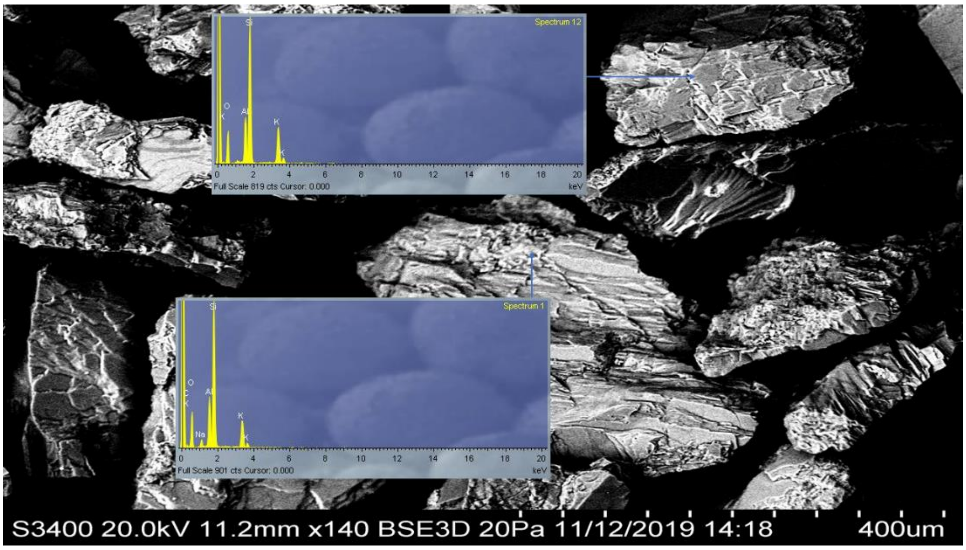

RC174

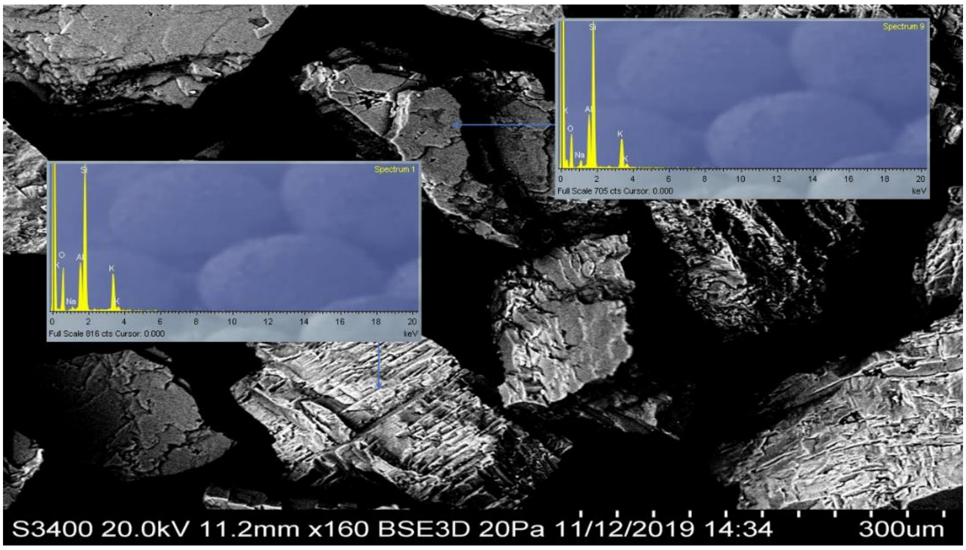

RC72

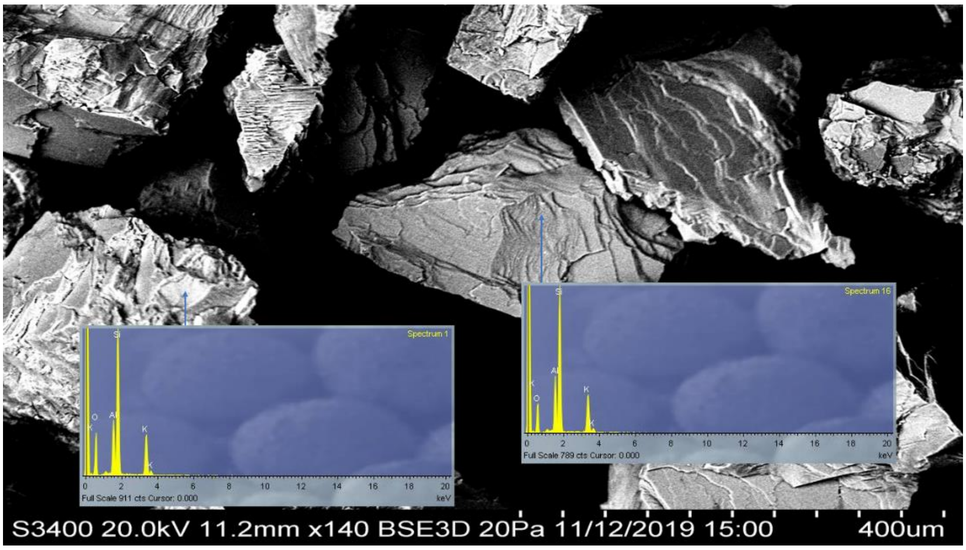

RC64

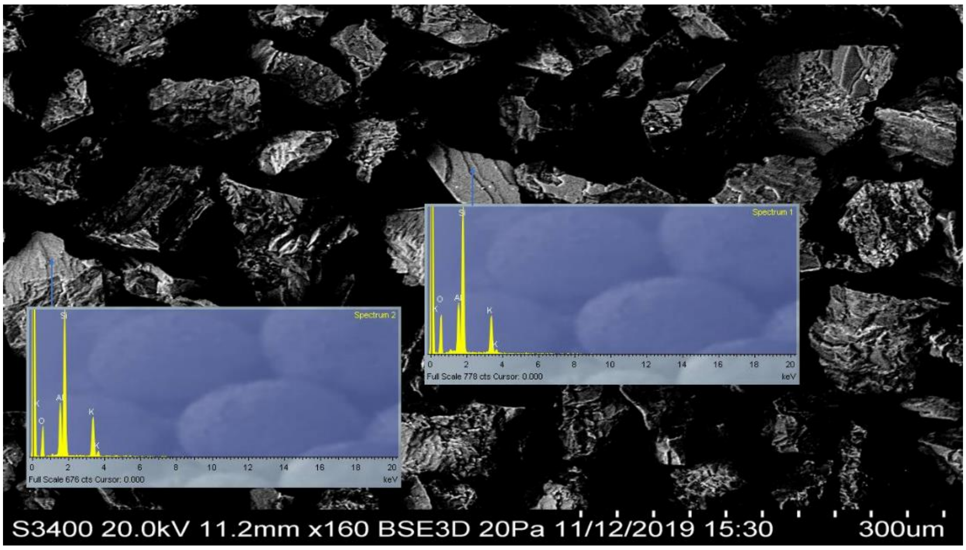

RC1396C

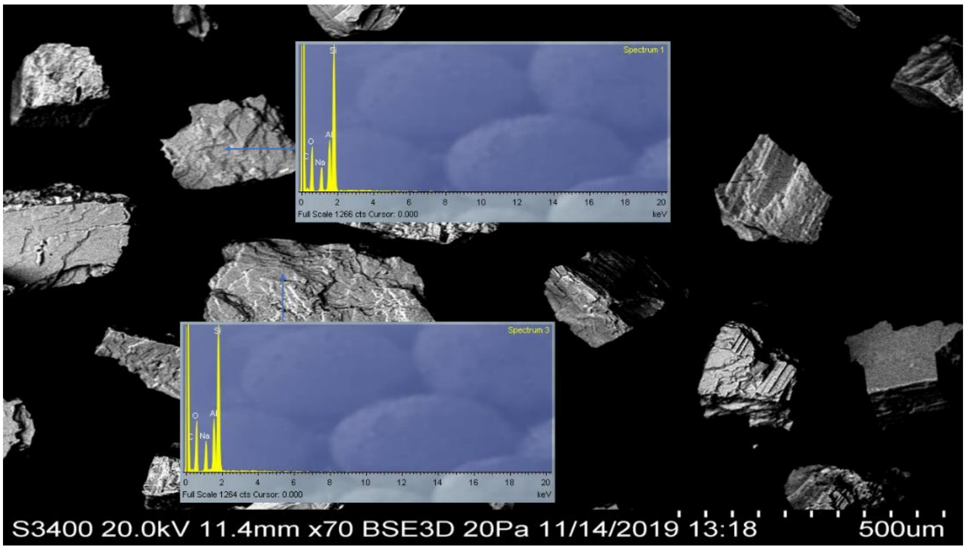

RC168

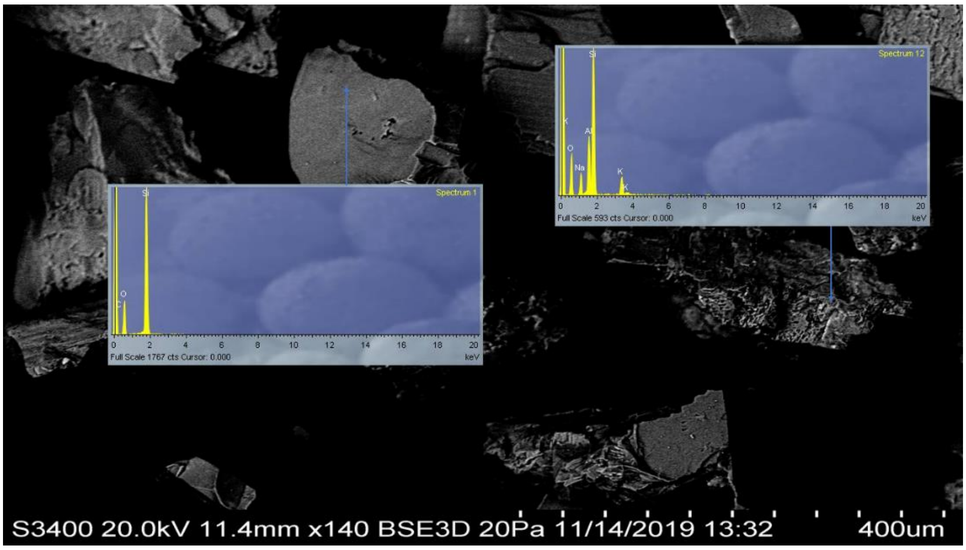

RC169

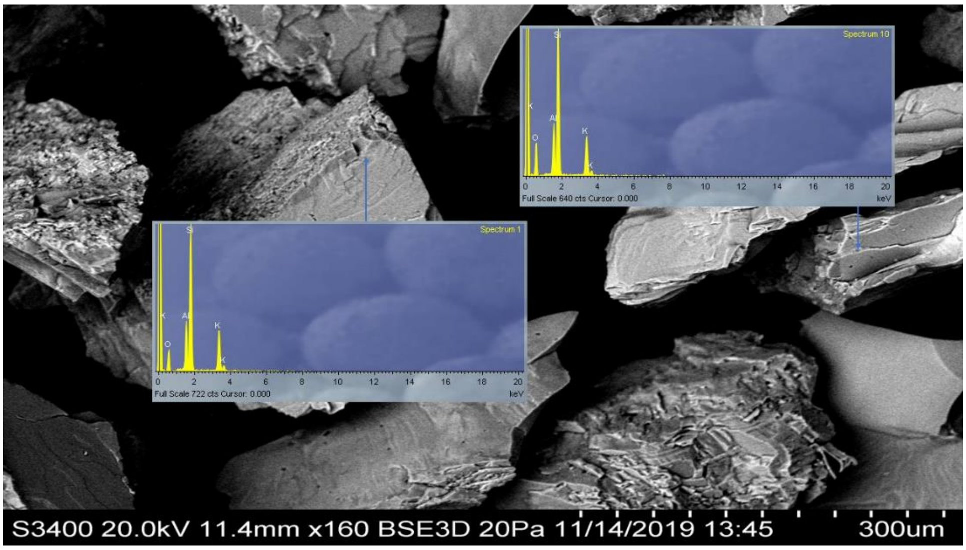

RC167

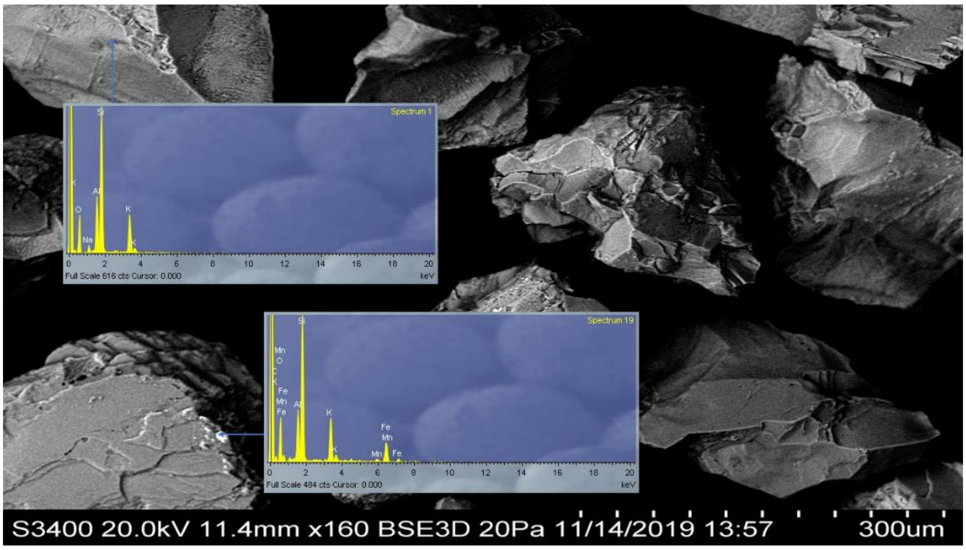

RC484

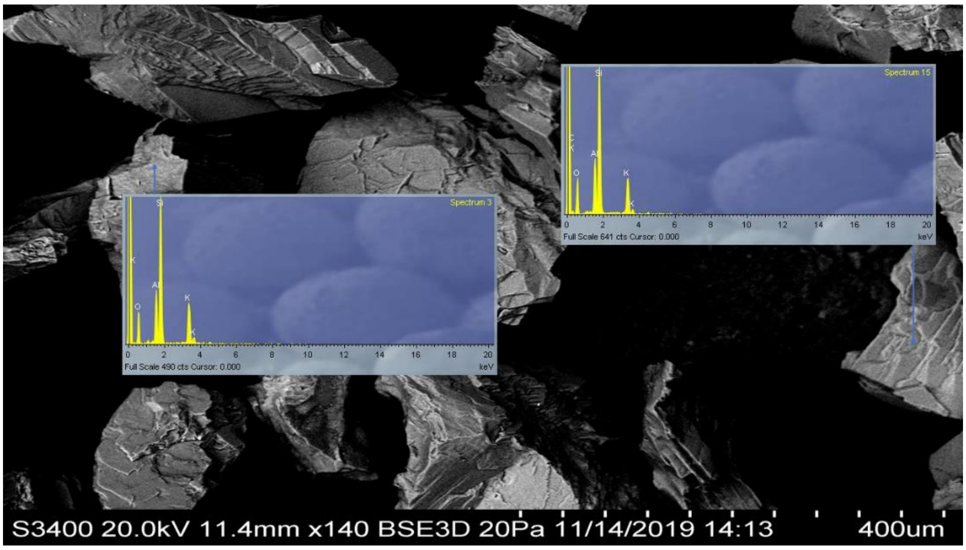

RC491

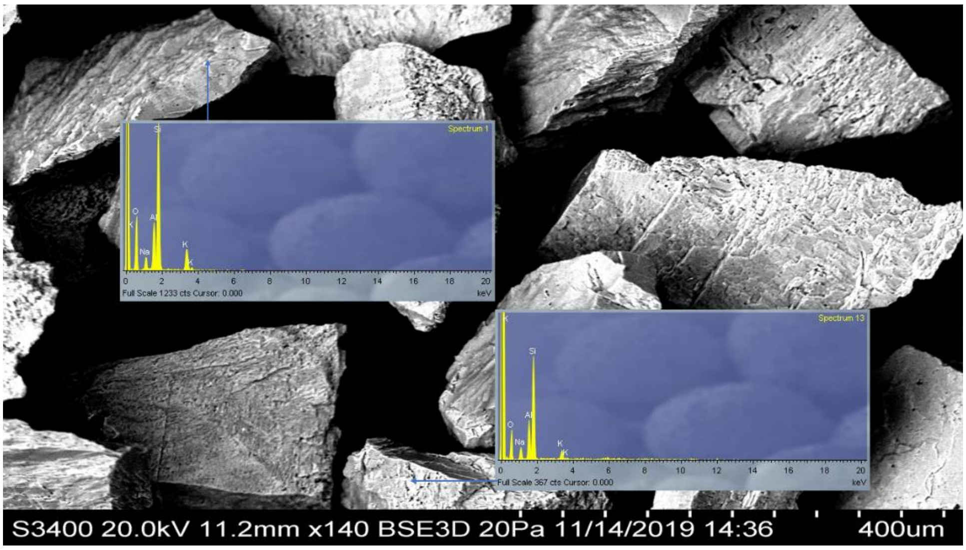

RC389

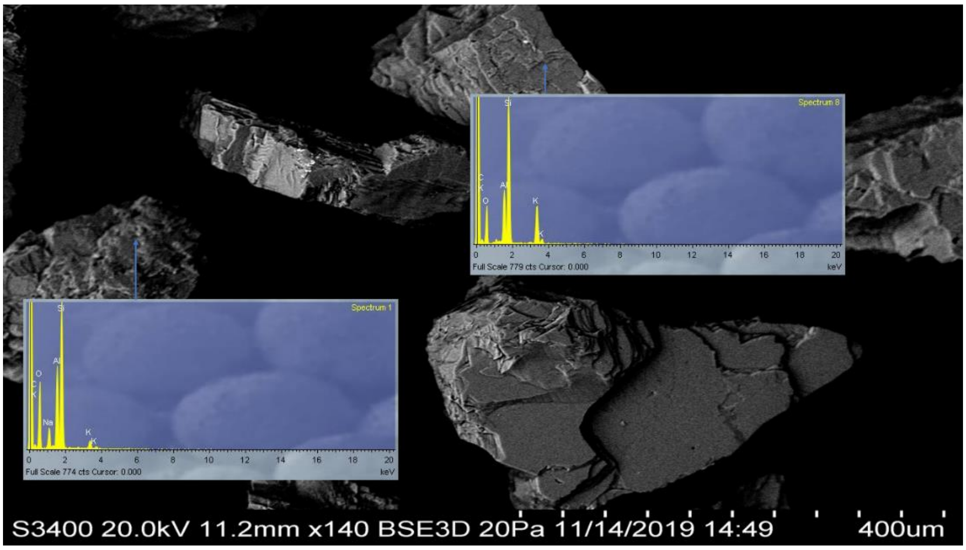

RC81

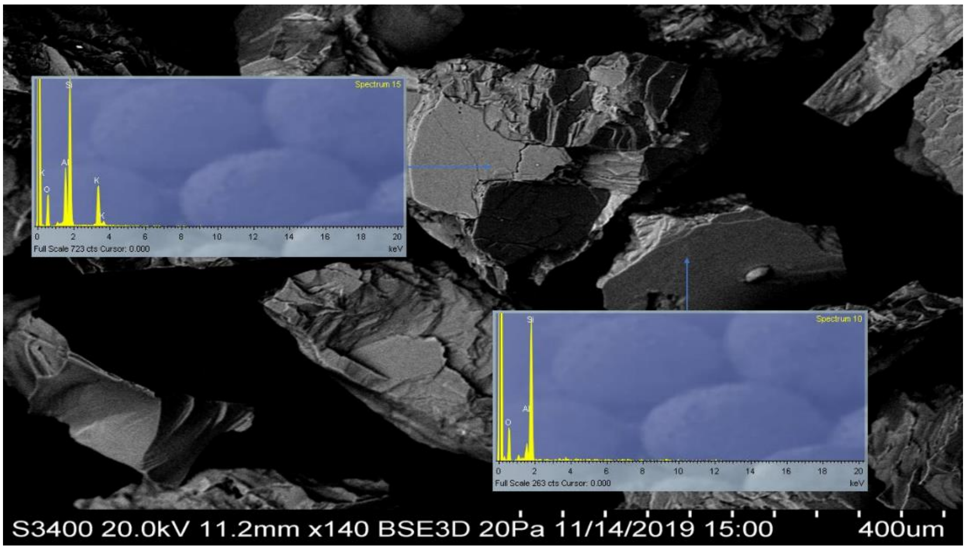

RC485

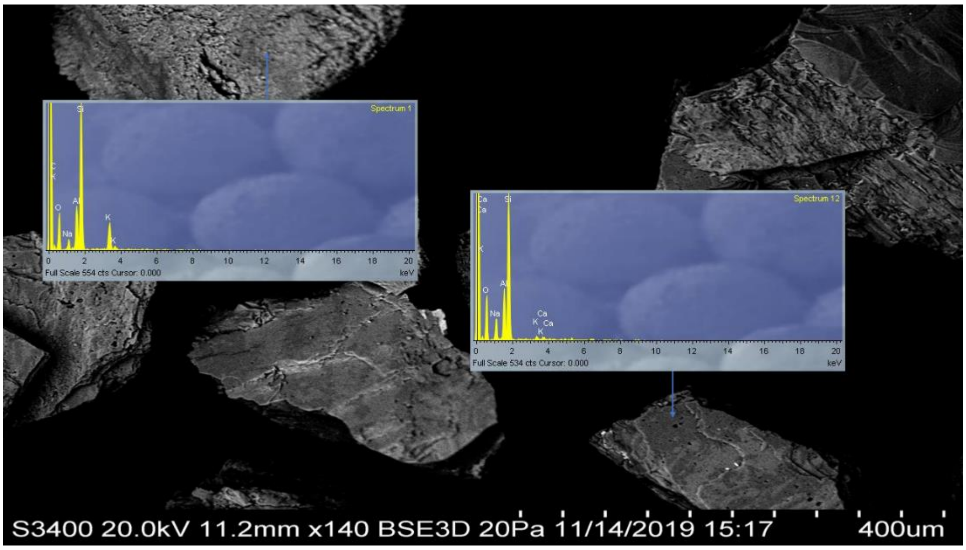

RC456

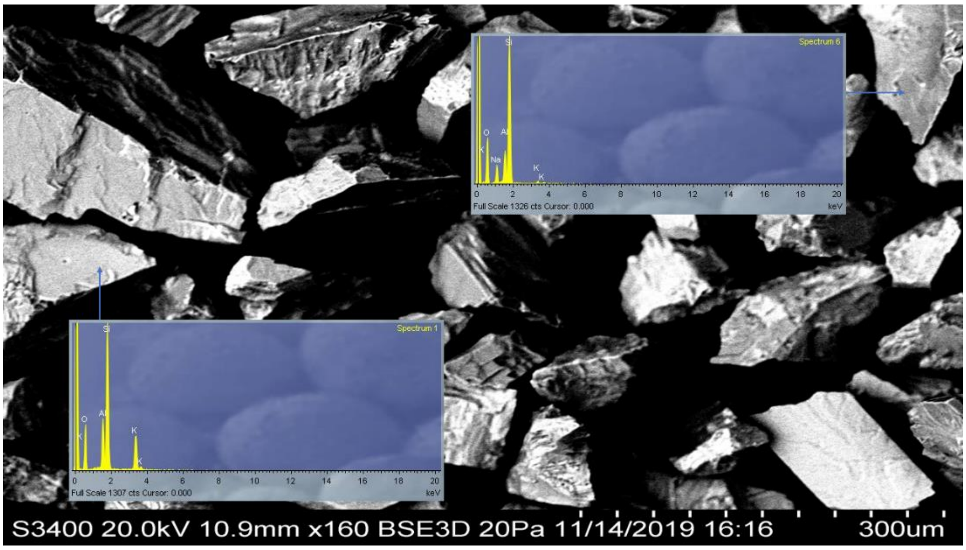

RC683B

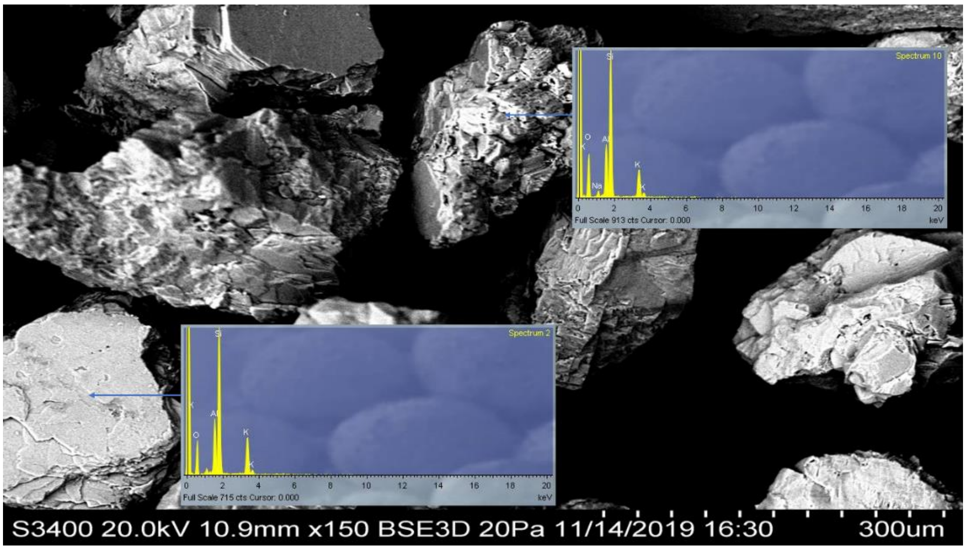

RC630

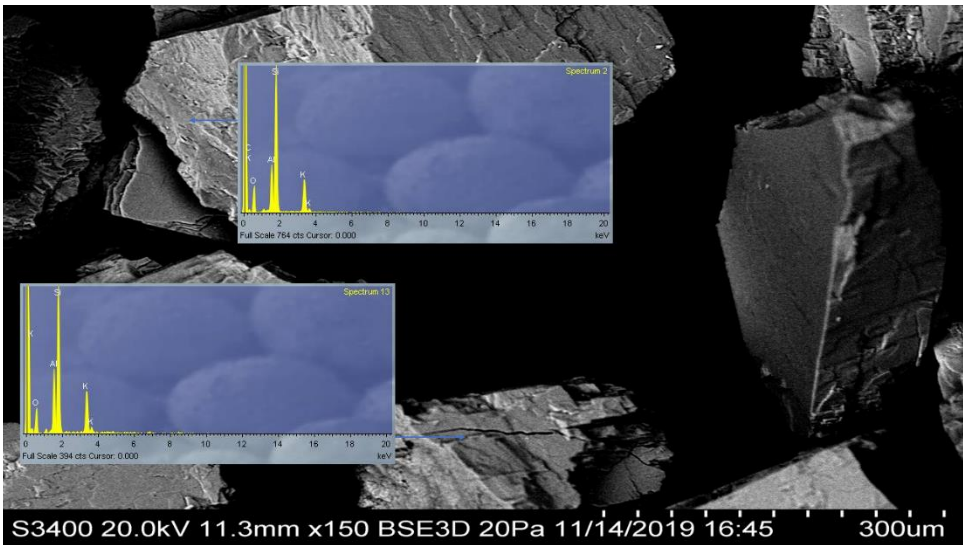

RC165

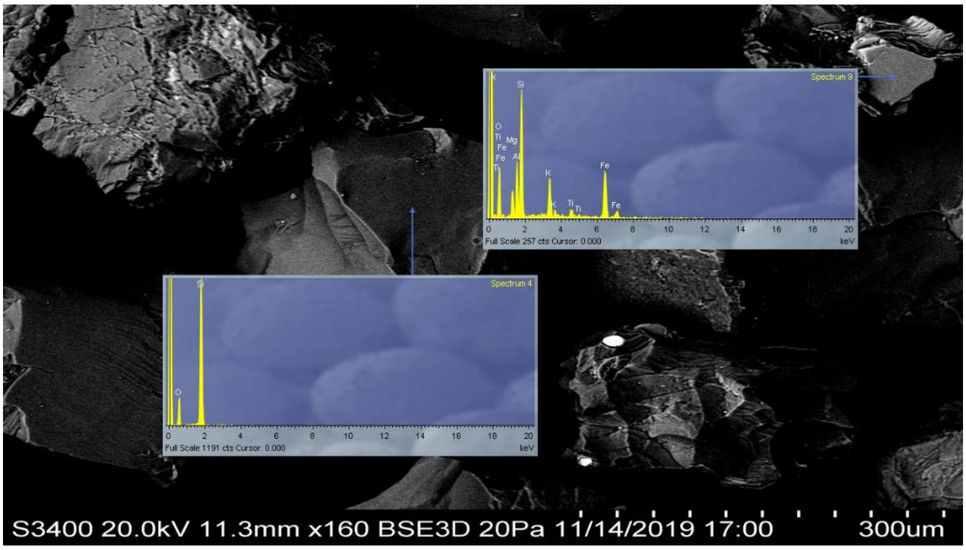

RC246

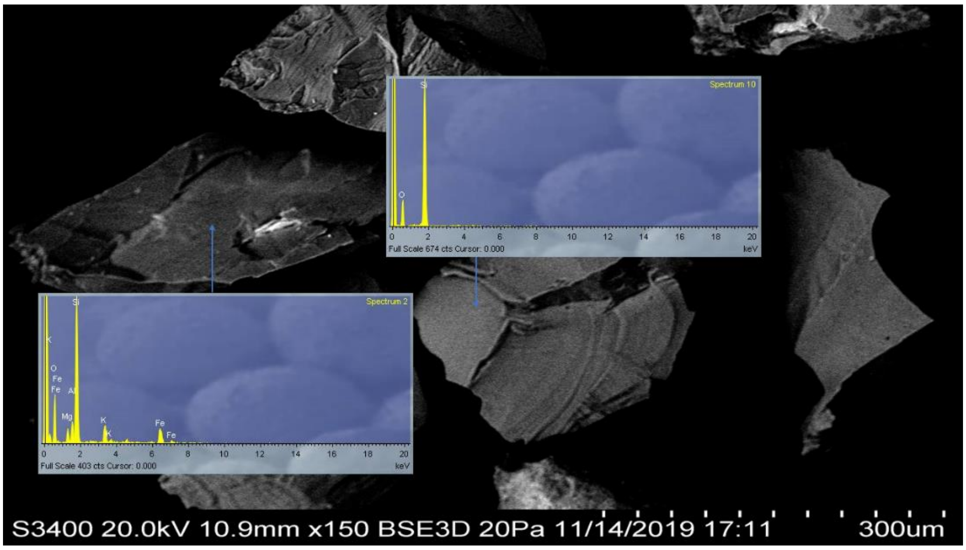

RC659

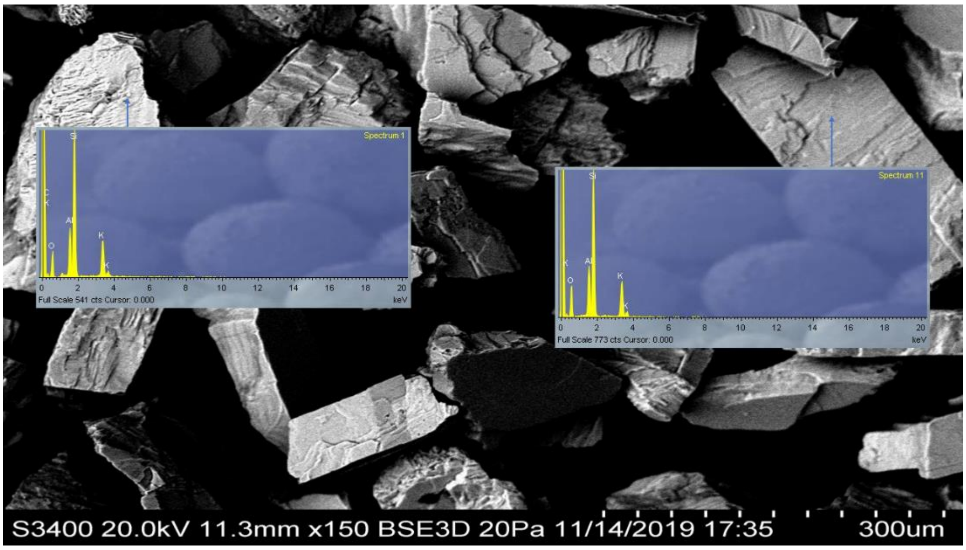

F1

APPENDIX 2

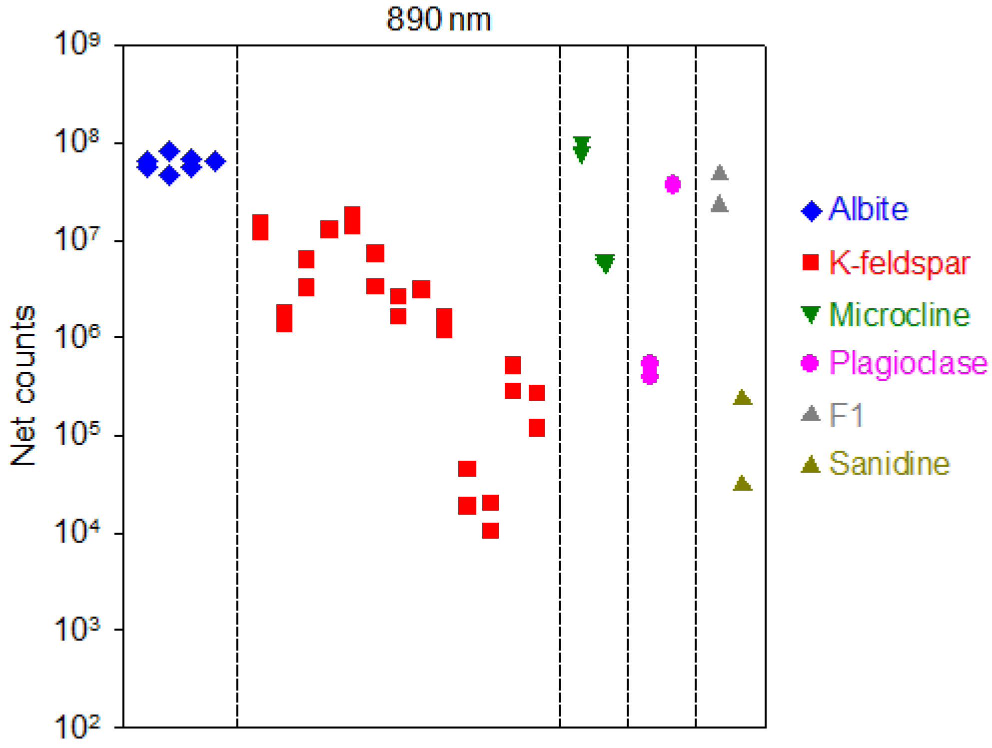

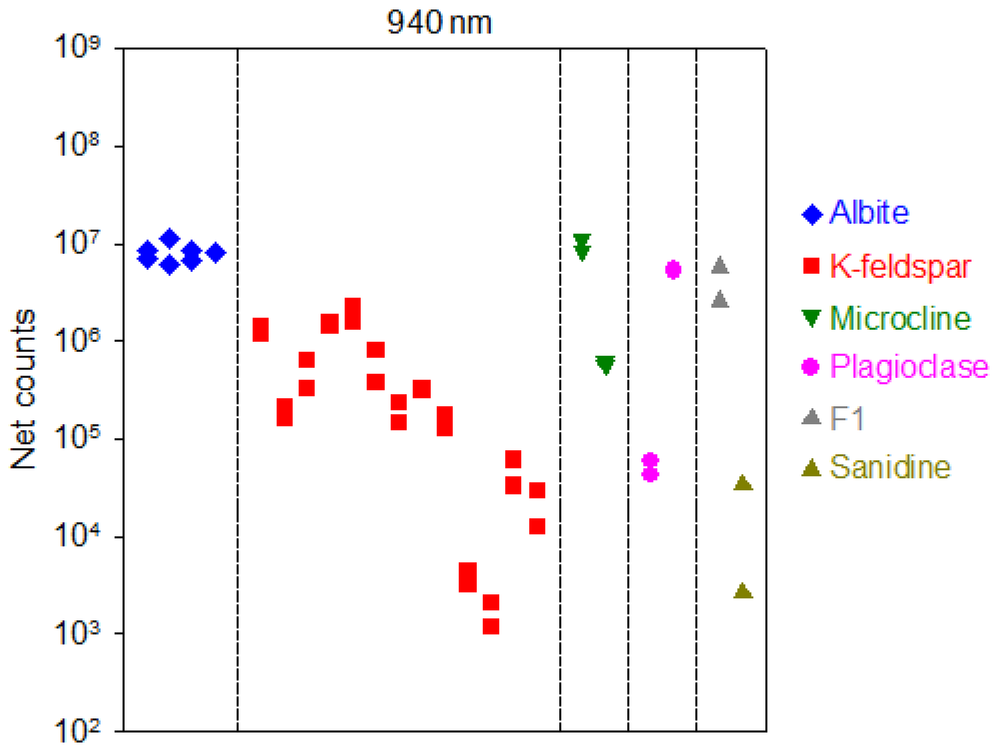
940 nm
Net counts
10⁹
10⁸
10⁷
10⁶
10⁵
10⁴
10³
10²
◆ Albite
■ K-feldspar
▼ Microcline
● Plagioclase
▲ F1
▲ Sanidine

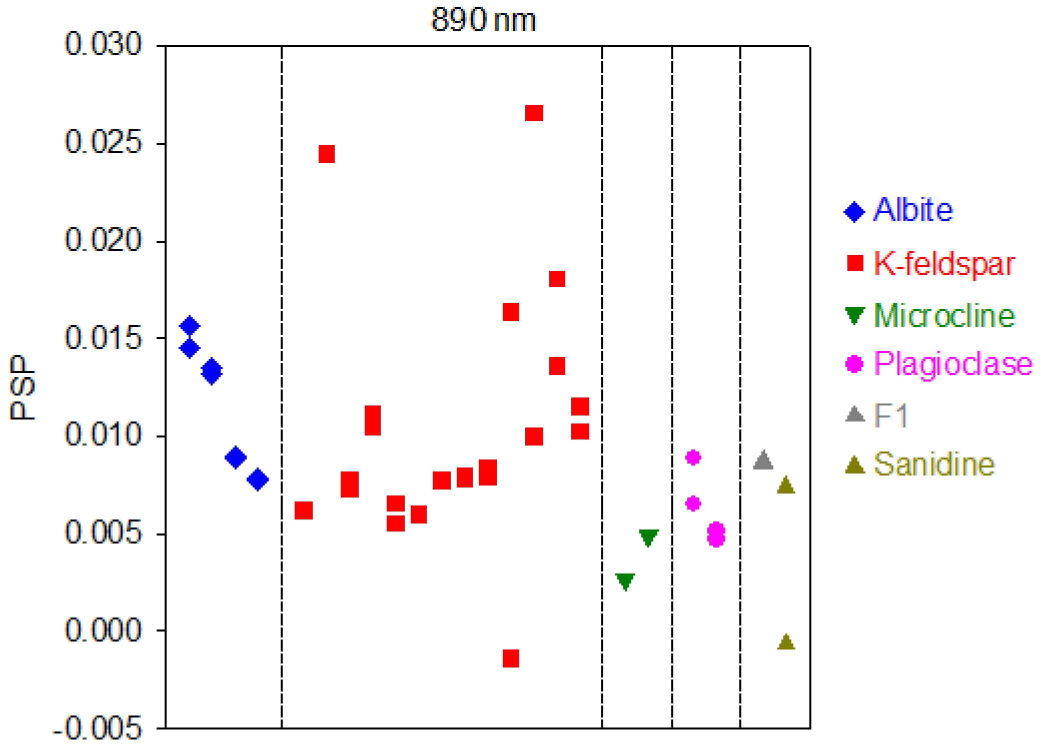
890 nm
PSP
0.030
0.025
0.020
0.015
0.010
0.005
0.000
-0.005
◆ Albite
■ K-feldspar
▼ Microcline
● Plagioclase
▲ F1
▲ Sanidine

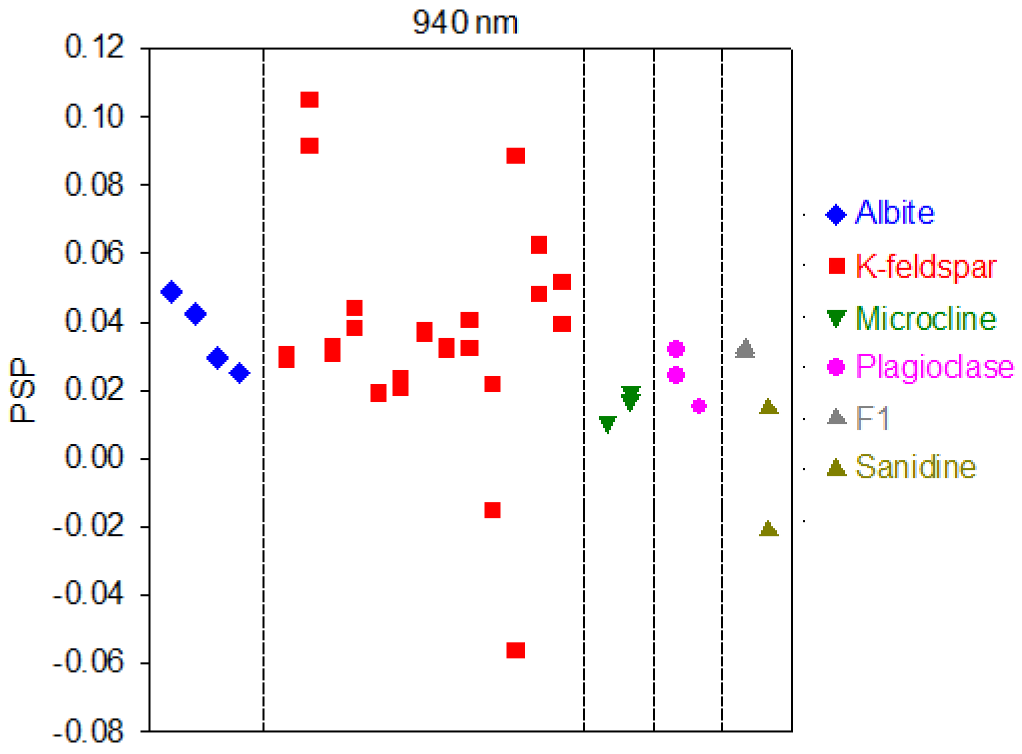
940 nm
PSP
0.12
0.10
0.08
0.06
0.04
0.02
0.00
-0.02
-0.04
-0.06
-0.08
◆ Albite
■ K-feldspar
▼ Microcline
● Plagioclase
▲ F1
▲ Sanidine

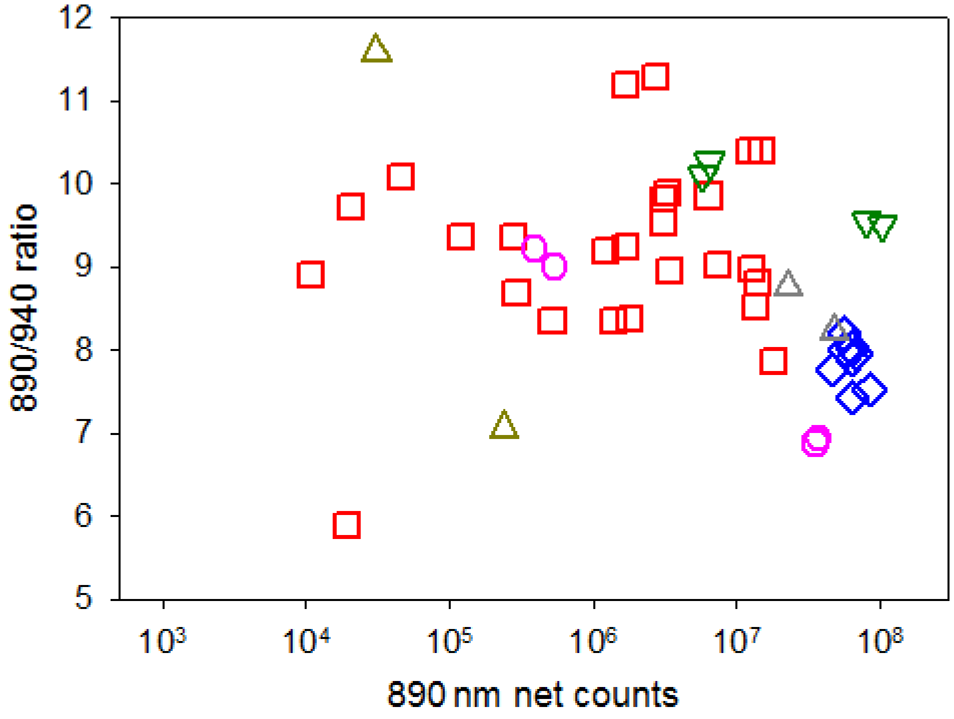
890/940 ratio
12
11
10
9
8
7
6
5
10^3
10^4
10^5
10^6
10^7
10^8
890 nm net counts

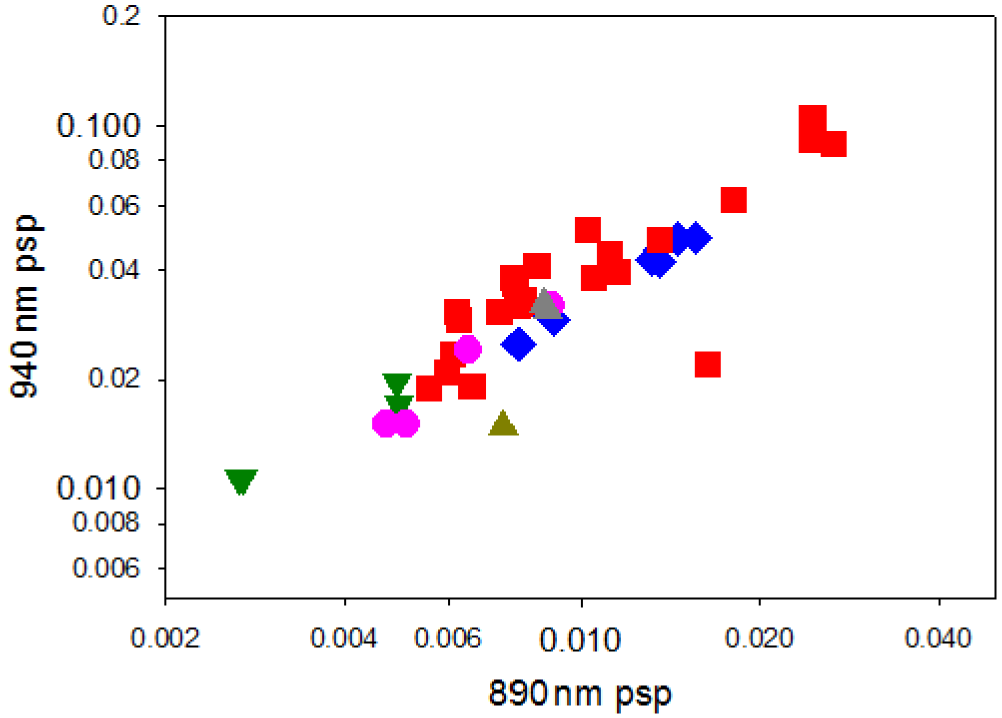
0.2
0.100
0.08
0.06
0.04
0.02
0.010
0.008
0.006
940 nm psp
0.002
0.004
0.006
0.010
0.020
0.040
890 nm psp

APPENDIX 3

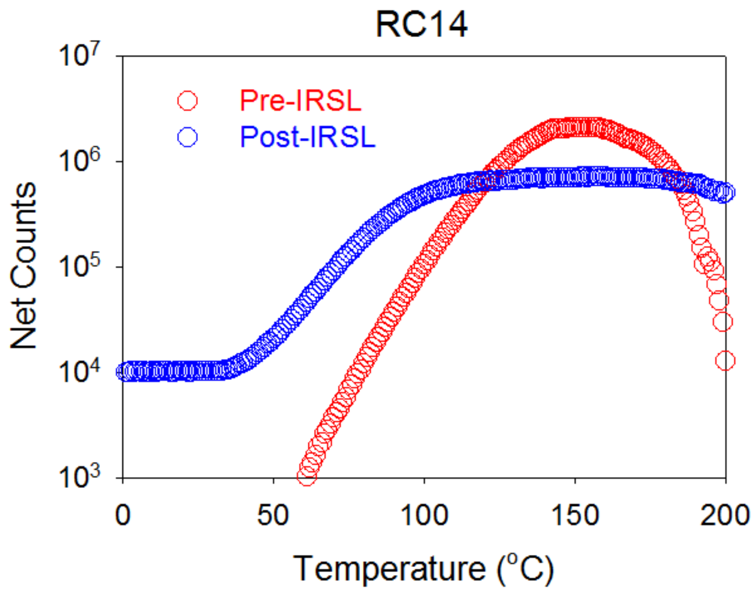
RC14
Pre-IRSL
Post-IRSL
Net Counts
10^7
10^6
10^5
10^4
10^3
0
50
100
150
200
Temperature (°C)

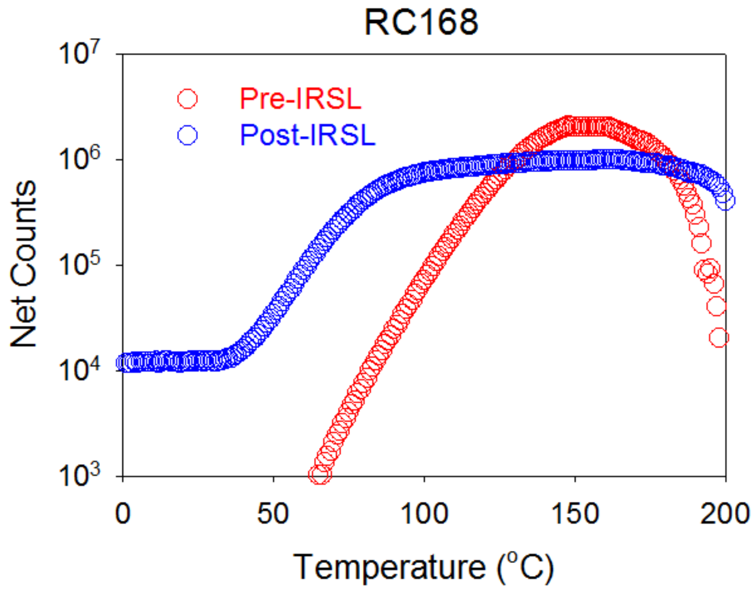
RC168
Pre-IRSL
Post-IRSL
Net Counts
10^7
10^6
10^5
10^4
10^3
0
50
100
150
200
Temperature (°C)

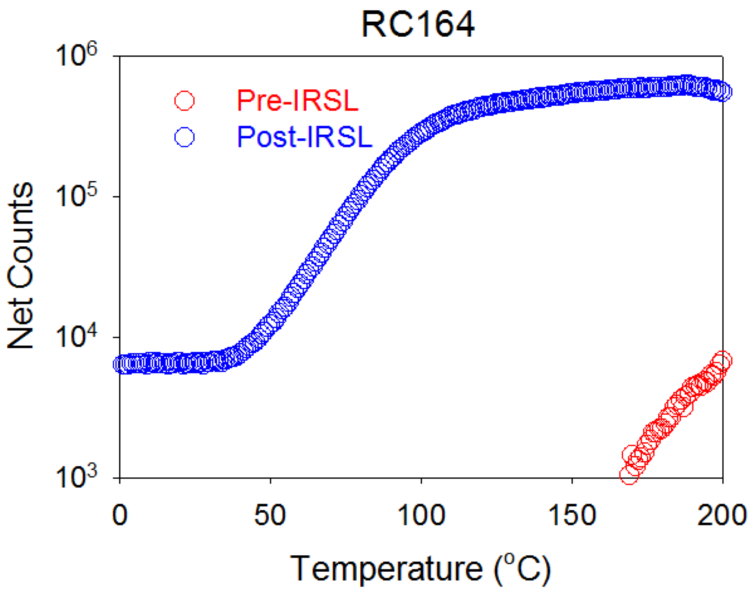

RC164

Pre-IRSL
Post-IRSL
Net Counts
10^6
10^5
10^4
10^3
0
50
100
150
200
Temperature (°C)

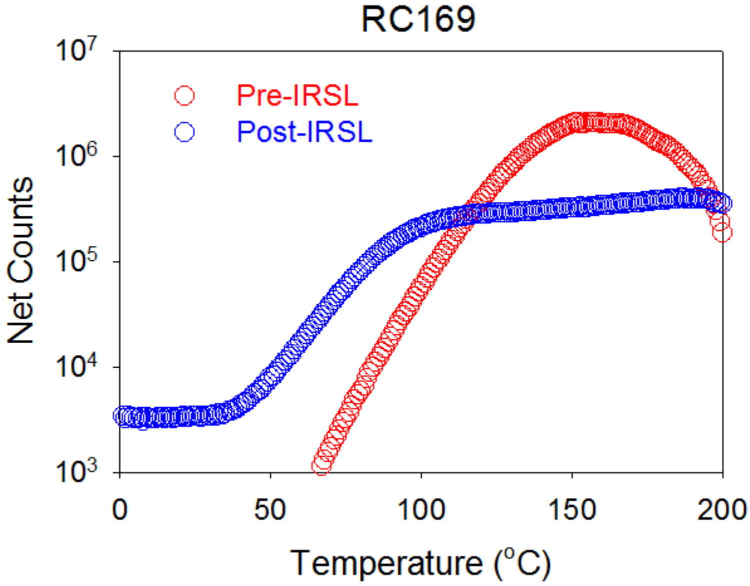

RC169

Pre-IRSL
Post-IRSL
Net Counts
10^7
10^6
10^5
10^4
10^3
0
50
100
150
200
Temperature (°C)

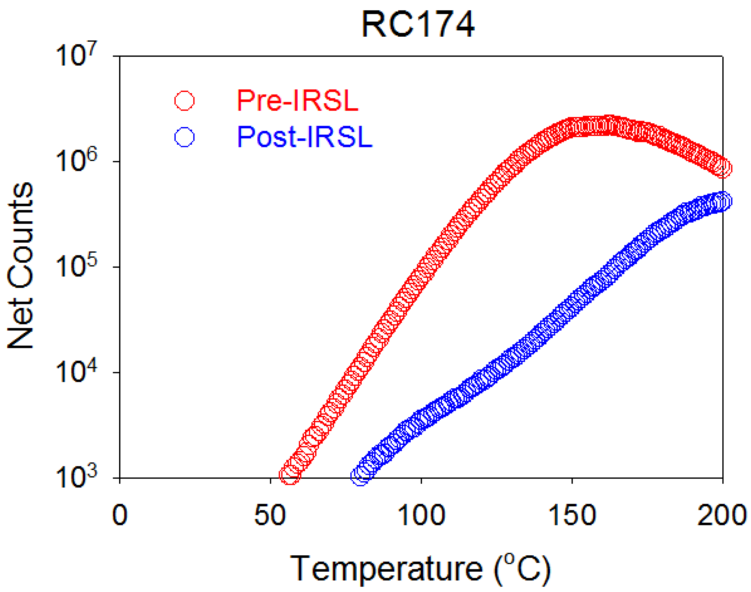
RC174
Pre-IRSL
Post-IRSL
Net Counts
10^7
10^6
10^5
10^4
10^3
0
50
100
150
200
Temperature (°C)

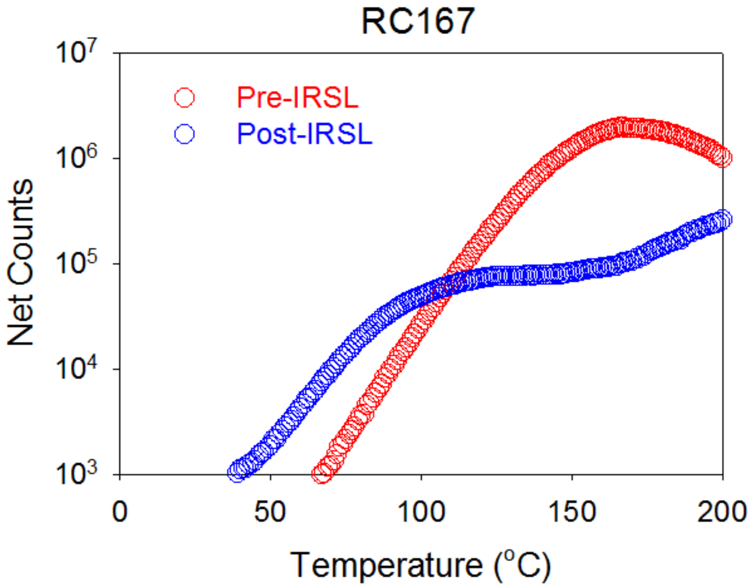
RC167
Pre-IRSL
Post-IRSL
Net Counts
10^7
10^6
10^5
10^4
10^3
0
50
100
150
200
Temperature (°C)

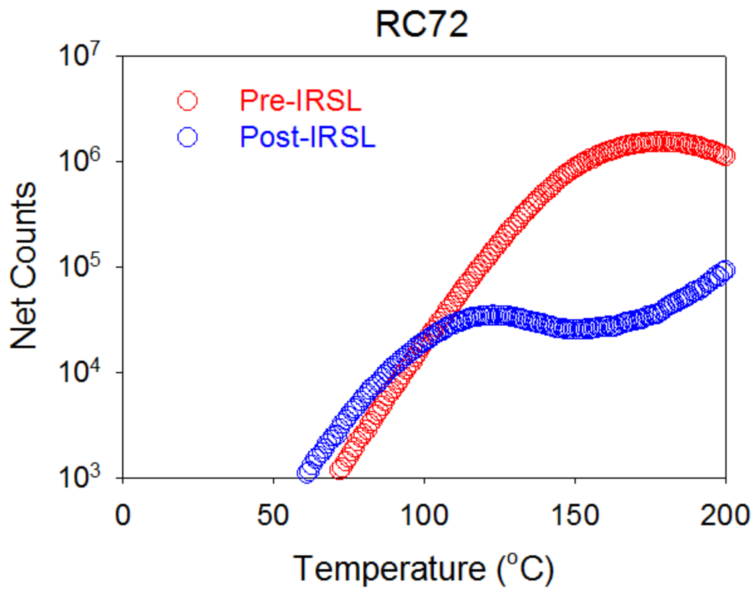
RC72
Pre-IRSL
Post-IRSL
Net Counts
10^7
10^6
10^5
10^4
10^3
0
50
100
150
200
Temperature (°C)

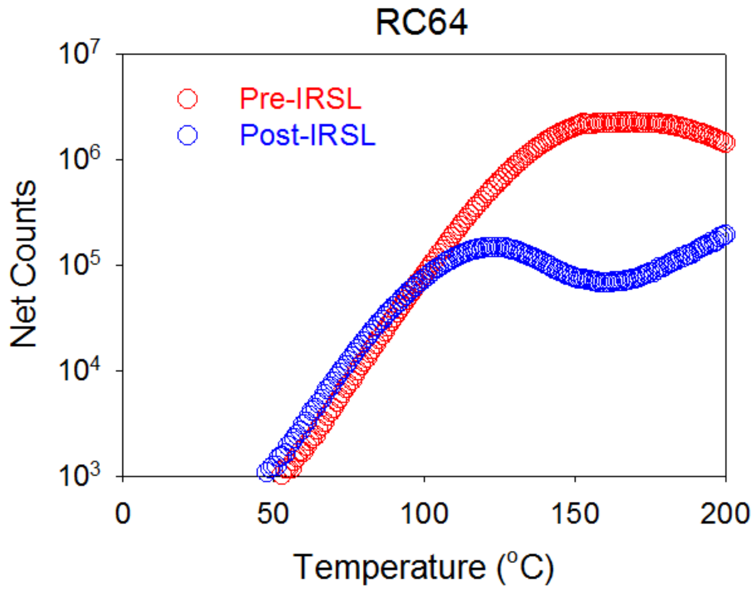
RC64
Pre-IRSL
Post-IRSL
Net Counts
10^7
10^6
10^5
10^4
10^3
0
50
100
150
200
Temperature (°C)

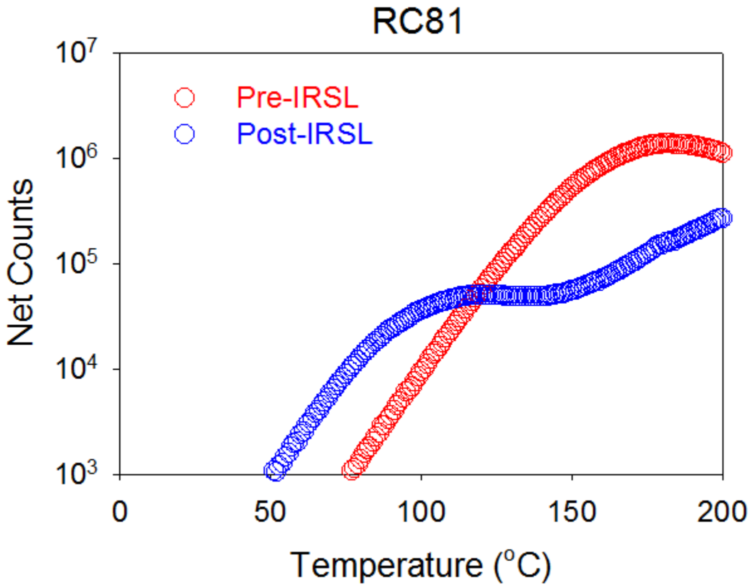
RC81
Pre-IRSL
Post-IRSL
Net Counts
10^7
10^6
10^5
10^4
10^3
0
50
100
150
200
Temperature (°C)

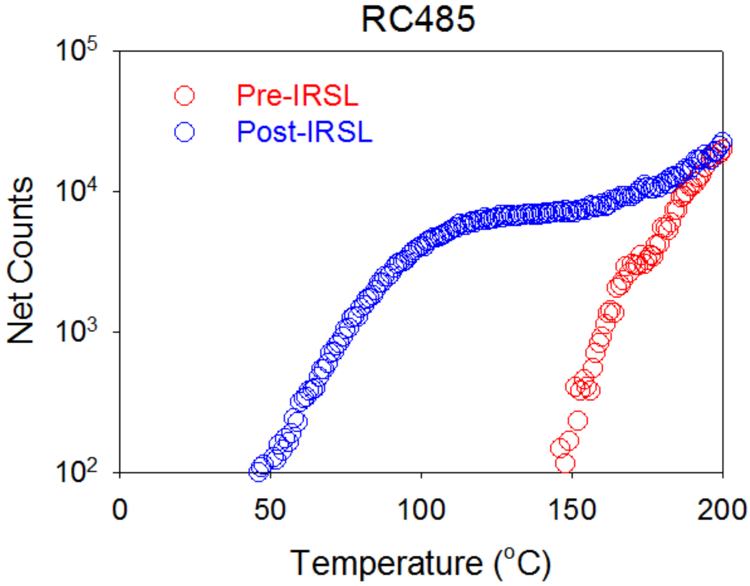
RC485
Pre-IRSL
Post-IRSL
Net Counts
10^5
10^4
10^3
10^2
0
50
100
150
200
Temperature (°C)

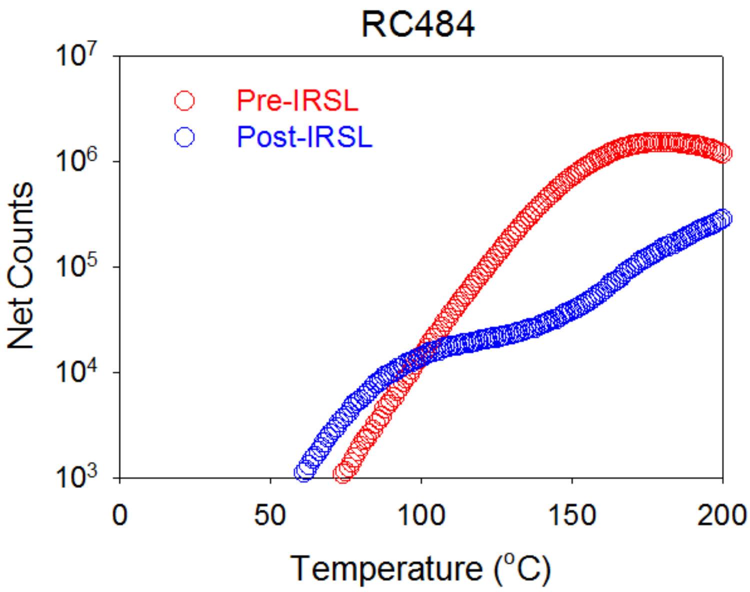
RC484
Pre-IRSL
Post-IRSL
Net Counts
10^3
10^4
10^5
10^6
10^7
0
50
100
150
200
Temperature (°C)

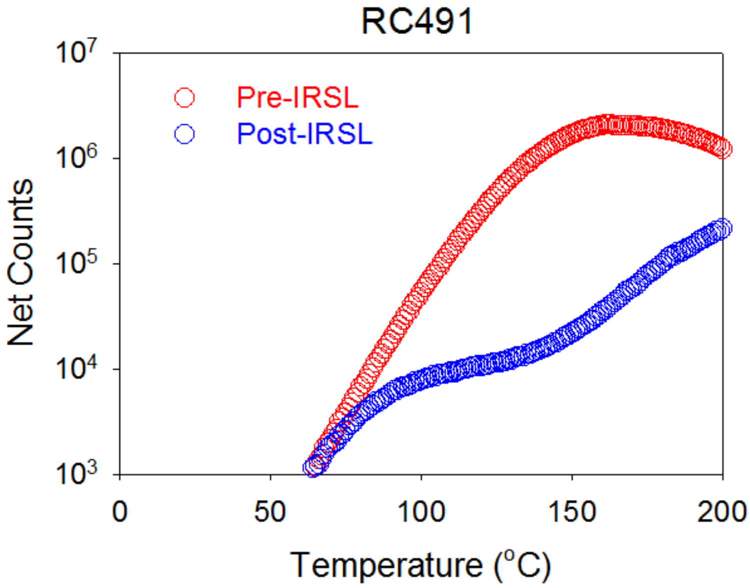
RC491
Pre-IRSL
Post-IRSL
Net Counts
10^3
10^4
10^5
10^6
10^7
0
50
100
150
200
Temperature (°C)

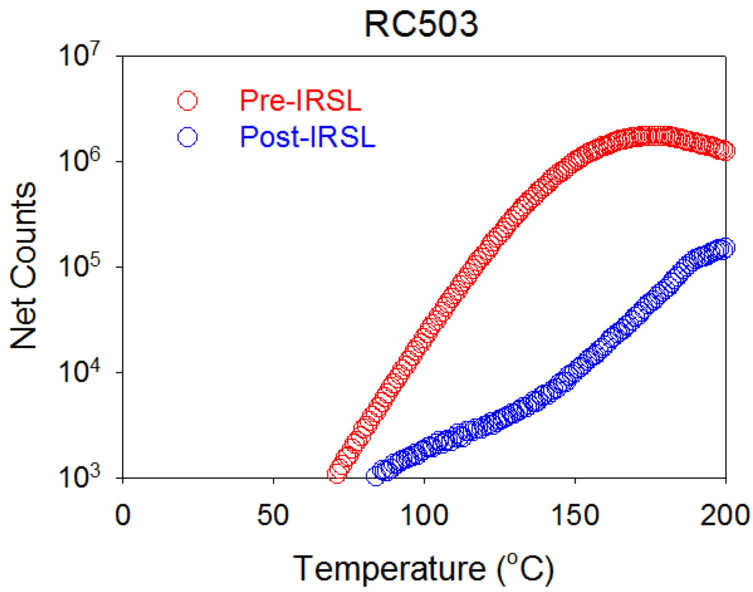
RC503
Pre-IRSL
Post-IRSL
Net Counts
10^3
10^4
10^5
10^6
10^7
0
50
100
150
200
Temperature (°C)

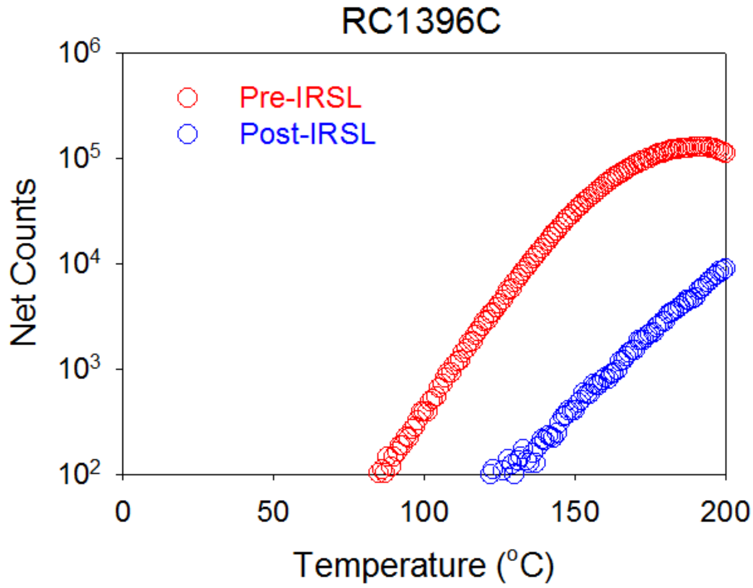
RC1396C
Pre-IRSL
Post-IRSL
Net Counts
10^2
10^3
10^4
10^5
10^6
0
50
100
150
200
Temperature (°C)

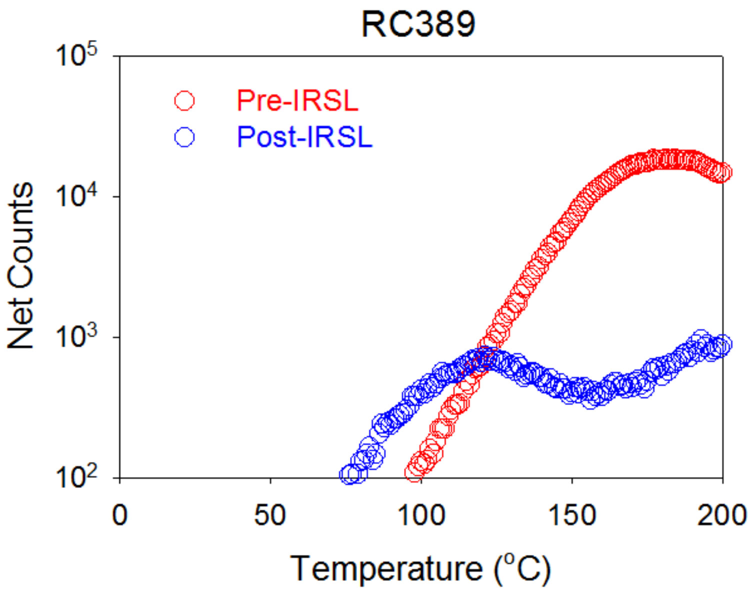
RC389
Pre-IRSL
Post-IRSL
Net Counts
10^5
10^4
10^3
10^2
0
50
100
150
200
Temperature (°C)

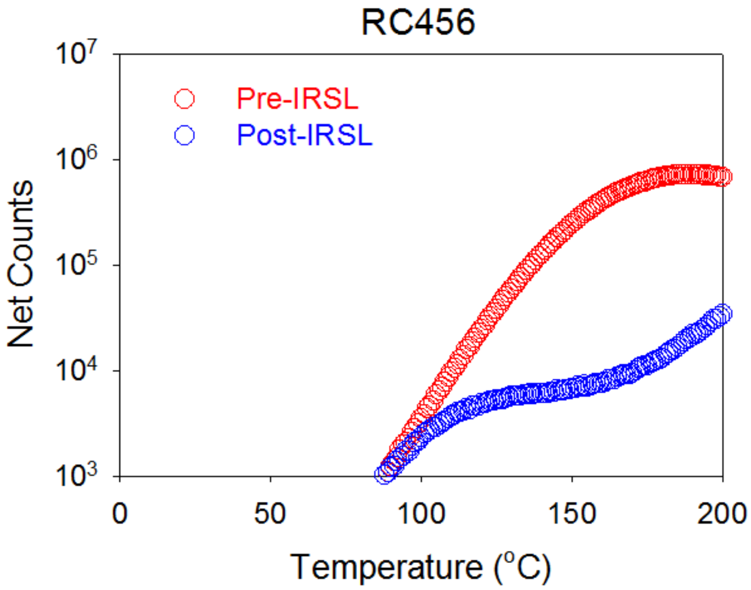
RC456
Pre-IRSL
Post-IRSL
Net Counts
10^7
10^6
10^5
10^4
10^3
0
50
100
150
200
Temperature (°C)

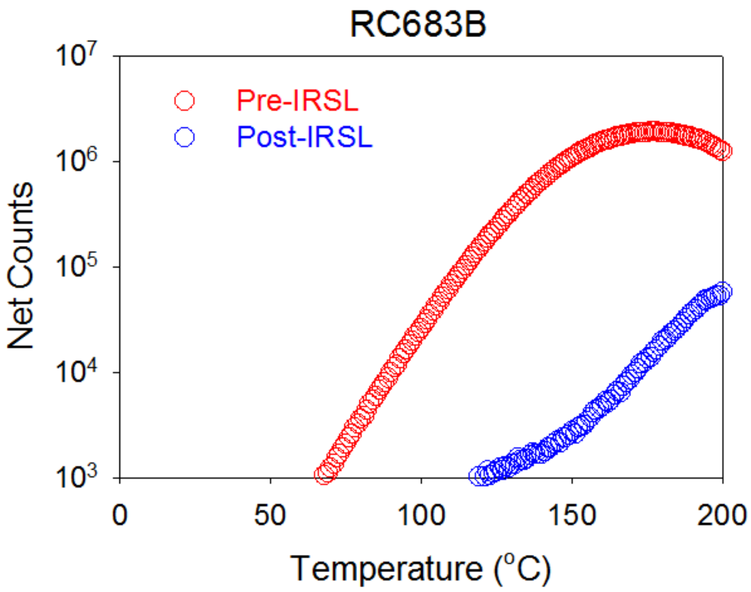

RC683B

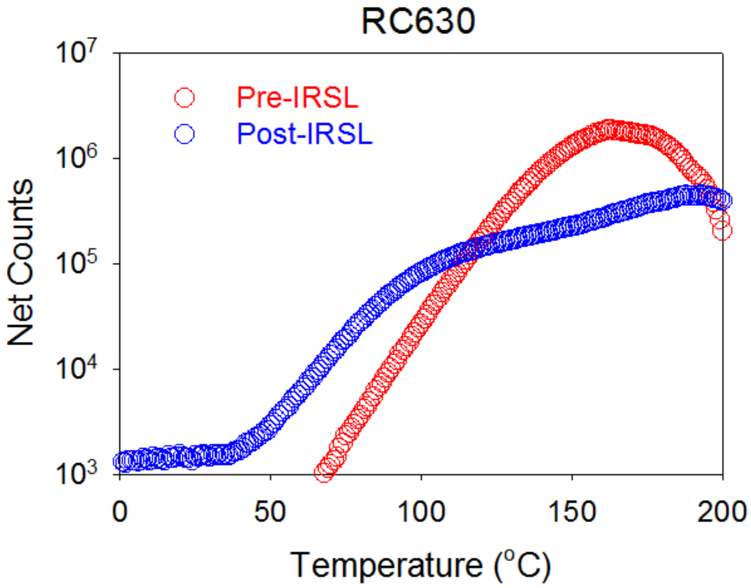

RC630

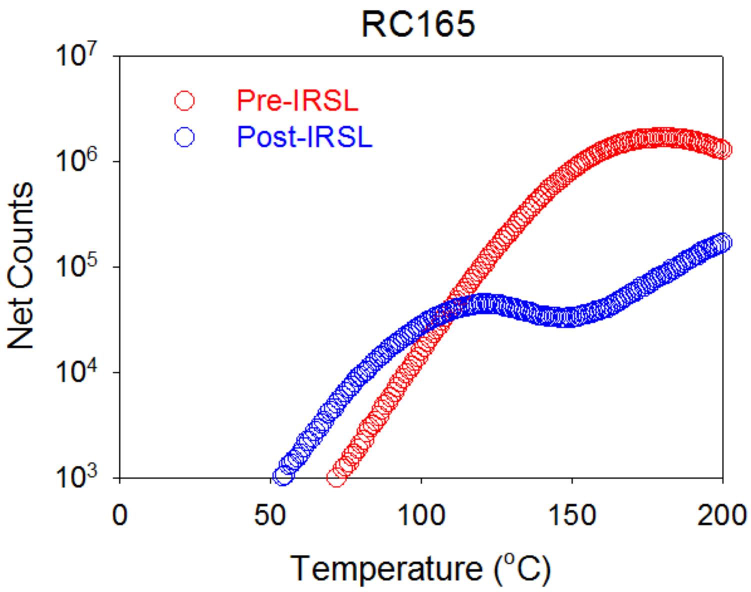
RC165
Pre-IRSL
Post-IRSL
Net Counts
10^7
10^6
10^5
10^4
10^3
0
50
100
150
200
Temperature (°C)

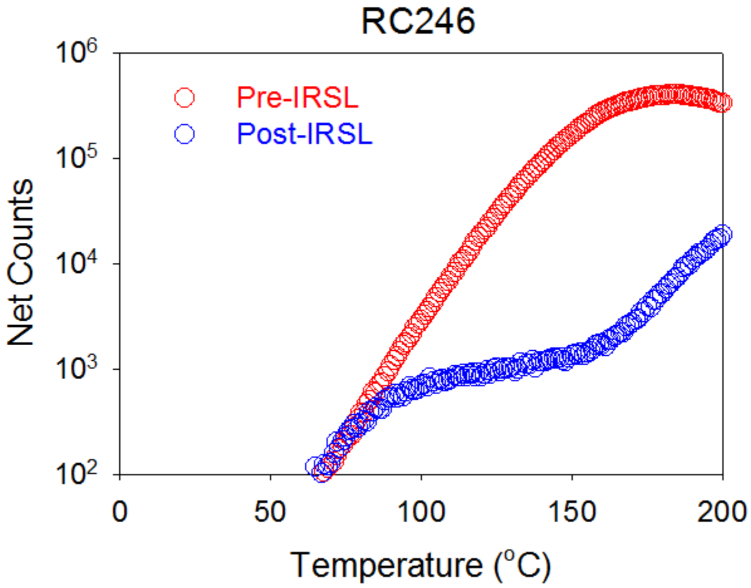
RC246
Pre-IRSL
Post-IRSL
Net Counts
10^6
10^5
10^4
10^3
10^2
0
50
100
150
200
Temperature (°C)

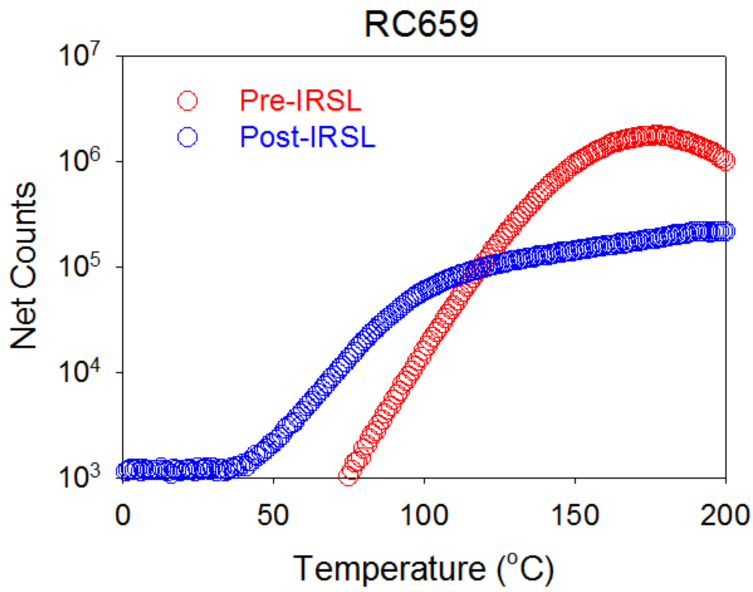
RC659

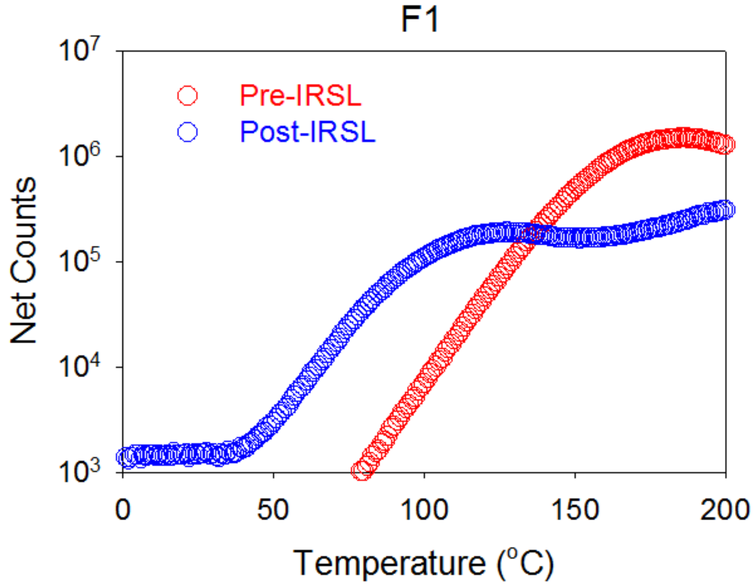
F1

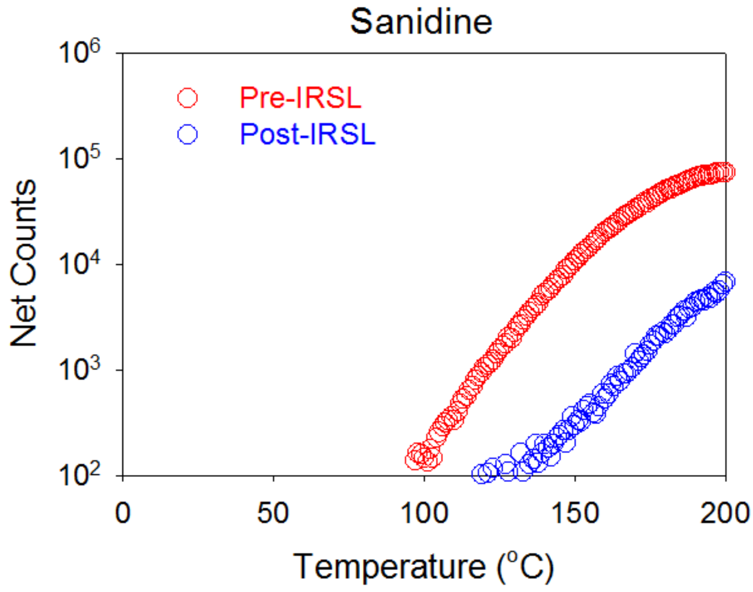
Sanidine

APPENDIX 4

TL Run	Peak Activation Temperature (°C)	Activation Energy (eV)	Mean Lifetime at 0°C (s)	Frequency Factor (s^{-1})
RC14 Pre-IRSL	150	1.1514 ± 0.005	1.129x10^{6}	1.954x10^{13}
RC14 Post-IRSL	154	0.7352 ± 0.003	2.016x10^{4}	1.114x10^{8}
RC168 Pre-IRSL	150	1.2156 ± 0.004	2.201x10^{6}	1.201x10^{14}
RC168 Post-IRSL	160	0.8678 ± 0.006	1.119x10^{5}	3.388x10^{9}
RC164 Pre-IRSL	151	1.1926 ± 0.006	1.88x10^{6}	5.774x10^{13}
RC164 Post-IRSL	120	0.8012 ± 0.002	5.089x10^{3}	5.668x10^{9}
RC169 Pre-IRSL	172	1.1969 ± 0.003	1.016x10^{7}	1.261x10^{13}
RC169 Post-IRSL	125	0.7275 ± 0.002	5.571x10^{3}	1.746x10^{9}
RC174 Pre-IRSL	167	1.1088 ± 0.005	2.544x10^{6}	1.668x10^{12}
RC174 Post-IRSL	125	0.7731 ± 0.004	5.571x10^{3}	1.746x10^{9}
RC167 Pre-IRSL	162	1.0796 ± 0.003	1.285x10^{6}	1.067x10^{12}
RC167 Post-IRSL	199	0.7132 ± 0.009	1.251x10^{5}	7.663x10^{6}
RC72 Pre-IRSL	177	1.1056 ± 0.003	4.904x10^{6}	7.646x10^{11}
RC72 Post-IRSL	122	0.8775 ± 0.009	1.076x10^{4}	5.129x10^{10}
RC64 Pre-IRSL	167	1.0811 ± 0.001	1.855x10^{6}	7.835x10^{11}
RC64 Post-IRSL	177	1.1056 ± 0.005	4.904x10^{6}	7.646x10^{11}
RC81 Pre-IRSL	180	1.1059 ± 0.004	6.024x10^{6}	6.297x10^{11}
RC81 Post-IRSL	114	0.8417 ± 0.009	4.629x10^{3}	2.985x10^{10}
RC485 Pre-IRSL	199	3.1662 ± 0.226	2.932x10^{19}	5.305x10^{33}
RC485 Post-IRSL	134	0.8940 ± 0.023	2.836x10^{4}	3.684x10^{10}
RC484 Pre-IRSL	179	1.0979 ± 0.003	5.113x10^{6}	5.444x10^{11}
RC484 Post-IRSL	199	0.2081 ± 0.005	3.467x10^{2}	9.038
RC491 Pre-IRSL	161	1.1090 ± 0.005	1.655x10^{6}	2.583x10^{12}
RC491 Post-IRSL	199	0.2113 ± 0.003	3.572x10^{2}	9.928
RC503 Pre-IRSL	176	1.1135 ± 0.005	5.035x10^{6}	1.011x10^{12}
RC503 Post-IRSL	199	0.3420 ± 0.004	1.393x10^{3}	3.996x10^{2}
RC1396C Pre-IRSL	191	1.1911 ± 0.005	3.682x10^{7}	2.781x10^{12}
RC1396C Post-IRSL	199	0.5014 ± 0.229	8.988x10^{3}	2.950x10^{4}
RC389 Pre-IRSL	183	1.1316 ± 0.012	1.010x10^{7}	1.015x10^{12}
RC389 Post-IRSL	120	0.8724 ± 0.050	8.969x10^{3}	5.053x10^{10}
RC456 Pre-IRSL	187	1.1741 ± 0.005	2.254x10^{7}	2.354x10^{12}
RC456 Post-IRSL	137	0.8131 ± 0.011	1.647x10^{4}	2.775x10^{9}
RC683B Pre-IRSL	176	1.0663 ± 0.006	2.868x10^{6}	2.858x10^{11}
RC683B Post-IRSL	199	0.3743 ± 0.007	2.007x10^{3}	9.676x10^{2}
RC630 Pre-IRSL	161	1.1532 ± 0.002	2.699x10^{6}	8.759x10^{12}
RC630 Post-IRSL	187	0.7427 ± 0.004	1.841x10^{6}	2.794x10^{7}
RC165 Pre-IRSL	180	1.1379 ± 0.003	6.914x10^{8}	1.471x10^{12}
RC165 Post-IRSL	119	0.8378 ± 0.009	1.567x10^{5}	1.870x10^{10}
RC246 Pre-IRSL	182	1.1376 ± 0.005	7.891x10^{8}	1.272x10^{12}
RC246 Post-IRSL	199	0.1802 ± 0.005	5.384x10^{2}	3.941
RC659 Pre-IRSL	177	1.1682 ± 0.006	9.082x10^{8}	4.060x10^{12}
RC659 Post-IRSL	128	0.7448 ± 0.004	9.114x10^{4}	6.172x10^{8}
F1 Pre-IRSL	185	1.1380 ± 0.006	9.732x10^{8}	1.049x10^{12}
F1 Post-IRSL	125	0.8332 ± 0.004	2.221X10^{5}	1.085x10^{10}
Sanidine Pre-IRSL	199	1.1317 ± 0.008	2.184x10^{9}	3.580x10^{11}

Sanidine Post-IRSL	199	0.8551 ± 0.040	2.032x10^{7}	3.009x10^{8}

APPENDIX 5

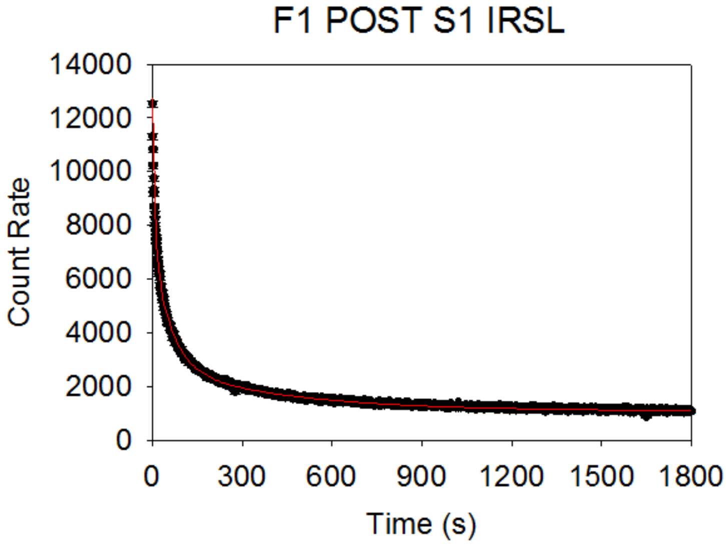

R = 0.99895494 Rsqr = 0.99791097 Adj Rsqr = 0.99790398

Standard Error of Estimate = 48.8797

	Coefficient	**Std. Error**	**t**	**P**
y0	1088.5890	3.4276	317.5971	<0.0001
a	5235.7987	51.1076	102.4466	<0.0001
b	0.1231	0.0024	52.1023	<0.0001
c	4683.3795	40.1966	116.5117	<0.0001
d	0.0172	0.0002	72.1964	<0.0001
g	1726.2745	20.5886	83.8463	<0.0001
h	0.0024	0.0000	67.9841	<0.0001

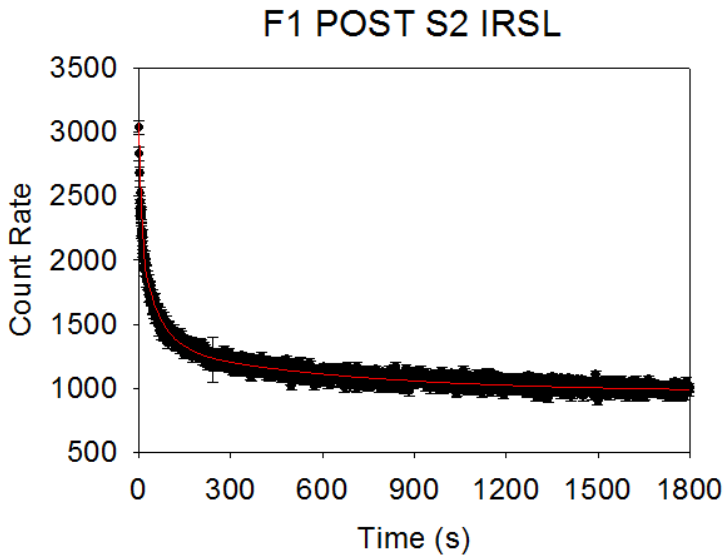

R = 0.98478172 Rsqr = 0.96979504 Adj Rsqr = 0.96969397

Standard Error of Estimate = 34.3899

	Coefficient	Std. Error	t	P
y0	970.4965	4.4395	218.6059	<0.0001
a	922.3825	34.2375	26.9407	<0.0001
b	0.1442	0.0107	13.4190	<0.0001
c	809.4961	23.5197	34.4179	<0.0001
d	0.0170	0.0008	22.4276	<0.0001
g	369.2980	7.6842	48.0595	<0.0001
h	0.0016	0.0001	19.4659	<0.0001

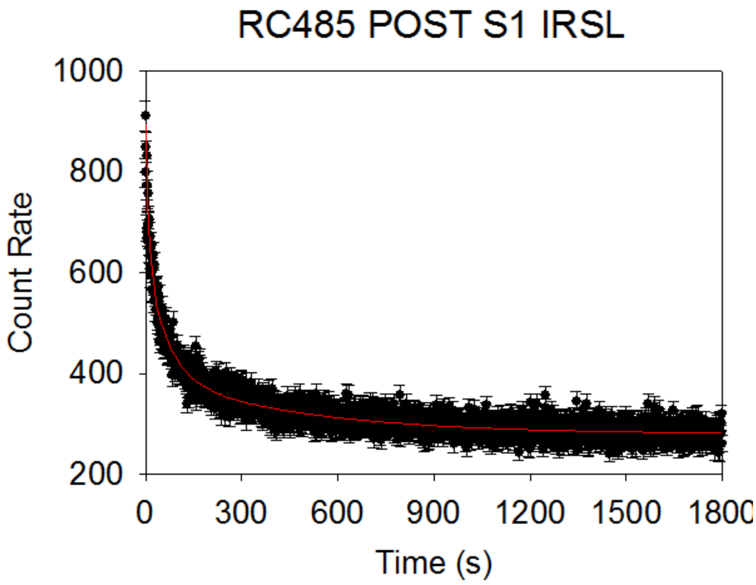

R = 0.96106440 Rsqr = 0.92364478   Adj Rsqr = 0.92338927

Standard Error of Estimate = 18.4304

	Coefficient	**Std. Error**	**t**	**P**
y0	279.0005	1.5585	179.0225	<0.0001
a	245.8959	19.5420	12.5829	<0.0001
b	0.1046	0.0158	6.6240	<0.0001
c	249.8423	16.3441	15.2864	<0.0001
d	0.0160	0.0016	10.0102	<0.0001
g	119.9164	7.3002	16.4265	<0.0001
h	0.0022	0.0002	11.8384	<0.0001

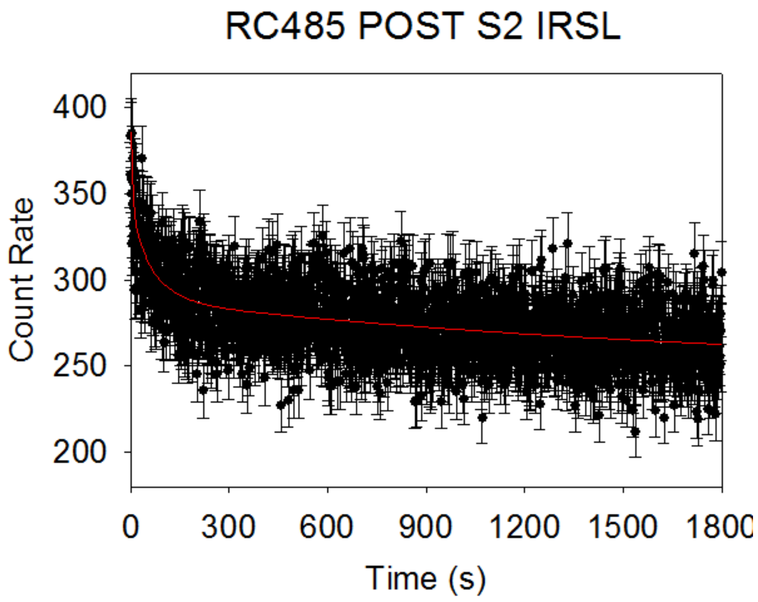

R = 0.60518805 Rsqr = 0.36625257 Adj Rsqr = 0.36413183

Standard Error of Estimate = 17.1398

	Coefficient	Std. Error	t	P
y0	247.4858	16.1836	15.2924	<0.0001
a	45.8558	18.8564	2.4318	0.0151
b	0.1892	0.1425	1.3271	0.1847
c	50.7619	7.9811	6.3603	<0.0001
d	0.0149	0.0038	3.9096	<0.0001
g	41.4317	13.3796	3.0966	0.0020
h	0.0006	0.0004	1.4121	0.1581

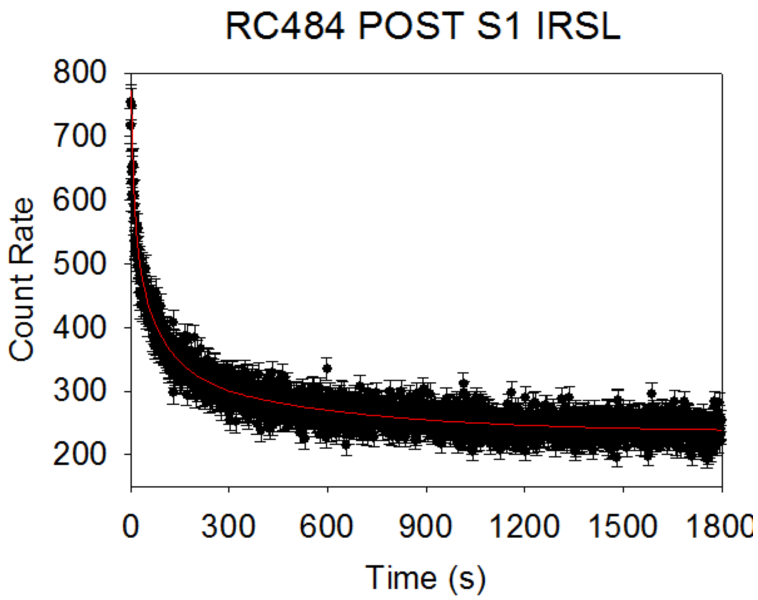

R = 0.96106440 Rsqr = 0.92364478 Adj Rsqr = 0.92338927

Standard Error of Estimate = 18.4304

	Coefficient	Std. Error	t	P
y0	279.0005	1.5585	179.0225	<0.0001
a	245.8959	19.5420	12.5829	<0.0001
b	0.1046	0.0158	6.6240	<0.0001
c	249.8423	16.3441	15.2864	<0.0001
d	0.0160	0.0016	10.0102	<0.0001
g	119.9164	7.3002	16.4265	<0.0001
h	0.0022	0.0002	11.8384	<0.0001

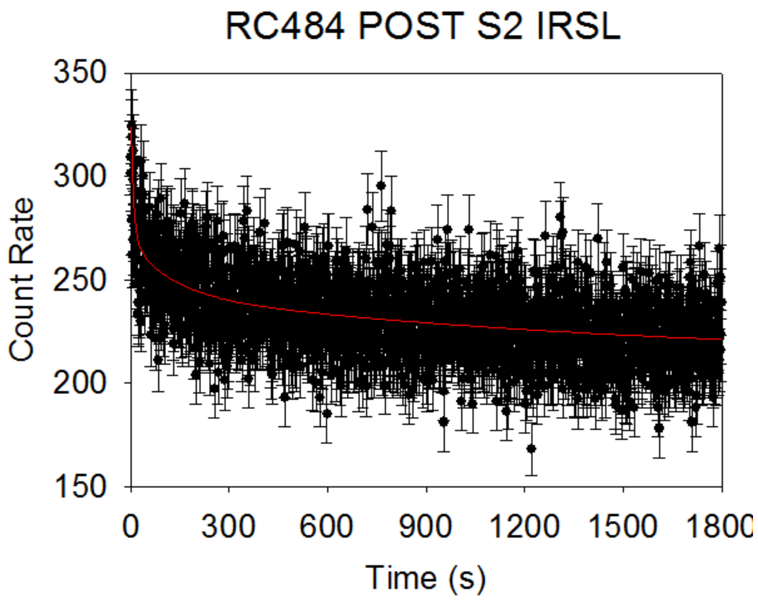

R = 0.96106440 Rsqr = 0.92364478   Adj Rsqr = 0.92338927

Standard Error of Estimate = 18.4304

	Coefficient	**Std. Error**	**t**	**P**
y0	279.0005	1.5585	179.0225	<0.0001
a	245.8959	19.5420	12.5829	<0.0001
b	0.1046	0.0158	6.6240	<0.0001
c	249.8423	16.3441	15.2864	<0.0001
d	0.0160	0.0016	10.0102	<0.0001
g	119.9164	7.3002	16.4265	<0.0001
h	0.0022	0.0002	11.8384	<0.0001

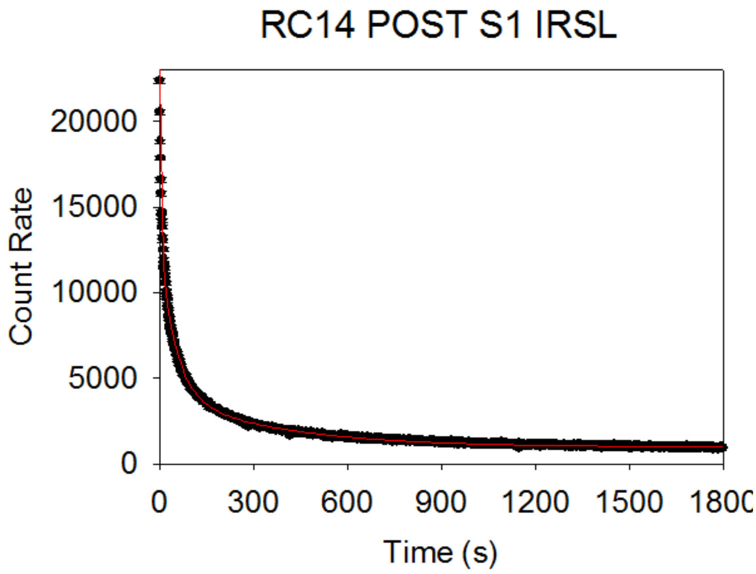

R = 0.99928001 Rsqr = 0.99856054 Adj Rsqr = 0.99855572

Standard Error of Estimate = 71.2862

	Coefficient	**Std. Error**	**t**	**P**
y0	987.4198	4.0469	243.9924	<0.0001
a	10472.0820	79.2837	132.0837	<0.0001
b	0.1526	0.0023	65.9538	<0.0001
c	8883.0603	59.6720	148.8649	<0.0001
d	0.0201	0.0002	93.8422	<0.0001
g	3136.2269	29.4521	106.4856	<0.0001
h	0.0028	0.0000	93.1233	<0.0001

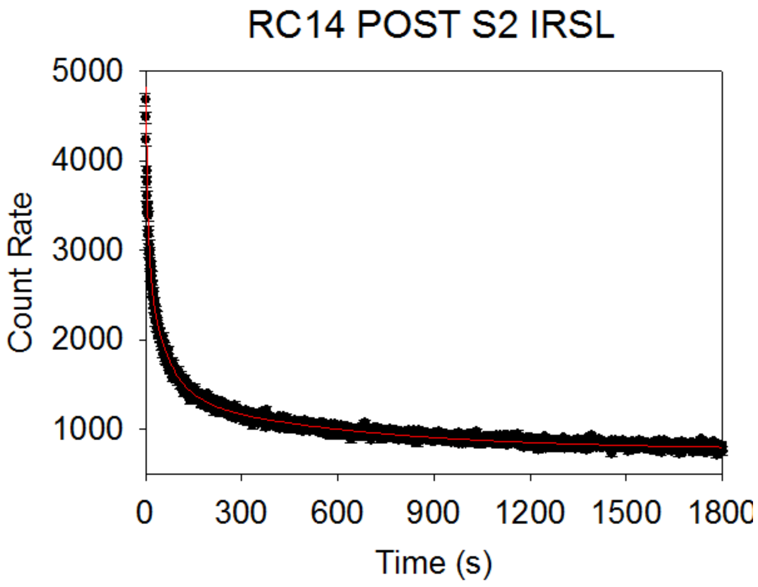

R = 0.99577625 Rsqr = 0.99157034 Adj Rsqr = 0.99154213

Standard Error of Estimate = 33.9791

	Coefficient	**Std. Error**	**t**	**P**
y0	771.6917	4.0358	191.2133	<0.0001
a	1972.9009	34.1427	57.7840	<0.0001
b	0.1138	0.0039	29.4673	<0.0001
c	1439.0970	27.9179	51.5474	<0.0001
d	0.0162	0.0005	35.5336	<0.0001
g	642.1790	9.2017	69.7894	<0.0001
h	0.0017	0.0001	33.5819	<0.0001

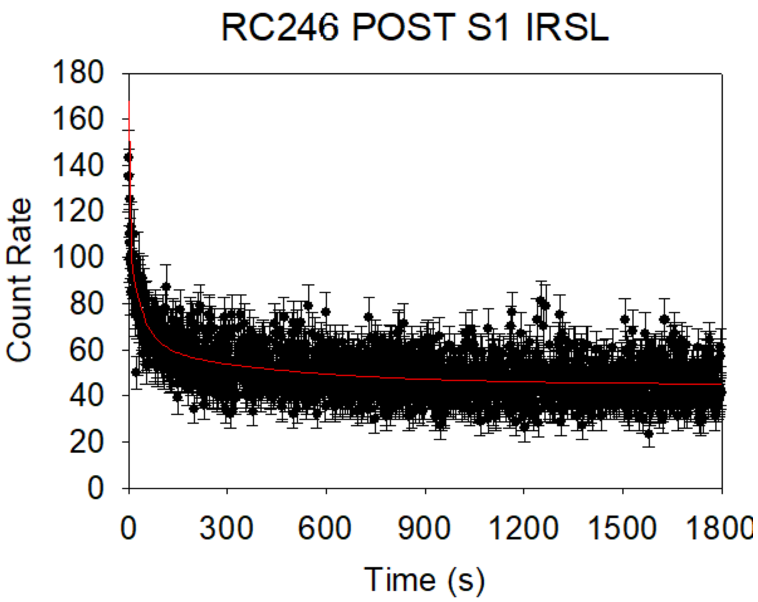

R = 0.70612517 Rsqr = 0.49861275 Adj Rsqr = 0.49693493

Standard Error of Estimate = 8.3953

	Coefficient	**Std. Error**	**t**	**P**
y0	44.8528	0.6109	73.4169	<0.0001
a	65.0013	16.6317	3.9083	<0.0001
b	0.3946	0.1502	2.6270	0.0087
c	41.0428	4.1947	9.7845	<0.0001
d	0.0228	0.0042	5.4599	<0.0001
g	17.0909	1.9891	8.5922	<0.0001
h	0.0022	0.0004	4.9721	<0.0001

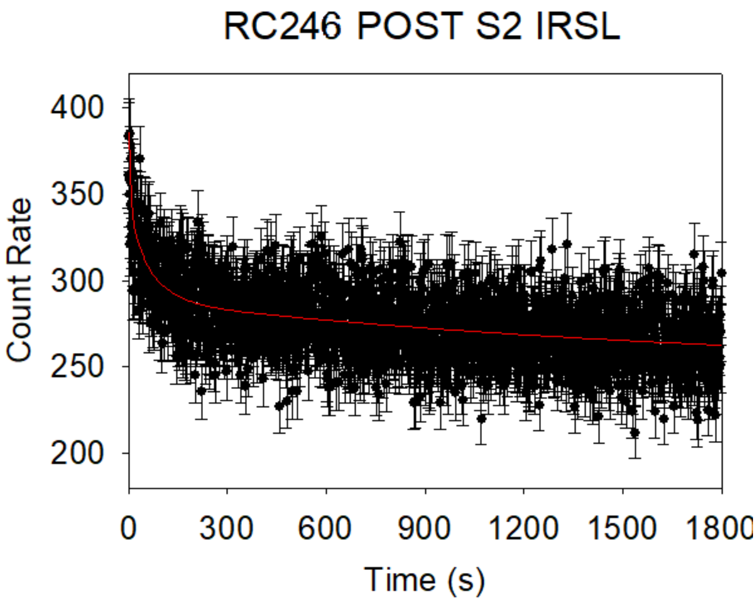

R = 0.70612517 Rsqr = 0.49861275 Adj Rsqr = 0.49693493

Standard Error of Estimate = 8.3953

	Coefficient	Std. Error	t	P
y0	44.8528	0.6109	73.4169	<0.0001
a	65.0013	16.6317	3.9083	<0.0001
b	0.3946	0.1502	2.6270	0.0087
c	41.0428	4.1947	9.7845	<0.0001
d	0.0228	0.0042	5.4599	<0.0001
g	17.0909	1.9891	8.5922	<0.0001
h	0.0022	0.0004	4.9721	<0.0001